Precision Laser Spectroscopy of Rubidium with a Frequency Comb

Luke Anthony Mavilio Johnson
School of Physics and Astronomy
University of Leeds

A thesis submitted for the degree of
Doctor of Philosophy

31st August 2011

The candidate confirms that the work submitted is his own, except where work which has formed part of jointly-authored publications has been included. The contribution of the candidate and the other authors to this work has been explicitly indicated below. The candidate confirms that appropriate credit has been given within the thesis where reference has been made to the work of others.

This submitted thesis contains work from the following list of publications.

Chapter 4: Absolute frequency measurements of ^{85}Rb $n\mathbf{F}_{7/2}$ Rydberg states using purely optical detection
L. A. M. Johnson, H. O. Majeed, B. Sanguinetti, Th. Becker and B. T. H. Varcoe
Published: New Journal of Physics. **12**, 063028 (2010).

Myself: Construction of experiment, collecting experimental data, analysing data, error analysis, writing the paper.
H. O. Majeed: Construction of experiment, collecting experimental data.
B. Sanguinetti: Development of metrology techniques.
Th. Becker: Useful discussion.
B. T. H. Varcoe: Supervisor.

Chapter 5: A three step laser stabilisation scheme for excitation to Rydberg levels in ^{85}Rb
L. A. M. Johnson, H. O. Majeed and B. T. H. Varcoe
Published: Applied Physics B: Lasers and Optics. **106**(2) (2011).

Myself: Construction of experiment, collecting experimental data, analysing data, writing the paper.
H. O. Majeed: Construction of experiment.
B. T. H. Varcoe: Supervisor.

Luke Johnson **Benjamin Varcoe**

I dedicate this thesis to the memory of both my Grandads,
Norman Johnson and Antonio Mavilio.

Acknowledgements

To begin, I would like to thank my supervisor Ben Varcoe for making this research possible. He has always supported my new ideas in the lab, and I will always be grateful of my time spent with him at Leeds. Also, many thanks to the EPSRC and STFC for funding this research. And of course, a special thanks to the University of Leeds for both funding my scholarship and supporting me as a student.

I would like to acknowledge all my lab colleagues. Many thanks to Matt Hill and Joe Cotter for looking after me for the first few months of my PhD. I am especially indebted to Matt, who showed me the way in the lab from day one and supported me throughout my entire first year, Skål! Another very special thanks to Martin Jones, who has always been there to answer my physics-related questions and has become a good friend. Your services throughout writing this thesis are truly appreciated, thank you for spotting all my 'none-sensical' spelling mistakes! I must also say how grateful I am of Hawri Majeed, who was the first to introduce me to Rydberg spectroscopy. We made some excellent progress together in the lab and I will never forget the first time we saw the 60F state in the cell! Also many thanks to Melody Blackman, who I had the pleasure of working with for several months (including the odd weekend), you always kept me company in the lab during quiet times. I won't forget the afternoon of sugar-fuelled office antics! I also want to say thank you to Bruno Sanguinetti, who taught me many things about precision spectroscopy and is a genuinely clever and kind person. Finally, thanks to Mark Everitt (the fountain of knowledge for all things computing) and Nick Lewty (the lab funny-guy). You all made my time at Leeds unforgettable.

On the technical side of things, I must say thank you to everyone in the mechanical workshop, especially Stuart Weston. In the electronics workshop my thanks go to Andrew Price and Paul Ogden. I am also appreciative of Brian Chesworth for taking care of many complicated orders and shipping returns! I am grateful of Marc Fischer at Menlo for all the technical support, and also everyone else at Menlo for lending me a Rb reference in a time of need. Also a very special thanks to Thomas Becker at the MPQ who got us detecting our first Rydbergs in the cell. And finally a big thank you to Steve Green for his workshop skills!

Most importantly, I must thank my family. My mum, dad and sister have always been there for me through 10 years of studying physics. I would never be where I am now if it was not for their love and support from the beginning to end. Thank you to all of you, and to all my other great family and friends. Finally, the biggest thanks will always go to my beautiful wife Tash who has been there for me everyday throughout this PhD, and has always been understanding and supportive through the good and bad days. I would never have got this far without you, thank you for believing in me and thank you for being a 'Northerner' with me!

Abstract

The development of the optical frequency comb technique has transformed the field of spectroscopy, allowing the measurement of atomic transition frequencies to unprecedented levels of accuracy. In this thesis a frequency comb has been used to make absolute frequency measurements of optical transitions to highly excited Rydberg levels in Rb. The reliable measurement of these levels plays an important role in improving the accuracy of atomic models and the widely used Rb atom is an excellent candidate for such studies. A laser system has been constructed and optimised for resolving these highly excited states in an ordinary vapour cell, using a Doppler-free technique of purely optical detection. After several developments to the apparatus, the absolute energies of a collection of Rydberg levels have been measured to an accuracy of 3 parts in 10^{10}, demonstrating the first sub-megahertz accuracy optical Rydberg spectroscopy. A vapour cell is a convenient and straightforward solution for finding Rydberg levels and these findings show that cell-based detection techniques could potentially permit rapid advances in the field.

Along the way, the vapour cell sample has also highlighted many interesting areas of exploration: For example, it has allowed long term laser stabilisation to Rydberg levels for experiments such as the micromaser. Also, the Rydberg atoms in the cell have been manipulated by microwaves, allowing the study of high $\ell = 4$ states, which has illuminated a whole range of new experiments. It has even been found that one of the limiting factors of these cell-based schemes may be the knowledge of the frequency of lower lying transitions, which has ultimately led this research into a secondary area, involving the measurement of the Rb D lines with a frequency comb. Together, these findings have exposed a large variety of atomic physics to be investigated in the future.

Abbreviations

AC	Alternating current
AMD	Alkali metal dispenser
AOM	Acousto-optic modulator
APC	Angled-physical-contact
APD	Avalanche photodiode
BDU	Beat detection unit
CW	Continuous wave
DAC	Digital to analogue converter
DBM	Double balanced mixer
DC	Direct current
DDS	Direct digital synthesiser
DRO	Dielectric resonator oscillator
ECDL	External cavity diode laser
EDFA	Erbium doped fibre amplifier
EIT	Electromagnetically induced transparency
EOM	Electro-optic modulator
FET	Field-effect-transistor
FM	Frequency modulation
FP	Fabry Pérot etalon
FWHM	Full width at half maximum
GL	Glan-laser polariser
GT	Glan-Thompson polariser
GPIB	General-purpose-interface-bus
GPS	Global positioning system
INF	Interference filter
IF	Intermediate frequency
IR	Infra-red
LC	Inductor-capacitor
LED	Light emitting diode
LIA	Lock-in amplifier
LO	Local oscillator
MOT	Magneto-optical trap
ND	Neutral-density filter
NIR	Near infra-red
PBS	Polarising beam splitter
PD	Photodiode
PI	Proportional-integral
PID	Proportional-integral-differential
PLL	Phase-locked-loop
PM	Polarisation-maintaining
PMT	Photomultiplier tube
PPLN	Periodically-poled $LiNbO_3$
QA	Quantum amplification
QED	Quantum electrodynamics
RAM	Residual amplitude modulation
RBW	Resolution bandwidth
RF	Radio frequency
SAS	Saturated absorption spectroscopy
SHG	Second harmonic generation
SMF	Single-mode fibre
SNR	Signal to noise ratio
UV	Ultra-violet
VCO	Voltage controlled oscillator
1PPS	One pulse per second

Contents

List of Figures

List of Tables

Chapter 1

Introduction

Spectroscopy plays an integral part in our understanding of the laws of the universe, with a huge array of physics open to study via the measurement and implementation of atomic resonances. The development of lasers in the 1960s (1), Doppler-free techniques in the 1970s (2; 3; 4; 5) and optical counting techniques in the 1990s (6) has transformed the field of spectroscopy, introducing a new era of 'precision laser spectroscopy'. Experiments have become so sensitive that from the precise measurement of atomic resonances it is now possible to check for deviations between experiments and well known physical theories with extraordinary accuracy. For example, energy levels of H can now be compared with the predictions of QED to 14 significant digits (7; 8; 9). No other branch of science offers such a variety of truly fundamental physics to be studied, from what are often table-top experiments. These studies include precision measurements of Lamb shifts (10; 11), searching for time variations of the fundamental constants including α (8; 12), studying the symmetry of matter and antimatter (13; 14), verifying the predictions of Special Relativity, (15; 16), observing General Relativistic effects in the lab (17; 18) and many more. The frequencies of atomic resonances have rapidly become the most accurately measured quantities in physics.

1.1 Atomic spectroscopy

The measurement of atomic resonances began as early as 1817 when Fraunhofer made wavelength measurements of the dark absorption bands in the Sun's spectrum (19). By 1860 Kirchhoff and Bunsen had identified some of the same lines emitted from heated elements in the lab and realised that each element could be recognised by a unique set

of spectral lines (20). This discovery made spectroscopy a new scientific field, and in 1868 Angstrom was successful in identifying and accurately measuring the wavelengths of the first visible lines of H (21). This subsequently led to the famous Balmer equation in 1885 (22), describing the positions of these lines, which ultimately gave the foundations of Bohr's quantum theory in 1913 (23).

These early lab studies involved capturing *emitted* light from excited atoms and using a spectrograph as a wavelength ruler. In this case, the spectral resolution was always limited by the resolving power of the spectrograph. Even for a very good modern-day spectrograph this is typically several hundreds of megahertz (24). Another technique involves monitoring instead the *absorption* of a light source by a sample of atoms. This was the technique of choice for microwave spectroscopy, which was developed in the 1940s (25). With a single frequency widely tunable microwave synthesiser, one can readily study the frequency response of a sample. In optical spectroscopy however, light sources were broadband, incoherent and non-tunable, therefore these types of measurement were limited to studying dark absorption lines on a spectrograph.

It was the development of lasers in the 1960s (1) that supplied, for the first time, a tunable and monochromatic light source. This opened up the possibility of orders of magnitude of improvement, in both the spectral resolution and detection sensitivity of atomic spectroscopy. Lasers with linewidths on the 1 MHz level meant that the spectral resolution of laser absorption spectroscopy was now limited by the transition linewidth. Therefore for laser spectroscopy of thermal atomic vapours, it was now the Doppler broadening of the spectral lines (caused by the motion of the atoms) which limited the resolution. The 1970s saw breakthroughs in non-linear spectroscopic techniques to eliminate this broadening mechanism, and to ultimately achieve sub-Doppler resolution.

1.2 Beyond Doppler broadening

1.2.1 The Doppler width

An atomic resonance of frequency f_{12} between two atomic levels 1 and 2 can be described by a homogeneously broadened Lorentzian line profile. The absorption of laser light with frequency f follows a relation

$$L(f - f_{12}) = \frac{\Gamma}{2\pi} \frac{1}{(f - f_{12})^2 + (\Gamma/2)^2}, \tag{1.1}$$

where Γ is the full width at half maximum (FWHM) of the line, or the natural linewidth. For an atom that is moving relative to the laser with velocity v, the laser frequency must be replaced with $(1 \pm \frac{v}{c})f$ to account for the first order Doppler shift of the laser in the atom's frame [1]. For a collection of thermal atoms, this Lorentzian line shape is therefore integrated over all velocity classes, with a Maxwell-Boltzmann thermal velocity distribution, giving an absorption coefficient

$$\alpha(f - f_{12}) \propto \int_{-\infty}^{+\infty} \frac{1}{u\sqrt{\pi}} \exp(-\frac{v^2}{u^2}) L(f + \frac{v}{c}f - f_{12})\, \mathrm{d}v. \tag{1.2}$$

The result is a Doppler broadened line profile, where $u = \sqrt{\frac{2k_B T}{M}}$, T is the thermal temperature and M is the mass of the atoms involved. The Doppler width is defined as $\Delta f_D = 2\sqrt{\ln 2}(\frac{u}{\lambda})$, where λ is the laser wavelength. For many atomic or molecular species existing as a room temperature vapour $\Delta f_D \gg \Gamma$. Therefore the resonance linewidth is broadened to an inhomogeneous Gaussian line shape, which can limit the resolution of laser spectroscopy to hundreds of megahertz. The Doppler width is also often larger than the hyperfine splittings, meaning that atomic detail is masked.

1.2.2 Doppler-free techniques

Collimated beam spectroscopy

Generating a collimated beam of atoms gives a highly non-isotropic atomic sample, and by probing this beam with a laser perpendicular to the beam propagation direction, one can largely reduce the effect of Doppler broadening. This is depicted in Figure 1.1.

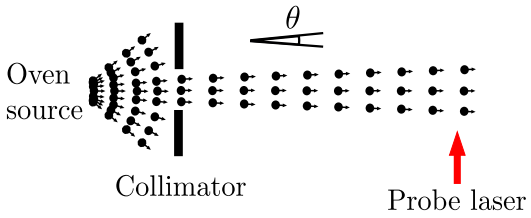

Figure 1.1: Collimated beam spectroscopy. If the atoms are probed with a laser at 90° to the beam direction, the Doppler width of the atoms can be made much smaller than the equivalent thermal Doppler width.

[1] The higher order Doppler shift terms are not considered throughout this thesis, they are typically more than $10^6\times$ smaller than the first order shift. The second order shift is discussed in Section 9.5.5.

If the beam has a velocity distribution along its axis with Doppler width Δf_D and a small divergence angle of θ, the Doppler width to a perpendicular observer is $\sim \theta \Delta f_D$. With sufficient collimation, Doppler broadening can be reduced by a few orders of magnitude. This was the first technique of Doppler-free spectroscopy and was actually developed by Meissner (26) well before the development of lasers. In these experiments atoms were typically excited using electron impact and emitted light was captured perpendicular to the beam and measured with a spectrograph.

Saturated absorption spectroscopy

Saturated absorption spectroscopy (SAS) was developed independently by Hänsch and Borde in 1970 (2; 3). The technique was the first demonstration of eliminating Doppler broadening in laser spectroscopy of thermal atoms outside the laser cavity. The approach is based around the velocity-selective saturation of an atomic transition, depicted in Figure 1.2.

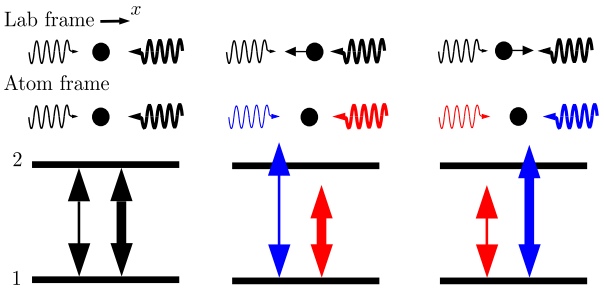

Figure 1.2: Saturated absorption spectroscopy (SAS). Only stationary atoms are in resonance with the pump and probe laser simultaneously and can contribute to the spectroscopic signal.

A strong pump beam and a weak probe beam derived from the same laser counter-propagate through a thermal distribution of atoms. The laser is tuned onto resonance with a transition and the probe absorption is monitored. When the pump beam acts on the transition, atomic population is moved from level 1 to 2 and the transition becomes saturated, as a result the probe absorption is reduced. If the two laser frequencies are f_{pr}=f_{pu}=f, the two laser detunings in the atomic frame are

$$\delta_{pr} = f - \frac{v}{c}f - f_{12} \qquad (1.3) \qquad\qquad \delta_{pu} = f + \frac{v}{c}f - f_{12}. \qquad (1.4)$$

When $f = f_{12}$, only atoms that move perpendicular to the lasers, with zero velocity component along this axis, can achieve the $\delta_{pr} = \delta_{pu} = 0$ condition. Atoms with a finite velocity component along this axis cannot be resonant with the pump and probe laser simultaneously. Therefore the decreased absorption signal of the probe beam, known as the 'Lamb dip' (27), is free from Doppler broadening and can approach the natural linewidth of the transition. The pump beam 'burns' a hole in the thermal velocity distribution of ground state atoms at v=0.

The first SAS experiments allowed the hyperfine structure of I_2 and the Na D lines to be resolved for the first time, with resolutions of 10 MHz (3; 28). Famously SAS also allowed the first sub-Doppler optical study of the H Balmer α line, allowing the fine structure to be resolved and giving the first optical determination of the Lamb shift between the $2s_{1/2}$ and $2p_{1/2}$ states (29). This later gave a value for the Rydberg constant R_∞ with an order of magnitude improvement in accuracy over previous studies, at 1 part in 10^8 (30). Other more sensitive methods of SAS have since been developed such as polarisation spectroscopy (31).

Two-photon spectroscopy

Two-photon spectroscopy was also proposed in 1970 (32) and was demonstrated in 1974 in Na vapour (4; 5). An atom can absorb two photons simultaneously and undergo a two-photon excitation, of the form $\Delta\ell = 0, \pm 2$, depicted in Figure 1.3.

Two intense beams, derived from the same laser, counter-propagate through a thermal distribution of atoms. The laser's double-frequency is tuned onto resonance with a two-photon transition and the atoms are monitored for fluorescence as they relax from level 2 to 1. If the laser frequency is f, and the atom absorbs one photon from each beam, the detuning from two-photon resonance in the atomic frame is

$$\delta_{2\gamma} = (f + \frac{v}{c}f) + (f - \frac{v}{c}f) - f_{12}. \qquad (1.5)$$

From this one can see that $\delta_{2\gamma} = 2f - f_{12}$ for any velocity v; Doppler shifts are equal and opposite, meaning that when $\delta_{2\gamma} = 0$ all velocity classes become resonant with the

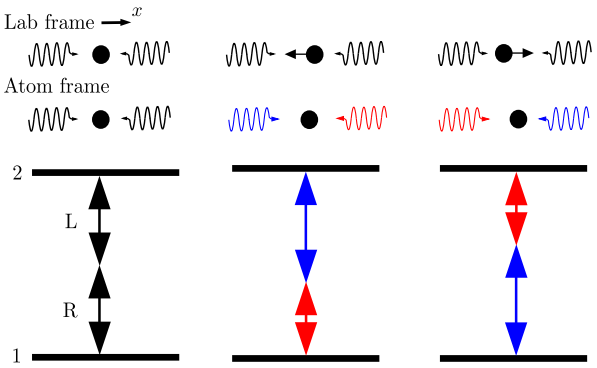

Figure 1.3: Two-photon spectroscopy: The atom absorbs one photon from each beam. In a counter-propagating arrangement, perfect cancellation of Doppler shifts from the two lasers results in all velocity classes contributing to a Doppler-free spectroscopic signal.

two-photon transition. The fact that v does not appear in the detuning expression implies that the signal is Doppler-free.

This technique has been very powerful in precision spectroscopy because these transitions have very narrow natural linewidths. With two-photon spectroscopy it became possible to measure the $1s_{1/2}$-$2s_{1/2}$ transition frequency in H, which has a natural linewidth of just 1.3 Hz (33).

1.2.3 The advent of precision spectroscopy

Doppler-free techniques unleashed the true potential of the laser as a spectroscopic light source in fundamental physical measurements. However, the development of these techniques was also accompanied by a strong drive to develop methods for directly counting the laser frequency, especially with regards to H spectroscopy (34). In the 1970s, experiments were reaching a position where the uncertainty associated with measuring the laser wavelength was now considerably worse than the resolutions achievable with Doppler-free spectroscopy. After 30 years of effort, optical frequency counting is now a reality and the recent development of optical frequency combs (derived from mode-locked lasers) has transformed the field of spectroscopy once again (6). These extraordinary developments are nicely demonstrated in the most recent measurement of the $1s_{1/2}$-$2s_{1/2}$ transition in H which shows an accuracy of 1.4 parts in 10^{14} (8).

1.3 Measuring optical frequencies

1.3.1 Wavelength or frequency?

It was not until the development of the monochromatic laser source that spectroscopists began to consider the direct measurement of the frequency of light. The wavelength of a laser can be measured accurately by comparing it against a known length standard using an interferometric method. However, wavelength measurements are always limited by the deviation of the laser wavefronts from an ideal plane and local changes in the refractive index (24). As a result, a lab-size wavemeter can not exceed a measurement accuracy of a part in 10^{10} (6). In contrast, the direct measurement of the laser frequency against a clock only involves counting oscillations and does not suffer from these limitations. Such a measurement can therefore be significantly more accurate.

1.3.2 Laser heterodyne measurements

The idea of laser heterodyne measurements was first studied by Javan immediately after the development of the laser (35). In the same way that one can hear an audible beat

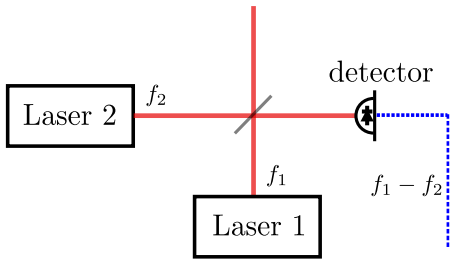

Figure 1.4: A laser heterodyne measurement.

note between two acoustic oscillators of nearly equal frequency, one can also detect radio frequency (RF) beat notes between two lasers, see Figure 1.6. If the electric fields of two laser beams are $\mathbf{E}_1(t) = \mathbf{E}_1 \cos(2\pi f_1 t)$ and $\mathbf{E}_2(t) = \mathbf{E}_2 \cos(2\pi f_2 t + \phi)$, and the two overlap on a square-law photodetector, the detector will output a photocurrent (36)

$$I(t) \propto \frac{1}{2}\mathrm{E}_1^2 + \frac{1}{2}\mathrm{E}_2^2 + \mathbf{E}_1 \cdot \mathbf{E}_2 \cos(2\pi(f_1 - f_2)t + \phi), \tag{1.6}$$

where ϕ is the phase difference between the two oscillating fields. It is assumed that the detector does not respond to fast oscillations at frequencies f_1 or f_2, and has sufficient bandwidth to respond at the difference frequency. For two lasers polarised in the same

plane, an RF beat note at $f_1 - f_2$ can then be measured. Physically, laser 1 can have a frequency higher or lower than laser 2, therefore one must separately find the sign of the beat note to deduce which is the case.

Heterodyne measurements play a fundamental role in optical frequency metrology because they allow ordinary RF counting techniques to be used in the optical domain. By measuring the beat note between an unknown laser frequency and a pre-determined laser frequency, one can translate frequency information between the two with no loss in accuracy. However, to complete an *absolute* measurement, an optical frequency measurement is still required of the pre-determined laser.

1.3.3 Counting an absolute optical frequency

The first successful absolute optical frequency measurements of lasers were made with frequency chains constructed at the NBS in Boulder (37) and the PTB in Braunschweig (38). Frequency chains consist of up to 10 phase-locked oscillators of increasing frequency, locked to one another via non-linear frequency multiplicative stages. With enough links in the chain, the large portion of the electromagnetic spectrum can be coherently bridged from a primary Cs standard at 9.192,631,770 GHz to a 100 THz laser frequency, allowing optical counting relative to the SI second. After the first optical frequency measurements, in 1983 it was globally decided to fix the speed of light at 299 792 458 ms^{-1}, directly tying the SI metre and the SI second.

1.4 Optical frequency combs

Frequency chains were extremely complex systems, designed to work at only one specific optical frequency, and for this reason they were only used to make several measurements (37; 38). It is the more recent development of femtosecond frequency combs (6) that has truly revolutionised the area of optical frequency metrology.

1.4.1 Mode-locked lasers: Optical frequency synthesisers

In the 1990s, Kerr-lens mode-locking techniques of Ti:Sapphire lasers were achieving pulse durations of T_P ~10 fs, equivalent to a few optical cycles (39). Figure 1.5 shows the output of a femtosecond laser in the time domain. The repetition frequency of the pulses f_{rep} (typically ~100 MHz) is simply related to the round trip time of the laser cavity

$T_{rt} = 1/f_{rep}$. Importantly, due to dispersion in the laser cavity, after each round trip there is also an incremental phase slip $\Delta\phi$ between the carrier and pulse envelope.

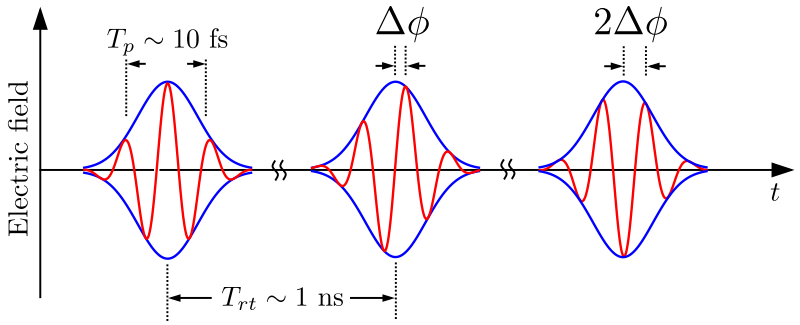

Figure 1.5: A pulse train from a typical femtosecond pulsed mode-locked laser in the time domain. The blue line shows the pulse envelope and the red line shows the carrier laser frequency.

In the frequency domain, this pulse train describes a comb of narrow lines spaced regularly by f_{rep}, see Figure 1.6. The frequency span of this comb is related to the pulse duration by $\Delta f = 1/T_p$. Therefore 10 fs pulses correspond to a comb spanning 100 THz

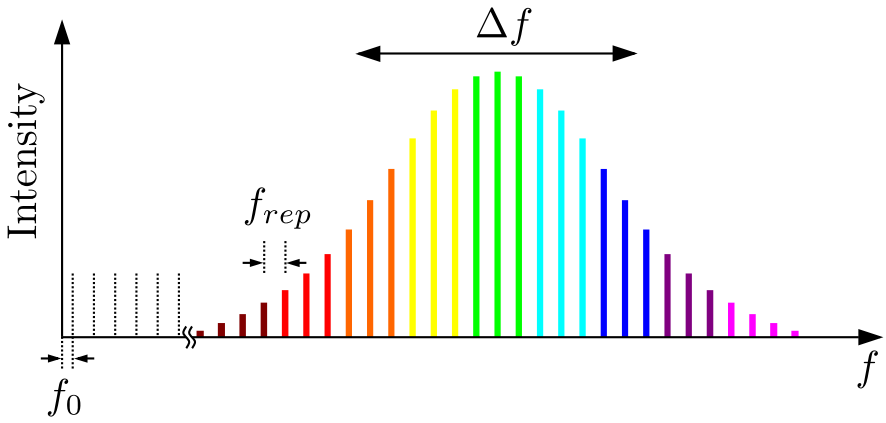

Figure 1.6: A frequency comb: The output of a mode-locked laser in the frequency domain. The lines of the comb are equally spaced by the repetition rate f_{rep} and can span up to 100 THz around the carrier. The phase slips $\Delta\phi$ mean that the comb lines are all offset from exact integer multiples of f_{rep}, by a frequency f_o.

around the carrier frequency, which can equate to millions of comb teeth. A typical mode-locked Ti:Sapphire laser will produce a comb centred at 370 THz and spanning up to 15

THz FWHM.

Because there are beat notes between each pair of comb lines, the light from a mode-locked laser contains a strong frequency component at f_{rep}. This beat note is easily measured on a photodetector, and as a result can be stabilised and counted relative to a highly accurate microwave frequency standard using ordinary RF electronics. This makes a comb a powerful tool for bridging the gap between different optical frequencies by a fixed number of precisely known RF intervals. For example, the first use of a comb was to measure the absolute frequency of a Cs D line transition relative to a chain-counted He-Ne laser, with the comb coherently bridging the 18.4 THz gap between the two (40).

1.4.2 The absolute frequency of a comb line

The incremental phase slips $\Delta\phi$ mean that the comb teeth do not lie at exact integers of f_{rep}, instead there is some offset frequency equal to

$$f_o = f_{rep}\frac{\Delta\phi}{2\pi}, \tag{1.7}$$

where f_o is typically ~10 MHz. The absolute frequencies of the comb lines f_n are therefore described by [1]

$$f_n = nf_{rep} \pm f_o. \tag{1.8}$$

This equation indicates that with knowledge of f_{rep} and f_o the absolute frequency of every line of the comb can be deduced relative to 0 Hz. The comb teeth therefore define absolute optical frequency markers across a wide range of frequencies, described by two countable radio frequencies f_{rep} and f_o. By stabilising these parameters to a microwave standard, the relative accuracy and stability of the standard can be translated to the lines of the comb. In essence, the comb scales-down optical frequencies (or scales-up RF frequencies) by the large factor of $n \sim 10^6$, in a perfectly phase-coherent manner.

1.4.3 Self-referencing

With an octave-spanning comb, an $f - 2f$ self-referencing scheme can be used to access f_o. This technique was first described by Hänsch (41) and is depicted in Figure 1.7. Comb lines at the lower frequency section of the comb are frequency doubled to have a frequency

[1] The ± sign will be easier to interpret in the next section.

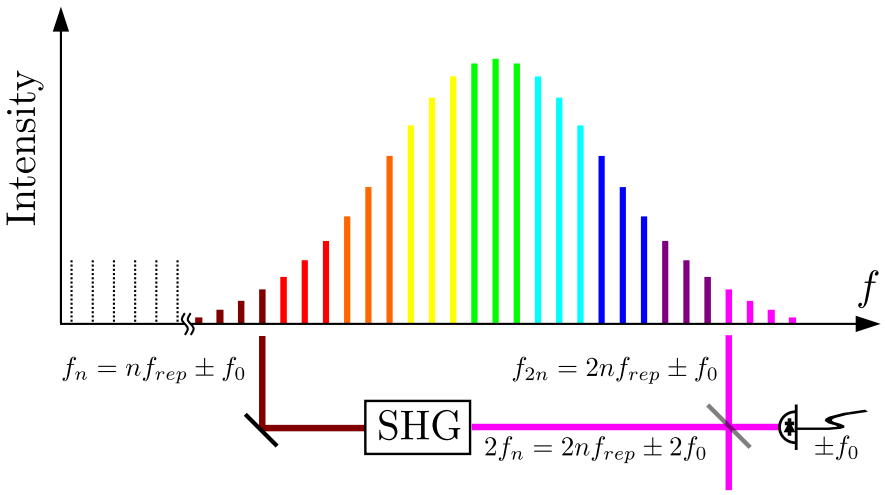

Figure 1.7: $f - 2f$ detection of the comb offset frequency: Comb lines from the lower end of the spectrum are frequency doubled and mixed with comb lines originating from one octave higher in frequency. The resultant RF beat note on a photodetector is equal to $\pm f_o$.

$f_n = 2nf_{rep} \pm 2f_o$, these are then mixed with lines from one octave higher in frequency $f_n = 2nf_{rep} \pm f_o$ on a photodetector. This gives a beat note frequency equal to

$$f_{beat} = 2nf_{rep} \pm 2f_o - 2nf_{rep} \mp f_o = \pm f_o. \tag{1.9}$$

Notice that there is a physical difference between the second octave lines being higher or lower in frequency than the frequency doubled lines, which is the origin of the $\pm$ sign.

At the time of Hänsch's proposal (41), octave-spanning combs were not available with modelocking techniques. However, the development of photonic crystal fibres in the late 1990s supplied a solution to this problem (42). These fibres have a high third order non-linear susceptibility which, for the intense pulses of the comb light, can cause spectral broadening of the comb-spectrum through self-phase modulation. Coupling the light from a comb through such a fibre results in a so called 'supercontinuum' of comb lines at the far end, which can span many hundreds of terahertz, covering more than an octave. In 2000 these methods allowed the first absolute optical frequency measurement to be made relative to the SI second, directly with a Ti:Sapphire self-referenced comb (43).

1.4.4 Frequency combs in metrology

Impact

Self-referenced combs have dramatically simplified optical frequency measurements as a single mode-locked laser can now take the place of an entire frequency chain of oscillators. Also, because the mode-locked laser is a true optical synthesiser, it can provide an optical reference at any arbitrary frequency across its working range. Recently self-referenced combs, based on compact mode-locked Er-doped fibre lasers working at 1550 nm, have become commercially available devices (44). With frequency doubling, these combs also allow visible operation.

Combs have had a great impact in the field of precision laser spectroscopy, where hertz level measurements of a laser frequency are now routine by taking a beat note measurement against a line of a self-referenced comb. The area of *direct* frequency comb spectroscopy is also a growing field (45). Most importantly, the comb is able to act as the missing optical clockwork which will eventually be required to relate the next generation of optical clocks to the current Cs primary standards. The most accurately measured optical frequency to date is a UV transition of an Hg^+ ion optical clock, measured as 1064 721 609 899 145.30(69) Hz, an uncertainty of 7 parts in 10^{16} (46).

Reliability

Since the comb technique was developed, several experiments have been carried out to verify its reliability and accuracy in metrology. For example, Udem *et al* has shown that the regularity of the comb line spacing f_{rep} is reliable to 3 parts in 10^{17}, even after spectral broadening in fibre (47). Also, Holzwarth *et al* have demonstrated agreement of 5.1 parts in 10^{16} between a self-referenced comb and a frequency chain (48). More recently, Ma *et al* has shown agreement approaching parts in 10^{19} between neighbouring lines of different combs, referenced to the same optical standard (49). Finally, Zimmerman *et al* has used a comb to verify the accuracy of the second harmonic generation (SHG) process to 6.6 parts in 10^{21} (50).

1.5 Frequency comb spectroscopy of Rb

1.5.1 The motivation of this thesis

Simple atomic systems such as H are chosen as testing grounds for fundamental physics such as QED (34), measurement of the Rydberg constant (51) and the proton charge radius (11). The simple two-body physics of H means that theoretical transition frequencies can be computed analytically from well known formulae and compared with experiment. However, heavier atoms such as Rb involve more complicated multi-body physics and exact analytical solutions are not possible. Nevertheless, because the heavier alkalis are easier to work with, they are often chosen to investigate new atomic physics. A good example is the first Bose-Einstein-Condensate, which was created with ^{87}Rb atoms (52). Rb has an appreciable vapour pressure at room temperature and also has strong D line optical transitions at convenient near infra-red (NIR) wavelengths for cheap, commercial, laser diodes; this makes it widely used in quantum optics and atomic physics labs. It is therefore important to have an accurate understanding of this atom's properties. Appendix A outlines some of the physical and electronic properties of Rb.

In this thesis a frequency comb is used to make absolute frequency measurements of optical transitions to highly excited Rydberg levels in ^{85}Rb. The initial focus is to contribute to the area of high precision measurements of Rydberg levels by considering the recently demonstrated techniques of purely optical detection in vapour cells (53; 54; 55; 56; 57); using the comb to demonstrate if these new schemes could improve Rydberg spectroscopy. One of the primary aims of this study is to stabilise a laser onto a Doppler-free Rydberg signal over long time scales, for use in the micromaser experiment in our lab (58; 59; 60). Ultimately it is found that a limiting factor in the accuracy of this Rydberg spectroscopy comes from the knowledge of the frequency of lower lying transitions in Rb. This limitation leads the research into a second area, involving frequency comb measurements of the Rb D lines, where there are still several large discrepancies between different measurements in the literature (61; 62; 63; 64).

1.5.2 Precision spectroscopy of Rydberg states

Motivation

As will be described in Section 2.1, Rydberg states are loosely bound, highly excited atomic states with large principal quantum number n (65). They are found ∼1000 THz

above the ground state and close to the ionisation threshold, forming a large map of closely spaced levels separated by RF intervals. High resolution spectroscopy of Rydberg states is interesting because these large atoms can experience a variety of unusual interactions that do not apply to ground state atoms. From their study, a wealth of new physics can be understood. For example, researchers have recently observed strong Rydberg-Rydberg interactions (66), Rydberg-plasma evolution (67) and, most interestingly, exotic Rydberg molecules (68). Accurate measurements of unperturbed Rydberg levels will be useful for studying these new effects, plus new techniques of high resolution laser spectroscopy of Rydberg states will drive forward these new areas of research.

The accurate measurement of Rydberg levels in alkali atoms also plays a fundamental role in improving complex multi-electron atomic models (69; 70). The quantum defect δ describes how the levels of an alkali atom differ from those of H, and contains the effects of the core electrons (65). For the case of the non-penetrating high ℓ states, accurate quantum defects are especially important as they supply values for the alkali core polarisabilities (71), which are important quantities in chemistry. In the literature, there are no precise experimental numbers of these polarisabilities for the Rb^+ core (72). Via accurate measurement of the fine structure splittings of the alkalis, and how they vary with n, one can also learn more about the relativistic and non-central field effects which occur within the atom, such as exchange interactions between the valence and core electrons (73).

On a more practical note, accurate values for the Rb ionisation threshold and defects will be important for predicting the laser frequencies required for current interesting applications with Rydberg atoms such as fast quantum-gates (74), cavity QED (75) and ultra-sensitive electric field probing (76). Assuming the ionisation threshold is well known, for a low ℓ state at n=30, defects must be accurate at the 10^{-6} level to predict laser frequencies at the megahertz level.

Previous measurements

Rydberg level energies and fine structure in the alkali atoms were studied and measured well before the invention of the laser using broadband light and spectrographs, see for example Reference (77). After the invention of the laser, laser excitation followed by microwave spectroscopy between neighbouring Rydberg levels has been a very successful technique for measuring the quantum defects in Rb (78; 79). Microwave methods are favourable because of the strong and narrow transitions that couple neighbouring Rydberg

levels and, with microwaves having negligible Doppler shift, the very high resolutions attainable of ∼10 kHz. These techniques allow measurements of Rydberg level energies relative to the ionisation threshold. Most recently, in 2003 and 2006 this technique was used with cold ^{85}Rb atoms held in a Magneto-optical trap (MOT) to extract the most accurate values of the ℓ=0 − 3 quantum defects of Rb to date, with accuracies of 10^{-7} and 10^{-5} for the s, p, d and the f series respectively (80; 81).

In this thesis a different approach is taken, exploiting the accuracy and stability of an optical frequency comb to measure Rydberg levels in an absolute sense, using laser spectroscopy. Such measurements are relative to the ground state, as opposed to the ionisation threshold. Figure 1.8 displays the two different approaches. Laser spectroscopy gives an independent check of the quantum defects, in a different regime. Plus, unlike

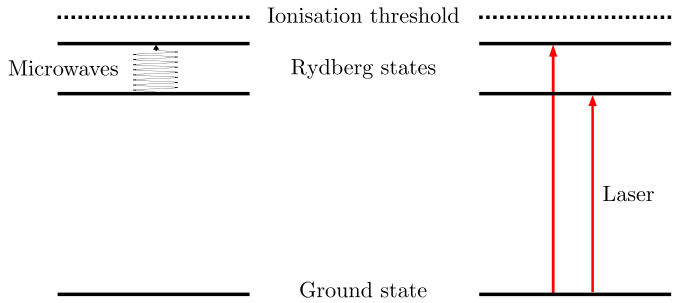

Figure 1.8: Microwave spectroscopy and laser spectroscopy of Rydberg atoms.

microwave techniques, these absolute measurements allow a highly accurate value for the ionisation threshold, and therefore binding energy of the Rb $5S_{1/2}$ ground state. These types of measurement also supply optical frequency markers in the UV range of the spectrum which may be useful in metrology, especially as the large number of Rydberg levels form a continuous comb of spectral lines (82; 83).

Although there is a large body of work on precision interval and fine structure measurements of the different Rb Rydberg series (79; 80; 81; 84), absolute measurements are more difficult to carry out, and are limited to the lower ℓ=0, 1, 2 series (82; 83; 85; 86; 87). Many of these measurements were made in the 1970s using Doppler-free, two-photon spectroscopy with a frequency doubled dye laser and thermionic detection (82; 84; 85; 88; 89). Some of the most accurate of these absolute measurements were made by Lee *et al* with uncertainties of 7.5 MHz (82). However, it appears that absolute measurements of the Rb

f series have only been made once by Johansson in 1961 (90) for n = 4-8 and absolute measurements for ℓ >3 have not been considered. As new tools are now available in laser spectroscopy, such as the optical frequency comb method, it is interesting to return to some of these previous measurements with a hope of improving accuracy and technique.

Current state of the field

Since 2000, there have been significant advances in Doppler-free Rydberg laser spectroscopy of Rb using ordinary room temperature vapour cell samples with purely-optical, non-destructive detection methods (53; 54; 55; 56; 57). These papers are mostly technical in nature or have considered only measurement of the fine structure (53; 54; 57), with no focus on the potential of making absolute measurements or extracting quantum defects. A vapour cell is a convenient and straightforward solution for finding Rydberg levels, which could potentially permit rapid advances in Rydberg spectroscopy. It is therefore important to verify performance. These compact setups are also ideally suited for laser stabilisation applications onto Rydberg levels, plus in the vapour cell the Rydberg atoms have shown an insensitivity to external DC electric fields (54; 55), which can be attributed to efficient screening of the atoms. This makes a vapour cell particularly attractive for studying high ℓ Rydberg states with large polarisabilities, where Stark shifts can be large sources of systematic error.

1.5.3 Precision spectroscopy of the D lines

Motivation

In a similar manner to Rydberg spectroscopy, Rb D line spectroscopy can be divided into two types: Absolute measurements of the NIR transitions between the hyperfine components of the D lines $5S_{1/2} \rightarrow 5P_{1/2}$ and $5S_{1/2} \rightarrow 5P_{3/2}$ (∼380 THz), and relative measurements of the hyperfine splittings of the $5P_{3/2}$ and $5P_{1/2}$ levels (∼100 MHz). Figure 1.9 displays the transitions that make up the D lines in ^{85}Rb and ^{87}Rb.

There are several motivations for high precision measurements of both types. Firstly, the strong D line transitions are widely used in experiments and so it is important that these transition frequencies be well known. Secondly, both types of measurement are important on a fundamental level; in the same manner as Rydberg measurements, accurate absolute frequency measurements and hyperfine splitting measurements in the D lines can give insight into the many body physics within the Rb atom, and can be compared with

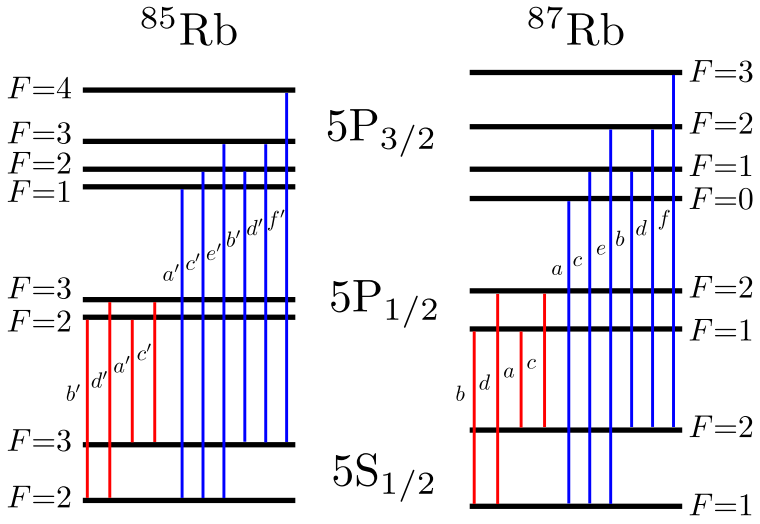

Figure 1.9: The Rb D line components and hyperfine structure: The labelling convention is taken from Reference (61). The blue lines make up the D_2 transitions at 780 nm and the red lines make up the D_1 transitions at 795 nm.

the most advanced calculated wavefunctions (70). Specifically, precision measurements of the hyperfine-structure (which is largest on the D lines at $n = 5$) can show what effect the nucleus has on the atomic wavefunction, and can give details on the structure of the nucleus such as its multipole moments (91). Finally, absolute measurements are of interest in optical frequency metrology; a diode laser stabilised to a Doppler-free D line hyperfine component makes a cheap, straight forward and transportable optical frequency standard (61; 92).

Previous measurements

One of the first detailed studies of the Rb D lines was made from the emission of a collimated beam of excited Rb atoms by Beacham *et al* (93). However, with the advent of lasers, the hyperfine structure of the D lines is now readily studied with high resolution using Doppler-free SAS (61; 62; 92; 94). Absolute frequencies can be compared against well known optical frequency standards (61; 92) or more recently against frequency combs (45; 64). Laser spectroscopy is also the most common method for measuring the hyperfine splittings of the excited states. This can be done by constructing two identical SAS spectrometers and stabilising lasers onto different D line hyperfine components to accurately

measure the intervals directly (61; 63; 92; 95). Such relative measurements are not affected by systematic errors associated with absolute frequency calibration.

It was Barwood *et al* (61) who completed the first complete catalogue of absolute frequencies of both of the D lines in both Rb isotopes using SAS. In this work, the absolute measurements were made with an error of $\pm$400 kHz using a wavemeter calibrated against an I_2 stabilised HeNe standard. Two identical spectrometers were constructed which allowed direct measurements of the hyperfine splittings to be made with $\sim$10 kHz error. Since this work, many of these measurements have been repeated (62; 63; 64; 92; 94; 95). In the case of the absolute measurements the accuracies have been improved by generally one to two orders of magnitude. The most recent measurements of both type now present $\sim$10 kHz error or less, this is equivalent to a few thousandths of the 6 MHz natural linewidth of these transitions.

Current state of the field

With such a large body of work dedicated to these transitions, it is perhaps surprising that there is any more to learn from frequency measurements of the Rb D lines. However, a review of the literature exposes several very large discrepancies that still remain between different papers, in both the absolute and relative type measurements. In some cases these differences are as large as 100σ. The problems were brought to light in a recent 2008 paper by Maric *et al* (64), where a frequency comb was used to carry out a set of absolute measurements of the D_1 line transitions in laser cooled Rb, with the motivation of solving these discrepancies. All previous studies have used SAS and vapour cells, therefore this investigation hoped to eliminate any unaccounted systematic shifts associated with these techniques. The results were encouraging but have in many ways caused a divide in agreement between two parties (61; 62; 63; 64), which will be discussed in Section 9.1.1. However, the MOT system used in Reference (64) was not able to study *all* of the hyperfine components, plus repeated precision measurements will be important to build up a stronger case for one particular party.

A full catalogue of both D lines and for both isotopes with $\sim$10 kHz absolute error has not been carried out. Also, out of the absolute measurements made to date, it is only References (45; 64) who have used a frequency comb as an absolute reference, and in both cases only a few transitions in the manifold have been targeted. A modern day 'Barwood type' catalogue using a frequency comb would be invaluable. Additionally,

improved measurements of the D_2 line f and f' transitions may ultimately improve the accuracy of three-step Rydberg spectroscopy, as will be seen in Chapter 6.

1.6 This thesis

Chapter 2: Background

This background chapter introduces some of the concepts of Rydberg atoms in more detail, and establishes the idea of optical detection. The three-step laser scheme is also presented with some modelling of the quantum amplification detection method.

Chapter 3: Apparatus

An apparatus chapter describes some of the general equipment that was used throughout the project, with a large chunk of the chapter devoted to the Menlo comb system at Leeds.

Chapter 4: Rb Rydberg spectroscopy in a vapour cell with three diode lasers

This is the first of the experimental chapters and describes the construction, characterisation, optimisation and first absolute frequency measurements from a Rb Rydberg vapour cell spectrometer using a three-step laser excitation. The $n\mathrm{F}_{7/2}$ state frequency measurements from this chapter are published in Reference (96).

Chapter 5: Three-step laser stabilisation for excitation of Rb Rydberg states

In this chapter the Rydberg spectrometer is applied to a laser stabilisation application. The three laser steps are stabilised to three independent vapour cells and their stabilities are monitored. The results show that the stability of the Rydberg levels is <100 kHz, demonstrating that the spectroscopy of Chapter 4 can be significantly improved with relevant modifications. Long term laser stabilisation to the $63\mathrm{P}_{3/2}$ level now also meets the needs of the micromaser experiment in our lab. The work from this chapter is published in Reference (97).

Chapter 6: Three-step comb-stabilised Rb Rydberg spectroscopy

Chapter 6 is the culmination of the three-step Rydberg spectroscopy work in this thesis. It describes how the modifications, discussed in the previous chapter, have been achieved.

The new laser setup and metrology scheme involves stabilising all three laser steps simultaneously to different lines of the frequency comb. The system gives a reduction in random error of over 100× and an increase in absolute accuracy of 10×, compared to the measurements in Chapter 4. This is the first demonstration of sub-megahertz accuracy optical Rydberg spectroscopy. The error analysis concludes that knowledge of the D_2 line transitions will be one of the limiting factors to any further improvements in accuracy.

Chapter 7: Four-photon Rb spectroscopy in a vapour cell

This chapter considers the feasibility of adding a fourth microwave step to the three-step excitation scheme. It is found that with this addition, it is possible to carry out precision spectroscopy of nG Rydberg states. Stark-induced nH state excitations are also observed, which gives a useful method for measuring small stray electric fields within the cell. This setup is used to make absolute frequency measurements of the 55G, 57G and 61G states in ^{85}Rb for the first time.

Chapter 8: Rydberg spectroscopy in a vapour cell: Future directions

In this chapter an overview is made of some of the interesting observations that were made throughout the Rydberg spectroscopy work, which involved only pilot measurements or could not be understood in the scope of this thesis. Some of these observations could lead onto several interesting future avenues of research, especially the observation of potential Rydberg-Rydberg energy shifts. This chapter also discusses the possible improvements that could be made to the Rydberg spectrometer to make more accurate measurements in the future.

Chapter 9: Frequency comb spectroscopy of the Rb D lines

Finally, Chapter 9 describes two Doppler-free Rb spectrometers that have been developed for precision absolute frequency measurements of the D lines. These new measurements will allow future improvements of the Rydberg spectroscopy in the previous chapters. So far, absolute frequency measurements have been made of the D_1 line in both Rb isotopes to an accuracy of ∼50 kHz, using an SAS spectrometer.

Chapter 10: Conclusion

Future work for the Rydberg spectroscopy is summarised in Chapter 8, whilst future work for the D line spectroscopy is summarised at the end of Chapter 9. This short chapter is therefore simply an overview of the thesis as a whole. Interestingly, since the work in Chapter 6 another group has made new absolute measurements of Rydberg states in ^{87}Rb. This chapter takes the opportunity to discuss these new developments and as a result shows a new, significantly more accurate, derivation of the isotope shift in Rb.

Chapter 2

Background

This chapter begins by introducing some of the basic properties of Rydberg atoms. There is then a brief description of possible laser excitation schemes and detection techniques for Rydberg spectroscopy. The rest of the chapter is dedicated to the three-step scheme used throughout this thesis. The principle of quantum amplification is introduced and dipole matrix elements are computed for the Rydberg transitions involved. Finally, a rate equation model is considered to describe the system.

2.1 Rydberg atoms

2.1.1 Properties

Rydberg atoms are atoms where one or more electrons have been promoted to highly excited energy levels with principal quantum number $n \gg 1$ (65). In the case of H and the alkalis, a Rydberg atom can be created by exciting the single valence electron to such a level. These high lying states have low binding energy and lie close to the ionisation threshold, making Rydberg atoms particularly susceptible to ionisation. Importantly, because the classical orbital radius scales with n^2, Rydberg atoms can be very large. For example, an n=100 Rydberg atomic state has a radius of $\sim$1 μm. These large sizes result in exaggerated properties when compared to ground state atoms. Table 2.1 summarises some of these properties and how they scale with n.

Table 2.1: Properties of a typical Rydberg atom and how they scale with the principal quantum number n (65). For comparison, the orders of magnitude are shown for an n=5 and n=50 state.

Property	scaling	n=5	n=50
Binding energy	n^{-2}	1000 THz	10 THz
Energy between adjacent states	n^{-3}	100 THz	100 GHz
Orbital radius	n^2	$10a_0$	$1000a_0$
Dipole moment	n^2	$10ea_0$	$1000ea_0$
Polarisability	n^7	10 Hz $V^{-2}cm^2$	100 MHz $V^{-2}cm^2$
Radiative lifetime (FWHM)	n^3	10 ns (10 MHz)	10 μs (10 kHz)

2.1.2 Energies

For an alkali atom, the energy of a Rydberg level (relative to the ground state) is well described by the Rydberg formula

$$E_n = E_i - \frac{R_X}{[n-\delta(n)]^2} = E_i - \frac{R_X}{n^{*2}} \ , \tag{2.1}$$

where E_i is the ionisation energy, E_n is the excitation energy from the ground state to a state with principal quantum number n, R_X is the Rydberg constant for the atom of interest, $\delta(n)$ is the quantum defect and $n^* = n - \delta(n)$ is the effective quantum number. R_X is related to the universal constant R_∞ via the reduced mass ratio

$$R_X = R_\infty \frac{m_e m_X}{m_e + m_X}, \tag{2.2}$$

where m_e is the electron mass and m_X is the mass of the nucleus. For the special case when $\delta = 0$, the Rydberg formula becomes the familiar Bohr formula describing the levels of H.

2.1.3 The quantum defect

The atomic physics of an alkali atom is very similar to that of H because the additional $Z-1$ charge on the nucleus is screened by the inner core of $Z-1$ electrons, which reside in spherically symmetric closed shells. The single valence electron therefore sees a central charge on the nucleus which is almost equivalent to that of a single proton. However, as discussed next, the screening is not perfect and also the inner core electrons have a subtle effect on the valence electron. This causes the alkali levels to be shifted

from those of H and these effects are described by the quantum defect parameter $\delta(n)$ [1]. Traditionally the quantum defects are determined for the fine structure levels. Table 2.2 lists the approximate sizes of the quantum defects for different states in ^{85}Rb.

Table 2.2: The approximate sizes of the quantum defects for states in ^{85}Rb (65).

State	$\delta(n)$
$n\mathrm{S}_{1/2}$	3.13
$n\mathrm{P}_{1/2}$	2.65
$n\mathrm{P}_{3/2}$	2.64
$n\mathrm{D}_{3/2,5/2}$	1.35
$n\mathrm{F}_{5/2,7/2}$	0.016

$\delta(n)$ includes contributions from two effects: Firstly, the valence electron can pass close to the central core and polarise it. This leads to a $1/r^4$ interaction between the electron and the induced dipole. Secondly, for a portion of its orbit, the valence electron may penetrate the core and be exposed to a greater nuclear charge and therefore a modified potential $\not\propto 1/r$. For these reasons, it is electron states with the highest probability of being found close to the core, that have the highest quantum defect; these are the states with lowest angular momentum ℓ. The quantum defect is therefore a strong function of ℓ. Eventually, at some high value of ℓ, the electron no longer penetrates the core at all and for these states the quantum defect arises purely from core polarisation (71).

The quantum defect can be written as a Ritz expansion (65), with defect series parameters δ_i of increasing order

$$\delta(n) = \delta_0 + \delta_2 t_n + \delta_4 t_n^2 + \dots \,, \tag{2.3}$$

where

$$t_n = \frac{1}{[n-\delta(n)]^2} = \frac{E_i - E_n}{R_X}. \tag{2.4}$$

In series form, the weak n dependence is exposed. Reference (69) describes how these series parameters relate to the core polarisability and structure.

[1] The levels are also shifted due to the larger nuclear mass, see Equation 2.2, and the isotope shift.

2.1.4 Radial wavefunctions

Schrödinger equations

In H the radial and angular components of the time-independent Schrödinger equation can be separated due to the spherical symmetry of the potential (98). The radial Schrödinger equation in H is given by

$$-\frac{\mathrm{d}^2U(r)}{\mathrm{d}r^2}+\left[\frac{\ell(\ell+1)}{r^2}-\frac{2\mu Ze^2}{\hbar^2 r}-\frac{2\mu E}{\hbar^2}\right]U(r)=0, \tag{2.5}$$

where μ is the reduced mass, E is the energy, Z is the nuclear charge and ℓ is the angular momentum. The substitution $U(r)=R(r)r$ is made where $R(r)$ is the normalised radial wavefunction such that $\int_0^\infty R^*(r)R(r)\mathrm{d}r$=1. Equation 2.5 is analytically solvable for $U(r)$ and the solutions follow the form of the Laguerre polynomials.

In the alkalis, once again the radial and angular components can be separated, however the central potential seen by the valence electron does not follow a simple $1/r$ relation, and as a result, the radial Schrödinger equation cannot be analytically solved (98). From Reference (99) an effective radial Schrödinger equation for an alkali atom can be written as

$$-\frac{\mathrm{d}^2\chi(v)}{\mathrm{d}v^2}+\left[\frac{4v^2}{n^{*2}}+\frac{(1/2+2\ell)(3/2+2\ell)}{v^2}-8-\frac{8\alpha_d}{4v^6}\right]\chi(v)=0, \tag{2.6}$$

where the substitution $r=v^2$ is made and $\chi(v)=R(r)r^{3/4}$. The substitution means that the oscillation period (with r) of the radial wavefunction, which scales with r^2, becomes linear with v. α_d is the dipole core polarisability, this final term accounts for the polarisation of the core electrons by the valence electron (100). Equation 2.6 can be numerically solved using a Numerov algorithm (101), taking equal steps in v.

Computing wavefunctions

A MATLAB code was made to compute radial wavefunctions of Rb using the above technique. The integration was carried out from a radius much larger than the classical radius n^2a_0 to a distance close to the ionic core. As the Numerov integration approaches the core, the wavefunction solution tends to diverge and therefore care was taken to stop the integration before this occurred. This results in a region from $r=0$ to the ionic core radius which is not included in the numerical solution; the wavefunction is truncated.

To test the validity of the program, the wavefunction of the 5P state in H was analytically computed from Equation 2.5 and numerically computed from Equation 2.6 (with

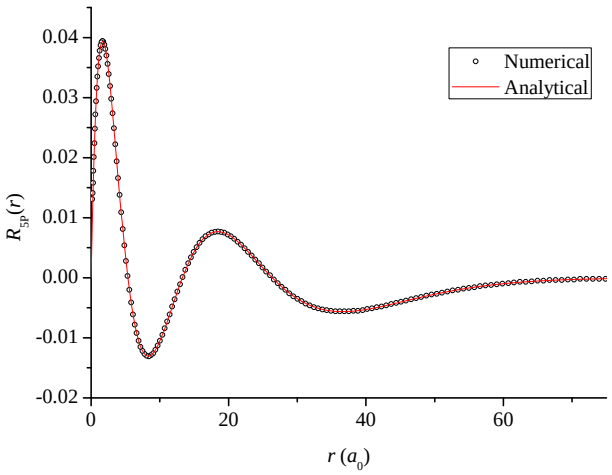

Figure 2.1: The 5P radial wavefunction of H solved analytically and numerically. The numerical solution was computed using a Numerov algorithm with 200 steps, from $125a_0$ to $0.18a_0$. Ignoring the truncation for $r < 0.18a_0$, the agreement is excellent.

$\alpha_d = 0$ and $n^* = n = 5$). The two normalised wavefunctions are plotted together in Figure 2.1. The numerical-analytical agreement was found to be excellent for all ranges of n and ℓ, with the only discrepancy occurring in the truncation.

Figure 2.2 displays the normalised probability distribution $R^*(r)R(r)r^2$ of the 60F state in Rb computed from the same program. This figure demonstrates some of the properties of a Rydberg atom: It is clear that the valance electron is much more likely to be found far from the nucleus, behaving almost like a free electron.

2.1.5 Laser excitation

Rydberg atoms have historically been excited using charge exchange, electron impact or with broadband light sources (65). More recently, laser excitation has become the favoured method, allowing individual Rydberg levels to be addressed. The frequency gap from the 5S to nL Rydberg states in Rb is 297 nm and can be driven with a frequency doubled dye laser. This scheme was famously used for the first single-atom-maser cavity QED experiment (60). The introduction of tunable diode lasers has since opened up other excitation possibilities. Figure 2.3 displays some of the different possible Rb excitation schemes taken from References (54; 55; 56; 57). The three-step excitation scheme shown

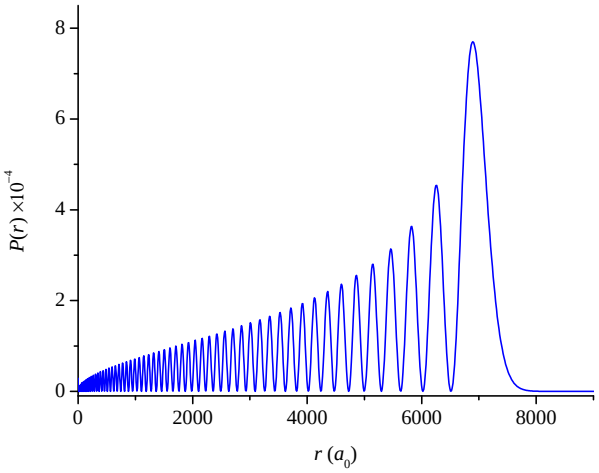

Figure 2.2: The radial probability distribution for the 60F state in Rb. This is the probability of finding the valence electron between r and $r + \mathrm{d}r$.

in Figure 2.3(c) is currently used in our lab for exciting Rydberg atoms for a modern-day micromaser experiment (58; 59).

2.1.6 Field-ionisation and thermionic detection

As will be shown in the next section, transitions spanning many n can be incredibly weak, meaning very few photons are scattered and making optical detection difficult. Therefore conventionally, Rydberg detection is done in an indirect manner, via field-ionisation (65; 87). Rydberg atoms in a beam can be easily ionised in a modest electric field, subsequent detection of the removed electrons with an electron multiplier then gives excellent levels of sensitivity. It is possible to achieve counts of $10^6\,\mathrm{s}^{-1}$ using such schemes, giving high signal to noise ratios (SNR) (75). More recently, cold atoms in a MOT have been excited to Rydberg levels and detected in this way (80; 81).

An alternative form of sensitive ionisation detection, that has proven very popular with vapour cell samples, is thermionic detection (82; 84; 85; 86). In this case Rydberg atoms are exited in a dense vapour, such that once excited they are instantly ionised via collisions with ground state atoms. The ionisation products then allow a current to flow between a set of field plates that are placed inside the cell (surrounding the Rydberg excitation zone)

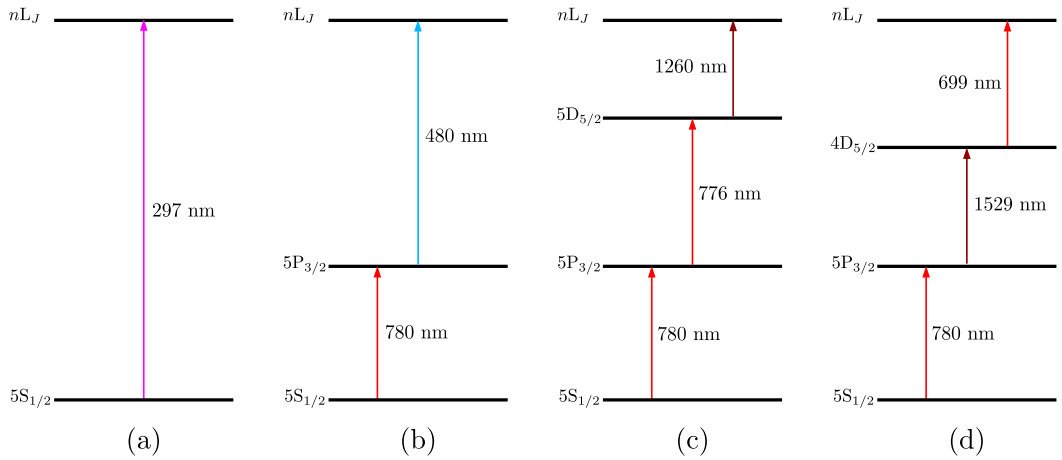

Figure 2.3: Some of the different laser excitation schemes used for Rydberg excitation in Rb. (a) can be excited with a frequency doubled dye laser whilst (b), (c) and (d) can be excited with diode lasers, where scheme (b) requires frequency doubling of 960 nm light. These schemes have been used in the following references from left to right (54; 55; 56; 57)

with a small potential applied across them. The plates make up a so-called 'space-charge limited diode' (88).

2.1.7 Purely optical detection

One optical method for detecting Rydberg atoms is to measure the small number of photons that are scattered with a photomultiplier tube (PMT). Several laser studies have successfully used this technique, see for example Reference (89). However, optical detection of Rydberg atoms has become more widely publicised since a 2007 paper by Mohapatra *et al* (54). In this work Rb atoms were detected via laser *absorption* in an ordinary room temperature vapour cell with a two-step ladder excitation scheme, as in Figure 2.3(b). A 780 nm laser was used to excite a D_2 transition and act as a weak probe in an electromagnetically induced transparency (EIT) system. A 480 nm frequency doubled diode laser was then used as a strong pump beam on the $5P_{3/2} \rightarrow nL_J$ transition. This two-step laser excitation allows Doppler-free EIT signals to be detected for nS and nD type Rydberg states, and is a purely optical detection technique. In contrast to ionisation detection methods, it is non-destructive by nature, plus the cell used is a cleaner environment than the cell arrangement required for thermionic detection.

This demonstration has been a breakthrough for Rydberg spectroscopy, opening up the possibility of using compact vapour cell setups with simple photodiode detectors. Both beam and MOT arrangements for field ionisation schemes naturally require bulky vacuum setups, as well as an involved and delicate detection section. Plus, one generally has to contend with stray electric and magnetic fields, as a vacuum apparatus is typically difficult to shield. For the case of the vapour cell, the sample is small, maintenance-free and the interaction region can be easily shielded and isolated from the environment.

Since the demonstration of EIT detection, vapour cell based Doppler-free Rb Rydberg spectroscopy has been shown with laser absorption using other excitation and detection schemes. In 2009 Thoumany *et al* used a V-scheme, where a 297 nm frequency doubled dye laser is used to directly drive the $5S_{1/2} \rightarrow nL_J$ UV transition (as in Figure 2.3(a)) whilst the absorption of a 780 nm laser is used for detection on a strong D_2 cycling transition (56). This exploits the phenomenon of quantum amplification (QA), which will be discussed in Section 2.10. This one-step laser excitation allows excitation to nP type Rydberg states. Shortly after, the same lab displayed Rydberg spectroscopy in a cell with a three-step laser excitation scheme (55), as in Figure 2.3(c). Again the 780 nm laser is used for detection, however this three-step scheme allows excitation to nP and nF type Rydberg states [1]. It is this three-step excitation and detection scheme which is used throughout this thesis.

2.2 Three-step laser excitation

2.2.1 Energy level scheme

The four level system used in this work consists of a 780 nm transition $5S_{1/2}, F = 3 \rightarrow 5P_{3/2}, F = 4$, a 776 nm transition $5P_{3/2}, F = 4 \rightarrow 5D_{5/2}, F = 5$ and finally a 1260 nm transition $5D_{5/2} \rightarrow nL_J$ (see Figure 2.4). The $\Delta\ell = \pm 1$ and $\Delta j = 0, \pm 1$ selection rules, for electric dipole transitions, allow $nP_{3/2}$ and $nF_{5/2,7/2}$ Rydberg states to be excited from the $5D_{5/2}$ state. With chosen polarisations of the laser steps, optical selection can be used to address particular hyperfine F and m_F levels, so the largest couplings can be achieved.

[1] Purely optical detection in a vapour cell, with a very similar three-step excitation and detection scheme, as in 2.3(d), was originally demonstrated as early as 2002 by Brandenburger *et al* (53). However, in this work only low lying n <10 states of Rb were studied.

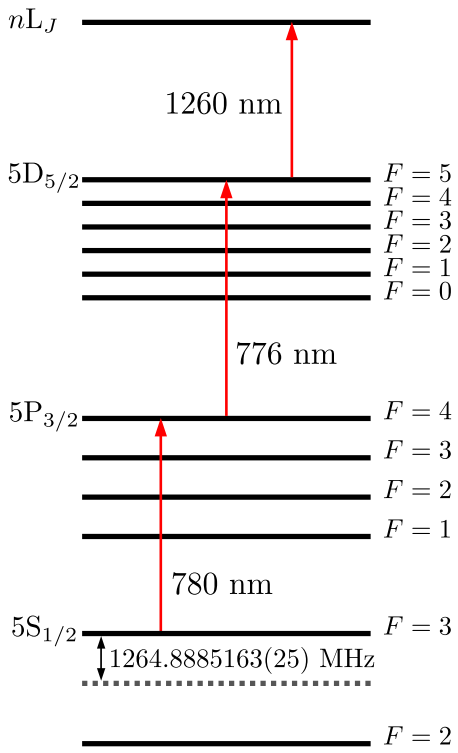

Figure 2.4: The three-step level scheme used to excite ^{85}Rb Rydberg states throughout this thesis. The hyperfine levels are also shown. The offset of the $5S_{1/2}, F = 3$ level from the centre of mass of the ground states is taken from Reference (91).

2.2.2 Advantages of the three-step system

The three-step scheme has advantages over the one or two-step schemes:

- It uses only conventional IR diode lasers. This makes the lasers more user-friendly and affordable
- There is no need for SHG, therefore more laser power is available, giving higher excitation rates
- It allows excitation to the nF series of Rydberg states
- All steps can use similar optics and optical fibres

2.2.3 Dipole matrix elements

Introduction

The dipole matrix element between two atomic states describes the strength of the transition between these states, and is related to the overlap of the two wavefunctions (98). The radial dipole matrix element is defined as

$$D_{ik} = \int_0^\infty R_{n_k,\ell_k}(r)\, er\, R_{n_i,\ell_i}(r)\, r^2\, \mathrm{d}r. \tag{2.7}$$

This expression depends only on the quantum numbers n and ℓ of the initial and final states. The complete matrix element is D_{ik} multiplied by an angular component $\mathfrak{I}_{ang}$, where the angular component gives the relative weightings for transitions to different fine and hyperfine components, and their magnetic sublevels. The radial matrix element alone gives a good indication of the transition coupling strength, which scales with $|D_{ik}|^2$.

Calculating radial matrix elements

It is useful to know how strongly the third step transition will couple to the third step laser field in this experiment, therefore a MATLAB code was produced to calculate the radial matrix elements between atomic states in Rb. The program carries out a numerical integration of the overlap of two radial wavefunctions, which are generated using the Numerov method (101) described in Section 2.1.4. The program has been used to compute some of the relevant matrix elements for the three-step excitation scheme, shown in Table 2.3, and also matrix elements as a function of n^* for 5D$\rightarrow$ nL transitions, these are shown in Figure 2.5.

Table 2.3: Computed radial dipole matrix elements in atomic units.

Transition	$\lvert D_{ik}\rvert$ (ea_0)
5S$\rightarrow$5P	5.93
5P$\rightarrow$5D	3.31
5D$\rightarrow$33F	0.118
5D$\rightarrow$63F	0.044
5D$\rightarrow$33P	0.044
5D$\rightarrow$63P	0.016

One can see that the matrix elements for the third step Rydberg transitions are considerably smaller than for the first and second steps because of the small overlap between

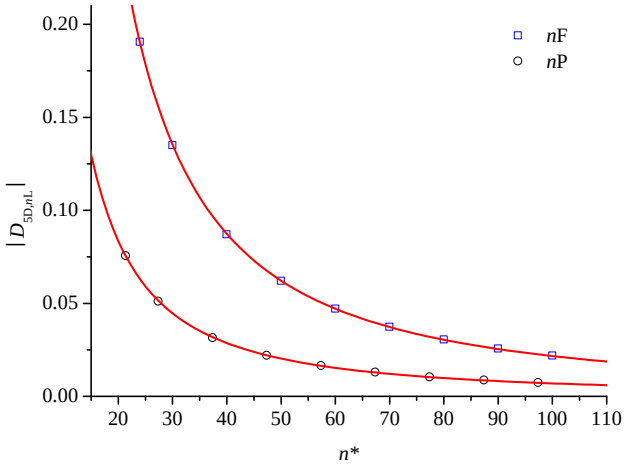

Figure 2.5: Computed dipole matrix elements against n^* for 5D→ nL transitions to nF and nP Rydberg states. The fitted red curves are described by Equations 2.8 and 2.9.

the 5D and nL radial wavefunctions. Figure 2.5 also shows how the elements are smaller for the transitions to nP states, again due to a smaller overlap in this case. By carrying out a fit of the form $y = Ax^B$ to these points, the following relations can be obtained

$$|D_{5\mathrm{D},n\mathrm{F}}| \approx 24.0 \times {n^*}^{-1.5} = 24.0 \times (n - 0.016)^{-1.5}, \tag{2.8}$$

$$|D_{5\mathrm{D},n\mathrm{P}}| \approx 8.5 \times {n^*}^{-1.5} = 8.5 \times (n - 2.64)^{-1.5}. \tag{2.9}$$

These indicate that there is an ${n^*}^{-3}$ scaling of the 5D→ nL transition strengths.

2.3 Quantum amplification

In the previous section it was found that the small radial part of the matrix element for the third step transitions results in line strengths up to $10^4\times$ weaker than for the first step transition. It is for this reason that detecting Rydberg atoms via laser *absorption* is difficult. QA, also known as electron shelving, is a technique used with single ions (102). It allows the indirect detection of a weak transition to a long lived state, via the reduced absorption of a strong transition to a short lived state (where the two transitions share a common state). In the case of Rydberg spectroscopy, QA can allow optical detection of

Rydberg atoms, in a non-destructive manner, by observing the absorption of a secondary laser through the sample (55; 56).

2.3.1 Principle of QA for Rydberg detection

The lifetime of a Rydberg state $\tau_{n\mathrm{L}_J}$ scales as n^3 and can easily be three orders of magnitude greater than that of a lower $n = 5$ state. In this scheme, the lifetimes of the intermediate $5\mathrm{P}_{3/2}$ and $5\mathrm{D}_{5/2}$ states are $\tau_{5\mathrm{P}_{3/2}}$=26.2 ns (103) and $\tau_{5\mathrm{D}_{5/2}}$= 238.5 ns (104) respectively. In contrast, a typical $n = 60$ Rydberg level will have a lifetime of ∼100 μs.

When a single ground state atom is promoted to a Rydberg level, the atom is shelved for $\tau_{n\mathrm{L}_J}$ seconds. If a strong $5\mathrm{S}_{1/2} \rightarrow 5\mathrm{P}_{3/2}$ transition is also being driven, then this Rydberg atom 'loses out' on $\tau_{n\mathrm{L}_J}/\tau_{5\mathrm{P}_{3/2}}$ absorption-emission cycles on the strong transition. This ratio of lifetimes gives the QA factor A_q; this is the factor of improvement in sensitivity by monitoring the decrease in absorption on the strong transition, instead of the direct absorption of weak Rydberg transitions. The weak Rydberg transitions could be from either one of the levels that make up the strong transition, for example from the $5\mathrm{S}_{1/2}$ level with 297 nm excitations (see Reference (56)) or from the $5\mathrm{P}_{3/2}$ level with 480 nm excitations.

In the three-step scheme, the intermediate $5\mathrm{D}_{5/2}$ state modifies the QA factor (55). Because $\tau_{5\mathrm{P}_{3/2}} < \tau_{5\mathrm{D}_{5/2}} < \tau_{n\mathrm{L}_J}$ there will be QA for $5\mathrm{D}_{5/2}$ excitation also, with $\tau_{5\mathrm{D}_{5/2}}/\tau_{5\mathrm{P}_{3/2}}$ absorption-emission cycles hindered on the first step for each $5\mathrm{D}_{5/2}$ atom excited. There is therefore a reduction in contrast as one is looking for hindered absorption-emission cycles from Rydberg excitation on top of the absorption-emission cycles already hindered by $5\mathrm{D}_{5/2}$ excitation. The resultant QA factor becomes

$$A_q = \frac{\tau_{n\mathrm{L}}}{\tau_{5\mathrm{P}}} \Big/ \frac{\tau_{5\mathrm{D}}}{\tau_{5\mathrm{P}}} = \frac{\tau_{n\mathrm{L}}}{\tau_{5\mathrm{D}}} \sim 100. \tag{2.10}$$

Therefore, whilst the third step laser is scanned over a Rydberg level, if one monitors the *transmitted* intensity of the first step laser instead of the *absorbed* intensity of the third step laser, one can achieve a factor of 100× amplification in detection sensitivity.

Unfortunately, in a vapour cell collisions and the limited interaction time reduces the effective lifetime of the Rydberg level and the QA factor is reduced. However, as described in Reference (55) under these conditions this still offers $A_q \sim 10$, which is sufficient for direct detection of Rydberg excitations using a photodiode.

2.3.2 Modelling quantum amplification

There are several papers which consider semi-classical models describing the coherent effects in laser-driven multi-level ladder systems, such as those in Figure 2.4 (105; 106). However, these derivations all involve approximations which assume the populations of the excited levels are negligible in comparison to that of the ground state, by setting all of the diagonal elements of the density matrix ρ_{ik} to zero except ρ_{11}. These models consider the off-diagonal elements, which describe the coherences between the levels. Unfortunately, this does not give a full picture of the population dynamics, which is required to understand QA. A full treatment of such a system would require numerical solutions of the on and off diagonal elements, without the approximations. Such a solution was outside the scope of this research, however one can understand the population dynamics alone with a four level rate equation model. This type of description is adequate to predict what is expected using QA detection.

2.3.3 Four level rate equation model

Making the approximation that the dominant decay channels from the $5D_{5/2}$ and nL_J levels are to the $5P_{3/2}$ and $5S_{1/2}$ levels respectively, the rate equations for the four levels can be written as

$$\begin{aligned}
\frac{dN_1}{dt} &= N_2A_2 + N_4A_4 + N_2B_{21}\rho_1(f_{12}) - N_1B_{12}\rho_1(f_{12}), \qquad (2.11)\\
\frac{dN_2}{dt} &= N_3B_{32}\rho_2(f_{23}) + N_1B_{12}\rho_1(f_{12}) - N_2B_{21}\rho_1(f_{12}) - N_2B_{23}\rho_2(f_{23}) - N_2A_2 + N_3A_3,\\
\frac{dN_3}{dt} &= N_2B_{23}\rho_2(f_{23}) + N_4B_{43}\rho_3(f_{34}) - N_3B_{32}\rho_2(f_{23}) - N_3B_{34}\rho_3(f_{34}) - N_3A_3,\\
\frac{dN_4}{dt} &= N_3B_{34}\rho_3(f_{34}) - N_4B_{43}\rho_3(f_{34}) - N_4A_4,
\end{aligned}$$

where B_{ik} is the Einstein B coefficient for the transition $i \to k$ with frequency f_{ik}, $A_i = 1/\tau_i = 2\pi\Gamma_i$ is the decay rate from level i, N_i is the population of level i per unit volume and $\rho_i(f)$ is the spectral energy density of Laser i per unit frequency at frequency f. i, k =1, 2, 3 and 4 for the levels of the excitation [1].

The Einstein B coefficients assume excitation from broadband radiation, and therefore the spectral energy density is assumed to be constant $\rho_i(f_{ik})$ across the linewidth of the

[1] This is a simplified model and does not include sublevels or the branching ratios to all other possible levels in the decay.

transition (98). For a monochromatic laser with linewidth γ, if $\gamma \ll \Gamma$ one can re-write the excitation term $B_{ik}\rho_i(f_{ik})$ in terms of the intensity of laser i and the detuning of laser i from the transition frequency f_{ik}

$$B_{ik}\rho_i(f_{ik}) \approx B_{ik}\frac{I_i L_{ik}(f_i - f_{ik})}{c}. \tag{2.12}$$

$L_{ik}(f_i - f_{ik})$ is a Lorentzian lineshape with FWHM Γ_k, describing the shape of the transition. Notice from Equation 1.1 that on resonance $f_i = f_{ik}$ and this expression becomes

$$B_{ik}\rho_i(f_{ik}) \approx B_{ik}\frac{2I_i}{\pi c \Gamma_k}. \tag{2.13}$$

The Einstein B coefficient can be related to the dipole matrix element of the transition via the expression (24)

$$B_{ik} = \frac{2\pi^2}{g_i}\frac{\mid D_{ik} \mid^2}{3\epsilon_0 h^2}, \tag{2.14}$$

where g_i is the degeneracy of state i. Importantly the stimulated-emission and absorption rates are related via the degeneracy g_k of state k:

$$B_{ik} = \frac{g_k}{g_i}B_{ki}. \tag{2.15}$$

Equations 2.11 were analytically solved using MAPLE, assuming both a closed and steady state system, by setting $N_1 + N_2 + N_3 + N_4 = N$ and $\frac{dN_i}{dt} = 0$. The solutions give expressions for the the steady state level populations N_i, based on the three-step laser intensities, matrix elements and the level decay rates.

The observable signal in this experiment is the first step laser absorption and how this is affected by the presence of the second and third step lasers. The populations of the levels can be related to the power absorbed per unit volume on each of the transitions (24) via the expression

$$\Delta P_i = \frac{h f_{ik}}{c}\Delta N_{ik} B_{ik} I_i L_{ik}(f_i - f_{ik}), \tag{2.16}$$

where $\Delta N_{ik} = N_i - N_k$ is the population difference between levels i and k.

Two level system

For a simple two level system, the absorbed power is expected to be linear for low intensities and become non-linear for higher intensities, as a significant atomic population is moved from level 1 into level 2. As the transition is driven with more laser power, the excitation

rate increases and the populations N_1 and N_2 approach $N/2$; ΔN_{12} therefore approaches zero. As this happens, the excitation rate begins to approach a constant value, governed by A_2. For the *on resonance* case, the power absorbed is

$$\Delta P_1 \approx \frac{2hf_{12}B_{12}I_1N}{\pi c\Gamma_2(1+S)}, \tag{2.17}$$

where $S = \frac{2B_{12}}{A_{21}}\frac{2I_1}{\pi c\Gamma_2}$. The intensity at which S=1 is the Saturation Intensity of the transition I_{sat} (24). Importantly, the Lorentzian frequency response of the transition results in power-broadening of the atomic transition when saturated. Saturation reduces the absorption near the centre of the Lorentzian profile, however in the wings absorption can still be strong. This effect causes a broadened line profile (98) with a FWHM of

$$\Delta f_{\text{power}} = \Gamma\left(1+\frac{I}{I_{sat}}\right)^{1/2}. \tag{2.18}$$

Four level system

The model was tested using realistic experimental parameters for the excitation of the 63P Rydberg state. The dipole matrix elements for the three transitions were taken from those

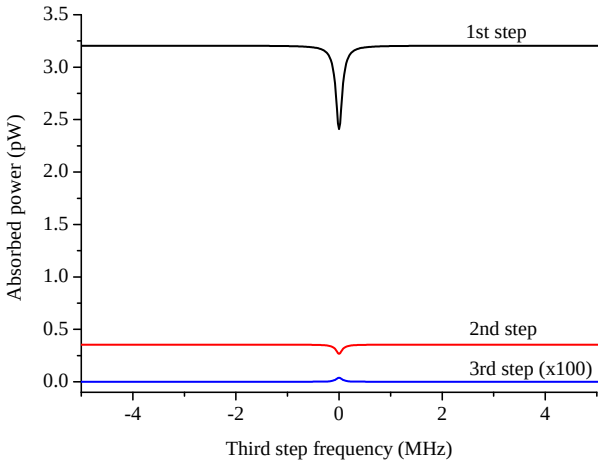

Figure 2.6: The absorption per atom ($N = 1$) on each of the transitions, for 63P excitation. The absorption of the third step is magnified by 100×, and is approximately 1000× smaller than the change in first step absorption; this is QA. All the resonances are Lorentzian in profile.

in Table 2.3 and the decay rates were taken as 38.1×10^6 s^{-1} (103), 4.19×10^6 s^{-1} (104) and 0.01×10^6 s^{-1} for levels two, three and four respectively. The laser powers were taken as 6 μW, 60 μW and 6 mW for the first, second and third steps respectively, focussed to a $\sim$100 μm spot diameter. Figure 2.6 displays the absorbed power per atom ($N = 1$) on the three-steps, as the third step laser is tuned into resonance with the Rydberg transition. Notice how the loss of power absorbed on transition 1 is much larger than the amount of power absorbed on transition 3, which is the effect of QA. This loss of power absorbed on transition 1 is the Rydberg signal of interest. With these parameters a QA factor of $\sim$1000 is seen, which is in reasonable agreement with the simple lifetime argument in Section 2.3.1. Figure 2.7 shows how the Rydberg signal size scales with the first step laser power, the data can be described well by a saturation like function

$$y = \frac{Ax}{1 + Bx}, \tag{2.19}$$

as in Equation 2.17. Adjusting the powers of the other two laser steps shows the same behaviour, following the same type of saturation curve.

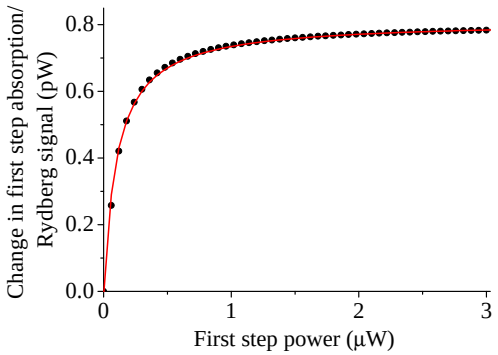

Figure 2.7: The change in the first step absorption by the presence of 63P Rydberg excitation, with first step laser power. This is equivalent to the size of the Rydberg signal. The circles are points predicted by the model and the red line is a fit of Equation 2.19.

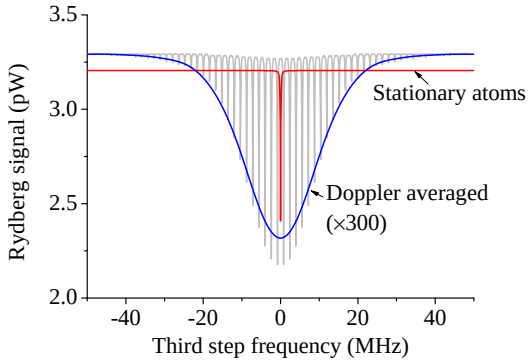

Figure 2.8: The red line is the Rydberg signal for a stationary atom. The grey peaks are the contributions from each 1 ms^{-1} velocity step, these are magnified by 300$\times$ and an offset of 2.7 pW is added. The blue curve is the total Doppler averaged signal (the smoothed total of the grey peaks).

The model successfully demonstrates saturation and power broadening on each of the three transitions. There are also two important observations that should be noted:

Firstly, only power broadening of the third step transition affects the linewidth of the detected Rydberg signal. Secondly, the linewidth of the detected Rydberg signal without power broadening is that of the third step natural linewidth Γ_4. To understand how this behaviour will be different in the vapour cell, the expressions for the level populations must be integrated over a Maxwell-Boltzmann velocity distribution, as in Equation 1.2.

Doppler broadening

To account for the effects of the atomic motion, a Doppler shift factor must be included in the laser detunings of the Lorentzian factors. These factors therefore become $L((1 \pm v/c)f_i - f_{ik})$, where the velocity signs are governed by the relative propagation directions of the three lasers. The absorbed powers are then integrated over velocity and weighted by a Maxwell-Boltzmann velocity distribution, this was completed numerically in MATLAB. Figure 2.8 shows the Doppler averaged Rydberg signal against the unaveraged signal from Figure 2.6, all other parameters were left the same, and the lasers were all chosen to co-propagate. The averaging was completed between velocities of ± 200 ms^{-1} with 1 ms^{-1} steps. The Rb room temperature Doppler width is 600 MHz and therefore from Figure 2.8 it is clear that the scheme achieves sub-Doppler resolution of the Rydberg signals.

Integrating the Rydberg signal over all velocity classes has several consequences: The signal can now be power broadened via all three-steps, this occurs because a power broadened transition can select a larger range of velocities, resulting in more Doppler broadening on the third step. This effect results in a much broader Rydberg signal linewidth, which is very prominent in Figure 2.8. As the *total* laser power approaches zero, this linewidth approaches Γ_{41}. Another significant effect of integrating is the lineshape of the signal, which now has a strong inhomogeneous Gaussian component. The line shape can be described by a Voigt profile, which is the convolution of a Lorentzian and Gaussian line profile (107). The total FWHM of the Voigt profile can be approximated by

$$\Delta f_V \approx 0.5346\Delta f_L + \sqrt{0.2166{\Delta f_L}^2 + {\Delta f_G}^2}, \tag{2.20}$$

where $\Delta f_V, \Delta f_L$ and Δf_G are the Voigt, Lorentzian and Gaussian linewidths respectively, and usually $\Delta f_L = \Gamma$. A brief investigation shows that the Gaussian component in the signal is introduced by both the wavelength mismatch of the lasers and the different natural linewidths of the three steps. Also, the signal is unchanged for all combinations of laser

propagation directions, which is in contrast to regular two-photon spectroscopy with an off-resonance intermediate state.

As expected, the relative populations of the levels are drastically modified by velocity averaging, see Figure 2.9. If the first step is fixed on resonance, only a small slice of the velocity distribution (governed by the first step FWHM) can be excited to the second level, and therefore contribute to the Rydberg signal. For this reason, in the Doppler averaged case, 91% of the atoms are in level 1 and non-contributing, whilst 6% are in level 2, 3% are in level 3 and <1% are in level 4, the Rydberg level.

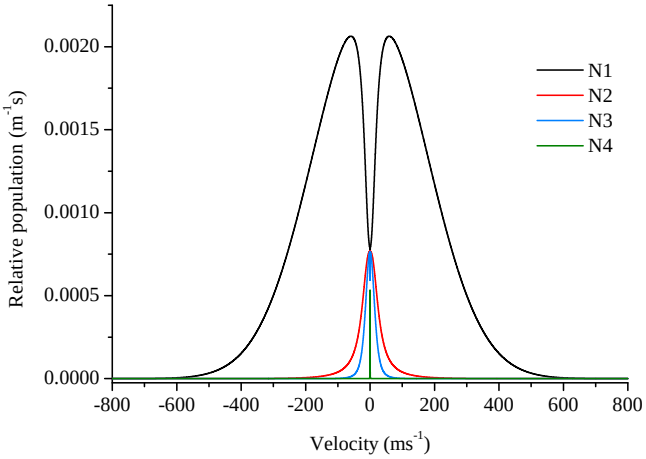

Figure 2.9: The velocity profiles of the four levels for a thermal distribution of atoms. All experimental parameters are the same as in Figure 2.6. The total area underneath the four curves is equal to one.

2.3.4 Focussing

In conventional *unsaturated* two-level absorption spectroscopy, Equation 2.17 says that the excitation rate is proportional to the product of the laser intensity and the number density of atoms. In this case, changing the beam radius will have no effect on the power absorbed through a cell: The associated increase of intensity and decrease of interaction volume exactly compensate each other. However, the size of the Rydberg signal in this three-step excitation scheme is not dependent on the absolute excitation rate of Rydberg atoms. Instead it is a difference measurement, and is proportional to the *change* in first

step absorption with and without Rydberg excitations present. The effect of Rydberg excitations is to reduce the relative atomic population in the lower levels and therefore reduce the absolute absorption rate on the first step. Assuming linear absorption on all three steps, it is found that the Rydberg signal size is therefore proportional to the *fraction* of atoms which are removed from the interaction volume $A \times \mathrm{L}$ by Rydberg excitation, where A is the laser cross-sectional area and L is the interaction length. Focussing all three lasers gives the largest fraction of non-interacting Rydberg atoms within the interaction volume, without affecting the absolute absorption rate on the first step. The Rydberg signal therefore scales as

$$\text{Rydberg signal size} \propto \frac{P_3}{A}, \tag{2.21}$$

where P_3 is the third step laser power.

2.3.5 Other effects

The rate equation model in Section 2.3.3 was a simplification of the excitation scheme, assuming only one-photon transitions could occur and ignoring coherence. However, here is a qualitative description of several other competing effects which one might expect to see in this system.

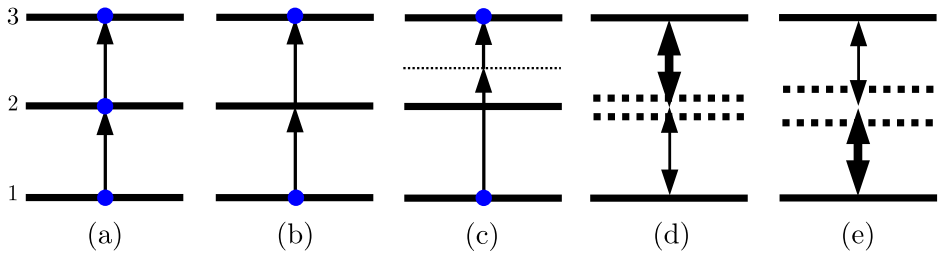

Figure 2.10: Different effects in a three level system. (a) shows step-wise excitation, (b) and (c) are simultaneous two-photon excitation processes, (d) shows an EIT system and (e) is an Autler-Townes splitting process.

Two-step: Step-wise and simultaneous excitation

The QA idea described so far assumes so-called step-wise excitation (Figure 2.10(a)). This process relies on level 2 being populated and therefore only a small range of velocities in the cell will contribute to the Doppler-free signal. Another possibility is the *simultaneous*

absorption of two photons (Figure 2.10(b)). This will excite the atom from level 1 to level 3 via a virtual level, with level 2 never being populated. This is an off-resonance process. When the first two lasers are counter-propagating and of (near) equal wavelength, in this case all velocity classes of atom will contribute to a Doppler-free signal (98). This is a competing process to the step-wise excitation because it also removes atoms from the strong 1→2 transition. However, the coupling strength of a two-photon transition is orders of magnitude smaller than that of the step-wise process and therefore the reduced first step absorption from this effect plays a much smaller contribution to the signal. As well as reduced absorption on the first step, a simultaneous two-photon excitation will also naturally show a degree of *increased* absorption. Again, due to the much weaker coupling, this is expected to be negligible. It has been shown in Reference (108) that for vanishingly small laser intensities, the simultaneous and step-wise processes can be treated equally.

One consequence of the above discussion is that if the first step laser is tuned outside of the Doppler width, no atoms can populate level 2 and two-photon excitation is the only process which can populate level 3 (Figure 2.10(c)). With correct parameters, one would expect to see a crossover in the first step absorption signal between a Doppler-free peak from QA, to a Doppler-free dip from two-photon absorption, as the first step laser is tuned outside the Doppler width.

Two-step: EIT

EIT is a coherent effect and involves coupling a ground state to an excited state via an intermediate level. It has been studied in a two-step ladder system before by Banacloche *et al* (109) [1]. It too is a resonant two-photon process, however in an EIT scheme level 2 and level 3 are not populated. A very weak probe beam couples levels one and two, and a strong pump beam couples levels two and three (Figure 2.10(d)). When the pump is fixed on resonance and the probe is tuned around resonance, a very narrow sub-natural transparency peak is observed in the probe absorption (110). This transparency is a consequence of quantum interference between different pathways from level 1 to 2. In a similar manner to the simultaneous two-photon process, in EIT all velocity classes contribute to the signal, with the main difference being that the pump and probe laser must be tuned inside the Doppler profile to observe the feature (the two transitions must be coupled by the lasers). To observe the EIT feature in the thermal vapour, with a ladder excitation

[1] EIT in the Λ arrangement is also possible (110).

scheme, requires using counter-propagating pump and probe lasers, otherwise the feature is washed out by Doppler broadening (110).

Two-step: Autler-Townes splitting

Intense laser light, resonant with an atomic transition, can cause a splitting of the excited level into two dressed states (Figure 2.10(e)), known as Autler-Townes splitting (111). This splitting occurs about the line centre and the two levels are split by the Rabi frequency Ω. One can observe this splitting by probing the level via a separate transition with a separate laser. In this particular excitation scheme, the first step laser couples very strongly with the first step transition and can achieve Rabi frequencies many times the natural linewidth. When the first step is driven far beyond saturation, one expects the second step laser to observe this effect, which should appear as a splitting of the QA signal from the $2 \rightarrow 3$ transition. Such a splitting has been observed experimentally in the Rb $5S_{1/2} \rightarrow 5P_{3/2} \rightarrow 5D_{5/2}$ excitation scheme by Akulshin *et al* (112).

Three-step: Four level effects

Finally, a word on analogous effects in the three-step system. As already emphasised, the third step transition coupling is significantly smaller than for the first and second steps. This means that analogous simultaneous three-photon excitations are expected to play an even smaller contribution than for the two-photon case. The dominant signal from Rydberg excitation is expected to be from QA on the first step. However, quantum interference and EIT have been considered theoretically in a four level system, with a microwave frequency third step by Sandhya *et al* (105). Regrettably, in this paper it was found that using an optical frequency third step (as is the case in this experiment), with the associated large Doppler broadening, results in a washing out of any EIT feature.

Chapter 3

Apparatus

This chapter outlines the workings of some of the general equipment used throughout this research, including details of the frequency comb system and its performance.

3.1 Frequency comb system

The frequency comb system is a commercially available, Menlo Systems FC1500 optical frequency synthesiser (44). It is based on a mode-locked fibre laser, with additional units for supplying comb light at specific wavelengths for the lab. The comb has a tunable repetition rate of 248.4 MHz to 251.1 MHz.

3.1.1 Optical components

The comb of frequencies is initially generated with an Er-doped fibre laser, centred at 1550 nm and spanning 50 nm FWHM. The comb light is divided to a set of three individual

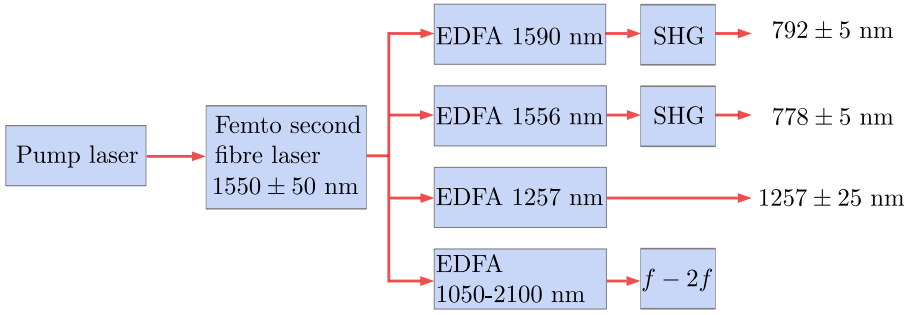

Figure 3.1: A schematic of the comb optical layout. EDFA: Er-doped fibre amplifier, SHG: Second harmonic generation stage, $f - 2f$: Non-linear interferometer for detecting f_o.

Er-doped fibre amplifiers (EDFA), supplying outputs at 1590 nm, 1556 nm and 1257 nm. The 1590 nm and 1556 nm outputs are subsequently frequency-doubled through non-linear crystals. The resulting comb light is available at 1257±25 nm, 792±5 nm and 778±5 nm. Figure 3.1 is a schematic of this optical layout.

To access the comb offset frequency, an $f-2f$ interferometer is implemented. A portion of the fibre laser output is sent through a special non-linear photonic crystal fibre and EDFA which supplies the comb super-continuum, spanning from 1050-2100 nm (a single octave). The light from this stage is sent through a non-linear interferometer. Inside the interferometer the supercontinuum light is focussed into a non-linear, periodically-poled crystal which frequency doubles the comb lines in the 2100 nm region. The beat note between these frequency-doubled lines and the undoubled lines, in the 1050 nm region of the comb, is detected with a photodiode, see Figure 3.2.

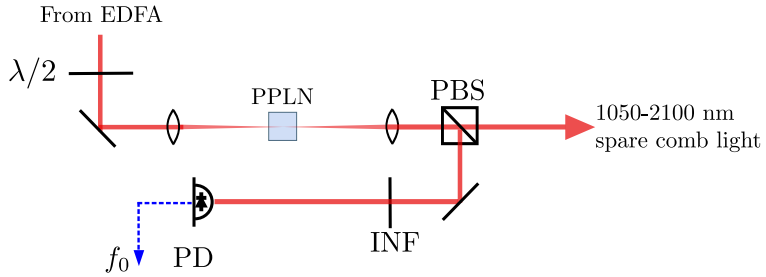

Figure 3.2: The non-linear interferometer for detection of the comb offset frequency f_o. EDFA: Er-doped fibre amplifier, PPLN: Periodically-poled $LiNbO_3$ crystal, PBS: Polarising beam splitter, INF: Interference filter, PD: Photodiode.

3.1.2 Electronic components

Figure 3.3 shows a schematic of the main electronic components of the comb system.

Repetition rate measurement and stabilisation

The fourth harmonic of the comb repetition rate at ∼1000 MHz is detected in the fibre laser head with a photodiode. This is mixed with a stable, fixed 980 MHz dielectric resonator oscillator (DRO), and the difference frequency at ∼20 MHz is locked to a tunable direct digital synthesiser (DDS). When locked, the comb repetition rate is therefore given by

$$f_{rep} = 245\,000\,000 + \frac{f'_{rep}}{4} \quad \text{Hz}, \tag{3.1}$$

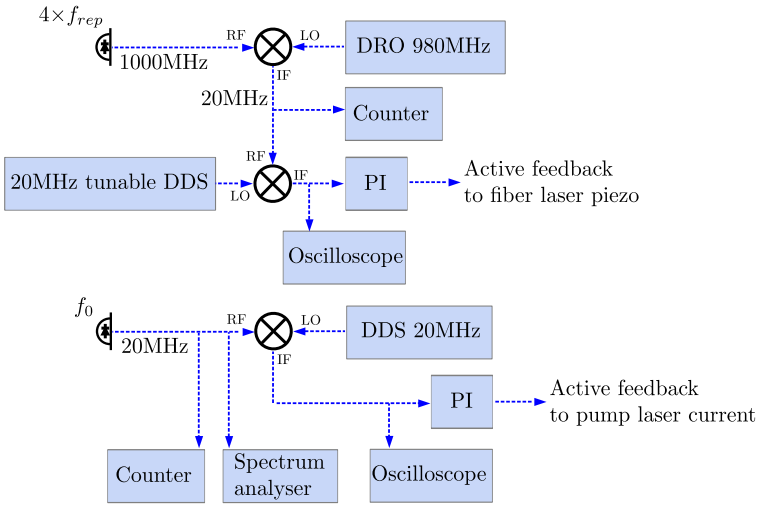

Figure 3.3: Schematic of the comb core electronics. All filters and amplifiers have been omitted for clarity. RF: Radio frequency input, LO: Local oscillator input, IF: Intermediate frequency output, DRO: Dielectric resonator oscillator, DDS: Direct digital synthesiser, PI: Proportional-integral controller.

where f'_{rep} is the 'down-converted' repetition rate, and is equal to the frequency of the DDS used for locking. The repetition rate is phase-stabilised using a digital phase detector and proportional-integral (PI) lockbox which feeds back to the fibre laser piezo, adjusting the cavity length. f'_{rep} is monitored with a frequency counter. By using the fourth harmonic of the repetition rate, higher phase sensitivity is achieved.

Offset frequency measurement and stabilisation: Self-referencing

The signal from the $f - 2f$ interferometer is phase-locked to a fixed 20 MHz synthesiser. This stabilisation is carried out with a digital phase detector and PI lockbox which feeds back to the pump power of the fibre laser. f_o is also monitored with a frequency counter.

3.1.3 CW laser measurement and offset-locking

Beat detection units

The comb system has three fibre-coupled beat detection units (BDU) for measuring beat notes between continuous wave (CW) lasers and the comb light, see Figure 3.4. Two of these are optimised to make measurements in the 780-795 nm region and the third is optimised at the 1257 nm region. The units detect beat notes using photodiodes which

operate up to 200 MHz and are optimised at the respective wavelengths. Fibre coupling to the units with single-mode fibre (SMF) ensures perfect mode matching of the two lasers on the photodiode, which gives the largest beat note SNR. The units also contain waveplates and polarising beam splitters (PBS) to clean the polarisations of the two laser inputs and to project them onto the same plane. In this way the two laser intensities can also be balanced on the photodiode.

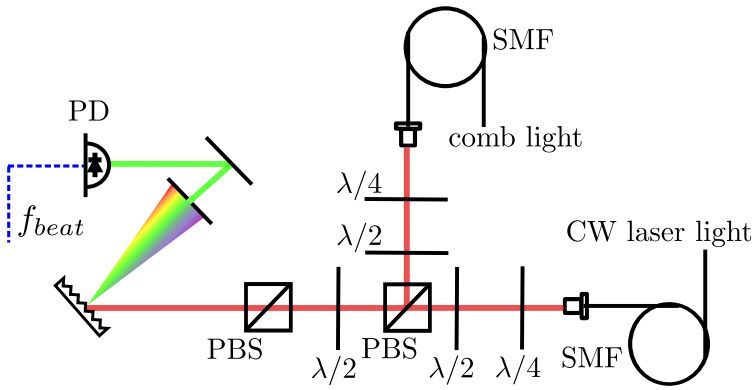

Figure 3.4: The fibre-coupled beat detection units (BDU). Waveplates translate the laser polarisations so they are both linear and in the same plane. The grating spatially disperses the comb light which allows the comb lines, that are not in the vicinity of the CW laser frequency, to be blocked from the photodiode; this reduces shot noise. SMF: Single-mode fibre, PBS: Polarising beam splitter, PD: Photodiode.

Absolute frequency measurements

If f_{beat} is the beat note with line n of the comb, the absolute frequency of the CW laser f_{cw} is given by

$$f_{cw} = nf_{rep} \pm f_o \pm f_{beat}, \tag{3.2}$$

where positive and negative beat notes correspond with the CW laser being higher or lower in frequency than the nth comb line respectively. There are standard procedures for deducing the signs of f_o and f_{beat} which are outlined in Reference (44). For the comb light used in the 780 nm and 776 nm BDUs, there is an important difference; the frequency doubling of the comb light means that the CW laser has an absolute frequency of

$$f_{cw} = nf_{rep} \pm 2f_o \pm f_{beat}. \tag{3.3}$$

A wavemeter was used throughout this research for deducing the nearest comb line n to the CW laser when making an absolute frequency measurement. A simple MATLAB comb calculator was made for computing CW laser frequencies using Equations 3.3 and 3.2.

Offset-lock electronics

The BDU photodiode bandwidth means that beat notes between the CW laser and the two nearest comb lines are observed; one positive and the other negative. Therefore this output is initially sent through a 100 MHz low-pass filter (100 MHz being less than $f_{rep}/2$), leaving only the beat note with the single closest line. The comb system is designed to offset-lock the laser beat note f_{beat} at either 20 MHz or 30 MHz. Therefore, the output from the low-pass filter is amplified and band-pass filtered at either 21.6±3.7 MHz or 30.0±5.0 MHz, to remove noise and spurious frequency components around the vicinity of f_{beat}. All this signal conditioning is completed within a BFD100 unit on the comb rack. Finally, the beat note f_{beat} is phase stabilised to a tunable DDS, forming a phase-locked-loop (PLL) laser offset-lock (113). This stabilisation is carried out with a digital phase detector and PI lockbox which feeds back to the CW laser, usually via the diode injection current. The beat note f_{beat} is monitored using a frequency counter. It is important that the SNR of the beat note is large enough that the background noise does not bias the counting of the beat. For a 30 dB SNR, systematic counting errors become smaller than 1 mHz.

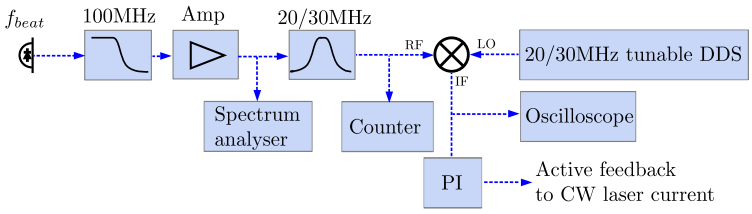

Figure 3.5: The electronics for offset-locking a CW laser to the comb. RF: Radio frequency input, LO: Local oscillator input, IF: Intermediate frequency output, DDS: Direct digital synthesiser, PI: Proportional integral controller. The amplifiers and filters are housed in a BFD100 unit.

The comb system has identical electronics for offset-locking and counting up to four CW lasers, with four BFD100 boxes; two centred at 20 MHz and two centred at 30 MHz. Figure 3.5 shows a schematic of the electronics involved for a single offset-lock.

3.1.4 Frequency referencing

All of the counters and synthesisers in the comb electronics are referenced to an SRS FS725 Rb frequency standard with a 10 MHz output. The output is scaled and distributed to the relevant pieces of electronics in the system. This ensures that the relative stability of the comb, and the relative accuracy of all counter readings, is limited by the stability and accuracy of the Rb reference. The stability of the reference can be seen in Figure 3.6. The comb itself has an intrinsic stability of 5×10^{-13} over 1 s (44).

3.1.5 Frequency counters

The frequency counter unit is based on the FXM method described in Reference (114), and allows up to six channels to be counted simultaneously without dead time. The counters have a default gate time of 1 s and a resolution of 1 mHz, corresponding to eleven digits when counting a 20 MHz signal.

3.1.6 Disciplining with GPS

Like many off-the-shelf atomic references, the SRS FS725 has excellent short term stability. However on longer time scales it has an ageing rate of up to 5×10^{-10} per year, which corresponds to 192 kHz when scaled by the comb to optical frequencies at 780 nm. It is therefore important to regularly calibrate the reference against a more accurate frequency standard to reduce this error. A common method that is used is to steer an atomic reference using the one pulse per second (1PPS) signal from the global positioning system (GPS), which itself is steered via primary Cs time standards, and therefore gives traceability to the SI second (115; 116). In contrast to the Rb reference, the GPS 1PPS has excellent long-term stability but poor short term stability, see Figure 3.6. Therefore a long time constant is often chosen for this steering.

During this research a GPS aerial was mounted on the roof of the lab, see Figure 3.7, and a Trimble Resolution-T timing receiver was installed to extract the 1PPS signal. A default time constant of two and a quarter hours was used to steer the Rb reference, which had aged for approximately two years. On attaching the timing receiver for the first time, the reference calibration was slowly adjusted by approximately 4.59 mHz on the 10 MHz output. This implies the comb lines at 780 nm were in error by ∼170 kHz before installing the GPS receiver. Based on previous studies with GPS referencing (115),

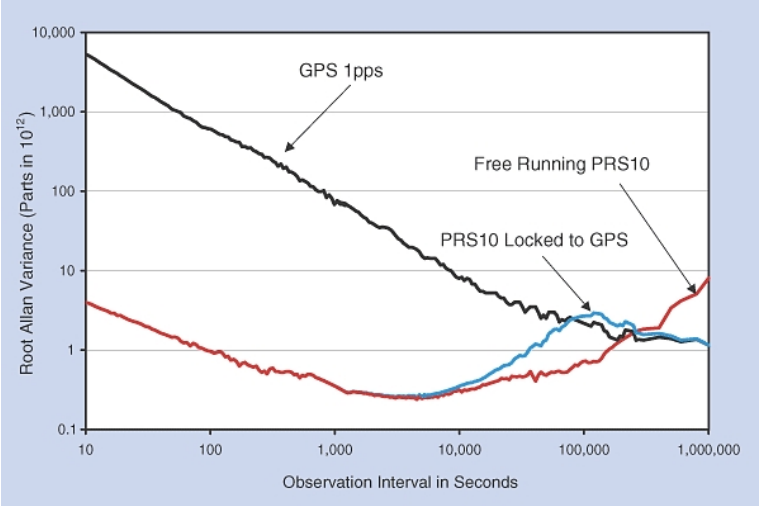

Figure 3.6: Stability of the GPS 1PPS and the SRS FS725 frequency standard with and without GPS referencing. Taken courtesy of Stanford Research Systems (117).

Figure 3.7: The GPS aerial which was installed on the roof of the lab.

one can expect the GPS disciplined comb system to have an absolute accuracy of at least 5×10^{-12}, equivalent to ~1 kHz when scaling to the laser frequencies involved in this work. In comparison, the intrinsic accuracy of the comb's RF-optical conversion process is 10^{-14} (44).

3.1.7 Performance

Offset beat note

The offset beat note used for self-referencing is monitored from the filtered output of the $f - 2f$ interferometer. Typically a beat note SNR of 30 dB with 100 kHz resolution bandwidth (RBW) is sufficient for locking, see Figure 3.8. The linewidth of the offset beat note was measured as 593 kHz using a 2 kHz RBW.

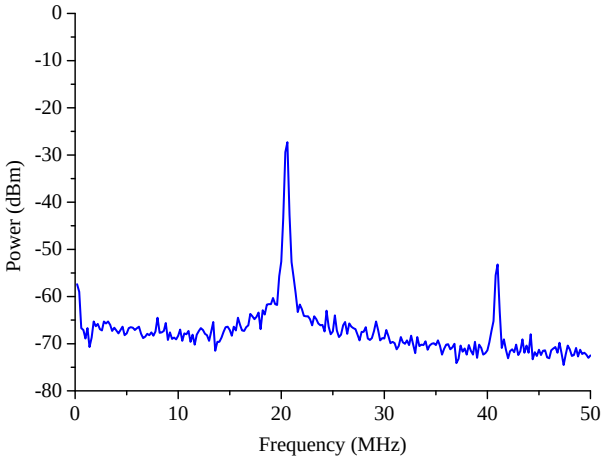

Figure 3.8: The stabilised f_o beat note from the $f-2f$ interferometer, used for stabilisation of the comb offset frequency. The second harmonic can also be seen. This scan was taken with an RBW of 200 kHz.

Stability results

Unlike the offset frequency, the repetition rate is scaled up by $\sim 10^6$, so absolute fluctuations of f_{rep} must be very well controlled for good stability at optical frequencies. This is why a 10 MHz source with excellent short term stability is required for referencing. Figure 3.9 is an Allan deviation plot (118) showing the stability of the comb offset frequency and repetition rate when locked; both parameters follow a $1/\tau$ character, implying phase-locked operation. Notice that the stability is higher for the repetition rate than for the offset frequency by a factor of 10^3. This is because the repetition rate is inherently more stable as it depends only on the cavity length and air pressure fluctuations, whilst the offset frequency depends directly on the pump laser power which is more noisy (119).

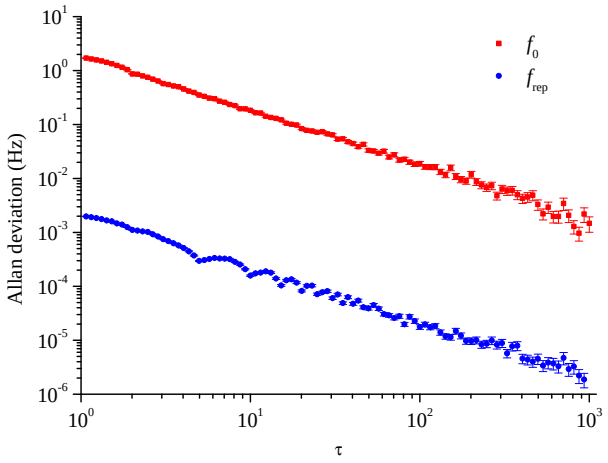

Figure 3.9: The Allan deviation (118) of the repetition rate and offset frequency when phase-locked.

The counter readings for f_{rep} in this system are only a way of detecting phase slips in the phase-lock; they are not capable of resolving the true stability of the repetition rate.

3.2 Diode lasers

Table 3.1 displays the lasers that were used throughout this research with their specifications. All lasers are external cavity diode lasers (ECDL). The Sacher Lion laser operates in the Littman configuration, whilst all the other lasers operate in the Littrow configuration. The speed of the fast feedback is an important property when comb-locking the lasers, all the lasers were able to be reliably comb-locked except the Toptica DL100 SB and New Focus Vortex laser. When in use, each laser was always followed by a shutter and a 30 dB Faraday optical isolator.

3.3 High-Finesse WS7 wavemeter

The wavemeter used throughout this research is a High-Finesse WS7 model, which is based on multiple Fizeau interferometers, and can measure CW laser wavelengths from 350-2250 nm (120). The wavemeter has an absolute accuracy of 60 MHz in the 780 nm region and 40 MHz in the 1260 nm region, which allows the nearest comb line number n to be easily deduced for any of the CW lasers in the lab.

Table 3.1: Laser specifications.

λ	Model	Max tuning range grating	Power	Linewidth	Fast feedback
780 nm	Toptica DL100 LB	Piezo 21 GHz	50 mW	<1 MHz	5 MHz FET
776 nm	Toptica DL100 SB	Piezo 10 GHz	20 mW	<1 MHz	7 kHz driver
776 nm	Sacher Lynx	Course-piezo 764-797 nm	150 mW	<1 MHz	120 kHz driver
1260 nm	Sacher Lion	Motor-piezo 1159-1269.8 nm	15 mW	300 kHz	2 MHz Bias-Tee
795 nm	Toptica DL100 LB	Piezo 15 GHz	120 mW	<1 MHz	5 MHz FET
780 nm	New Focus Vortex 6000	Piezo 75 GHz	70 mW	300 kHz	1 MHZ driver

In Section 4.6 the wavemeter is used to make high precision spectroscopy measurements across a 1253-1268 nm range. During this work the wavemeter's stability was monitored over a two and a half hour period by recording the wavelength of a comb-locked 1268 nm ECDL. Figure 3.10 displays the Allan deviation plot of this data (118). The wavemeter is stable to within 2 MHz over all time periods up to one and a half hours; a similar result was found for this wavemeter at 780 nm in Reference (87).

3.4 Photodiodes

The photodiodes used for all spectroscopy applications throughout this work were designed and constructed by Bruno Sanguinetti (121). Figures 3.11 and 3.12 show the sensitivity and frequency response respectively. The diodes operate across the wavelength range 776-795 nm.

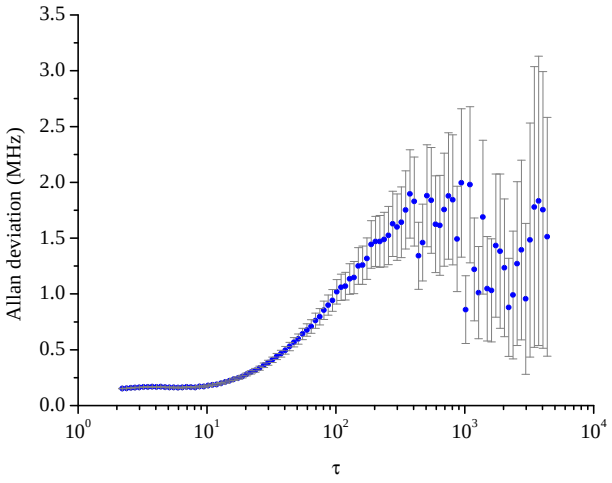

Figure 3.10: The long-term stability of the WS7 wavemeter when measuring a comb-locked 1268 nm diode laser.

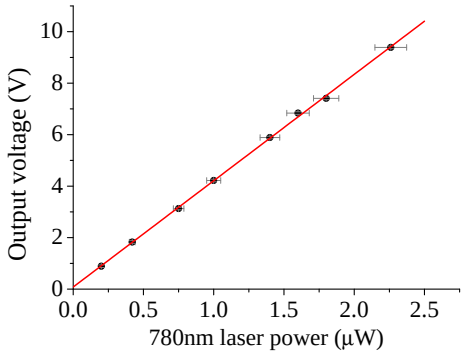

Figure 3.11: The light intensity response of the home made photodiodes. The gradient is 4.1 V/μW. The diodes saturate at around 12 V output voltage.

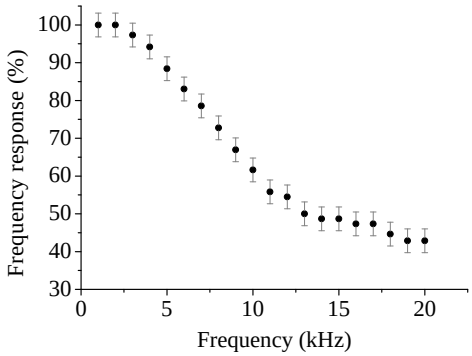

Figure 3.12: The frequency response of the home made photodiodes.

Chapter 4

Rb Rydberg spectroscopy in a vapour cell with three diode lasers

This chapter describes the initial construction, characterisation and optimisation of an experiment for detecting Rydberg atoms in a vapour cell using the three-step laser excitation scheme introduced in Chapter 2. After optimisation, the setup was used to measure a set of absolute frequencies of Rb $n\mathrm{F}_{7/2}$ Rydberg states using the frequency comb as an absolute frequency reference. These add to the very few existing absolute measurements of these high ℓ states in Rb (90). The construction and operation of the apparatus described in this chapter, along with the frequency measurements presented, were carried out in conjunction with my colleague, Hawri Majeed. All the plots and analysis were carried out by myself. A proportion of the work from this chapter has been published in New Journal of Physics (96).

4.1 Experimental setup

The optical setup used for Rydberg spectroscopy in this chapter is shown in Figure 4.1, and is based around that from Reference (55). Figure 4.1 also displays the electronics used throughout this chapter, which allows Rydberg detection using either amplitude modulation or frequency modulation (FM) spectroscopy. It also allows either slow stepped scans or faster ramped scans over the Rydberg levels. Rydberg signals are monitored using either a NI LabVIEW interface or a normal oscilloscope. These two techniques will be discussed throughout this chapter.

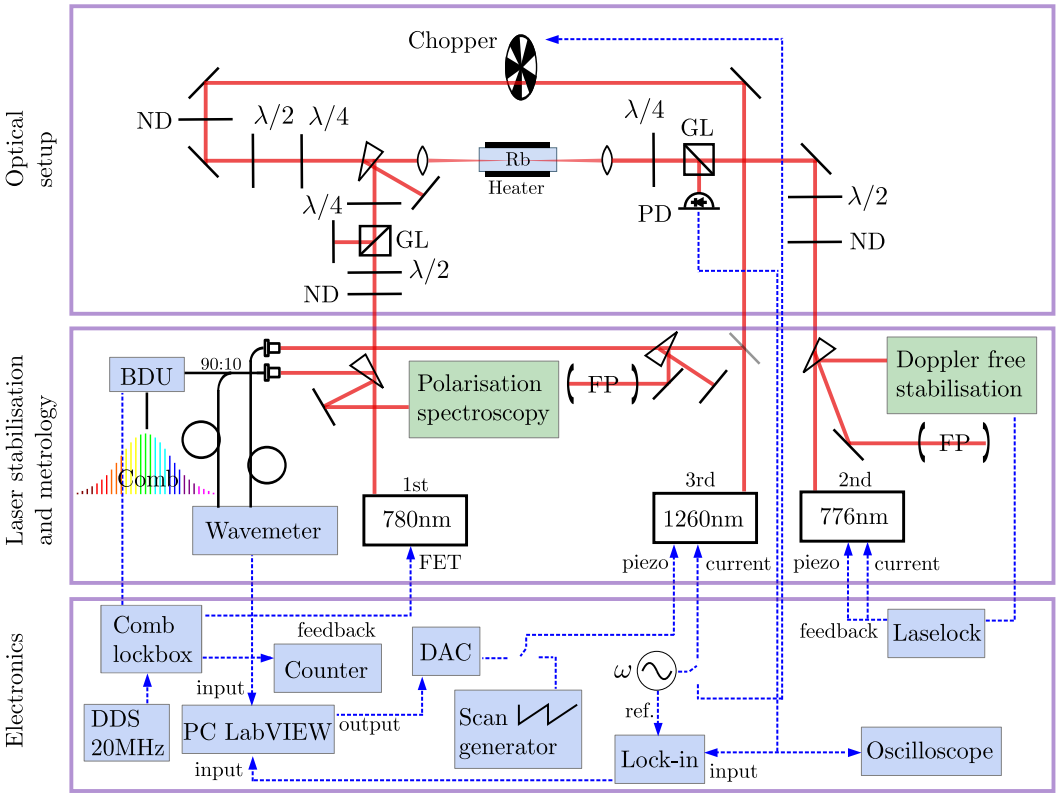

Figure 4.1: The optical and electronic setup used throughout this chapter for detecting Rydberg states in a heated Rb vapour cell. Light from the first and third step lasers is sent to the wavemeter via SMF fibre. In the case of the first step, a 90:10 fibre beam splitter sends 90% to a comb BDU. ND: Variable neutral-density filter, GL: Glan-laser polariser, PD: Photodiode, FP: Fabry Pérot resonator, BDU: Beat detection unit, FET: Field-effect-transistor input, DAC: Digital to analogue card.

The vapour cell is made from Pyrex and contains natural Rb with no buffer gas, it is 75 mm in length and 25mm in diameter. The cell can be heated to a maximum temperature of 63 °C using a Thorlabs cell heater, this increases the atomic density by 56× compared to room temperature (see Appendix A.3). Two lenses with equal focal lengths of 250 mm are used to focus the light such that the focal points of all three lasers lie approximately at the centre of the cell. Each of the lasers has a $1/e^2$ beam radius of ∼1 mm before the lenses, giving a beam waist diameter of ∼100 μm inside the cell after focussing. This focussing results in a ∼100× increase in Rydberg signal size, based on Equation 2.21.

The linearly polarised light from each of the lasers is circularly polarised using $\lambda/4$ zero-order waveplates in the case of the 780 nm and 776 nm lasers, and a $\lambda/4$ Fresnel-

rhomb retarder in the case of the 1260 nm laser. The 1260 nm laser and 780 nm laser are combined using a glass wedge to maintain the maximum third step laser power, which is required for Rydberg excitation. The beam geometries and orthogonal polarisations of the 780 nm and 776 nm lasers allow them to be separated with polarisers, so that the 780 nm absorption signal can be monitored independently with a photodiode. The laser powers are all controlled using variable neutral-density (ND) filters, and when required fine control is achieved using a $\lambda/2$ zero-order waveplate and PBS cube.

4.2 First step spectroscopy

4.2.1 Polarisation spectroscopy of the $5P_{3/2}$ state

Polarisation spectroscopy allows the stabilisation of a laser to the top of a Doppler-free spectral feature without the need for modulation of the laser frequency (31). In all previous work in the lab the first step laser has been stabilised to the $5S_{1/2}, F = 3 \rightarrow 5P_{3/2}, F = 4$ transition by a separate polarisation spectroscopy setup, which was developed by Gary Wilkes, Bruno Sanguinetti and Hawri Majeed (121; 122). Figure 4.2 shows signals from

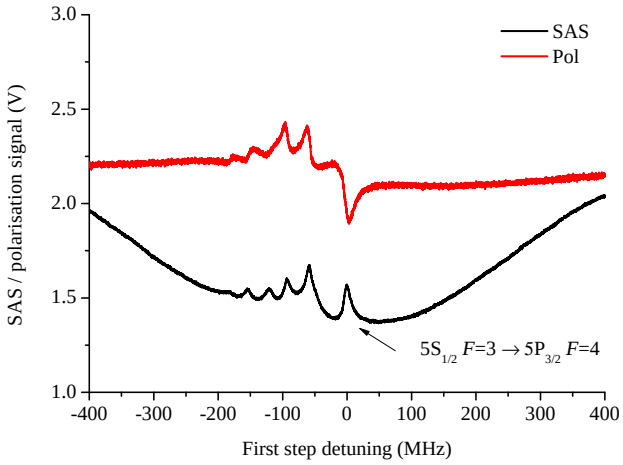

Figure 4.2: The ^{85}Rb polarisation spectroscopy signal used as a reference when locking to the comb. The first step $5S_{1/2}, F = 3 \rightarrow 5P_{3/2}, F = 4$ transition is indicated. The frequency axis is calibrated via the known hyperfine splittings of the $5P_{3/2}$ manifold. The black and red lines are the single and subtracted polarisation signals respectively.

this setup. The polarisation spectroscopy lock was not used for laser stabilisation in the

work of this chapter, however the signal served as a useful frequency reference, and is used for locking in the work of Chapter 5.

4.2.2 Comb-locking

In this experiment the first step laser Doppler selects those atoms which take part in the subsequent excitations, therefore it is important that the first step frequency is well known and well stabilised. For this study of Rydberg states it was chosen to offset-lock the first step laser to a line of the frequency comb. The feedback for this lock is supplied via the field-effect-transistor (FET) input on the first step laser head.

By monitoring the beat note of the first step laser against a comb line it was found that locking with the polarisation lock, although supplying excellent laser stability (∼10 kHz, 10 s), could not give an absolute frequency reproducibility of better than 2 MHz. Locking this laser directly to a comb line not only means the lock is highly repeatable but

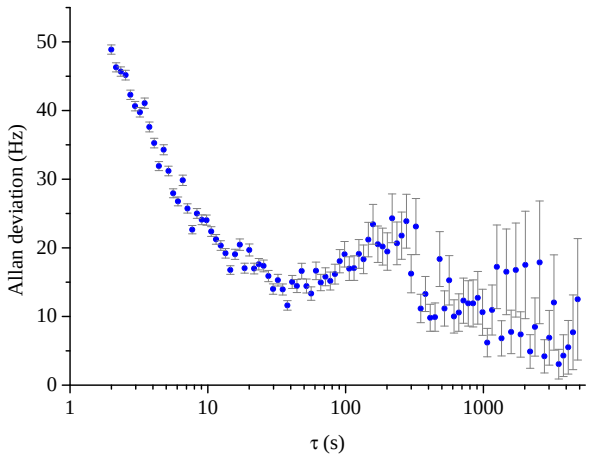

Figure 4.3: The Allan deviation (118) of the first step laser whilst locked to a line of the frequency comb.

also gives a very high level of stability. Figure 4.3 displays the Allan deviation (118) of the comb-lock, the plot was computed from three hours of counter data. On average, the laser deviates by less than 30 Hz over several hours, with excellent short term stability of <60 Hz over a few seconds.

The laser was locked at f_1=384 229 242.8 MHz, which is the literature value of the first step transition frequency from Reference (61). To compute the required comb repetition rate (to give a comb line exactly 20 MHz from the transition frequency), firstly a value of n was deduced for the closest comb line by rounding the quantity $f_1/250$ MHz to the nearest integer: n=1536 917. Then the comb equation was solved for f_{rep}

$$f_{rep} = \frac{f_1 - 2f_o - f_{beat}}{n} = 249.999\,956\,276\,103 \text{ MHz}, \tag{4.1}$$

where f_o and f_{beat} are both 20 MHz and all beat signs are positive. Before locking, the laser is manually tuned to within ±5 MHz of the transition using the wavemeter or polarisation signal as a reference.

4.2.3 First step absorption in the heated cell

The first step saturation intensity is much lower than the other two steps and, with focussing, this laser easily saturates the atoms, meaning the absorption on this step can be small. For ordinary absorption spectroscopy, one would prefer to use a larger beam radius on this step so as to excite more atoms, however as the third step transition needs the largest third step *intensity* possible, focussing is crucial. To increase the ground state atomic density and therefore the first step absorption, the vapour cell was heated. It was

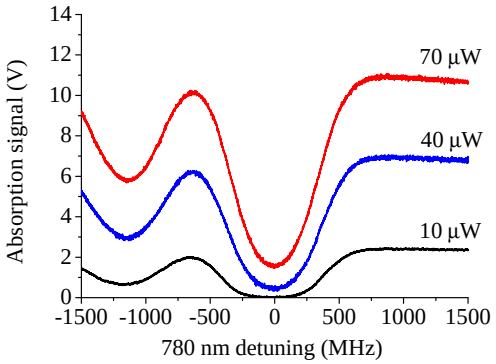

Figure 4.4: First step absorption across the $5S_{1/2}, F = 3 \rightarrow 5P_{3/2}$ Doppler width for 10, 30 and 70 μW laser powers, with a 63 °C cell. Complete absorption appears below about 30 μW.

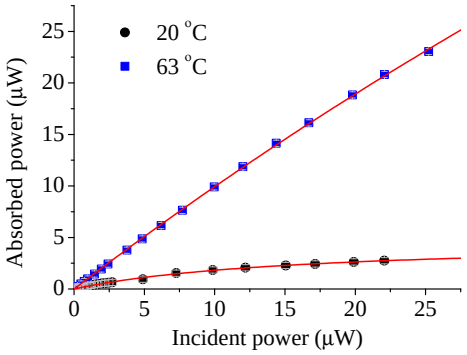

Figure 4.5: Absorbed first step power against incident first step power for the Doppler broadened $5S_{1/2}, F = 3 \rightarrow 5P_{3/2}$ transitions, with a 63 °C and room temperature cell.

found that heating the cell could cause a very large attenuation of the first step laser.

Figure 4.4 shows the absorption of a 63 °C vapour cell across the Doppler profile for different first step laser powers. Below about 30 μW one observes complete absorption of the laser. Figure 4.5 compares the maximum absorption against the first step laser power for the room temperature and 63 °C cell. The fitted lines are saturation type curves, see Equation 2.19. Throughout the rest of this chapter, unless otherwise stated, the cell was kept at 63 °C.

4.3 Second step spectroscopy

4.3.1 $5D_{5/2}$ detection methods

In this experiment the second step transition is observed using QA by monitoring the effect excitations have on the first step absorption. However, an alternative method of detection is to monitor the 420 nm fluorescence from the $5D_{5/2} \rightarrow 6P_{3/2} \rightarrow 5S_{1/2}$ cascade with a PMT (112; 123). Figure 4.6 shows the energy levels involved and the two detection techniques. It is also possible to excite to the $5D_{5/2}$ state with a single 778 nm laser, via off-resonance simultaneous two-photon excitation (123).

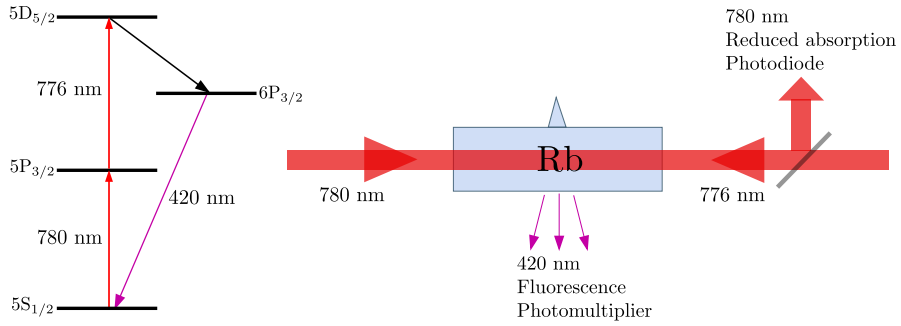

Figure 4.6: $5D_{5/2}$ detection methods: QA and fluorescence detection with a photomultiplier.

The method of QA detection has two advantages in this experiment:

- It only requires an ordinary photodiode for detection, which is cheap and compact
- The photodiode monitors absorption through the cell, so it can be positioned far from the cell if required and will always see the total signal (equivalent to 4π solid angle of fluorescence)

Even so, it was found that with sufficiently high laser power, the 420 nm fluorescence was easily visible with the naked eye. Figure 4.7 shows a photograph of the room temperature vapour cell with the first and second step lasers locked to the relevant transitions.

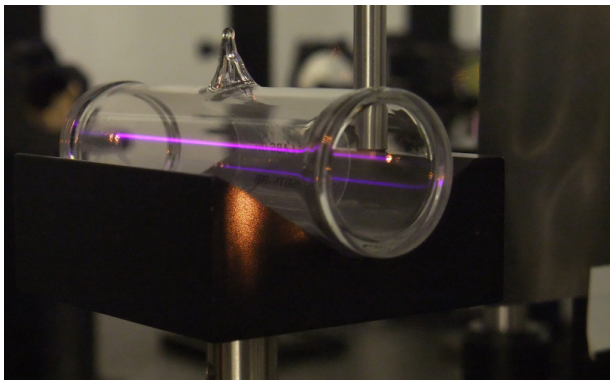

Figure 4.7: The 420 nm fluorescence observed from a room temperature cell, with the first and second step lasers locked to the relevant transitions. The light is emitted from the final decay of the $5D_{5/2} \rightarrow 6P_{3/2} \rightarrow 5S_{1/2}$ cascade.

4.3.2 Quantum amplification

Figure 4.8 shows a typical second step $5P_{3/2}, F = 4 \rightarrow 5D_{5/2}, F = 5$ signal detected using QA from the setup in Figure 4.1 (after optimisation of laser powers and alignment).

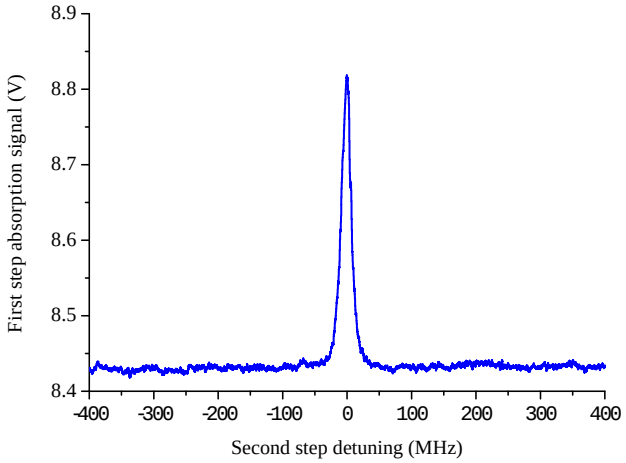

Figure 4.8: A typical $5D_{5/2}$ transition signal detected using QA. The FWHM is 14 MHz. The frequency axis was calibrated with a Fabry Pérot etalon.

4.3.3 Effect of first step laser power

Figures 4.9 and 4.10 are plots of the $5D_{5/2}$ transition signal size and FWHM against the first step laser power. One can see power broadening of the signal, although this is also

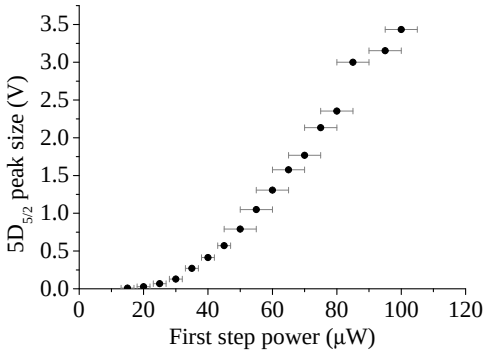

Figure 4.9: $5D_{5/2}$ peak amplitude against first step laser power.

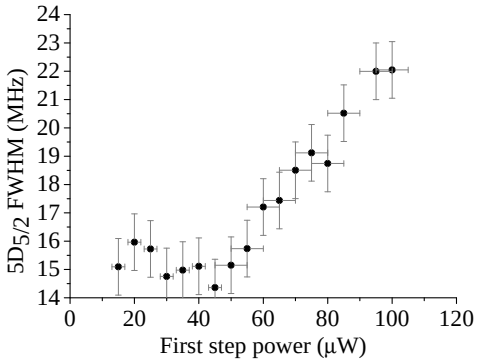

Figure 4.10: $5D_{5/2}$ peak FWHM against first step laser power.

accompanied by an exponential fall off for low first step laser powers of <60 μW. This is due to the complete absorption inside the cell, there is also no power broadening below this threshold. This laser must therefore have a power which is high enough that any reduction in absorption can reach the photodiode, and not to be instantly reabsorbed in the cell. For this purpose, a power of 70 μW was chosen. Unfortunately, at these powers the atoms at the front of the cell are exposed to laser intensities far higher than those at the back. Importantly, the observed $5D_{5/2}$ signal is a summed contribution from all atoms along the beam path of the 780 nm laser, where it intersects the 776 nm laser. For this reason, the alignment of the two lasers becomes a crucial factor; it allows the second step to interact with atoms which observe different intensities of the first step laser. Ultimately it was found that rather than keep the lasers overlapped and reduce the first step power ($\ll$1 μW) until saturation effects were not evident (this would result in a negligible amount of first step laser power leaving the cell), it was more beneficial to run at a higher first step laser power ($\sim$10 μW) and to carefully align the second step laser until saturation effects were minimised in the signal. Figure 4.8 shows the optimised case.

4.3.4 Autler-Townes splitting

For high first step laser powers of several hundred microwatts, Autler-Townes splitting of the $5D_{5/2}$ signal was observed (111). Figure 4.11 shows the second step signal with increasing first step laser powers and Figure 4.12 shows how this splitting scales with the power.

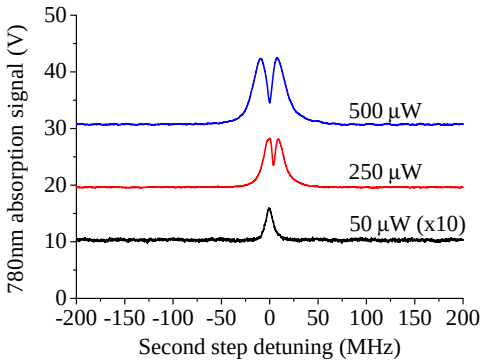

Figure 4.11: Autler-Townes splitting of the second step peak.

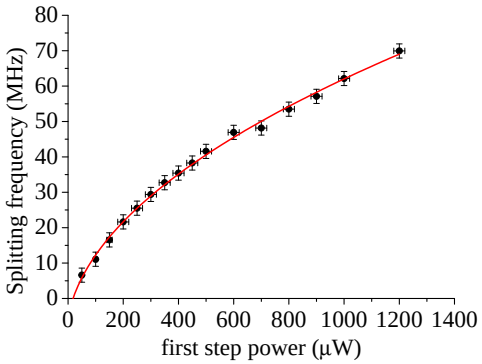

Figure 4.12: Splitting frequency vs. first step laser power.

For Autler-Townes splitting, one expects the splitting frequency to equal the Rabi frequency Ω_{12} on the first step transition (110). This is proportional to $\sqrt{P_1}$, where P_1 is the first step laser power. Figure 4.12 shows a square-root fit which confirms this. However, notice the 20 μW offset from zero, which may be a consequence of the total absorption of the cell below this power. The data shows the true first step average intensity felt by the atoms contributing to the signal; a basic analysis shows that I_1 is $\sim$400$\times$ lower than expected based on the waist diameter. This is a result of the deliberate misalignment mentioned in Section 4.3.3.

4.3.5 Effect of first and second step alignment

As mentioned above, the second step $5D_{5/2}$ signal was very sensitive to the relative alignments of the first and second step lasers. This is to be expected due to the small beam waists of the lasers within the cell. It was found that for different alignments one could see asymmetric signals, split peaks, broad single peaks and narrow single peaks. The narrow single peak, as shown in Figure 4.8, can be explained as the case where efficient optical pumping is occurring and the second step is not interacting with any atoms that

are exposed to a high first step intensity; therefore splitting and power broadening are minimised. This narrow single peak corresponds to the $5P_{3/2}, F = 4 \rightarrow 5D_{5/2}, F = 5$ transition. The other variety of signals can be explained by the second step interacting with atoms which are exposed to a high first step intensity.

4.3.6 Effect of second step laser power

The second step $5D_{5/2}$ signal was also sensitive to the second step laser power. Most importantly, the signal FWHM and peak size increased with increasing second step power, see Figures 4.13 and 4.14. The first step laser power was held constant at 70 μW for these plots. The signal size is fitted with a saturation curve (Equation 2.19) and the FWHM is fitted with a power broadening curve (Equation 2.18). Based on these findings, a power of 10 μW was ultimately chosen for the second step as a compromise between SNR and frequency resolution.

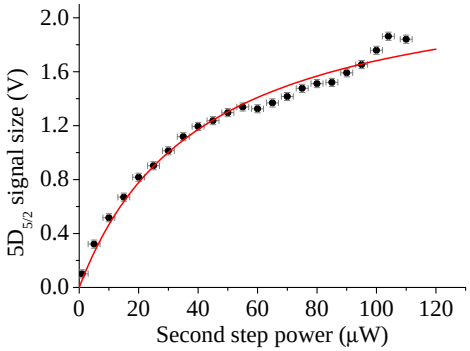

Figure 4.13: $5D_{5/2}$ signal peak amplitude against second step laser power.

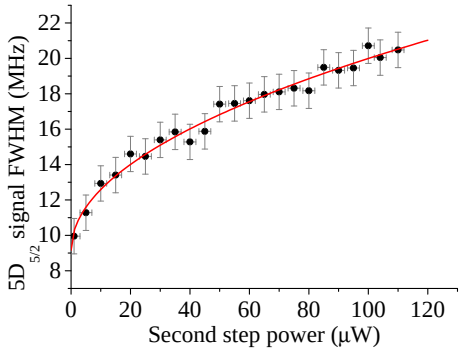

Figure 4.14: $5D_{5/2}$ signal peak FWHM against second step laser power.

4.3.7 Effect of cell temperature

Because of the strong link between the first step absorption and cell temperature, the effect of temperature was difficult to analyse quantitatively. Instead, the effect on the $5D_{5/2}$ signal was studied by changing the cell temperature, adjusting the first step power and observing the maximum SNR achievable. In all cases, higher temperatures were able to give higher SNRs with equal spectral resolution. Figures 4.15 and 4.16 show how the

second step $5D_{5/2}$ signal changes with cell temperature with fixed first and second step laser powers of 65 μW and 10 μW respectively.

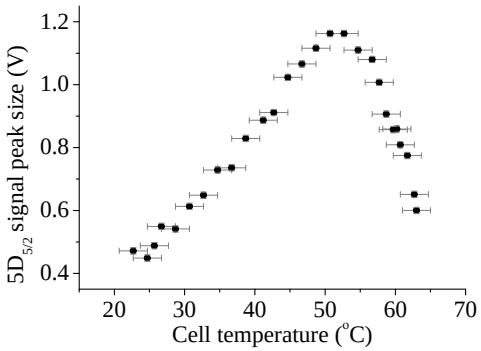

Figure 4.15: $5D_{5/2}$ signal peak amplitude with cell temperature.

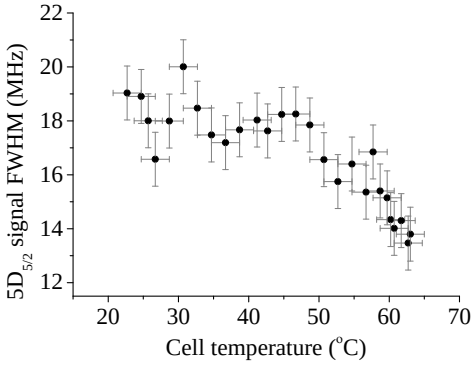

Figure 4.16: $5D_{5/2}$ signal peak FWHM with cell temperature.

In Figure 4.15 there is an increase in signal size with increased temperature. At room temperature the signal is approximately 3× smaller compared to at 50 °C, and the spectral resolution becomes worse at lower temperatures. The increased signal size can be explained by the increase in number density. The rapid fall off of the signal at high temperatures can be explained by the exponential decrease of transmission through the cell. This is also the reason for the reduction in linewidth with increased temperature in Figure 4.16. One can easily move the peak in Figure 4.15 to higher temperatures by increasing the first step power.

Interestingly, Figure 4.15 suggests that heating the cell is not beneficial, especially considering the increase in number density is 56×. However, one has to remember that these two plots are taken with a fixed first step laser power and the signal seen at room temperature is saturated and broadened at this point. To get a narrow $5D_{5/2}$ signal at room temperature requires reducing the first step laser power, resulting in a lower SNR. Therefore the temperature has the effect of giving a larger first step absorption signal, although higher first step powers are required to see this absorption from the other side of the cell. In conclusion, heating the cell allows higher SNRs on the $5D_{5/2}$ signal without reducing spectral resolution.

4.3.8 Hyperfine spectroscopy of the $5D_{5/2}$ state

In the same manner as Reference (55), this experiment uses optical pumping and dipole selection rules to give a well defined excitation pathway to the Rydberg levels. Figure 4.17 displays the optical selection scheme of the two-step system. $\lambda/4$ waveplates are used to produce the correct polarisations of the two laser steps. Optical pumping on the first

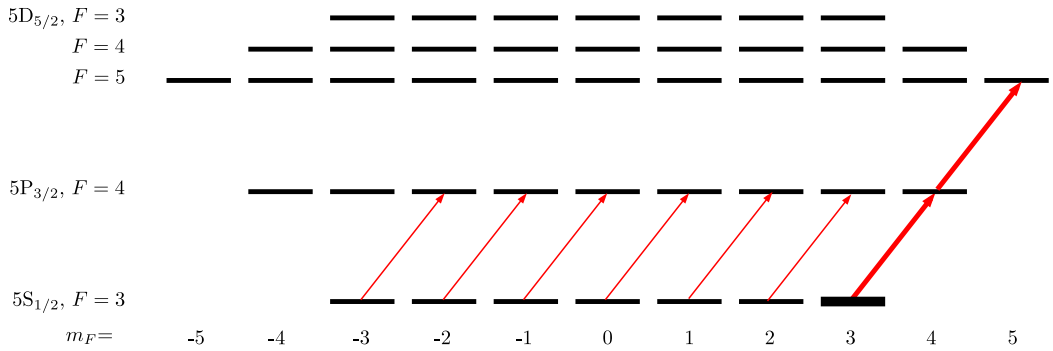

Figure 4.17: The magnetic sublevels m_F of the two-step scheme, using circularly polarised light on both steps. By transferring the ground state population to the $5S_{1/2}, F = 3, m_F = 3$ sublevel (via optical pumping) there is only one allowed, well-defined path to the $5D_{5/2}, F = 5, m_F = 5$ level.

step, and state selection of the second step, was verified in this setup by removing the $\lambda/4$ waveplates and inserting $\lambda/2$ waveplates to make the two beams linearly and orthogonally polarised. For the $\sigma_+\sigma_+$ case, a single peak is seen for the $5D_{5/2}$ signal corresponding to excitation to the F =5 hyperfine level. In the $\pi\pi$ case other features corresponding to the other hyperfine states of the $5D_{5/2}$ manifold are observed, see Figure 4.18. The laser powers used for these traces were 70 μW and 10 μW for the first and seconds steps respectively.

4.3.9 Second step stabilisation

Co-propagating setup

In all previous work in the lab, the second step laser has been stabilised using a separate vapour cell setup (75; 121; 122). This again uses QA to detect the $5D_{5/2}$ level but with co-propagating first and second step lasers, and with a room temperature cell (see Figure 4.19). The $5D_{5/2}$ signal achievable from this setup is comparable in size to that from the new counter-propagating setup, however the linewidth is larger at 18 MHz. This setup

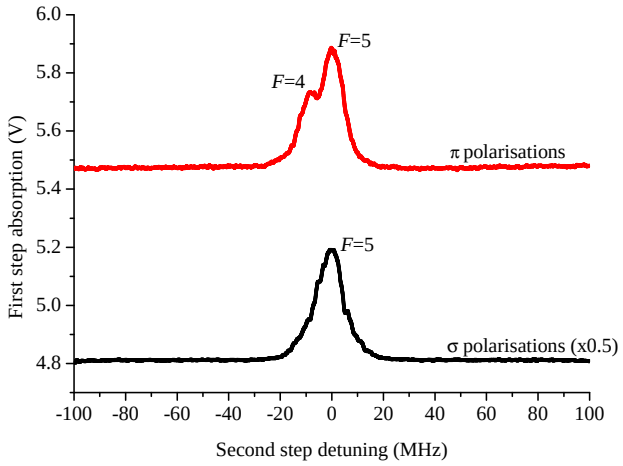

Figure 4.18: The $5D_{5/2}$ signal with and without optical selection, overlaid on the same axes. The $\sigma_+\sigma_+$ case is scaled by $\times 0.5$.

was first developed by Gary Wilkes, Bruno Sanguinetti and Hawri Majeed (121; 122). Throughout this chapter the second step laser was stabilised using this scheme.

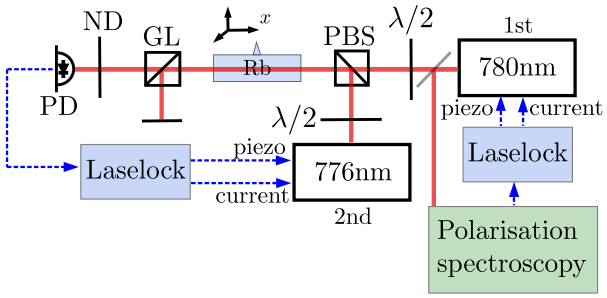

Figure 4.19: The separate second step stabilisation scheme. PD: Photodiode, ND: Neutral-density filter, GL: Glan-laser polariser, PBS: Polarising beam splitter.

FM spectroscopy: Locking

A frequency dither of 10 MHz amplitude is applied to the second step laser via the piezo and injection current and an error signal is derived using a lock-in amplifier (LIA), for top of peak stabilisation. The LIA and proportional-integral-differential (PID) servo electronics are contained in a universal Laselock unit. The second step laser can then be stabilised to the top of the peak in Figure 4.8. The frequency comb was used to check the repeatability

and stability of this lock. It was found that a 1 MHz absolute accuracy was achievable day-to-day, and a stability of better than 1 MHz over several hours.

4.3.10 Effect of first step frequency detuning

In the early parts of this research, it was observed that detuning the first step laser causes the $5D_{5/2}$ signals, from the co- and counter-propagating setups, to separate in frequency (in a scan of the second step). This can be explained from a simple velocity-selection argument. When the first step is detuned from resonance by $\delta_{12}{=}f_1 - f_{12}$, it selects atoms with a finite velocity

$$v = -\frac{\delta_{12}}{f_1}c \tag{4.2}$$

along the cell axis, based on the frame of reference shown in Figure 4.19. The old and new setups, having co- and counter-propagating second step geometries respectively, therefore see equal and opposite Doppler shifts of the second step laser:

$$\begin{aligned} \text{co} \qquad & \Delta f_{2\,\text{Dopp}} = -\frac{f_2}{f_1}\delta_{12}, \\ \text{counter} \qquad & \Delta f_{2\,\text{Dopp}} = +\frac{f_2}{f_1}\delta_{12}. \end{aligned} \tag{4.3}$$

These shifts are equal to the first step detuning scaled by the wavelength ratio 780/776=1.01 [1]. As an example, Figure 4.20 shows the $5D_{5/2}$ signals from the old and new setups on the same second step laser scan. The first step was comb-locked at the literature value of the first step transition (61). It is interesting that the two peaks do not overlap, suggesting that there is still a finite Doppler shift, and therefore a finite first step detuning. To investigate this further, the splitting was measured for a range of first step detunings. This was completed by comb-locking the first step laser at different absolute frequencies by tuning the comb repetition rate. The results from this study are shown in Figure 4.21.

Figure 4.21 shows a gradient of 2.02(5), in excellent agreement with the 780/776 ratio. The line also suggests that perfect overlap of the two peaks occurs for a first step frequency of 384 229 240.0(4) MHz, which should correspond to the exact first step resonance frequency. It is interesting that there is a 3 MHz offset between this number and the accepted literature value (61). This method could ultimately be used as a powerful method of precision spectroscopy of the first step transition, especially if the linewidths of the two

[1] A positive Doppler shift means a *lower* lab-frame second step frequency will be resonant and vice versa

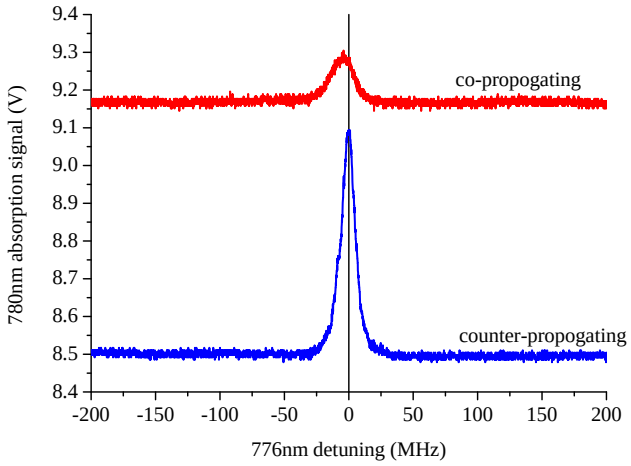

Figure 4.20: Signals from the co- and counter-propagating two-step setups simultaneously recorded during a second step frequency scan. The first step laser was comb-locked at the literature value for the first step transition. There is a clear splitting between the two peaks.

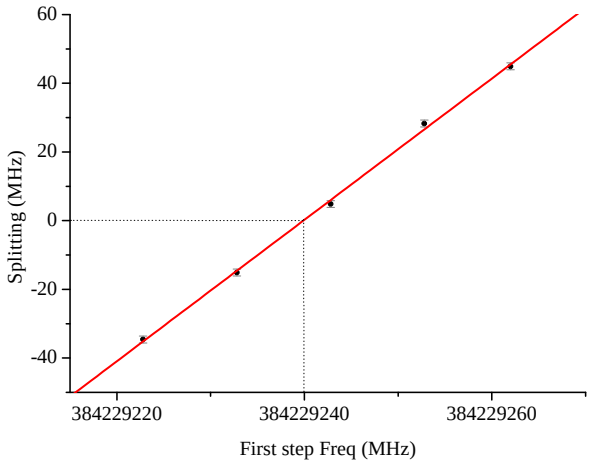

Figure 4.21: Splitting of the co- and counter-propagating signals for different first step frequencies. The dashed line indicates the point of perfect overlap for the two peaks.

$5D_{5/2}$ signals could be reduced below the natural linewidth of the first step transition. In this preliminary measurement, the linewidths were substantially different and there may have been other sources of systematic shift which were not addressed. Nevertheless, this

splitting was a very useful reference to inform whether the first step laser was locked on resonance.

4.4 Third step spectroscopy

In the three-step scheme, by choosing specific polarisations for the three laser steps, optical selection of particular Rydberg states can be achieved via optical pumping on the first step transition and dipole selection rules (55). The $n\mathrm{F}_{7/2}$, $F = 6$, $m_F = 6$ level can be selected with the three lasers set to $\sigma_+\sigma_+\sigma_+$ and the $n\mathrm{P}_{3/2}$, $F = 4$, $m_F = 4$ level can be selected with the three lasers set to $\sigma_+\sigma_+\sigma_-$. Figure 4.22 displays these two schemes. Note that for the $n\mathrm{F}_{7/2}$ and $n\mathrm{F}_{5/2}$ levels, only the hyperfine states with highest F are shown for clarity.

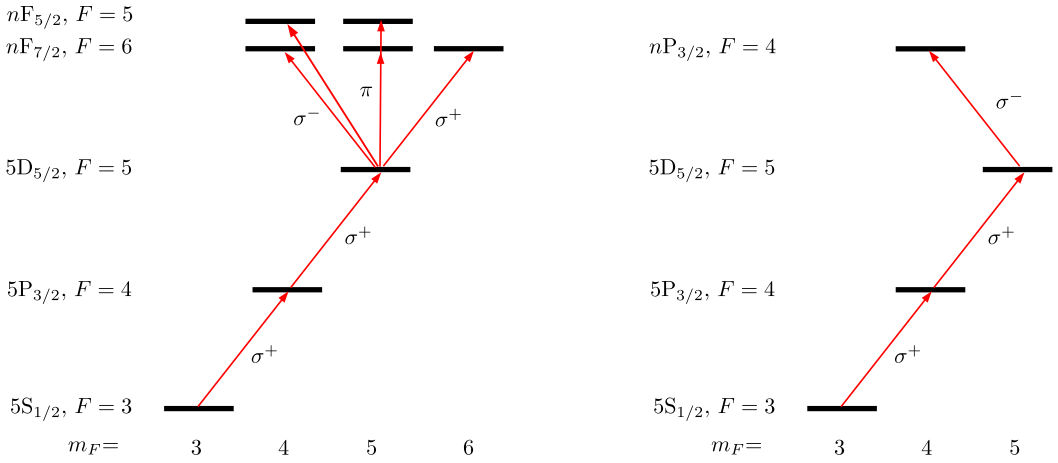

Figure 4.22: $n\mathrm{P}_{3/2}$ and $n\mathrm{F}_{7/2}$ Rydberg excitation schemes in ^{85}Rb. With $\sigma_+\sigma_+\sigma_+$ and $\sigma_+\sigma_+\sigma_-$ polarisations $n\mathrm{F}_{7/2}$, $F = 6$, $m_F = 6$ and $n\mathrm{P}_{3/2}$, $F = 4$, $m_F = 4$ Rydberg levels can be uniquely targeted respectively.

The expected frequency positions of Rydberg states were calculated within 100 MHz using previous values for the quantum defects and ionisation energies from the literature (65), along with Equation 2.1. The third step laser that was used is tunable via a precision stepper motor across a range of 1160-1269 nm and allows access to $n\mathrm{P}_{3/2}$ and $n\mathrm{F}_{7/2}$ states starting from n=36 and n=33 respectively, all the way to the ionisation threshold at 1252 nm.

4.4.1 Scans with a chopper

To improve the detection sensitivity of third step transitions, Rydberg levels were initially detected by intermittently chopping the third step laser with a chopper wheel at 1 kHz and monitoring the first step absorption using a LIA. A NI LabVIEW program was used to scan the third step laser across the transition of interest using a voltage ramp to the laser grating piezo. Data acquisition was simultaneously made from the LIA and from a High-Finesse WS7 wavemeter. The full schematic is shown in Figure 4.1.

Initial scans showed that it was possible to detect $n\mathrm{F}_{7/2}$ states with a much larger SNR compared to $n\mathrm{P}_{3/2}$ states. As expected, $n\mathrm{P}_{3/2}$ states could not be found in the $\sigma_+\sigma_+\sigma_+$ arrangement and $n\mathrm{F}_{7/2}$ states could be found in either arrangement, although the $\sigma_+\sigma_+\sigma_+$ case gave the largest signal. This is evidence of successful optical selection. Figures 4.23 and 4.24 show scans using the chopper technique over the $60\mathrm{F}_{7/2}$ and $63\mathrm{P}_{3/2}$ Rydberg levels. In both cases, the third step laser was not actively stabilised during the scans, the LIA time constant was set to 300 ms and the scans were carried out in 150 s.

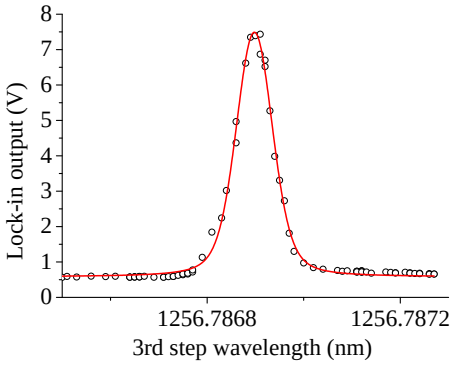

Figure 4.23: A third step laser scan over the $60\mathrm{F}_{7/2}$ level using the chopper technique. The LIA observes a decrease in the first step absorption.

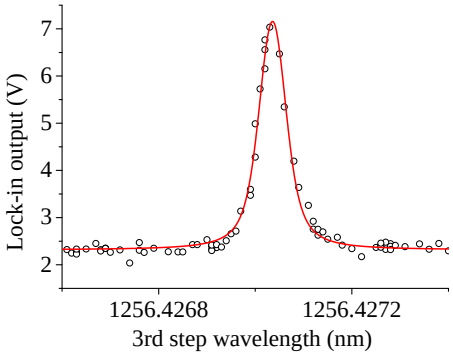

Figure 4.24: A third step laser scan over the $63\mathrm{P}_{3/2}$ level using the chopper technique. The LIA observes a decrease in the first step absorption.

Using the maximum available third step power of ∼3 mW and the chosen first and second step powers from Sections 4.2 and 4.3, the Rydberg signals' FWHMs were ∼20 MHz. This is similar to those found in References (55; 57), who use the same detection scheme.

4.4.2 Real-time scans

With some further optimisation, it was possible to observe the lower $n\mathrm{F}_{7/2}$ state signals in real-time on an oscilloscope, without a LIA. Figure 4.25 shows a real-time scan of the third step laser over the $5\mathrm{D}_{5/2}, F = 5 \rightarrow 33\mathrm{F}_{7/2}$ transition taken from an oscilloscope. It is very satisfying to observe Doppler-free transitions to Rydberg levels in almost the same manner as a simple SAS experiment of the Rb D lines. Conventionally the lab requires a vacuum setup, atomic beam and field ionisation apparatus to produce and detect Rydberg atoms.

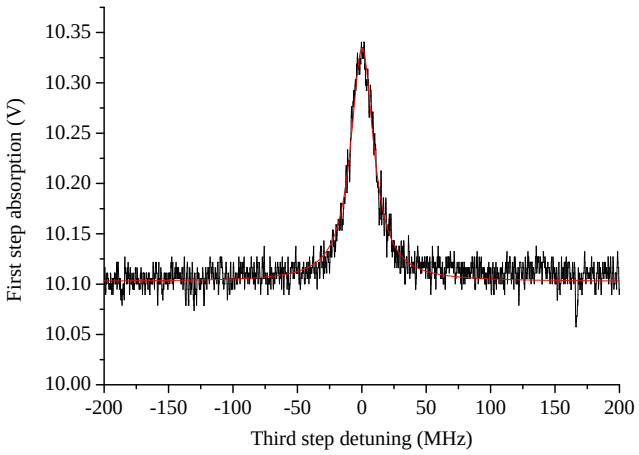

Figure 4.25: A real-time scan over the $5\mathrm{D}_{5/2}, F = 5 \rightarrow 33\mathrm{F}_{7/2}$ transition from an oscilloscope; the scan was completed in 10 ms. The red line is a Lorentzian fit with FWHM of 21 MHz; the frequency axis was calibrated with a Fabry Pérot etalon.

To capture the scan in Figure 4.25 the second step frequency dither was deactivated and this laser was simply tuned into resonance. With the second step laser locked, amplitude noise is added to the photodiode signal as the laser dithers across the top of the $5\mathrm{D}_{5/2}$ signal peak (see Figure 4.8). Because the baseline of the Rydberg signal is the top of the $5\mathrm{D}_{5/2}$ signal peak, the Rydberg signal is always observed on top of this noise. In the case of the slow scans with the chopper, this noise is effectively filtered by the LIA, however for fast real-time scans this noise can limit the detection sensitivity. Deactivating the second step dither also removes a source of broadening. As will be seen later in this section, the origin of the $\sim$20 MHz width appears to be predominantly from power broadening; the

transit-time limited linewidth will be ∼1 MHz.

4.4.3 Effect of cell temperature and first and second step laser powers

Using the real-time scans it was possible to study the behaviour of the $33F_{7/2}$ signal with respect to experimental parameters. Figures 4.26, 4.27, 4.28 and 4.29 show how the peak amplitude and FWHM scale with the first and second step laser powers. The second and first step laser powers were held constant for these plots at 10 μW and 65 μW respectively, as well as the third step laser power at 3.5 mW. The red fitted curves are the same as those used with previous data. Figures 4.30 and 4.31 show how the peak amplitude and FWHM scale with the cell temperature, in this case the first, second and third laser powers were all held constant at 65 μW, 10 μW and 3.5 mW respectively.

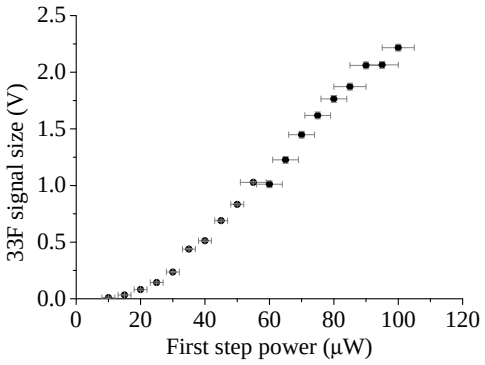

Figure 4.26: The $33F_{7/2}$ peak amplitude with first step laser power.

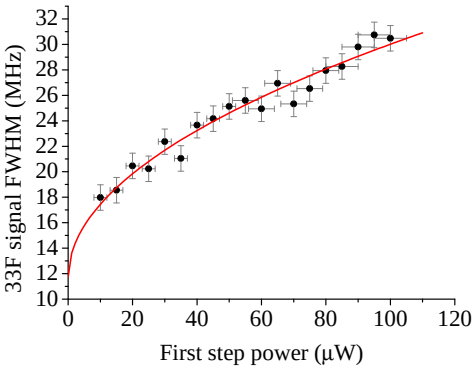

Figure 4.27: The $33F_{7/2}$ FWHM with first step laser power.

The signal behaviour is very similar to the way in which the $5D_{5/2}$ signal behaves with the same parameters, and can also be explained via similar arguments. One expects the Rydberg signal amplitude to be completely dependent on the population of the intermediate levels and therefore the amplitude of the $5D_{5/2}$ signal. The FWHM results in Figures 4.27 and 4.29 are interesting as they show that the Rydberg transition, although not directly coupled to the first and second step lasers, is still power broadened by them. This was theoretically predicted in Section 2.3.3 and occurs because the range of velocities reaching the Rydberg level is dependent on any power broadening on the lower transitions. Figure 4.27 exposes the origin of the ∼20 MHz Rydberg signal FWHM observed so

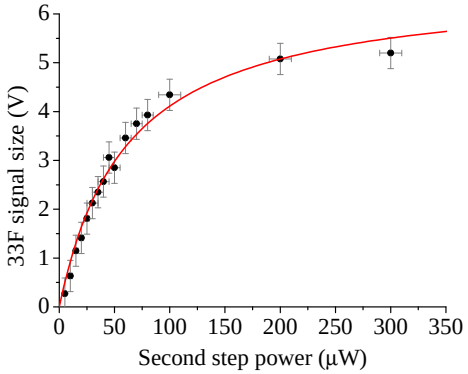

Figure 4.28: The $33F_{7/2}$ peak amplitude with second step laser power.

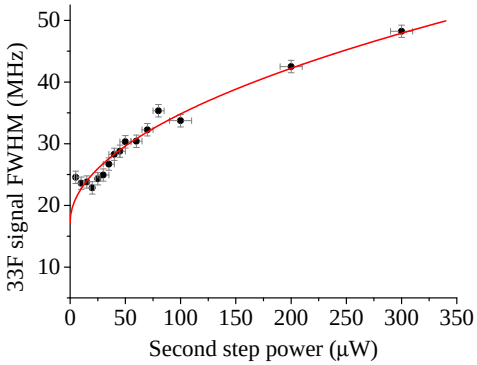

Figure 4.29: The $33F_{7/2}$ FWHM with second step laser power.

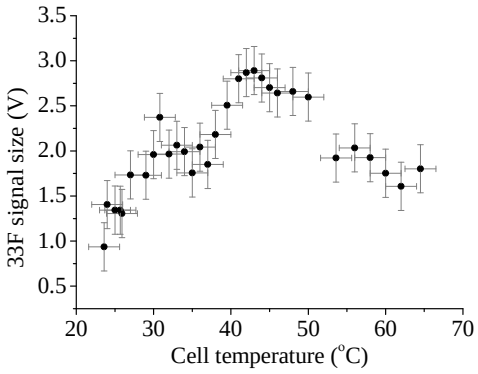

Figure 4.30: The $33F_{7/2}$ peak amplitude with cell temperature.

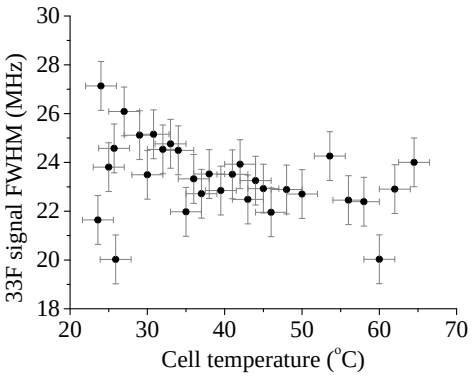

Figure 4.31: The $33F_{7/2}$ FWHM with cell temperature.

far. Unfortunately at lower first step powers, the signal sizes became too small to detect efficiently with the setup used.

4.4.4 Effect of third step laser power

Figures 4.32 and 4.33 show how the $33F_{7/2}$ Rydberg signal amplitude and FWHM scale respectively with the third step laser power. This data was also collected using real-time scans. The first and second step laser powers were held constant for these plots at 70 μW and 10 μW respectively. The red fitted curves are the same as those used with previous data. Interestingly, it is evident that the $5D_{5/2} \rightarrow 33F_{7/2}$ transition can actually be saturated at the large intensities used. However, this saturation has only a small effect

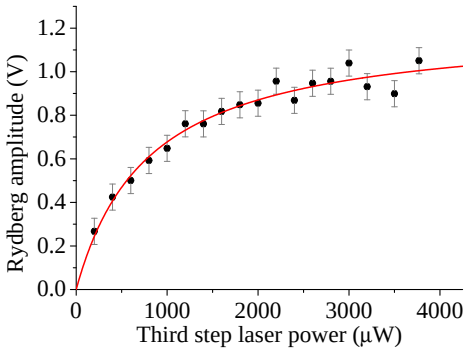

Figure 4.32: The $33F_{7/2}$ peak amplitude with third step laser power.

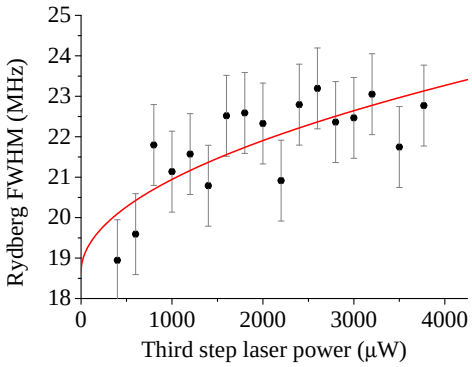

Figure 4.33: The $33F_{7/2}$ FWHM with third step laser power.

on the FWHM, in comparison to the first and second step laser powers.

4.4.5 Effect of focussing

A short study of the three-step excitation scheme was carried out, without use of the lenses. For the two-step spectroscopy, the $5D_{5/2}$ hyperfine structure was much more clearly resolved without focussing, which corresponds to less power broadening for equivalently sized signals. Figures 4.34 and 4.35 are examples and show spectroscopy of the $5D_{5/2}$ state without focussing in ^{85}Rb and ^{87}Rb respectively. $\pi\pi$ laser polarisations were used to excite all allowed hyperfine states. The beam powers were 150 μW and 350 μW for the first and second steps respectively. The FWHMs of the peaks are approximately 4, 4 and 2 MHz

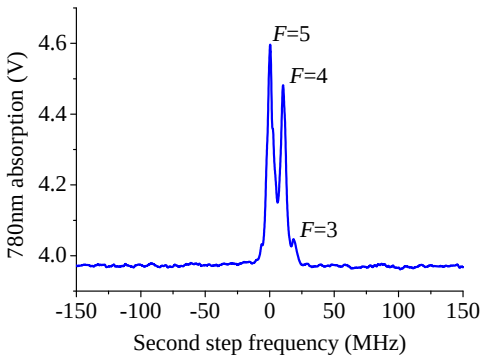

Figure 4.34: ^{85}Rb $5D_{5/2}$ two-step spectroscopy without focussing.

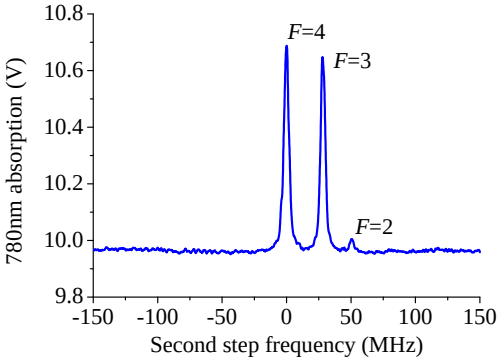

Figure 4.35: ^{87}Rb $5D_{5/2}$ two-step spectroscopy without focussing.

for the F=5, 4, 3 and F=4, 3, 2 transitions respectively. Such signals allow high precision measurements of the $5D_{5/2}$ hyperfine structure, similar to those in Reference (123).

As expected, focussing has a very positive effect on the detection sensitivity of Rydberg states. Without focussing, and even with much larger laser powers, the $33F_{7/2}$ Rydberg signal was at least $\sim$10$\times$ smaller in size and only just visible above the noise.

4.5 Rydberg fine and hyperfine structure

4.5.1 Introduction

The single peak in the $5D_{5/2}$ spectroscopy of Figure 4.18 indicates that excitation to the Rydberg levels occurs through a single, well known $5D_{5/2}$ hyperfine state. However, the Rydberg levels themselves have underlying fine and hyperfine structure also (65). Table 4.1 displays the fine structure splittings for the Rydberg levels accessible with this system. The fine structure splitting scales with $n^{*\ -3}$ and these numbers can be calculated from References (80; 81). The hyperfine interaction is much smaller and also scales with $n^{*\ -3}$, becoming larger for lower ℓ and j (98). Experimentally, the hyperfine structure has only been resolved up to n=59 for the $nS_{1/2}$ Rydberg series (79) and a splitting of 400 kHz has been observed for the $27P_{1/2}$ state (80). Because of the use of optical selection in this experiment, and the fact that the interaction is expected to be even smaller for $j > 1/2$ states, throughout this thesis the hyperfine structure of Rydberg states is not considered.

Table 4.1: The fine structure splitting for a range of ^{85}Rb Rydberg levels.

States	Fine structure splitting
$33F_{7/2}$-$33F_{5/2}$	4.34 MHz
$60F_{7/2}$-$60F_{5/2}$	680 kHz
$100F_{7/2}$-$100F_{5/2}$	157 kHz
$36P_{3/2}$-$36P_{1/2}$	18.6 GHz
$60P_{3/2}$-$60P_{1/2}$	4.02 GHz
$100P_{3/2}$-$100P_{1/2}$	869 MHz

For the whole range of n, the $nP_{1/2}$-$nP_{3/2}$ fine structure splitting is much larger than the linewidth of the observed Rydberg signals. Even so, selection rules state that the $nP_{1/2}$ levels cannot be excited with the current excitation scheme; although this would be possible by exciting through the $5D_{3/2}$ intermediate level instead. For the nF states there

are two differences: Firstly, the selection rules *do* allow excitation to both the $n\mathrm{F}_{5/2}$ and $n\mathrm{F}_{7/2}$ levels. Secondly, the fine structure splitting is smaller than the observed Rydberg signal linewidth. Therefore the fine structure cannot be ignored. Fortunately, if the optical selection is perfect in the three-step scheme, and all of the atoms in the $5\mathrm{D}_{5/2}$ level reside in the $F = 5$, m_F =5 magnetic sublevel, excitation is only possible to the $n\mathrm{F}_{7/2}$, $F = 6$, $m_F = 6$ sublevel, as described in Section 4.22. However, there is the likelihood of redistribution of the sublevels from precession of the atoms in the Earth's magnetic field. There may also be impurities in the third step polarisation. Both of these factors could result in some atoms being excited to the $n\mathrm{F}_{5/2}$ state, which will ultimately give some contribution to the observed Rydberg signal.

4.5.2 Relative transition strengths

To see how much of a contribution the $n\mathrm{F}_{5/2}$ state will make to the Rydberg signal, the relative strengths of the $5\mathrm{D}_{5/2} \rightarrow n\mathrm{F}_{7/2}/n\mathrm{F}_{5/2}$ transitions were considered. These can be found by successively reducing the dipole matrix element for an atomic transition between the two hyperfine sublevels $|n, L, J, F, m_F\rangle$ and $|n', L', J', F', m'_F\rangle$. This involves separating the angular orientation and the quantum numbers J, F and m_F from the dipole matrix element, and moving them into two Wigner 6j symbols and one Wigner 3j symbol using the Wigner-Eckart theorem (124). The relative line strengths are then given by the product of the symbols squared

$$\begin{aligned}(2J'+1)(2L+1)\begin{Bmatrix} L & L' & 1 \\ J' & J & S \end{Bmatrix}^2 \times (2F'+1)(2J+1)\begin{Bmatrix} J & J' & 1 \\ F' & F & I \end{Bmatrix}^2 \\ \times (2F+1)\begin{pmatrix} F' & 1 & F \\ m'_F & q & -m_F \end{pmatrix}^2,\end{aligned} \tag{4.4}$$

where I=5/2 for ^{85}Rb and q=−1, 0 and 1 for σ_+, π and σ_- transitions respectively. The first 6j term of Equation 4.4 shows the relative strengths of the different fine structure components. The second 6j term shows the relative strengths of the different hyperfine components within each fine structure component. The final 3j term shows the relative strengths of the possible transitions between different m_F magnetic sublevels.

Figure 4.36 displays these weighting terms for the $5\mathrm{D}_{5/2} \rightarrow n\mathrm{F}_{7/2}/n\mathrm{F}_{5/2}$ transitions, for the different fine and hyperfine transitions involved [1]. From these numbers one can

[1] These terms can also be found from tables such as those in Reference (125).

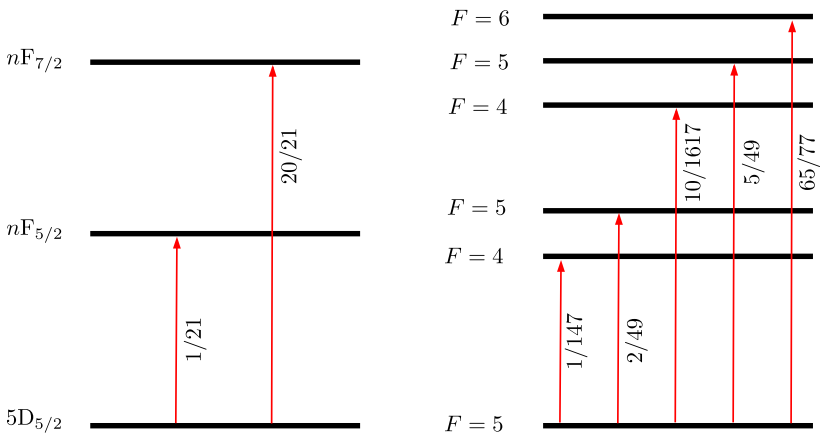

Figure 4.36: The relative weightings of each of the $5\mathrm{D}_{5/2} \rightarrow n\mathrm{F}_{7/2}/n\mathrm{F}_{5/2}$ components, calculated with the relevant Wigner 6j symbols. The left and right images display the weightings in the fine and hyperfine basis respectively, these are equivalent to the first term and the first and second terms of Equation 4.4 respectively.

conclude that even if the magnetic sublevels of the $5\mathrm{D}_{5/2}$, F=5 state were completely redistributed, the $5\mathrm{D}_{5/2} \rightarrow n\mathrm{F}_{5/2}$ component would contribute only $1/21 \sim 5\%$ at most to the signal. This is confirmed in the fact that the $33\mathrm{F}_{7/2}$ signal observed is highly symmetric, with no obvious shoulder from a $33\mathrm{F}_{5/2}$ contribution.

4.6 Absolute frequency measurements of $n\mathrm{F}_{7/2}$ states

After developing the experiment to the point where the $n\mathrm{F}_{7/2}$ signals were of optimum SNR, the setup was used to make a set of absolute frequency measurements of a range of $n\mathrm{F}_{7/2}$ states.

4.6.1 Slow scans with FM detection

To carry out the absolute measurements, FM spectroscopy was used by adding a frequency dither to the third step laser. This was chosen over using amplitude modulation with the chopper wheel. The FM method had several advantages in this case:

- It allowed a faster modulation frequency, limited by the 6 kHz limit of the third step injection current, rather than 1 kHz in the case of the chopper wheel
- There was less chance of the photodiode picking up spurious signals at the chopping frequency, from scattered light for example

- Moving parts were eliminated from the laser table which reduced vibrations and air currents

A frequency dither was added to the third step laser via the injection current, with a modulation amplitude of 15 MHz and frequency of 6 kHz. The laser was scanned and data acquisition was carried out from the LIA in the same way as the previous scans with a chopper wheel. Figure 4.37 shows a typical scan across a Rydberg transition using this technique, with the fitted line profile from Equation 4.5, given on the next page.

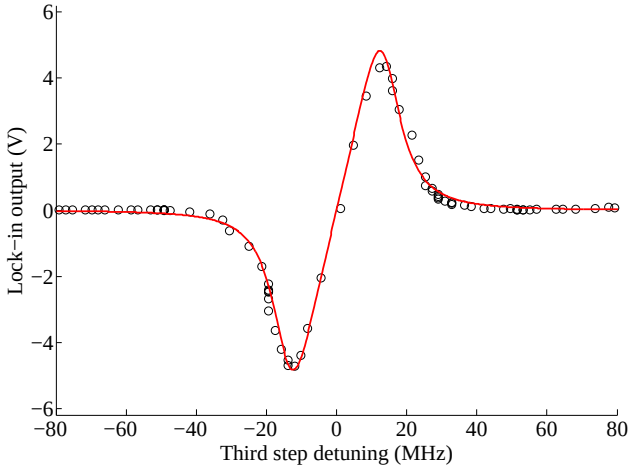

Figure 4.37: A slow frequency scan over the $5\mathrm{D}_{5/2}, F = 5 \rightarrow 33\mathrm{F}_{7/2}$ transition using FM detection. The wavemeter readings have been converted to frequency detuning from line centre. The red line is a Wahlquist first derivative function (126).

4.6.2 Laser frequency metrology

The free-running third step laser stability was measured as better than 1 MHz over 1 s using the comb, which is sufficient to carry out slow scans across the Rydberg transitions. Typically, scans were 150 s long and a LIA time constant of 1 s was used. The accuracy to which the third step transitions could be measured relied on the properties of the High-Finesse WS7 wavemeter. The stability of the wavemeter at the 1260 nm region stays below 2 MHz for times of ∼1000 s, see Section 3.3 for details. Therefore throughout this experiment, the wavemeter was calibrated every 30 minutes to the comb-locked first step

laser at 780.243 73 nm. This supplied a direct absolute frequency link with the comb. The same technique was used in Reference (87).

As well as studying the stability of the wavemeter, the absolute calibration accuracy was investigated. This was done by calibrating the wavemeter with the comb-locked first step laser, then immediately measuring a comb-locked 1260 nm laser with the wavemeter, which was locked at an arbitrary known frequency f_3. Such measurements were repeated across several days and for the range of wavelengths 1253-1268 nm. Figure 4.38 shows a histogram of a large set of frequency offset measurements $f_3 - c/\lambda_{\mathrm{wm}}$, where λ_{wm} is the wavemeter reading. From the spread of these readings, it is found that the wavemeter

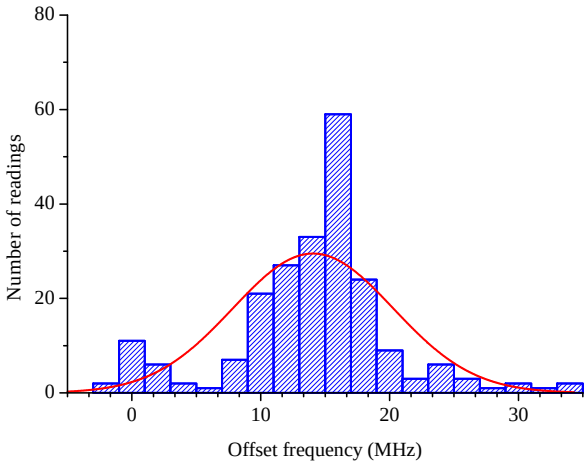

Figure 4.38: High-Finesse WS7 wavemeter frequency offset measurements around the 1260 nm region, after calibration at 780 nm. Offset=$f_3 - c/\lambda_{\mathrm{wm}}$. The red line is a normal distribution curve.

can maintain a day-to-day accuracy of 14.1±6.2 MHz across this range of wavelengths, when continuously calibrated. This consistent 14.1 MHz offset frequency was subsequently accounted for in all future measurements. The study demonstrates that the wavemeter is able to operate beyond its specified accuracy of ±40 MHz (120).

4.6.3 Absolute frequency measurements

The third step transition absolute frequencies were collected for n = 33-50 in intervals of one, and from n = 50-100 in larger intervals of five. Fitting to the transition data was done using a Wahlquist first derivative function (126). This line shape gives the familiar

Lorentzian derivative signal of FM spectroscopy, but also includes the effect of modulation broadening, for when significant modulation depths are used. The function is given by

$$f(H_\delta) = \frac{H_\delta}{|H_\delta|}\left(\frac{2}{H_\omega}\right)^2 \frac{\sqrt{2\gamma - u}}{2\sqrt{u-2}(u-\gamma)}, \tag{4.5}$$

where $\gamma = 1 + \beta^2 + \alpha^2$, $u = \gamma + \sqrt{\gamma^2 - 4\alpha^2}$, $\alpha = H_\delta/H_\omega$ and $\beta = (\frac{1}{2}H_{1/2}/H_\omega)$. $H_{1/2}$, H_ω and H_δ are the FWHM, modulation amplitude and frequency detuning respectively.

Ten traces were taken for each state in order to understand the repeatability of the measurements. It was found that on average, the standard deviation of each set of ten scans was 2 MHz, limited by the short-term drift of the wavemeter during the time taken to collect each set. The mean transition frequencies are summarised in the second column of Table 4.2. The third column of this table displays the total $5\mathrm{S}_{1/2} \rightarrow n\mathrm{F}_{7/2}$ frequency, measured from the centre of mass of the $5\mathrm{S}_{1/2}$ ground states. These values are calculated by adding a constant value of 770 571 549.6 MHz to the third step transition frequencies in column two; this added frequency is computed from literature values (91; 123).

4.6.4 Error analysis

The summarised error estimates are displayed in Table 4.3. The wavemeter calibration is a source of random error and all other uncertainties are systematic in nature. The errors add in quadrature to give a total error of 8.0 MHz.

Laser power and temperature

Rydberg atom interactions, for example the dipole-dipole interaction, scale strongly with inter-atomic spacing. It was therefore important to eliminate any pressure dependent shifts. The estimated inter-atomic Rydberg atom spacing is $\sim$10 μm, which is where one expects to see observable shifts of a few megahertz for the $100\mathrm{F}_{7/2}$ state (127).

As well as causing a broadening, increased power of any of the three lasers could also cause systematic shifts of the Rydberg signals. It is expected that both the Rydberg atom density and optical selection efficiency will have some dependence on laser power, both of which could result in a peak pulling. There will also be a contribution from the light shift (123).

Table 4.2: The third step transition frequencies $5\mathrm{D}_{5/2}, F = 5 \rightarrow n\mathrm{F}_{7/2}$ and total $5\mathrm{S}_{1/2} \rightarrow n\mathrm{F}_{7/2}$ transition frequencies E_n for n=33-100. The total frequencies are measured from the centre of mass of the two $5\mathrm{S}_{1/2}$ hyperfine ground states. The total accumulated error on all frequencies is 8.0 MHz.

n	$5\mathrm{D}_{5/2} \rightarrow n\mathrm{F}_{7/2}$ (MHz)	E_n: $5\mathrm{S}_{1/2} \rightarrow n\mathrm{F}_{7/2}$ (MHz)
33	236 429 214	1007 000 764
34	236 604 549	1007 176 099
35	236 765 078	1007 336 627
36	236 912 402	1007 483 952
37	237 047 954	1007 619 503
38	237 172 932	1007 744 481
39	237 288 417	1007 859 967
40	237 395 343	1007 966 892
41	237 494 542	1008 066 092
42	237 586 734	1008 158 283
43	237 672 570	1008 244 119
44	237 752 610	1008 324 159
45	237 827 379	1008 398 929
46	237 897 325	1008 468 875
47	237 962 850	1008 534 399
48	238 024 325	1008 595 874
49	238 082 056	1008 653 605
50	238 136 367	1008 707 917
55	238 364 972	1008 936 522
60	238 538 826	1009 110 376
65	238 674 124	1009 245 673
70	238 781 461	1009 353 011
75	238 868 053	1009 439 602
80	238 938 927	1009 510 477
85	238 997 658	1009 569 208
90	239 046 866	1009 618 416
95	239 088 516	1009 660 066
100	239 124 074	1009 695 624

To target systematic shifts from pressure and laser power, measurements were taken of the $33\mathrm{F}_{7/2}$ and $100\mathrm{F}_{7/2}$ transitions with a range of cell temperatures from 20-65 °C and a range of first, second and third step laser powers respectively. In all cases repeatable trends in the transition frequencies were undetectable within the wavemeter accuracy. Therefore, potential offsets from both temperature and power dependent shifts were not

added as corrections but instead the spread of measurements were used to estimate the maximum possible error in each individual case.

Magnetic fields

Using a fluxgate magnetometer, the magnitude of stray magnetic fields was measured along the axis of the vapour cell to be <20 μT. A Rydberg level experiences a linear and a diamagnetic (quadratic) energy shift in a magnetic field. If $n^4B \ll 1$, where B is given in units of 2.35×10^5 T, the quadratic term may be ignored and magnetic effects are of the same size as they are for a low lying excited state with the same ℓ; in this case the Zeeman shift has no n dependence (65). In this experiment for the n=100 state $n^4\mathrm{B}\sim 10^{-2}$. The magnetic shift can therefore be written as the familiar linear Zeeman shift in the hyperfine basis (98). For the most magnetically sensitive $n\mathrm{F}_{7/2}$, F=6, m_F=6 levels this is

$$\Delta f_{\mathrm{Zeem}} = \mu_B g_F m_F B_z = 0.06 \text{ MHz}/\mu T, \tag{4.6}$$

where μ_B is the Bohr magneton, g_F is the Landé g factor (see Appendix A.4), m_F is the magnetic sublevel and B_z is the magnetic field strength. This gives a Zeeman shift of <1.1 MHz for the fields around the cell. However, one actually expects Zeeman shifts of the *transitions* to be equal to the difference in Zeeman shifts between subsequent levels of the excitation scheme, in this case 14 kHz/μT for each of the three steps. Therefore, a maximum Zeeman shift of 840 kHz is estimated for the Rydberg signals.

To check for this shift, measurements of the $33\mathrm{F}_{7/2}$ state were made with both $\sigma_+\sigma_+\sigma_+$ and $\sigma_-\sigma_-\sigma_-$ polarised light on the three steps respectively. Equal and opposite Zeeman shifts are expected for these two cases. No frequency difference was measured within the short term drifts of the wavemeter and therefore it is assumed the contribution to the total uncertainty from this effect is negligible. As an additional test of the optical arrangement, and the magnetic field sensitivity, a magnetic field of 100 μT was applied along the axis of the cell with a permanent magnet. In this case shifts of the Rydberg signals of up to 5 MHz were observable.

Electric fields

In References (54; 55) no DC-Stark shifts were observed when detecting Rydberg atoms in a vapour cell for externally applied electric fields of up to 100 Vcm^{-1}. This makes a cell an excellent spectroscopic sample, by eliminating a potential systematic shift. To check

for similar behaviour in this setup, some simple field plates were placed around the vapour cell, separated by 6.6 cm. Potential differences of up to 200 V were applied across the vapour cell and frequency measurements of both the $33\mathrm{F}_{7/2}$ and $100\mathrm{F}_{7/2}$ transitions were measured to check for shifts. In each case there was no measurable deviation. This area is investigated further in Section 6.6.

Although such measurements show that the Rydberg atoms within the cell are shielded from *external* fields, it does not rule out the possibility of a small stray electric field originating from *within* the cell. This possibility is considered in Chapter 7, and a convenient method is demonstrated for measuring the size of such stray fields, which gives an upper bound on potential frequency shifts [1].

Data acquisition

Possible errors from hysteresis and time delays in the data acquisition process were eliminated by scanning the third step laser across the same transition in opposing directions. No significant difference was found between these two measurements.

Table 4.3: Estimated errors. All errors are 1σ. The total error is the sum in quadrature of the different sources.

Source	Error
Wavemeter calibration	6.2 MHz
First step frequency	750 kHz
Second step frequency	1.0 MHz
Temperature shifts	2.7 MHz
Power dependent shifts	4.0 MHz
Total	8.0MHz

4.6.5 Analysis

The frequency measurements from this experiment were analysed using three different Rydberg-Ritz fitting methods. The first two methods follow the same theme as that in Reference (128), whilst the third method is a consistency check of the data with previous work from microwave spectroscopy (81). These methods are outlined in the following sections. To aid in the analysis, five values of E_n for $n = 4 - 8$ were added to the data

[1] For the measurements in this chapter, the expected shifts are shown to be much smaller than those from other sources of error.

Table 4.4: The fit parameters from the Method 1, 2 and 3 fitting routines. The Method 1 fit gives the series parameters δ_0, δ_2 and δ_4. The Method 2 and 3 fits, and Reference (81), give the equivalent series parameters δ_0, a and b. Uncertainties are statistically derived from the fitting. The errors on the E_i values include possible systematic contributions outlined in Table 4.3. The parameters from Reference (81) are shown for comparison with the Method 3 results.

	E_i (MHz)	δ_0	δ_2,a	δ_4,b
Method 1	1010 024 719(8)	0.016 473(14)	-0.0783(7)	0.028(7)
Method 2	1010 024 719(8)	0.016 473(14)	-0.0784(7)	0.032(7)
Method 3	1010 024 717(8)	0.016 40(8)	0.00(9)	-
Han *et al* (81)	-	0.016 5437(7)	-0.086(7)	-

set from Johansson *et al* (90). Weighted fitting was important to take account of the larger 300 MHz uncertainties on these older measurements. Throughout the analysis, the Rydberg constant for ^{85}Rb was taken as R_{Rb}=10 973 660.672 249×c from Reference (87).

Method 1

In Method 1, the energy levels E_n were fitted using a least squares fitting procedure to the formula

$$E_n = E_i - \frac{R_{\mathrm{Rb}}}{[n - \delta_0 - \delta_2 t_n - \delta_4 t_n^2 - ...]^2} \ , \tag{4.7}$$

from Equation 2.1. A MATLAB code was written to iteratively balance both sides of Equation 4.7 to find the optimum parameters for E_i, δ_0, δ_2, δ_4,... The results from this fit are displayed in Table 4.4 and the residuals are shown in Figure 4.39.

Method 2

To remove the recursive nature of Equation 2.3, it is common to make the approximation

$$t_n \approx \frac{1}{(n - \delta_0)^2} \ , \tag{4.8}$$

which when substituted into Equation 4.7 gives a Rydberg-Ritz expression that can be evaluated with greater simplicity (128):

$$E_n = E_i - \frac{R_{\mathrm{Rb}}}{[n - \delta_0 - \frac{a}{(n-\delta_0)^2} - \frac{b}{(n-\delta_0)^4} - ...]^2} \ . \tag{4.9}$$

The Method 2 fit involved a direct least squares fit of Equation 4.9 to the energy levels E_n. The results from this fit are displayed in Table 4.4 where the a and b parameters are

placed underneath the equivalent δ_2 and δ_4 parameters from the Method 1 fit. It can be seen that the values of E_i and the series parameters extracted from the first two fitting methods agree to well within the uncertainties. This shows that the approximation has no effect at this level of accuracy and for this range of n. The value of E_i from this work also lies within 2σ of the previous value from our lab (87).

An analysis of the residuals shown in Figure 4.39, from the Method 1 fit, shows that the points are scattered around a mean of zero with a standard deviation of 4.4 MHz. The states were measured across several days and therefore this spread is expected to come mainly from the long term accuracy of the wavemeter.

The Rydberg-Ritz formula in Equation 4.9 has the significant advantage that it allows any energy level E_n to be calculated with knowledge only of the principal quantum number n. In this manner Equation 4.9 can be used with the relevant parameters in Table 4.4 to predict the absolute energies of other Rb $n\mathrm{F}_{7/2}$ states outside the range of this experiment.

Method 3

As a consistency check of the data, the Ritz series parameters extracted from the absolute measurements were compared with those from the most recent relative interval measurements from microwave spectroscopy (81). For this fit an abridged version of Equation 4.9 was used

$$E_n = E_i - \frac{R_{\mathrm{Rb}}}{[n - \delta_0 - \frac{a}{(n-\delta_0)^2}]^2} \ . \tag{4.10}$$

This is the equivalent function which was used for fitting in Reference (81), which is an accurate approximation for $n \geq 20$. For this reason this fit was restricted to the $n \geq 33$ levels. The parameters from this fitting method are shown in Table 4.4 alongside the values from Reference (81). The a parameter is placed underneath the equivalent δ_2 parameter from the Method 1 fit.

It can be seen that the δ_0 and a parameters from this fit agree at the 2σ level with those from the previous work (81). The larger errors on the series parameters, as compared to the Method 1 and 2 fits, arise because of the absence of lower n states. This makes extracting higher order series parameters less accurate: In Equation 4.9, for lower n states the parameters δ_0 and a make a bigger contribution than for higher n states, where E_n becomes dominated by E_i. As displayed in Table 4.4, the addition of the lower n states

from Reference (90) greatly aided in the reliable extraction of the higher order parameters in the Method 1 and 2 fitting routines.

4.6.6 Discussion

In Figure 4.39 the spread of the residuals for the five previous measurements (90) is 185 MHz, compared to the spread of these new measurements of 4.4 MHz; a 42× improvement in absolute accuracy. Access to lower n states, or higher accuracy measurements for this range of states, would be needed to give a lower uncertainty on the defect parameters. Table 4.3 shows that the limiting accuracy of these results comes from the wavemeter

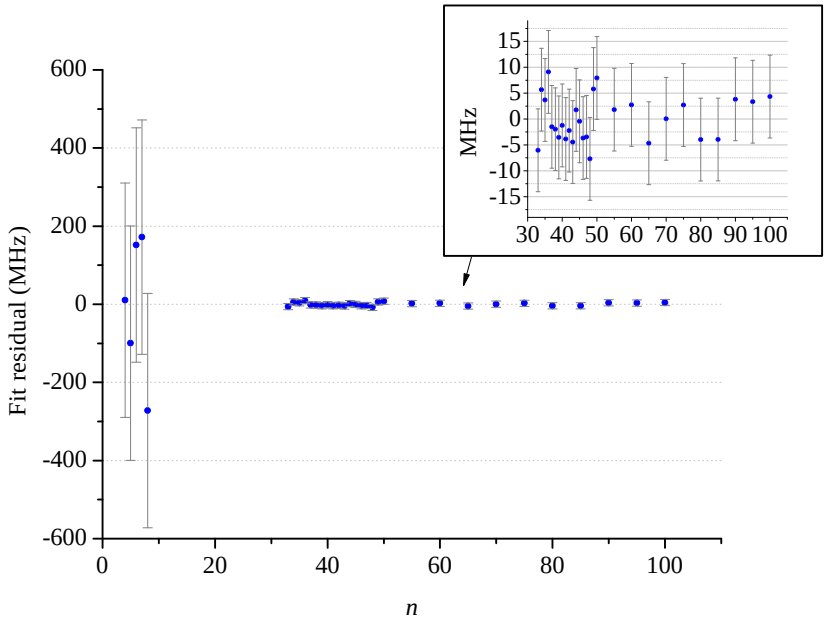

Figure 4.39: The residuals from the Method 1 fitting routine. The error bars on the older n=4-8 measurements are 300 MHz (90) and the error bars on these new n=33-100 measurements are 8.0 MHz. The inset figure shows a close up of the residuals from the new measurements, which have a spread of 4.4 MHz.

transfer of calibration. The ∼2 MHz shorter term drifts of the wavemeter also mean that sources of systematic shift cannot be studied reliably, as trends are often not detectable. Any significant improvement will require removing the wavemeter from the metrology process and instead using the comb directly to count the laser frequency. In this case, the limiting accuracy of frequency measurement will be the Rb 10 MHz reference used

to reference the comb electronics, with a fractional frequency accuracy of 5×10^{-12}. At this level the second step lock repeatability may become the limiting factor, as well as the knowledge of the first step transition frequency.

4.7 Conclusion

This chapter has described the optimisation and characterisation of an apparatus for detecting Rydberg states of ^{85}Rb atoms contained in a heated vapour cell. The apparatus has been used to measure absolute frequencies of $n\mathrm{F}_{7/2}$ Rydberg states to an accuracy of 8.0 MHz. This is a factor 42× improvement over previous measurements of the nF series in Rb (90), and gives measurements for a range of $n\mathrm{F}_{7/2}$ states between n = 33-100 for the first time. The Rydberg-Ritz series parameters that have been extracted from this work allow the absolute energies of $n\mathrm{F}_{7/2}$ states with higher or lower principal quantum number n to be predicted with a comparable accuracy. As will be shown in Chapter 6, this is important for future experiments with improved accuracy. These new measurements have also shown consistency with the results from recent microwave spectroscopy experiments (80; 81). This work has demonstrated that methods of Rydberg spectroscopy, involving purely optical detection and a vapour cell sample, can be used very effectively to carry out precision measurements in a simple way, with extraordinary robustness to DC-Stark shifts from external fields. Not only is the setup simple to construct and maintain, it is easier to use than beam experiments, and Rydberg signals can be monitored in real-time on an oscilloscope.

Chapter 5

Three-step laser stabilisation for excitation of Rb Rydberg states

Actively stabilising the third step laser to a weak Rydberg level transition using a reference cell has been a long term goal for the micromaser experiment in our lab. The first and second step laser locks have been constructed and optimised by Gary Wilkes, Bruno Sanguinetti and Hawri Majeed (121; 122), although a reliable third step lock has not been achievable. Using the new detection scheme introduced in Chapter 4, it has now become possible for such a stabilisation to be made to the upper level of the micromaser transition, the $63P_{3/2}$ state. This chapter will display the modifications that were required to get from the scheme demonstrated in Chapter 4 to a reliable third step lock. The frequency comb gives a unique opportunity to study the stability of each of the laser steps, when locked to their respective cells, and how the instability of the lower steps translates to the Rydberg signal. The results in this chapter were collected by myself. The first and second step stabilisation schemes were originally constructed by previous lab members. The work in this chapter has been published in Applied Physics B (97).

5.1 Introduction

5.1.1 Laser stabilisation to Rydberg levels

Long term laser stabilisation to atomic transitions is important for making precision measurements in spectroscopy (61; 92). For the case of optical transitions to Rydberg levels, laser stabilisation is required for many quantum optics experiments that require Rydberg atoms. For example, modern Rydberg atom cavity QED proposals such as the micro-

maser experiment in our lab (58; 59). In both cases long term frequency stability is of importance. For the micromaser experiment, it is important that the Rydberg excitation rate stays constant, which relies on the third step laser being well stabilised at the $5D_{5/2} \rightarrow 63P_{3/2}$ transition frequency. This becomes especially important when optimising detector designs, where a constant excitation rate is crucial for fair comparison (75). Unfortunately, the weak transitions to Rydberg levels mean that spectroscopic signals are difficult to obtain, so stabilising a laser at these frequencies is not trivial.

In our lab the first and second step locks can be stabilised using the polarisation spectroscopy and QA techniques, introduced in Sections 4.2.1 and 4.3.9. However, obtaining an error signal for stabilisation of the third step laser to a Rydberg level has been difficult. Previously a software lock has been achieved by Martin Jones with a field ionisation setup (75). In this scheme, a computer program sends feedback to the third step laser grating, which tunes the laser in steps to maximise the number of Rydberg counts; this keeps the laser on the top of the Rydberg line profile. However, such a scheme has limited bandwidth and does not supply a tight laser lock.

In Chapter 4, and in the work of References (54; 56), it has been well demonstrated that the optical detection of Rydberg states in compact thermal vapour cell arrangements can not only offer greatly reduced sensitivity to stray electric fields, but can also supply analogue spectroscopic Rydberg signals from an ordinary photodiode. In Section 4.6.1, the dispersion like signals which were extracted when scanning the third step laser over a Rydberg level are ideal for laser stabilisation applications. The signals occur on a zero background, with a steep zero crossing, and can have an excellent SNR.

5.1.2 Previous work

Recently lasers have been stabilised to optically detected Rydberg signals in Rb vapour cells, using some of the different excitation schemes introduced in Section 2.1.5. In Reference (55) FM spectroscopy with the one-step 297 nm scheme is used; a 400 Hz modulation frequency is used to obtain an error signal. In contrast, Reference (129) uses the two-step 780 nm-480 nm ladder EIT scheme and a novel high speed 10 MHz FM technique is developed to obtain an error signal. Other solutions for stabilising lasers for Rydberg excitation involve locking the Rydberg laser to a tunable optical transfer cavity, which itself is stabilised to a Rb D_2 reference line at a different wavelength (130).

5.2 Experimental modifications

5.2.1 Higher modulation frequencies

The slow scans carried out in Section 4.6.1 involved a reasonably slow third step FM of 6 kHz. A long 1 s time constant on the LIA was required to obtain a good SNR. Although attempts were made, it was not possible to use these signals directly for laser stabilisation due to this slow response time. By reducing the time constant significantly, the SNR became too low to observe the error signal for the majority of Rydberg states. To be able to use the Rydberg derivative signals for laser stabilisation ideally requires a shorter time constant on the LIA, to achieve a larger servo bandwidth on the feedback response. However, to maintain a good SNR requires lower levels of noise on the raw signal at the chosen modulation frequency. This can be achieved with a *higher* modulation frequency. Techniques for achieving this were studied with the existing optical setup. The injection current modulation limit of the third step laser driver is 6 kHz and therefore the higher speed FET input on the laser head itself was chosen instead.

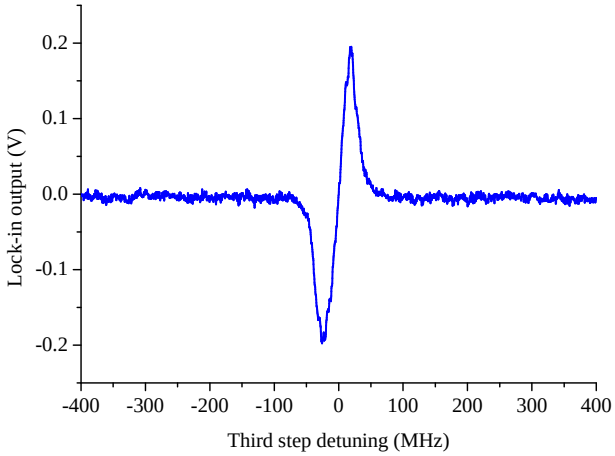

Figure 5.1: Error signal for stabilising the third step laser to the $5D_{5/2}, F = 5 \rightarrow 50F_{7/2}$ transition. The scan was carried out in 15 ms with a LIA time constant of 100 μs. The frequency axis has been calibrated with a Fabry Pérot etalon.

Modulation frequencies of ∼100 kHz were used (the upper limit of the LIA). Although the homemade photodiodes are specified to have a 12 kHz bandwidth, in this case the increased SNR achievable when working at 100 kHz outweighed the slightly lower response

(notice how the frequency response drops off slower than $1/f$ in Figure 3.12). Figures 5.1 and 5.2 show real-time piezo scans of the third step laser over the $50F_{7/2}$ and $63P_{3/2}$ levels. The traces were taken from an oscilloscope, using this improved detection scheme; all other experimental parameters were set as of Section 4.6. The modulation amplitude was 15 MHz and modulation frequency was 90 kHz. It is clear that error signals with a good SNR are achievable, which are ideally suited for laser stabilisation, with an accessible servo bandwidth of 10 kHz.

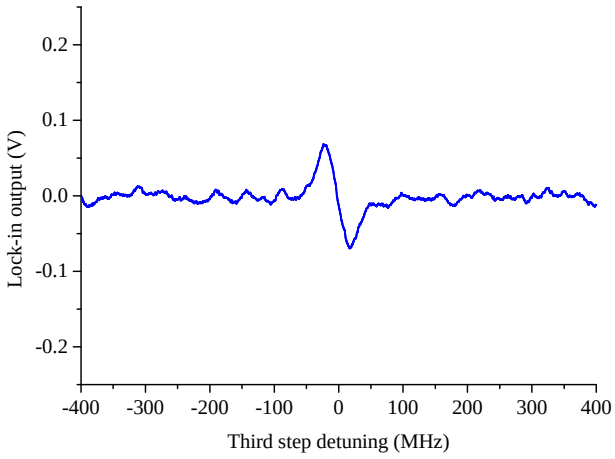

Figure 5.2: Error signal for stabilising the third step laser to the $5D_{5/2}, F = 5 \rightarrow 63P_{3/2}$ transition. The scan was carried out in 15ms with a LIA time constant of 100 μs. The frequency axis has been calibrated with a Fabry Pérot etalon.

5.2.2 A modified optical setup

At this stage, several improvements were made to the optical setup, see Figure 5.3. The Rydberg detection in the cell requires a large amount of third step laser power. For example in Section 4.4.1, *all* of the available laser power was required to detect the $63P_{3/2}$ state with a reasonable SNR. If this scheme were to be used for stabilising the third step laser for the micromaser experiment, some method would be required for accessing this third step laser power after traversing the cell. To achieve this a set of dielectric mirrors with polished back faces were installed. These mirrors reflect 780 nm light but transmit 1260 nm light, meaning that the third step light can be both introduced and removed from the setup with very little loss. The very weak coupling of the third step transition

also ensures that the laser suffers very little attenuation in the cell. A further advantage is that combining the first and third step beams using a mirror rather than a glass wedge leads to a higher polarisation purity for the first and third step lasers. Therefore this new setup achieves a higher separation efficiency for the first step laser to the photodiode.

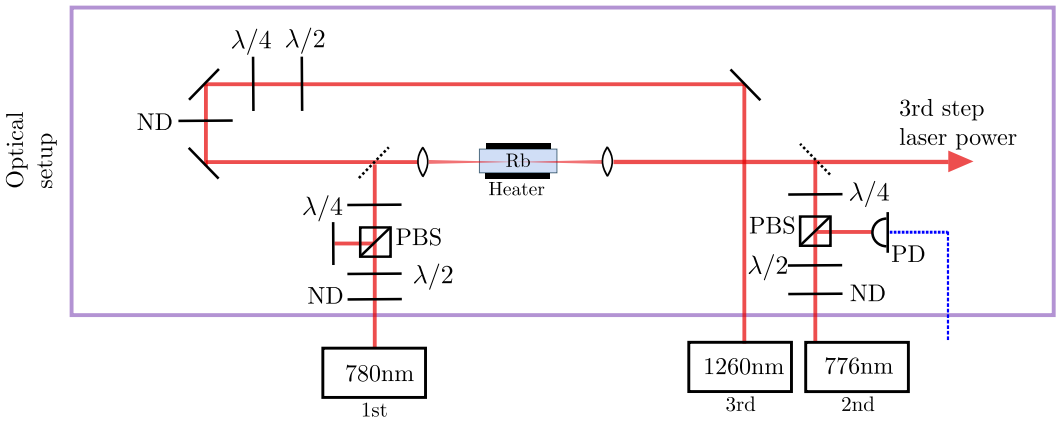

Figure 5.3: The improved optical layout. PBS: Polarising beam splitter, ND: Variable neutral-density filter, PD: Photodiode. The dashed black lines represent mirrors that reflect at 776/780 nm but transmit at 1260 nm.

Another change that was made involved moving to dielectric PBS cubes for separating the first and second step lasers. Unlike the Glan-laser polarisers in the previous setup, these cubes are transparent to 1260 nm light. In this new scheme, the properties of the dielectric mirrors and PBS cubes, along with a repositioning of the photodiode, means that 1260 nm light is no longer picked up by the photodiode and detection sensitivity is improved. Finally, to aid alignment the $\lambda/4$ Fresenel rhomb was repositioned behind the two third step steering mirrors. The overlap of the third step laser inside the cell can now be optimised without affecting the delicate alignment through the rhomb. The set of improvements results in an available third step power inside the cell of 4 mW compared to 3.5 mW in the previous setup.

5.3 A comb calculator

To study the stability of the three-step system, it was intriguing to lock all three lasers to their respective cells and *simultaneously* monitor their frequencies. Using the wavemeter for this purpose could swamp the true stability of the lasers; a more desirable method

is to count the beat notes of all three lasers against the comb simultaneously. This not only gives data on the performance of the individual locks, but also displays how the lock stabilities are linked on the various steps.

In order to achieve this goal, a comb repetition rate needs to be chosen such that each laser has a beat note of 20±2 MHz or 30±5 MHz with a nearby comb line; these correspond to the centre frequencies of the BFD100 units of the comb (see Section 3.1.3). To find a sensible repetition rate for this requires solving three simultaneous comb equations

$$f_1 = n_1 f_{rep} \pm 2f_o \pm f_{beat1}, \tag{5.1}$$

$$f_2 = n_2 f_{rep} \pm 2f_o \pm f_{beat2}, \tag{5.2}$$

$$f_3 = n_3 f_{rep} \pm f_o \pm f_{beat3}, \tag{5.3}$$

where $f_{1,2,3}$ are the first, second and third step laser frequencies, f_o is the comb offset frequency, f_{rep} is the comb repetition rate and $f_{beat1,2,3}$ are the first, second and third step beat notes with comb lines $n_{1,2,3}$. Assuming that f_o=20 MHz, that $f_{beat1,2,3}$ are all chosen as either 20 or 30 MHz and that all signs are positive, there are four unknowns: $n_{1,2,3}$ and f_{rep}; this means the equations do not have a unique solution. These unknowns also have constraints: $n_{1,2,3}$ must be integers and all the parameters must comply with the comb's repetition rate range of 248.391 MHz$< f_{rep} <$ 251.102 MHz (44). To find a sensible set of parameters, a MATLAB code was written to numerically solve the set of Equations 5.1, 5.2 and 5.3. The program scans the repetition rate in 1 Hz steps until a position is found where $f_{beat1,2,3}$ all lie within ±1 MHz of either 20 or 30 MHz (the centre frequencies of the BFD100 comb units). The program allows a relevant repetition rate to be calculated quickly for any arbitrary Rydberg level.

As an example, for the case of the $63P_{3/2}$ level, a set of relevant parameters is:

Inputs:

$f_1 = 384229242.8$ MHz, $f_2 = 386341041.9$ MHz, $f_3 = 238550142$ MHz,

$f_o = +20$ MHz.

Outputs:

$f_{rep} = 250.327038$ MHz, $n_1 = 1534909$, $n_2 = 1543345$, $n_3 = 952954$,

$f_{beat1} = -20.77$ MHz, $f_{beat2} = +19.47$ MHz, $f_{beat3} = -30$ MHz.

The values of $f_{1,2}$ are computed from References (61; 123) and f_3 comes from previous Rydberg measurements (121). Notice that in order to carry out this search, one needs prior knowledge of the absolute frequency f_3 for the Rydberg level being studied, to within a few megahertz. Before the measurements made in Chapter 4, such knowledge was not available for the nF series of states in Rb.

5.4 Laser stabilisation and measurement

5.4.1 Feedback loops

To study the three-step stabilisation scheme, all three laser steps were stabilised to individual Rb reference cells. The first step laser was stabilised using the polarisation spectroscopy scheme introduced in Section 4.2; this is modulation-free. Active feedback for this laser lock was supplied via the laser cavity piezo and the diode injection current. The second step laser was stabilised using the separate co-propagating setup described in Section 4.3.9; FM was added to the laser via the diode injection current. Feedback for this lock was also supplied via the laser cavity piezo and the diode injection current. The third step was stabilised to a Rydberg signal such as those shown in Figure 5.1 and 5.2. Active feedback for this lock was supplied via the laser cavity piezo only.

For all three stabilisation schemes, the error signals were sent through PID controllers and then to the laser drivers for feedback, via universal Laselock units (see Figure 5.4). The gradients of the Rydberg error signals were typically 4-10 mV/MHz at zero crossing. In each case the LIA gain was adjusted to achieve stable loop operation. Ideally, the FM on the second and third step lasers would be applied externally, for example with Acousto-optic modulators (AOM). This would leave the laser linewidths intact for experiments, where large modulations may be troublesome. A simpler, and perhaps more effective option, would be to modulate the atoms themselves using solenoids wrapped around the vapour cells. In this way modulation-free Zeeman locks could be achieved (131).

5.4.2 Frequency counting with the comb

A proportion of the light from each of the lasers was sent to individual comb BDUs, where the laser light was mixed with light from the frequency comb, see Figure 5.4. The 780 nm comb light was split using a 50:50 fibre beam splitter to supply comb light to two 780 nm BDUs, for the first and second step measurement. The first and second step beat notes

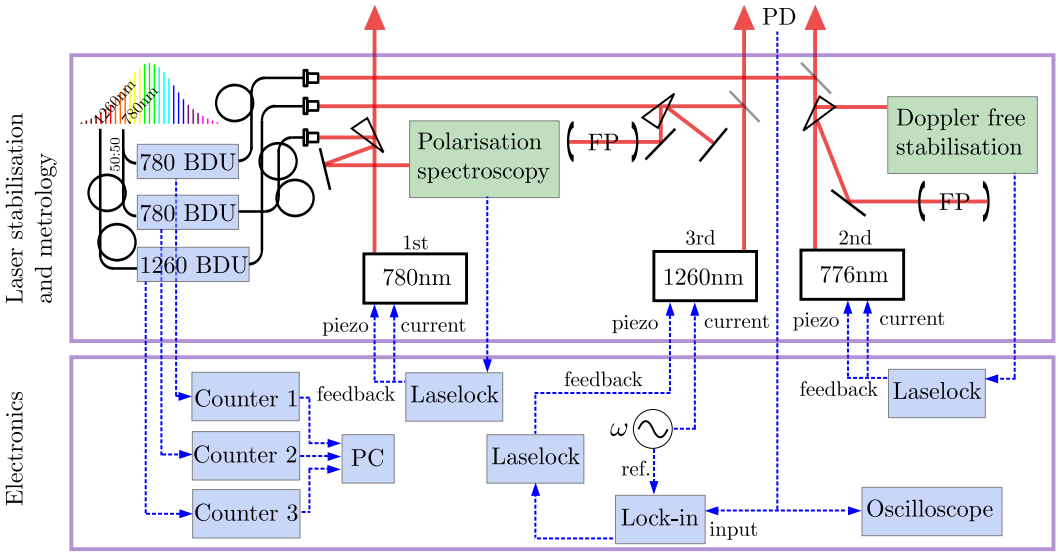

Figure 5.4: A schematic of the experimental arrangement for three-step stabilisation. The 780 nm and 776 nm lasers are locked to separate Rb reference cells with active feedback to the laser piezo and injection current. The 1260 nm laser is frequency modulated via the injection current and lock-in detection of the first step absorption is carried out to derive an error signal for frequency stabilisation. The 1260 nm laser is locked using active feedback to the laser piezo. Single-mode optical fibres transport laser light from all three lasers to the three frequency comb BDUs.

were at 20 MHz and the third step beat note was at 30 MHz. The band-pass filter in the BFD100 comb unit was bypassed in the case of the second and third step lasers because the dithered laser linewidths were not fully contained within the band-pass range; this could lead to biased counting. These two beat notes were instead sent only through the 100 MHz low-pass filter stages of the BFD100 units. In the case of the second step, an additional RF amplifier was used to amplify the beat note for counting. All three frequency counter channels were synchronized to take readings simultaneously every second.

5.5 Performance

With this setup it was possible to stabilise to the Rydberg states $36P_{3/2}$, $70P_{3/2}$, $33F_{7/2}$ and $90F_{7/2}$. In principle all states between these will also be accessible. However, for higher n, the lower SNR of the signals prevented a reliable third step lock. The only limiting factor was the available third step laser power. The stability of the system was

analysed using the beat note counter readings. Figure 5.5 shows data recorded over a period of 5000 s for all three lasers when locked to excite the $50F_{7/2}$ Rydberg level.

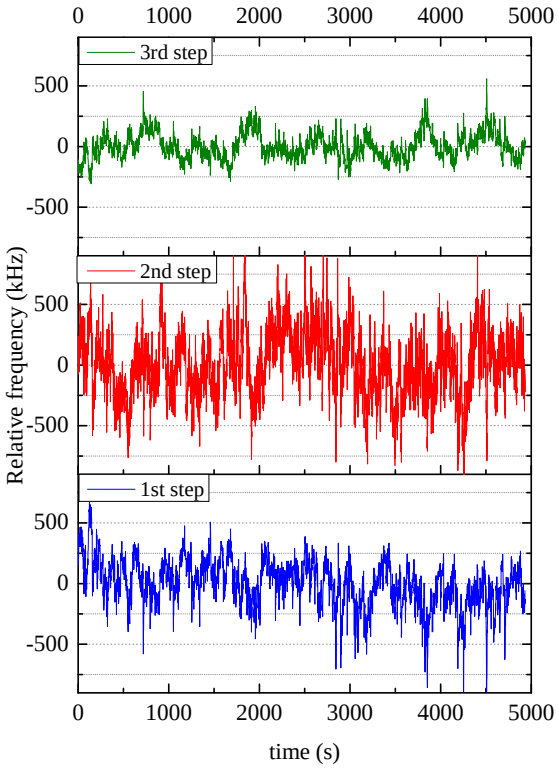

Figure 5.5: The three counter readings recorded for a period of 5000 s with all lasers locked to excite $50F_{7/2}$ Rydberg atoms. Counter readings were recorded simultaneously, once every second.

Figures 5.6 and 5.7 show the computed Allan deviations (118) for all three laser steps, when the third step laser was locked on to the $50F_{7/2}$ and $63P_{3/2}$ Rydberg levels respectively. [1] The data sets were 5000 s and 4000 s respectively. The stabilities are summarised in Table 5.1.

It can be seen in Figure 5.6 that the stability of the third step laser is better than 80 kHz for all time scales up to 10^3 s, and is better than 30 kHz over 1 s. In Figure 5.7 the stability of the third step laser remains better than 150 kHz for all time scales up to 1000

[1] These levels were not chosen for any particular reason, other than the $63P_{3/2}$ level being the upper level of the micromaser transition (58; 59; 60).

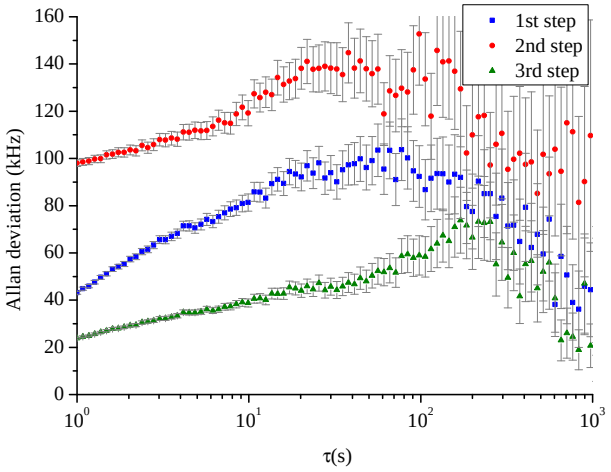

Figure 5.6: Computed Allan deviations (118) of the three-step laser locks, measured simultaneously using the comb, with the third step locked on to the $50F_{7/2}$ level.

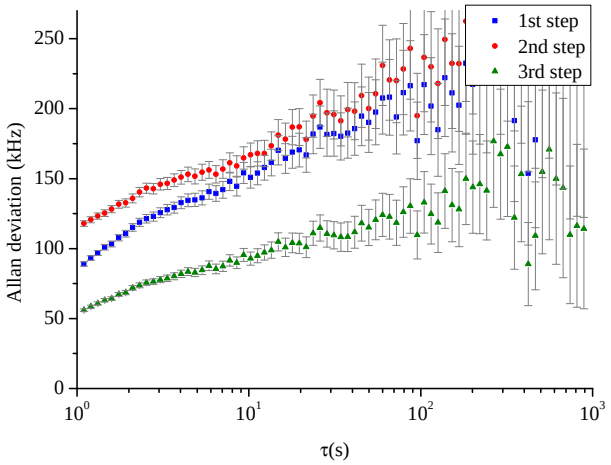

Figure 5.7: Computed Allan deviations (118) of the three-step laser locks, measured simultaneously using the comb, with the third step locked on to the $63P_{3/2}$ level.

s, and is better than 60k Hz over 1 s. The two sets of data were taken on different days and with slightly different first step lock settings which explains the differences in the first and second step Allan deviation plots in Figures 5.6 and 5.7. These results demonstrate that the Rydberg atoms are very well isolated from the environment, especially considering the

vapour cell used for third step locking was unshielded from magnetic and electric fields.

Table 5.1: The third step laser stability for different averaging times and different states.

State	1 s	10 s	100 s	1000 s
$50F_{7/2}$	24 kHz	39 kHz	59 kHz	16 kHz
$63P_{3/2}$	56 kHz	93 kHz	122 kHz	120 kHz

5.6 Discussion

In this setup the stability of the second step was generally lower than the first step, across all time scales. This can be associated with different feedback responses for the two locks. However, Figures 5.6 and 5.7 also show that the stability of the third step laser is not compromised by this poorer second step lock: The second laser appears to play only a small part in the third laser's stability. Most importantly, the stability of the third step laser is always considerably lower than the first step laser. This is a result of the mismatch of wavelengths and therefore Doppler shifts between the steps. In Section 6.6, a more powerful technique will be implemented for studying these properties.

As one would expect, the frequency fluctuations were correlated between each of the laser steps. For example, Figure 5.8 compares the counter readings for the first and third beat notes for the $50F_{7/2}$ lock data. The residuals of the fit show the technical noise of the locks, whilst the fit itself gives correlation information. The gradient of -0.42 appears to be an advantage of this particular excitation scheme. One would expect a gradient with magnitude greater than one for the two-step EIT scheme where $\lambda_2 < \lambda_1$ (129). From measuring these correlations, one can understand how the excitation scheme responds to laser detuning, which is important for making precision spectroscopy measurements.

The results from this study suggest that the absolute frequencies of Rydberg levels could be measured to an accuracy of <100 kHz using this locking technique. This far surpasses the accuracy of the work in Chapter 4, and would give an accuracy comparable to relative microwave spectroscopy measurements (80; 81). Unfortunately, in this study it was not possible to to be confident of the *absolute* accuracy of the second and third step counter readings due to observed counting errors. By removing the band-pass filters, less noise is removed from these two modulated beat note signals and offsets of up to 2 MHz were observed between the counter readings and spectrum analyzer traces. Even so,

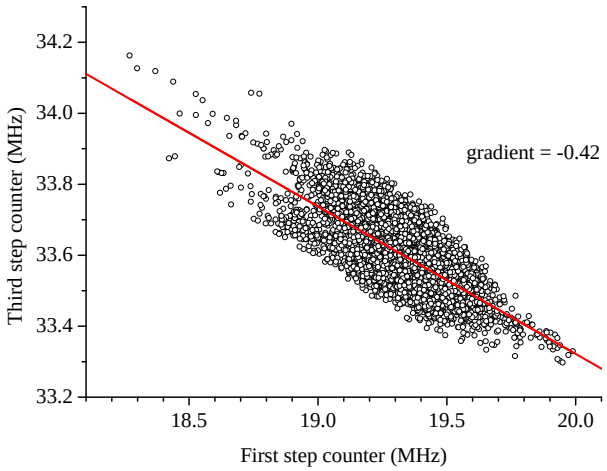

Figure 5.8: Correlations between the first and third step beat note frequencies for the $50F_{7/2}$ lock data. f_{beat1} and f_{beat3} had negative and positive signs respectively for this data. The red line is a linear line of best fit.

by looking at correlation results such as those in Figure 5.8, it was possible to check that the counters were accurately measuring *changes* in frequency, and therefore stability. The relationship between beat SNRs and counting errors in comb beat detection measurements is investigated in Reference (132).

5.7 Conclusion

The work in this chapter has completed the three-step locking procedure for the micromaser experiment in our lab, providing a reliable lock to the $63P_{3/2}$ state. It has also demonstrated some of the behaviour of the three-step scheme, especially the fact that frequency fluctuations of the first step laser are not directly transferred to the third step signal. The key result from this chapter is that the Rydberg levels inside the cell can be stable to less than ∼100 kHz over thousands of seconds. This confirms that the Rydberg spectroscopy measurements made in Chapter 4 could be greatly improved upon with the correct improvements in laser frequency metrology, so that the wavemeter does not swamp the true stability of the levels.

Chapter 6

Three-step comb-stabilised Rb Rydberg spectroscopy

In the previous chapter it was found that the stability of the Rydberg signals inside the cell could be almost two orders of magnitude greater than the stability of the wavemeter. This chapter will describe the construction and optimisation of a new three-step fully comb-stabilised technique for making Rydberg measurements with the maximum potential of accuracy, exploiting the stability and accuracy of the comb rather than the wavemeter. This has involved constructing a scannable comb offset-lock. A new set of absolute frequency measurements of the $n\mathrm{P}_{3/2}$ and $n\mathrm{F}_{7/2}$ Rydberg series are made. With this new scheme, accuracies of $\sim$100 kHz are achievable as well as excellent agreement with microwave measurements (80; 81). These are the most accurate optical measurements of Rydberg levels previously made. Because of this, a new value for the ionisation energy can be extracted with an order of magnitude improvement in accuracy over previous values (82; 83). In the final sections of this chapter, the excitation scheme is investigated in more detail using this new technique. All the work presented in this chapter was carried out by myself.

6.1 Improved Rydberg spectroscopy

In Section 5.3, a method was introduced for computing the comb repetition rate required to count multiple laser steps simultaneously using a single comb. This method can equally be used to simultaneously *stabilise* multiple lasers to a comb. This opens up the opportunity to not only stabilise the first step laser to the comb as in Chapter 4, but also the second step laser. The need for vapour cell locks on these two steps (with their associated lock errors) would therefore be eliminated as both of these transition frequencies are well known from the literature (61; 123). Comb stabilising the second step laser also removes the requirement for FM, which added noise and linewidth to the Rydberg signals previously.

6.1.1 Locking or scanning?

For detecting and measuring the positions of the Rydberg levels themselves, there are two obvious techniques:

- Carry out a slow frequency scan of the third step laser across the Rydberg signal, as carried out in Section 4.6, but using the comb as a counter rather than the wavemeter
- Lock the third step laser to the Rydberg transition of interest and count its frequency, as investigated in Chapter 5

The locking method is in many ways more straight forward and preferable, especially from a statistical and data analysis point of view. It only requires averaging a single frequency, which can be carried out over a chosen averaging time. However, it also has several disadvantages:

- Counting errors of the modulated third step, as mentioned in Section 5.6
- By only locking to the signal, asymmetries in the peak cannot be easily identified. With a laser lock, the lock frequency will be pulled by the asymmetry causing a systematic error, even though this may not be obvious. Firstly one needs to carry out a true linear frequency scan over the locking signal to check for asymmetries, only then can the lock point be trusted
- A reliable lock requires a high SNR on the error signal. This limits the Rydberg states which can be targeted. A frequency scan however, can target states with much lower SNR by using a lower time constant and a slower sweep

- When locking on to a transition centre to make a precision measurement, there is a class of new systematic errors that must be considered. Some of these are: Set point uncertainty and stability, phase delays in the feedback loop and residual amplitude modulation (RAM) from the FM and its effect on the error signal shape (133)

6.1.2 Locking solutions

Some of the above limitations could be solved by using an external modulation technique, which would leave an unmodulated laser linewidth. Alternatively, by modifying the BDU setups one could attempt to achieve a higher SNR for the third step beat note, which would remove counting errors (132). However, ultimately a linear frequency scan will always be required to check for asymmetries. This is especially important in this experiment because of the possible pathways to the Rydberg state through the different nearby $5D_{5/2}$ hyperfine states, and their effect on the lineshape.

6.1.3 Linear frequency scanning

Based on the discussion above, a decision was made to use a linear scanning technique for the third step laser. Although in Section 4.6 the third step laser scans were linear, the laser was not actively stabilised during this sweep, and therefore each point of the scan had a potential 1 MHz uncertainty associated with the laser's 1 s stability. With this new technique, the aim was to achieve $\ll$1 MHz levels of accuracy, and therefore the laser needed to be actively stabilised. It was therefore chosen to also stabilise this laser to the comb, and to develop a scannable comb-lock.

6.2 Three-step comb-locking and scanning

6.2.1 Three-step comb-locking

Using three comb-stabilised laser locks for the three steps means that all the cell locks previously used are eliminated; all lasers will benefit not only from the stability of the comb, but also from the absolute accuracy. In Chapter 4, measurements had to be made of the stability of the second step reference cell lock, the stability of the free running third step and also potential lock errors on the second step frequency. In contrast, with the frequency comb all the required reference frequencies are dialled in and synthesised on-demand, with relative accuracies approaching 10^{-12} (115).

In order to achieve three comb-locks, the second step laser was replaced by a Sacher Lynx ECDL. The previously used Toptica DL100 ECDL did not have sufficient feedback bandwidth for a reliable comb-lock. All three steps were comb-locked using feedback to the laser injection current. The first and third step lasers were stabilised using feedback via the FET on the laser head and the second step laser was stabilised using the FM input on the laser driver.

6.2.2 A comb-stabilised scannable offset-lock

In previous precision spectroscopy experiments, comb-stabilised CW laser scans have been carried out by scanning the comb repetition rate (64). This allows very large scan ranges, limited by the tuning range of the CW laser. However, this was not an option for scanning the third step in this experiment, as the first and second step frequencies must remain fixed. One option is to use an AOM to scan the frequency of the third step laser (whilst comb-locked), however as will be discussed in Section 9.3, this method can have limitations. For this reason a more elegant solution was developed: A scannable offset-lock.

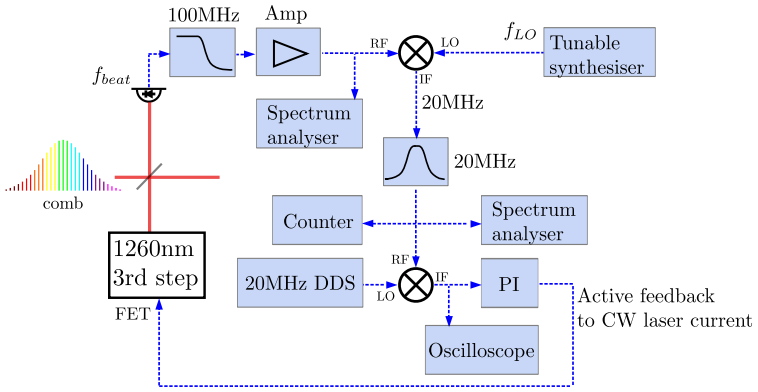

Figure 6.1: The comb-stabilised scannable offset-lock scheme allows the third step laser to be comb-locked and precisely tuned across 50 MHz using a synthesiser. Counting and locking the *difference* frequency between the beat note and a synthesiser means that this frequency remains fixed at 20 MHz at all times, ensuring accurate counting and stabilisation. RF: Radio frequency input, IF: Intermediate frequency input, LO: Local oscillator input, DDS: Direct digital synthesiser, PI: Proportional integral controller, FET: Field-effect-transistor input.

In Figure 3.5, the beat note between the laser and comb line f_{beat} is directly stabilised to a synthesiser. This synthesiser can be tuned to scan the laser frequency, however the

range is limited to 6 MHz due to the band-pass filter, which is centred at 20 MHz. Such a small scan range is not useful for the Rydberg spectroscopy. If this band-pass filter is removed, the range can be increased to 100 MHz (now limited by the low-pass filter). However, as mentioned in Section 5.6, by removing the filters counting errors are likely (132) and laser locking is not as robust, unless the beat note SNR can be made sufficiently large. In this work, with the available comb and CW laser powers, beat note SNRs were typically ∼30 dB and such problems were unavoidable without filtering.

One solution is to use a programmable band-pass filter, with a centre frequency which can move with the synthesiser as it is tuned. Unfortunately this was not available due to financial reasons. Instead, using the existing comb electronics, with the addition of a double balanced mixer (DBM) and an extra RF synthesiser, a scannable CW offset-lock scheme was constructed for the third step laser. The setup is shown in Figure 6.1.

In the modified scheme, the beat note f_{beat} is mixed with a local oscillator f_{LO} using the DBM. The *difference* frequency then passes through the band-pass filter and is locked to a fixed 20 MHz synthesiser, so that: $f_{LO} - f_{beat}$ =20 MHz [1]. Locking the difference frequency means that tuning the local oscillator also tunes the CW laser frequency, with the range of tuning limited only by the 100 MHz low-pass filter. Throughout this 100 MHz scan range, the 'down-converted' beat note frequency used for locking remains fixed at 20 MHz (the centre of the band-pass filter) and can always be counted accurately. With the local oscillator and synthesiser referenced to the same Rb 10 MHz reference, the CW laser frequency is always exactly equal to

$$f_{cw} = nf_{rep} \pm f_o \pm f_{LO} - 20 \text{ MHz}, \tag{6.1}$$

where the sign in front of f_{LO} replaces that in front of f_{beat} in Equation 3.2. This sign can be found using the same methods (44).

This technique is particularly useful when beat note SNRs of $\lesssim$ 30 dB are obtainable between a CW laser and a comb line and one wishes to count the beat note over a large bandwidth. In this work only frequency tuning of the third step is required, however in principle with additional BDUs and DBMs, this technique could be extended to stabilise a large number of lasers to a single comb whilst also having independent precision frequency tuning on each.

[1] Switching the sign of the PLL gives -20 MHz

6.2.3 Modified experimental setup

Figure 6.2 shows the modified metrology and electronics components for stabilising the three-step laser system and scanning the third step laser over Rydberg levels. The experimental rig is displayed in Figure 6.3.

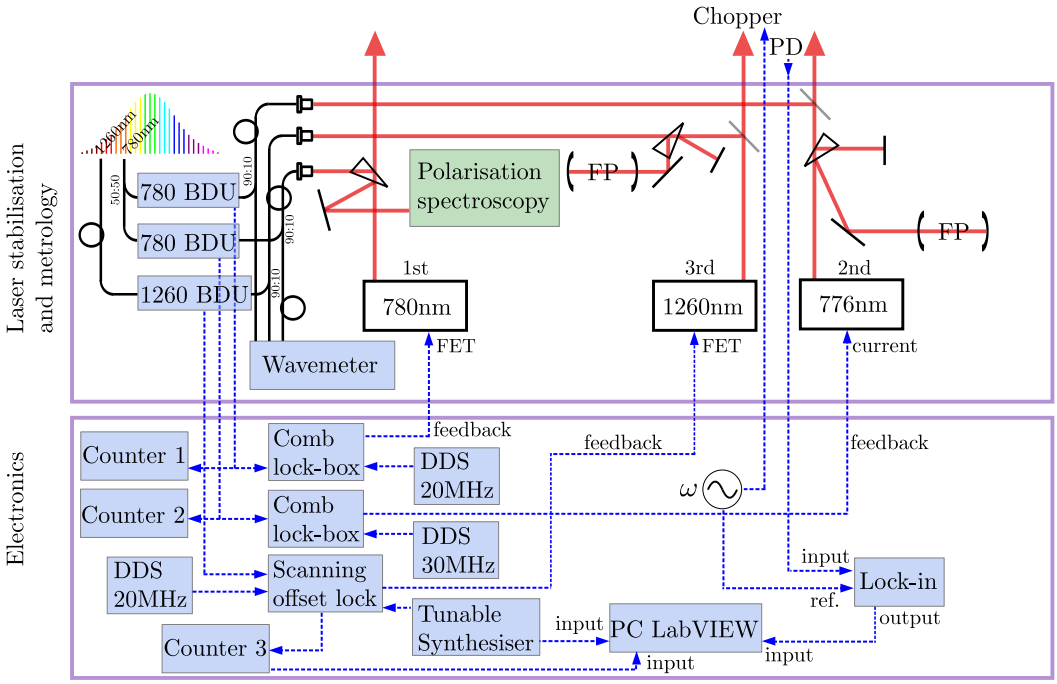

Figure 6.2: The new experimental setup, implementing the scannable offset-lock. The 780 nm and 776 nm lasers are offset-locked to different lines of the comb in the 780 nm region via feedback to the laser current. 780 nm comb light is split via a 50:50 fibre beam splitter for beat detection. The 1260 nm laser is offset-locked to a line in the 1260 nm branch of the comb and its offset frequency can be precisely tuned by 38 MHz. For all steps CW light is split 90:10 to wavemeter and BDU respectively. PD: Photodiode, BDU: Beat detection unit, FET: Field-effect-transistor input, FP: Fabry Pérot etalon, DDS: Direct digital synthesiser.

6.2.4 Performance

Beat notes

Figure 6.4 shows the beat notes for each of the three laser steps against independent comb lines. The lasers were actively locked when these traces were recorded, at the correct frequencies to excite the $63P_{3/2}$ Rydberg state. To find a repetition rate the program

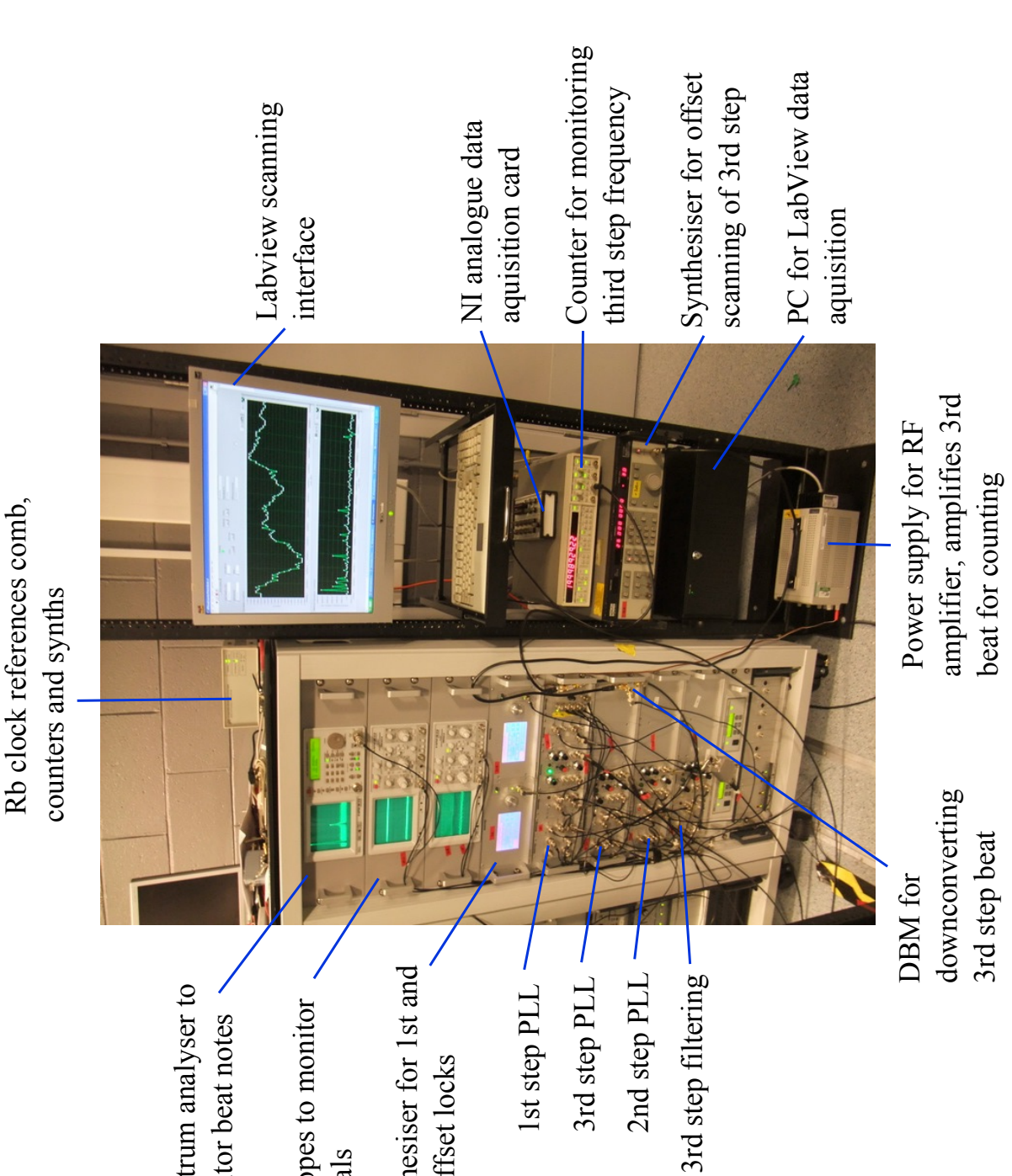

Figure 6.3: The experimental rig used for stabilising the three laser steps with the comb and performing third step laser scans over Rydberg levels. A wavemeter (not in shot) is used to check the lock positions of the three lasers and to deduce their nearest comb line numbers.

introduced in Section 5.3 was used, and the three beat notes $f_{beat1,2,3}$ were chosen to be between 19-21 MHZ, 29-31 MHz and 15-25 MHz respectively. In the case of the third step, the absolute frequency is only known to several megahertz from previous measurements (Section 4.4.1).

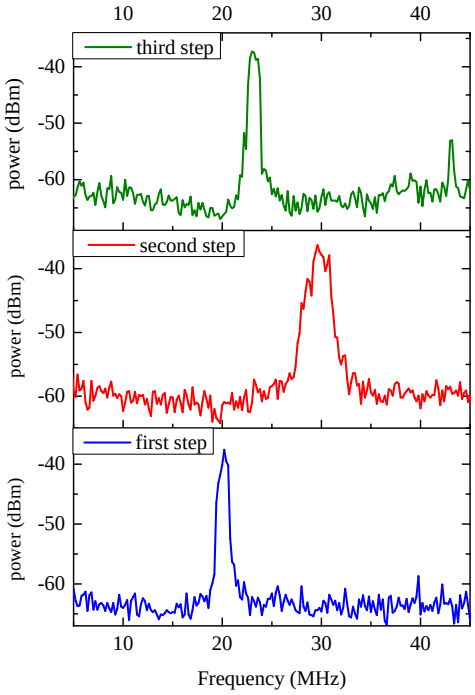

Figure 6.4: The three beat notes used for stabilisation to the comb. These traces were taken with an RBW of 300 kHz. Note that in the third step beat trace there is a sharp spectral feature at 43 MHz. This is the f_{LO} frequency component leaking through the DBM, exactly 20 MHz above the laser locked frequency of 23 MHz.

All the beat notes had a SNR between 20-30 dB. The first and third step lasers have linewidths of 1 MHz, whilst the second step laser is broader at 2 MHz. The second step Sacher Lynx ECDL is much more sensitive to picking up external noise and this is the origin of the broader linewidth. All the laser linewidths are slightly higher than expected from the specification sheets, which can be associated with electronic noise in the lab from an uninterrupted power supply unit. The noise added to the lasers, plus limited feedback bandwidth, meant that true phase-locking and linewidth narrowing was not possible; all locks were frequency locks using PLL electronics. With further work, these noise sources

could be eliminated. However for the purpose of this experiment, the free running laser linewidths were adequate.

Stability

The Allan deviations (118) of all three comb-locks are shown in Figure 6.5, computed from a 4000 s sample of data. This plot can be compared with the Allan deviation plots for the cell-based locks in Section 5.5; the laser stabilities are significantly better for all three lasers. The third step stability is excellent and stays below 30 Hz for all time scales below 1000 s. The first and second step stabilities are lower, both remaining below 500 Hz for all time scales below 1000 s. The differences in stability come mainly from the different beat note SNRs and laser properties. The third step Sacher Lynx laser is especially robust to external lab noise, which explains the excellent stability. This study demonstrates that the laser stabilities are not the limiting factor in the accuracy of the system. Instead it is the accuracy of the GPS discipled Rb reference which sets the accuracy limit at ∼1 kHz. This is a 6000× improvement over using the wavemeter.

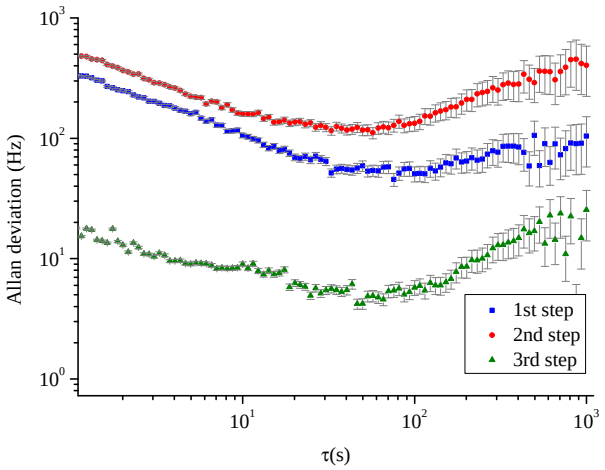

Figure 6.5: The Allan deviations (118) for the three comb-locked lasers, computed from a 4000 s data set.

Frequency scanning

It was found that the choice of synthesiser used as the local oscillator was of great importance. Some digital synthesisers did not supply a continuous-phase signal as the fre-

quency was stepped (in some cases the signal would drop out briefly between steps). This resulted in the momentary loss of the laser lock at certain points during the scan, making the scan unusable. Finally, it was found that a Systron Donner 1720B synthesiser could supply smooth frequency sweeps across the entire range required, with no phase slips or drop-outs. Frequency scans were carried out by interacting with this synthesiser using general-purpose-interface-bus (GPIB) commands through a LabVIEW interface.

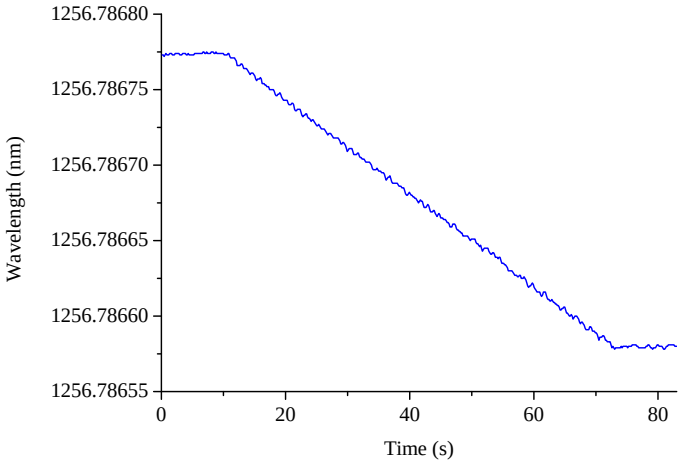

Figure 6.6: Readings from the High-Finesse WS7 wavemeter during a precision comb-stabilised scan of the third step laser across a range of 38 MHz.

Figure 6.6 shows wavelength readings of the third step laser from a WS7 High-Finnese wavemeter during a 60 s scan over a 38 MHz range. It shows the excellent linearity of the scan and also demonstrates that there is no loss of the laser lock. By counting the stabilised difference frequency $f_{LO} - f_{beat3}$ during a scan, it is seen that the frequency steps have no effect on the stability of the lock; the laser perfectly tracks f_{LO} across a scan range of 38 MHz. This corresponds to f_{beat3}=24-62 MHz. Beyond 62 MHz the roll-off of the low-pass filter begins to attenuate the beat note; the maximum available scan range whilst maintaining a lock with <1 kHz 1 s stability was 50 MHz, corresponding to f_{beat3}=24-74 MHz.

6.2.5 Advantages

The principle advantage of this new full comb-stabilised setup is that there is no longer a need for Rb reference cells for the laser stabilisation scheme of the micromaser experiment. Before working on this project, an entire table of optics and two racks of electronics were required for this purpose. With this new scheme, all that is required is the three fibre-coupled lasers and a wavemeter as a coarse reference. The three lasers and wavemeter could be placed on a single optics bench with the comb, and this compact system would allow full laser frequency control and stabilisation for the micromaser experiment.

The new scheme also solves the problem of atomic beam Doppler selection in the micromaser experiment, which has previously been an experimental challenge in our lab (121). By adding a finite angle θ, between the atomic beam unit vector $\hat{\mathbf{j}}$ and the first step laser wave vector $\mathbf{k}$, one can velocity-select atoms from the atomic beam by detuning the first step laser frequency from resonance. For a detuning of δ_{12} the selected velocity is

$$\mathbf{v} = \frac{2\pi\delta_{12}}{\mathrm{kcos}\theta}\,\hat{\mathbf{j}}. \tag{6.2}$$

Previously, AOMs have been proposed as a way of precisely detuning the first step laser. Also, in Reference (121), an offset-lock between two 780 nm lasers was attempted with one of these lasers locked to a reference cell. With this new scheme, arbitrarily sized detunings can be achieved by solving the set of comb Equations 5.1, 5.2 and 5.3 for the required laser positions then setting the comb repetition rate accordingly. Because the comb is an optical synthesiser, laser locking is achievable at any arbitrary frequency within its operating range. With an extra DBM and synthesiser the comb-stabilised scannable offset-lock could also be applied to the first step laser. This would then allow fine control of the velocity-selection across ±19 MHz by dialling the required detuning into the f_{LO} synthesiser.

6.3 Pilot Rydberg scans

Figure 6.7 shows a pilot scan over the $5D_{5/2}, F = 5 \rightarrow 60F_{7/2}$ transition using the new scheme discussed in Section 6.2. The comb equations were firstly solved to place the first and second step lasers at the literature values from References (61) and (123), and the centre of the third step scan at the expected $60F_{7/2}$ frequency from Section 4.6 (accurate to ±8 MHz). After locating the centre of the $60F_{7/2}$ peak to within ∼1 MHz, the comb

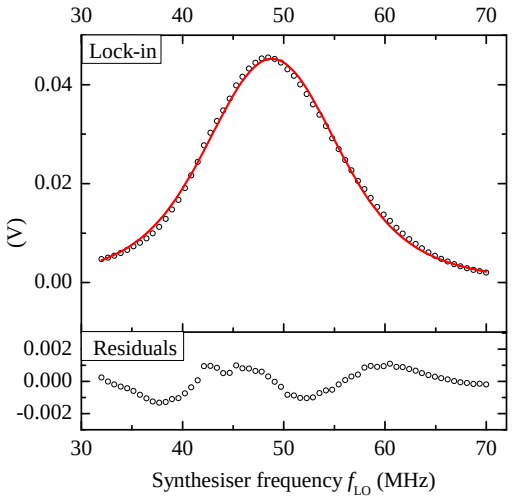

Figure 6.7: A pilot scan of the third step laser over the $5D_{5/2}, F = 5 \rightarrow 60F_{7/2}$ transition using the new comb scanning technique. The first and second steps were comb-locked at literature values. A Voigt profile is fitted to the peak with FWHM=16 MHz. The fit residuals show a clear sinusoidal oscillation due to peak asymmetry.

equations were then re-solved so as to position the peak in the exact centre of the third step scan. The third step was chopped at 1 kHz, and detection was carried out via an LIA. All other experimental parameters were set as in Section 4.6. The scan was made in 60 s, with 60 frequency steps and with a 300 ms time constant.

The SNR of the signal in Figure 6.7 is far superior to the equivalent scan in Figure 4.23 (from the original setup in Chapter 4). The main reasons for this improvement are the absence of the second step dither, the stabilised frequency of the third step laser during the scan and the negligible random error on the frequency readings. First observations showed a Voigt profile with a total linewidth of 16 MHz, indicating that the peak was previously being broadened by ∼5 MHz from laser instabilities. There was also a clear asymmetry, visible as a sinusoidal like oscillation in the fit residuals, which appeared to be a potentially large source of systematic error. This is an example of a systematic error which was unobservable during the earlier scans. The improved SNR has made this clear and demonstrates the increased sensitivity of the new scheme.

This asymmetry was dependent on the alignment and powers of the first and second

step lasers (changes of the second step signal with experimental parameters are reflected in the Rydberg signal). It was clear that its origin was from the contributions of the other $5D_{5/2}$ hyperfine states, which are only ∼10 MHz away. Similar behaviour was also seen in Reference (55) and throughout Chapter 4, when increasing the second step power. Without being able to resolve the other $5D_{5/2}$ hyperfine contributions in the Rydberg signal it is difficult to fit to them and therefore to know which pathways are being taken to the Rydberg level. Even with the improved laser stabilisation and scanning scheme, some finer control of the excitation pathway was needed to progress further with this technique.

6.4 Operating at room temperature

To observe the excitation to the Rydberg levels through each $5D_{5/2}$ hyperfine state, requires reducing the Rydberg signal linewidth below ∼10 MHz; this is the size of the $5D_{5/2}$ hyperfine splitting (123). In Section 4.2 it was found that the Rydberg signals were significantly power broadened by the first step laser, and a compromise was chosen between signal size and FWHM. With the improved SNR achievable from the new scanning scheme, the possibility of using a much lower first step power was of interest. Also, as demonstrated in Figure 4.26, a lower first step power requires a lower temperature cell. Therefore the cell was adjusted to room temperature.

6.4.1 $5D_{5/2}$ two-step spectroscopy

Effect of laser power

With the room temperature cell, studies of the $5D_{5/2}$ two-step spectroscopy were repeated, without the problems at lower first step powers. Figures 6.8, 6.9, 6.10 and 6.11 show how the first and second step laser powers affect the two-step $5D_{5/2}$ QA signal (F=5 component) amplitude and FWHM respectively. The red curves are saturation and power broadening curves (Equations 2.19 and 2.18), as are the others throughout this section. These figures can be compared with the corresponding Figures 4.9, 4.10, 4.13 and 4.14 of Chapter 4. The signal sizes are considerably smaller now and most importantly the FWHM can be ∼6 MHz (the FWHM of the first step transition) with reduced laser power. Powers of 5 μW and 50 μW were chosen for the first and second step lasers respectively, again as a compromise between resolution and signal size.

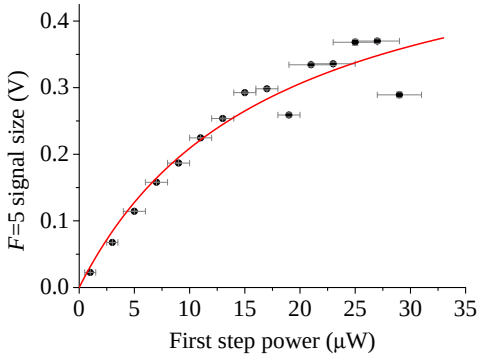

Figure 6.8: A plot of the $5D_{5/2}$, F=5 QA signal amplitude against first step laser power. The second step laser power was held at 50 μW.

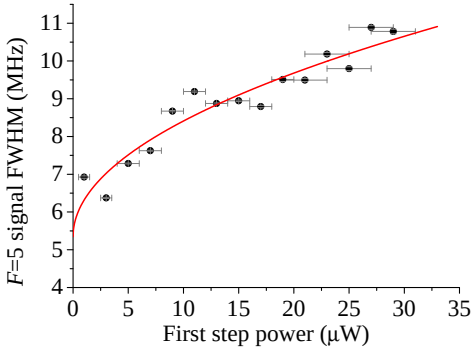

Figure 6.9: A plot of the $5D_{5/2}$, F=5 QA signal FWHM against first step laser power. The second step laser power was held at 50 μW.

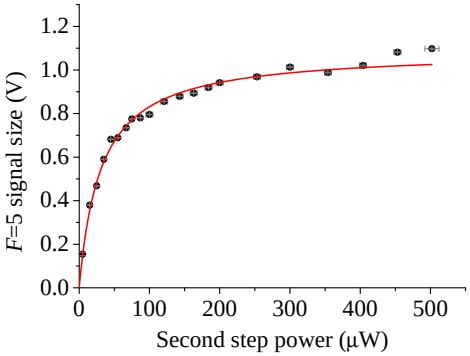

Figure 6.10: A plot of the $5D_{5/2}$, F=5 QA signal amplitude against second step laser power. The first step laser power was held at 5 μW.

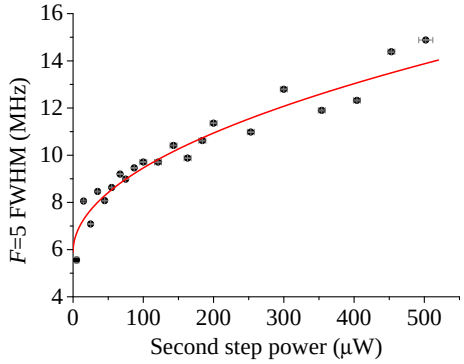

Figure 6.11: A plot of the $5D_{5/2}$, F=5 QA signal FWHM against second step laser power. The first step laser power was held at 5 μW.

Hyperfine structure

With a room temperature cell and reduced laser powers, the second step spectroscopy showed much higher resolution of the $5D_{5/2}$ hyperfine components. Figures 6.12 and 6.13 show the second step signal with and without optical selection. Looking at Figure 6.13 it is clear that the optical selection is not perfectly efficient in this setup, which is only obvious with the reduced linewidth now achievable. The possible reasons for this may be impurity in the laser polarisations, spin-exchange collisions or background fields redistributing the

m_F sublevels.

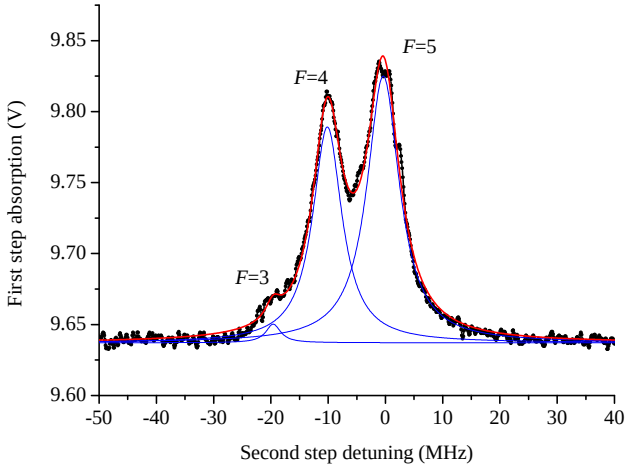

Figure 6.12: $5D_{5/2}$ hyperfine spectroscopy with $\pi\pi$ light polarisations on the first and second steps. The three hyperfine components $5P_{3/2}, F = 4 \rightarrow 5D_{5/2}, F =$5, 4, 3 are visible in the QA signal. The FWHMs are 7, 6 and 3 MHz respectively.

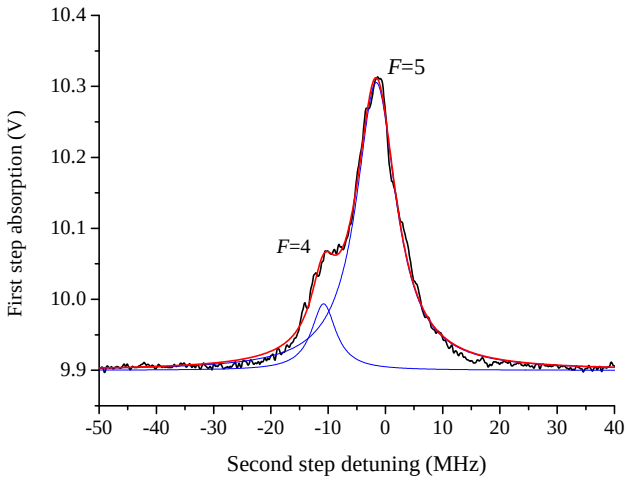

Figure 6.13: $5D_{5/2}$ hyperfine spectroscopy with $\sigma_+\sigma_+$ light polarisations on the first and second steps. The signal is strongly dominated by the $5P_{3/2}, F = 4 \rightarrow 5D_{5/2}, F = 5$ hyperfine component, with a FWHM of 8 MHz. However, residual excitation to the $F = 4$ level is also evident.

6.4.2 EIT in a three level system

For low first step laser powers (∼1 μW) and high second step laser powers (∼1 mW), it was possible to observe narrow peak features in the first step absorption (on top of the broader peaks shown in Figures 6.12 and 6.13). Figure 6.14 displays the onset of these narrow peaks as the second step power is slowly increased. These are expected to be

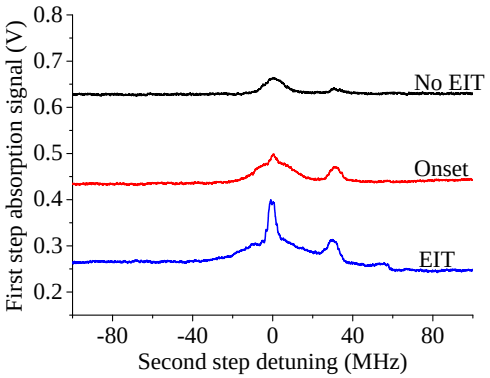

Figure 6.14: A frequency scan of the second step laser over the $5D_{5/2}$ level in ^{87}Rb whilst monitoring the first step absorption. The three traces show the onset of EIT from the conventional QA signal as the second step power is significantly increased.

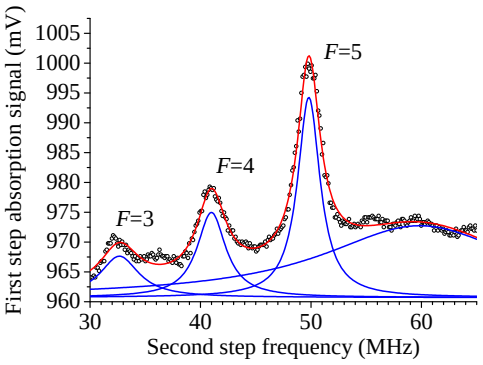

Figure 6.15: A precision laser scan of the second step over the $5D_{5/2}$ manifold in ^{85}Rb shows EIT peaks with 2 MHz linewidths. This scan was completed using the scannable comb offset-lock on the second step laser.

windows of EIT (see Figure 2.10(d)), where the first step laser acts as a probe and the second as a pump (109). In this regime $\Omega_{12} \ll \Omega_{23}$ and the atomic population in level 2 remains small. It was found that these narrow peaks were more sensitive to alignment compared to the broader peaks from QA. A small misalignment caused the EIT peaks to be extinguished. For optimum alignment and with laser powers of 1 μW and 4 mW, for the first and second steps respectively, EIT linewidths of ∼1 MHz were achievable, see Figure 6.15.

To see if these narrow peaks would be useful for improving the Rydberg spectroscopy, Rydberg states were targeted with the first and second step laser powers operating in this EIT regime. In this situation, the second step laser is locked to the top of a narrow EIT peak on the $5P_{3/2}, F = 4 \rightarrow 5D_{5/2}, F = 5$ transition. The resultant Rydberg spectroscopy showed a highly power broadened Rydberg signal, with FWHM of ∼100 MHz (similar

to the size and shape of the broader background beneath the EIT peaks in Figure 6.14). The SNR was also significantly degraded because the second step frequency noise is more readily converted to amplitude noise by the narrower EIT feature. This evidence indicates that these signals are certainly from EIT and not from simultaneous two-photon absorption (see Figure 2.10(b)). Such a two-photon absorption process would remove population from the ground state and therefore one would expect the narrow features to also be reflected in the Rydberg signal.

In a co-propagating first and second step arrangement, EIT signals will be washed out by Doppler broadening (110). It would therefore be better to use this geometry, to stop these narrow features from interfering with the signal from QA. However it has been noted in Reference (121), and was also observed in Section 4.3.10, that the resolution of the $5D_{5/2}$ hyperfine structure is better with a counter-propagating arrangement. Future work could confirm these ideas.

In Section 4.3.4, at large first step laser powers of $\sim$100 μW, it was possible to observe splitting of the $5D_{5/2}$ QA signal. By applying large second step powers whilst in this EIT regime, complex lineshapes were achievable where multiple effects act together. Figure 6.16 shows an example of this. It is clear that even this three level system is rich with atomic physics.

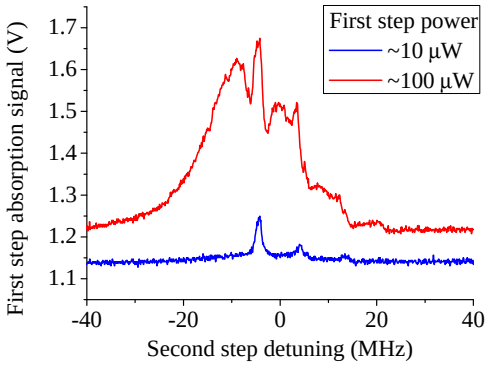

Figure 6.16: Complex $5D_{5/2}$ line shapes in a 60 °C cell; Autler-Townes splitting (111) and EIT effects (109) occur together. Turning down the first step laser power allows EIT to dominate.

6.4.3 Rydberg spectroscopy

The room temperature scheme gives much smaller Rydberg signal sizes compared to the setup in Chapter 4. For example, the $33F_{7/2}$ signal is approximately 30× smaller in this new configuration. However, this does not cause any disadvantage because the SNR of the signals is now much higher. The new experimental configuration also offers a much more reliable way of studying the behaviour of the Rydberg signals with different experimental parameters.

Effect of first and second step laser power

Figures 6.17 and 6.18 show the behaviour of the $33F_{7/2}$ Rydberg signal with the first and second step laser powers. In both cases the third step power was set at 200 μW. The fits to the Rydberg signals were made using a Voigt profile (107). Interestingly, the FWHM

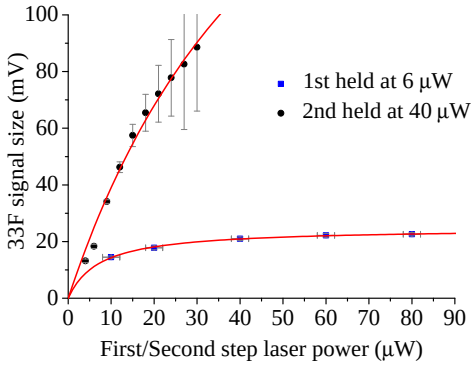

Figure 6.17: The $33F_{7/2}$ signal size with first and second step laser powers.

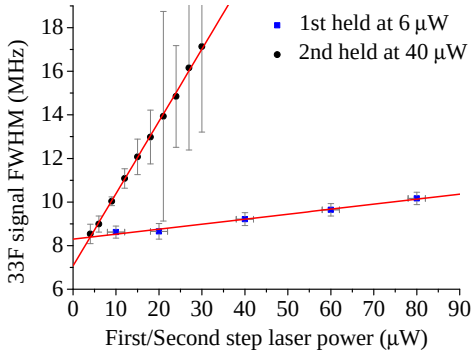

Figure 6.18: The $33F_{7/2}$ signal FWHM with first and second step laser powers.

scales faster than $\sqrt{P}$ in Figure 6.18. This indicates that the broadening is not only from conventional power broadening; as seen in Section 2.3.3 power broadening and residual Doppler broadening are linked in this system. Figures 6.17 and 6.18 can be compared with the corresponding Figures 4.26, 4.27, 4.28 and 4.29 of Chapter 4. The Rydberg signal sizes are considerably smaller and narrower in the room temperature case.

Effect of third step laser power

In this study, the first and second step powers were left at 5 μW and 40 μW respectively. Figures 6.19 and 6.20 show how the $33F_{7/2}$ signal size and FWHM scale with the third

step laser power. Again, these plots can be compared with the corresponding Figures 4.32 and 4.33 from Chapter 4. Notice that the Rydberg signal appears to saturate with lower third step power in the room temperature case, this is associated with the lower first step power used.

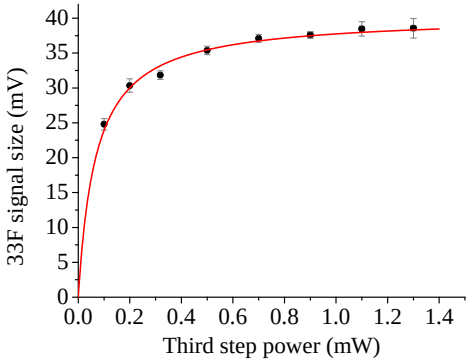

Figure 6.19: The $33F_{7/2}$ signal size with the third step laser power.

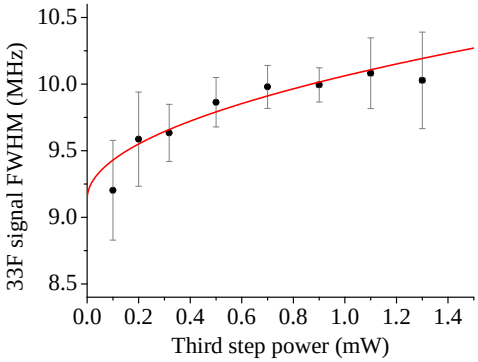

Figure 6.20: The $33F_{7/2}$ FWHM with the third step laser power.

Scaling with n

Figure 6.21 shows the behaviour of various Rydberg level signals with varying third step laser power. This gives an impression of how the third step absorption strength scales with n and changes with ℓ. The fitted curves are simple saturation functions (Equation 2.19). Figure 6.22 shows how the A fit parameters scale with n^{*-3} for the different $nF_{7/2}$ levels targeted. This implies a scaling with $|D_{ik}|^2$, as expected from Equation 2.15. Also, the ratio of the A parameters between the $45P_{3/2}$ and $45F_{7/2}$ levels is 8.7 (in good agreement with Equations 2.8 and 2.9).

Effect of second step laser power on saturation

To understand more about the excitation scheme, the behaviour was also compared for different second step laser powers (with the first step held at 5 μW), see Figure 6.23. This demonstrates how the third step saturation intensity is dependent on the second step power. The rate equation model (Section 2.3.3) describes this effect; more second step power results in a larger population of atoms in the $5D_{5/2}$ level and therefore more atoms to contribute towards the third step absorption.

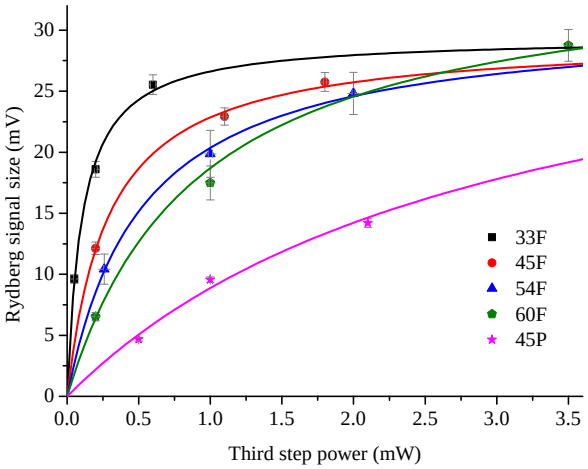

Figure 6.21: The scaling of various Rydberg signal sizes with third step laser power.

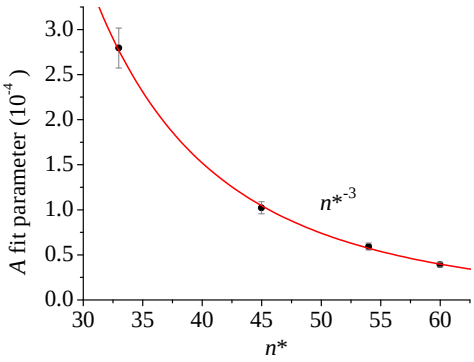

Figure 6.22: A plot of the the A parameters from a set of $y = \frac{Ax}{1+Bx}$ fits to the data in Figure 6.21.

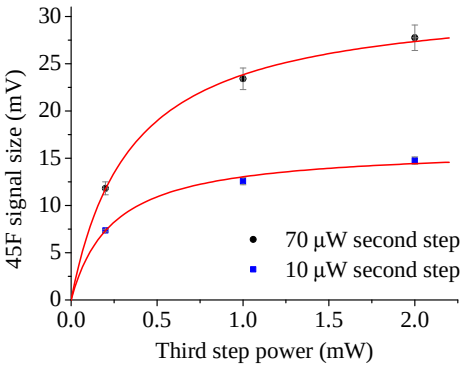

Figure 6.23: The $45F_{7/2}$ Rydberg signal size with the third step laser power, taken with different second step laser powers of 70 μW and 10 μW.

Optical selection

With the chosen first and second step powers of 5 μW and 50 μW respectively, and the third step laser power set just below saturation, the Rydberg signals now typically had a FWHM of 8 MHz. Figure 6.24(a) displays a precision scan over the $5D_{5/2} \rightarrow 60F_{7/2}$ transition with the new configuration. With this narrow linewidth, one can be confident that excitation to the Rydberg levels is through a perfectly defined pathway, governed by

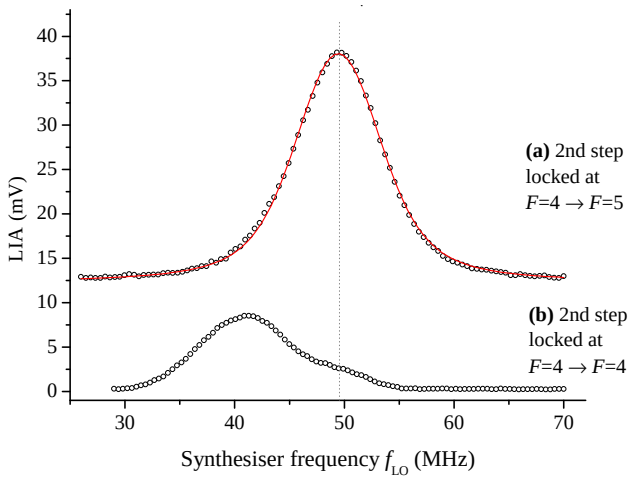

Figure 6.24: (a) A precision comb-locked third step laser scan over the $5D_{5/2}, F = 5 \rightarrow 60F_{7/2}$ Rydberg transition using the new room temperature configuration. A Voigt profile is fitted to the signal with FWHM ∼8 MHz. (b) An equivalent scan with the second step laser locked at the $5P_{3/2}, F = 4 \rightarrow 5D_{5/2}, F = 4$ hyperfine component. The absolute frequency scales are equivalent in both traces. Excitation through the $5D_{5/2}, F = 4$ and $5D_{5/2}, F = 5$ states is visible.

the second step comb-lock position. This is indicated by the high degree of symmetry in the signal. Any excitation through the other $5D_{5/2}$ hyperfine states, with separations of 9 MHz and 18 MHz, are now expected to be visible in the signal. To verify this, the second step laser was comb-locked at a different hyperfine component frequency, the $5P_{3/2}, F = 4 \rightarrow 5D_{5/2}, F = 4$. In this case, excitation to the $60F_{7/2}$ level was observed from both the $5D_{5/2}$,$F = 4$ and $5D_{5/2}$,$F = 5$ hyperfine states separated by ∼9 MHz, see Figure 6.24(b). The synthesiser frequencies in these plots correspond to equal absolute frequencies of the third step laser.

With some further investigation, it was found that the contribution to the Rydberg signal from each $5D_{5/2}$ hyperfine component is related directly to the contribution in the second step $5D_{5/2}$ signal, at the frequency at which the second step is locked (see Figures 6.13 and 6.12).

6.5 Improved absolute frequency measurements of Rydberg levels

6.5.1 $n\mathrm{P}_{3/2}$ states

To demonstrate the performance of the new scheme, the absolute frequencies of a set of $n\mathrm{P}_{3/2}$ Rydberg levels were measured. This was of interest because these states were not measured in Chapter 4, and have also not previously been measured using optical detection with a vapour cell. For these measurements, the third step laser power varied between 3-4 mW and the three laser steps were polarised in the $\sigma_+\sigma_+\sigma_-$ configuration. Figure 6.25 shows an example scan over the $54\mathrm{P}_{3/2}$ state with a Voigt profile fitted. The signals were highly symmetric and the line centre positions were reproducible to less than 100 kHz. In contrast to Figure 6.7, the residuals are structureless in Figure 6.25. For each step of the scan, the frequency difference $f_{LO} - f_{beat3}$ was recorded to be sure that the offset-lock was tracking the synthesiser properly.

Due to the low random error, only ten different $n\mathrm{P}_{3/2}$ level measurements were required to achieve a reliable Rydberg-Ritz fit to the data. The states from n=36-63 were chosen arbitrarily, and measured in steps of three. For each state, the comb calculator program (Section 5.3) was used to find the relevant comb repetition rate and beat notes for laser stabilisation. The most accurate previous $n\mathrm{P}_{3/2}$ measurements are from Reference (87) and are accurate to ±6 MHz (within the third step scan range). These previous numbers were used, along with the following iterative procedure, to centre the Rydberg signal in the scan:

Solve comb equations for previous $nP_{3/2}$ measurement (±6 MHz) → Scan third step laser and locate centre of $nP_{3/2}$ level to ±1 MHz → Re-solve comb equations to centre peak in the third step laser scan range.

Once three Rydberg levels had been accurately measured, a different procedure was used:

Fit Rydberg-Ritz Equation 4.10 to measurements collected so far → Use extracted E_i, δ_0 and a parameters to predict position of next level → Solve comb equations to centre peak in the third step laser scan range.

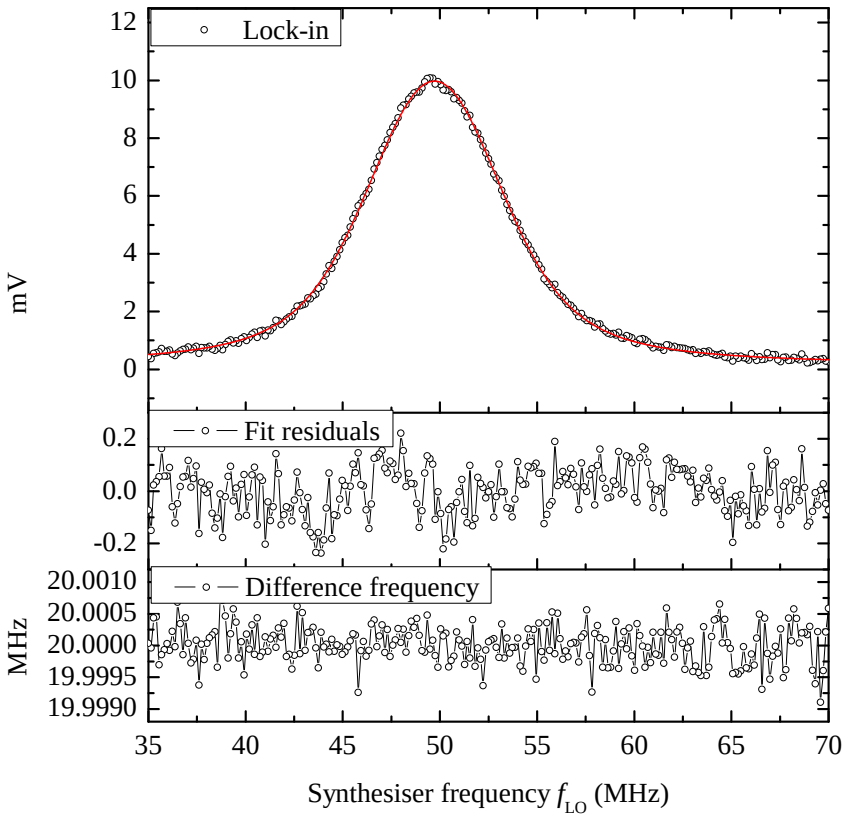

Figure 6.25: A third step comb-stabilised laser scan over the $54P_{3/2}$ Rydberg level, the third step power was 4 mW. A Voigt profile with FWHM=8.4 MHz is fitted and the fit residuals are shown. The difference frequency measurements are from counter 3, which monitors the third step offset-lock frequency $f_{LO} - f_{beat3}$. These fluctuations represent the error in frequency on each point.

Each level was measured six times. The ten average absolute frequency measurements from this work are shown in Table 6.1. The solved comb parameters are listed in Appendix B for future reference.

6.5.2 $n\mathrm{F}_{7/2}$ states

With an ionisation energy E_i extracted from the $n\mathrm{P}_{3/2}$ measurements above, and quantum defects from microwave spectroscopy (80; 81), it is possible to calculate the absolute frequencies of all Rydberg states for $n \geq 20$ and for $\ell = 0-3$. These will have an equivalent accuracy to the ionisation energy. However, as a self-consistency check, and a measure of systematic error, it was also of interest to remeasure the absolute frequency of the $n\mathrm{F}_{7/2}$ levels directly with this improved setup.

Pilot scans

Initial scans over the $n\mathrm{F}_{7/2}$ levels displayed a prominent asymmetry in the signals, when using $\sigma_+\sigma_+\sigma_+$ light and targeting states with lower principal quantum numbers. This is another example of an effect which was unnoticeable with the scheme in Chapter 4. The degree of asymmetry reduced with higher n and became unnoticeable for $n > 40$. A three layered μ-metal shield was placed around the cell to attempt to eliminate any effects from magnetic fields. Although this did not remove the asymmetry, it was successful in reducing the magnetic fields in the vicinity of the cell to 20 nT (a factor of 1000 reduction). After further investigation, it was found that the asymmetry was strongly dependent on the third step laser power and was also less prominent using a $\pi\pi\pi$ laser polarisation configuration. This may be an AC-Stark effect (124) and could therefore be more prominent at lower n, and for circularly polarised light, due to the higher third step coupling in these cases. The larger fine and hyperfine structure splittings for lower n states may also result in a larger effect, although this area requires further investigation.

Final scans

For the final scans, the asymmetry problems mentioned above were minimised by setting the third step laser power well below saturation, see Figure 6.21. The three laser steps were polarised in the $\sigma_+\sigma_+\sigma_+$ configuration. Small residual asymmetries meant that fitting to the $n\mathrm{F}_{7/2}$ levels was not always possible with the same degree of confidence as the $n\mathrm{P}_{3/2}$ levels. Figure 6.26 displays an optimised precision scan over the $36\mathrm{F}_{7/2}$ level. The $n\mathrm{F}_{7/2}$ levels were measured from n=33-60 in intervals of three. The comb parameters were computed using the same method as for the $n\mathrm{P}_{3/2}$ states, with the previous $n\mathrm{F}_{7/2}$ measurements from Section 4.6. These comb parameters can also be found listed in Appendix

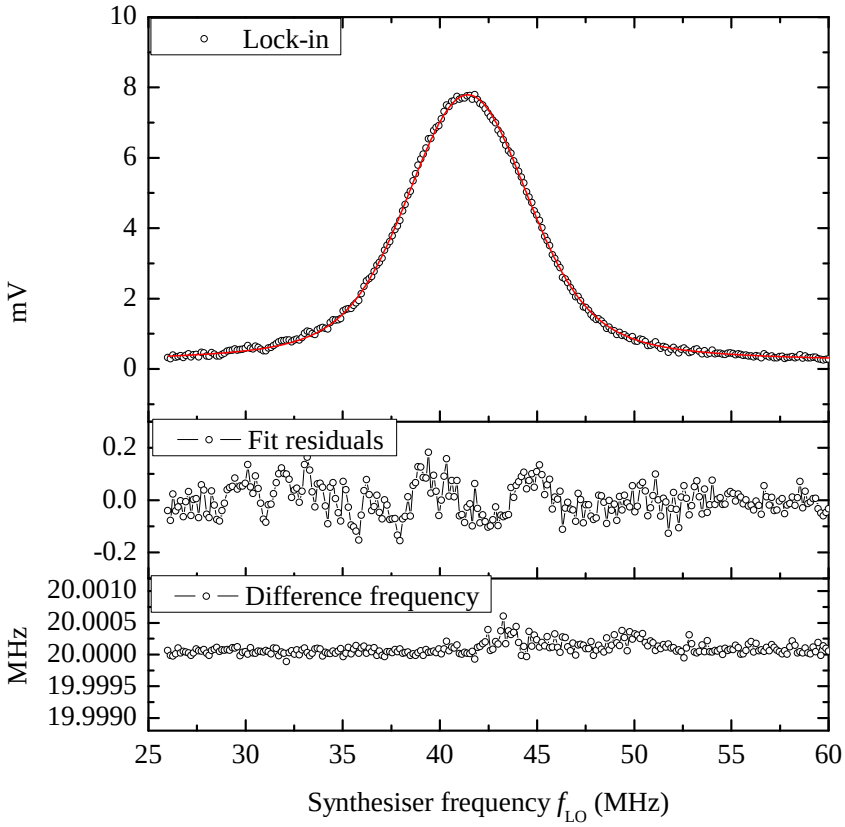

Figure 6.26: A third step comb-stabilised laser scan over the $36F_{7/2}$ Rydberg level. The third step power was 200 μW. A Voigt profile is fitted with FWHM=7.5 MHz and the fit residuals are shown. The difference frequency measurements are from counter 3, which monitors the third step offset-lock frequency $f_{LO} - f_{beat3}$. These fluctuations represent the error in frequency on each point.

B. The ten absolute frequency measurements from this work are shown in Table 6.1, each number is an average from two repeated measurements.

Table 6.1: The third step measured transition frequencies for $5D_{5/2}, F = 5 \rightarrow nP_{3/2}$ and $5D_{5/2}, F = 5 \rightarrow nF_{7/2}$ transitions. The total accumulated error on all frequencies is summarised in Section 6.8.

n	$5D_{5/2} \rightarrow nP_{3/2}$ (MHz)	$5D_{5/2} \rightarrow nF_{7/2}$ (MHz)
33	-	236 429 202.46
36	236 496 723.81	236 912 407.38
39	236 964 490.17	237 288 412.47
42	237 329 425.41	237 586 730.99
45	237 619 602.20	237 827 379.57
48	237 854 128.44	238 024 318.81
51	238 046 375.56	238 187 526.24
54	238 205 927.54	238 324 287.88
57	238 339 798.76	238 440 023.35
60	238 453 218.87	238 538 831.71
63	238 550 150.91	-

6.5.3 Analysis

From the measurements in Table 6.1, two Rydberg-Ritz fits were made using Method 3 from Section 4.6.5. The absolute frequencies from both series are plotted together in Figure 6.27 with the fitted functions. The residuals from these fits are shown in Figure 6.28. The extracted parameters are displayed in Table 6.2, alongside comparisons from the best microwave measurements from References (80; 81). The ionisation energy is computed by adding a value of 770 571 549.623 MHz to the values in Table 6.1, computed from References (91; 123). Other previous experiments with access to the ionisation energy are also shown for comparison (82; 83; 86; 87; 96). Unlike the analysis in Section 4.6.5, no other numbers were added to the data set in this analysis; the extracted parameters come purely from these measurements alone.

6.5.4 Discussion

Table 6.2 shows that the quantum defect parameters from this work (for both series) show excellent agreement with the most accurate microwave measurements (80; 81). For the $nP_{3/2}$ series the uncertainties are also comparable. It is also very pleasing that the ionisation energies from the two series agree with one another to within 1σ. This indicates that systematic errors which would affect both series differently are controlled within the ran-

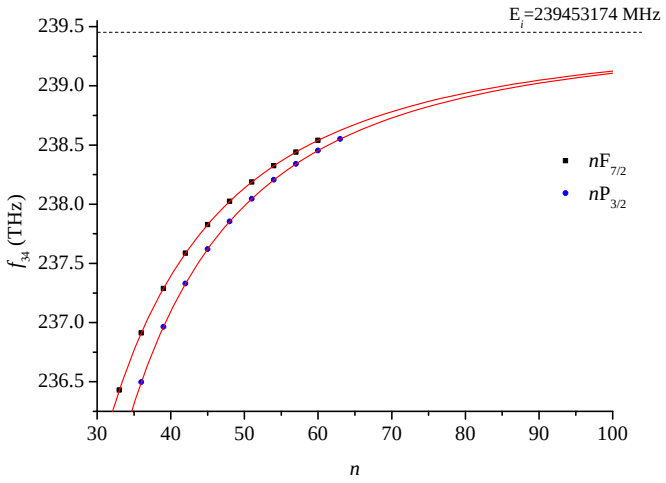

Figure 6.27: The $5D_{5/2}, F = 5 \rightarrow nP_{3/2}$ and $5D_{5/2}, F = 5 \rightarrow nF_{7/2}$ absolute transition frequencies plotted against the principal quantum number n. The figure shows the two series converging to the same ionisation energy of 239 453 174.2 MHz.

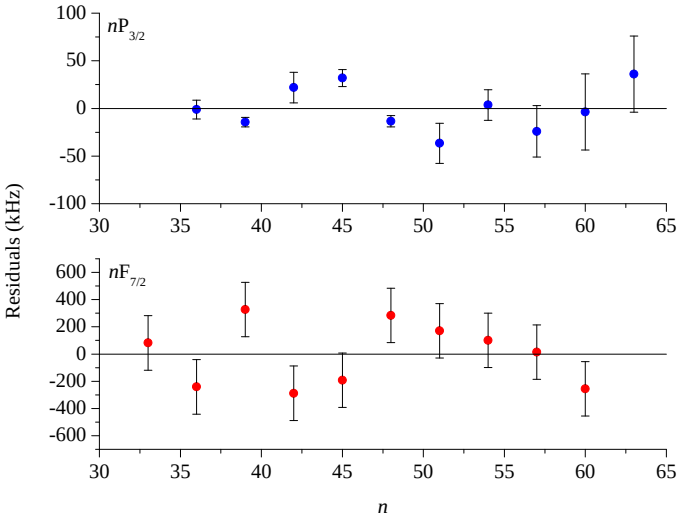

Figure 6.28: The fit residuals for the data shown in Figure 6.27. The residuals are scattered by 24 kHz and 230 kHz for the $nP_{3/2}$ and $nF_{7/2}$ measurements respectively. The error bars are based on the random error and fit error on each transition.

dom measurement error. Such systematic errors could be from electric and magnetic fields and/or temperature-dependent Rydberg-Rydberg interactions (127). It can also clearly

Table 6.2: The Rydberg-Ritz fit parameters from these new measurements are shown in bold type. Other parameters from different sources are also shown for comparison (80; 81; 82; 83; 85; 86; 87; 96). All uncertainties shown are statistically derived from the fitting procedure.

State	Source	E_i (MHz)	δ_0	a
$n\mathrm{P}_{3/2}$	**This work**	**1010 024 723.86(4)**	**2.641 6711(13)**	**0.2968(13)**
	(80) Han	-	2.641 6737(10)	0.2950(7)
	(87) Sanguinetti	1010 024 692(7)	2.641 352	0.4822
	(86) Lorenzen	1010 024 68(9)	2.641 45(20)	0.33(18)
$n\mathrm{F}_{7/2}$	**This work**	**1010 024 723.8(4)**	**0.016 533(12)**	**-0.078(12)**
	(96) Chapter 4	1010 024 717(8)	0.016 40(8)	0.00(9)
	(81) Han	-	0.016 5437(7)	-0.086(7)
$n\mathrm{S}_{1/2}$	(82) Lee	1010 024 741(6)	-	-
$n\mathrm{S}_{1/2}$	(83) Sansonetti	1010 024 729(7)	-	-
$n\mathrm{S}/n\mathrm{D}$	(85) Stoicheff	1010 024 697(45)	-	-

be seen that the $n\mathrm{F}_{7/2}$ state parameters are improved by almost an order of magnitude compared to the work of Chapter 4 using the wavemeter.

In Figure 6.28, it is quite remarkable how stably the $n\mathrm{P}_{3/2}$ states behave from n=36-63, with the residuals having a spread of just 24 kHz 1σ over the whole range of n. For the $n\mathrm{F}_{7/2}$ series the residual spread is around $10\times$ larger, which can be associated with the residual asymmetry problems. However, these measurements still show an improvement in absolute accuracy of over $20\times$ compared to Chapter 4, as well as being the only existing measurements for these states.

It is clear that the new measurement for E_i appears inconsistent with the most accurate previous measurements by Sanguinetti *et al* (87) and Lee *et al* (82). This disagreement may be explained as follows: There may be the possibility of a wavemeter offset in Reference (87), as was measured in Section 4.6.2. Also, the quantum defect parameters extracted in Reference (82) for the $n\mathrm{S}_{1/2}$ series, do not agree with the most recent microwave measurements (80). This implies that their value for E_i could also be in error. Sansonetti *et al* (83) repeated the measurements of Lee *et al* (82) using the same technique and also found disagreement.

6.6 The effect of electric fields

The resilience of the Rydberg lines to externally applied electric fields was a surprising observation made in Chapter 4. Similar behaviour has also been seen in References (54; 55). With the new laser scheme, it was interesting to return to this in more detail, with enhanced frequency accuracy.

6.6.1 DC-Stark shifts

The DC-Stark frequency shift of a Rydberg level in Rb is quadratic and is given from perturbation theory as

$$\Delta f_{n,\ell \text{ Stark}} = \sum_{n'} \sum_{\ell'=\ell\pm1} \frac{e^2 \mathrm{E}^2}{h} \frac{|\langle n,\ell|r|n',\ell'\rangle|^2}{(E_{n,\ell} - E_{n',\ell'})} \propto \frac{(n^2)^2}{n^{-3}}. \tag{6.3}$$

The dipole matrix elements can be computed using the method outlined in Section 2.2.3 and the energy differences by using Equation 2.1 with the relevant quantum defects. For the case of high n and ℓ levels in Rb, the sum is generally dominated by one nearby state only. It is important to note that Equation 6.3 is only valid when the dipole coupling is much smaller than the energy difference. For larger fields, the Stark shift in Rb becomes linear and eventually one sees avoided crossings between states (75).

Because of the large dipole matrix elements and small energy gaps between neighbouring Rydberg levels, the states are inherently sensitive to electric fields, this is clear from the n^7 scaling in Equation 6.3. For a fixed n, there is also a strong ℓ dependence: Due to the smaller quantum defects of higher ℓ states, one expects the smallest energy gaps and largest overlaps with neighbouring states. Small quantum defects also mean that the Stark shift is usually dominated by coupling with a nearby $\ell' = \ell+1$ state of higher energy. This leads to negative frequency shifts from electric fields. The most sensitive state studied in this work so far is expected to be the $60\mathrm{F}_{7/2}$ level; with a shift of $\sim$-125 GHzV^{-2}cm^2.

6.6.2 Experimental results

Some simple field plates were attached either side of the cell, separated by 25 mm. This entire unit was then placed inside the μ-metal shield and the field plates were connected to an adjustable high-voltage supply. The $60\mathrm{F}_{7/2}$ state was measured with potential differences of 0 V to 200 V applied across the field plates. The frequency measurements

from this investigation are shown in Figure 6.29. The error bars are based on the spread of a set of repeated readings with 0 V applied.

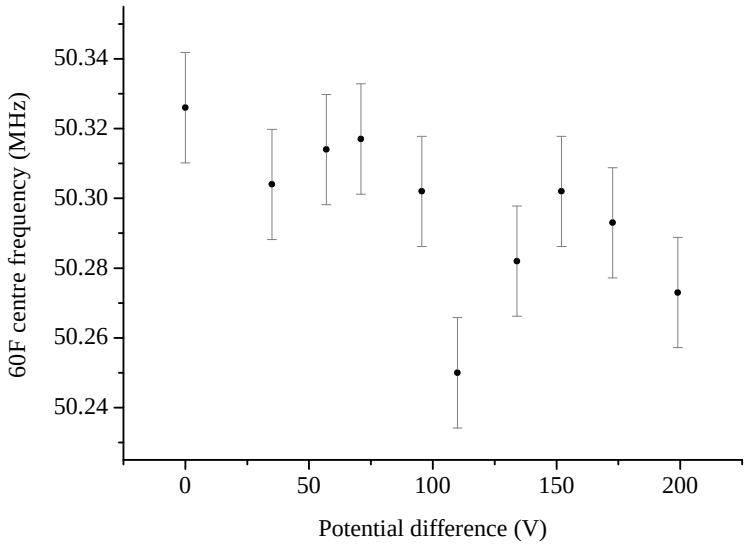

Figure 6.29: $60F_{7/2}$ measurements with varying potential differences applied over the vapour cell. The error bars are based on the spread of a set of repeated readings with 0 V applied. The frequency measurements are f_{LO} values.

The data shows a potentially small negative[1] shift of -0.9(5) HzV^{-2}, which is a factor of $\sim 10^{10}$ smaller than expected. It appears that the Rydberg atoms are being very efficiently screened from the applied electric field, in the same manner as a Faraday cage. It has been suggested by Mohapatra *et al* (54) that the interaction region is screened by free-charges within the cell, which are free to move and cancel out any externally applied field. The properties of this screening are investigated in more detail in Section 8.1, where the effect of electric field transients is considered.

6.7 The effect of first and second step frequency detuning

6.7.1 Experimental results

The new laser setup allows fine control of all three laser frequencies, so it is possible to study the effect of detuning the first and second step lasers with high accuracy. For this

[1] The f_{beat3} sign was positive for this investigation

study the $63P_{3/2}$ state was chosen, for reasons which will be outlined in Section 6.8.4. All three lasers were stabilised to the comb and third step scans were carried out over the $5D_{5/2}, F = 5 \rightarrow 63P_{3/2}$ transition for a set of different first and second step detunings. The first and second step lasers were detuned by adjusting their respective DDS frequencies. The results can be seen in Figures 6.30 and 6.31.

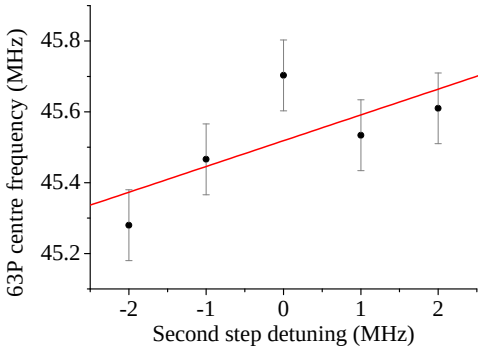

Figure 6.30: Shift of the $63P_{3/2}$ peak position with second step laser detuning. The frequency measurements are f_{LO} values, f_{beat3} had a negative sign for this work.

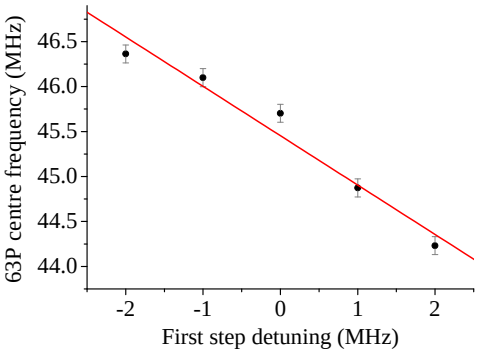

Figure 6.31: Shift of the $63P_{3/2}$ peak position with first step laser detuning. The frequency measurements are f_{LO} values, f_{beat3} had a negative sign for this work.

6.7.2 Analysis

In both cases, detuning either of the lasers caused an asymmetry in the Rydberg signal, which resulted in a less reliable fit to the peaks. However, approximate relationships between the detuning and observed centre frequency were extracted:

$$f'_{34} \approx f_{34} - 0.07(4)\delta_{23} \quad \text{when} \quad \delta_{12} = 0, \tag{6.4}$$

$$f'_{34} \approx f_{34} + 0.55(6)\delta_{12} \quad \text{when} \quad \delta_{23} = 0, \tag{6.5}$$

where $\delta_{12} = f_1 - f_{12}$ and $\delta_{23} = f_2 - f_{23}$ are the detunings of the first and second step lasers respectively. f_{34} and f'_{34} are the actual and observed third step transition frequencies respectively. Detuning either the first or second step laser pulls the signal in opposite directions.

6.7.3 Discussion

The origin of the scaling in Equation 6.5 can be explained from a velocity-selection argument. The first step selects a velocity class which interacts with the other two steps. The first step detuning will change the atomic velocity which is selected, and therefore a shift of the Rydberg signal is seen which scales with the wavelength ratio $\frac{780}{1260}$=0.62. However, the second step also sees a Doppler shift, which detunes the comb-locked second step by almost the same amount $\frac{780}{776}\delta_{12}$ but in the *opposite* direction. This is due to the counter-propagating first and second step geometry. Therefore, Equation 6.5 shows the effect of the 0.62 Doppler scaling *minus* the scaling from Equation 6.4, which acts in the opposite direction. This agrees with what is found: 0.62-0.07=0.55.

The origin of the 0.07 ratio in Equation 6.4 is unclear, although Figure 6.4.3 demonstrates that detuning the second step laser can cause contributions from other $5D_{5/2}$ hyperfine states to appear in the Rydberg signal; this causes an asymmetry. The small shift could therefore be an artefact of this asymmetry. To verify this, a scan of the $63P_{3/2}$ state was made with δ_{12}=-2 MHz and δ_{23}=+2 MHz. This corresponds to the situation where f_{12} is not known to high accuracy, but yet f_{13} is [1]. With this arrangement, the $63P_{3/2}$ peak was found to be symmetric and shifted down by 1.21(2) MHz, in good agreement with the prediction from the wavelength ratio of 0.62. This is the situation where the first step selects a velocity class, and the second step is detuned to perfectly account for the Doppler shift.

The findings from this section also agree well with the correlation plot in Figure 5.8 of Chapter 5. In this case, the second step was locked to a signal derived with co-propagating first and second step lasers. Therefore, one expects the Rydberg peak position to scale with the first step frequency with the ratio 0.62-(2×0.07(4))=0.48(8); this is in good agreement with what is observed. If instead, the second step were locked to a signal derived with counter-propagating first and second step lasers, one would expect this ratio to be 0.62-0.07+0.07=0.62 with the detunings always cancelling due to almost equal and opposite Doppler shifts.

[1] This is the case for this experiment, where f_{12} is known to ±750 kHz from SAS (61) and f_{13} is known to ±16 kHz from two-photon spectroscopy (123).

6.8 Error budget for $n\mathrm{F}_{7/2}$ and $n\mathrm{P}_{3/2}$ frequency measurements

Table 6.3 summarises the estimated error budget for the $n\mathrm{F}_{7/2}$ and $n\mathrm{P}_{3/2}$ absolute frequency measurements. These sources of error are discussed throughout this section.

Table 6.3: The estimated error budget for the improved Rydberg spectroscopy measurements in Table 6.1. All errors are 1σ and in units of kilohertz. The total error is the sum in quadrature of the different sources.

Source	$n\mathrm{P}_{3/2}$ states	$n\mathrm{F}_{7/2}$ states
Power dependent shifts	280	440
Random and fit errors	53	200
1st step frequency	80	80
Magnetic fields	25	60
Laser metrology	4	4
2nd step frequency	1	1
Total	297 kHz	494 kHz

6.8.1 Zeeman shifts

The $n\mathrm{P}_{3/2}$ measurements were taken before μ-metal casing was available to shield the cell. Therefore the $63\mathrm{P}_{3/2}$ and $42\mathrm{P}_{3/2}$ levels were re-measured with the μ-metal shielding, to estimate the maximum Zeeman shifts for the $n\mathrm{P}_{3/2}$ measurements. These shielded measurements were approximately 230(40) kHz and 280(20) kHz lower than the original measurements respectively. Therefore a mean of 255 kHz was subtracted from the $n\mathrm{P}_{3/2}$ measurements to account for this shift. The upper and lower bounds from this mean are used to estimate the maximum error from Zeeman shifts on the $n\mathrm{P}_{3/2}$ series. Finally, to check for any shifts from residual fields *inside* the shield, the $63\mathrm{P}_{3/2}$ state was measured with both polarisation configurations $\sigma_+\sigma_+\sigma_-$ and $\sigma_-\sigma_-\sigma_+$. There was no measurable difference between these cases within the random error.

The $n\mathrm{F}_{7/2}$ states were all measured within the μ-metal casing and therefore Zeeman shifts were checked by comparing the $60\mathrm{F}_{7/2}$ level with the two polarisation configurations $\sigma_+\sigma_+\sigma_+$ and $\sigma_-\sigma_-\sigma_-$. In this case a difference of 60(40) kHz was found, which is used as an estimate of the maximum Zeeman shift.

6.8.2 Power dependent shifts

To study power dependent shifts, the $33\mathrm{F}_{7/2}$, $60\mathrm{F}_{7/2}$, $36\mathrm{P}_{3/2}$ and $63\mathrm{P}_{3/2}$ levels were each measured with a range of first, second and third step laser powers. In the case of the first step laser, a repeatable shift of -90(20) kHz/μW was measured for all of these states, see Figure 6.32. This can be associated with the contributions from the other $5\mathrm{D}_{5/2}$ hyperfine states which are above the $F = 5$ level, and will therefore appear at lower frequencies in the Rydberg signal, becoming more prominent as the first step is saturated.

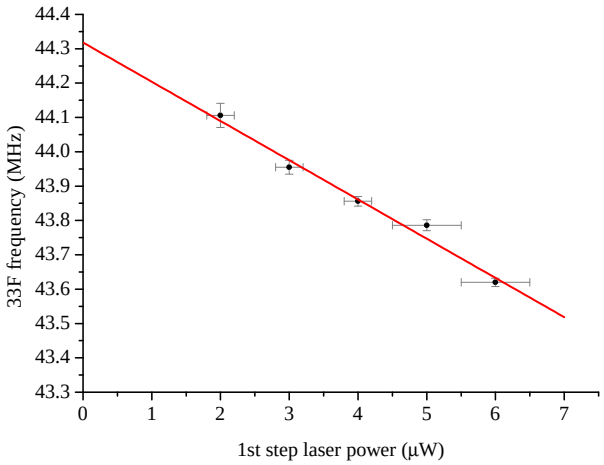

Figure 6.32: Power dependent shifts: This is a plot of the $33\mathrm{F}_{7/2}$ Rydberg state frequency against the first step laser power. Frequency error bars are from fitting, and power error bars are from the power meter. The frequency measurements are f_{LO} values, f_{beat3} had a positive sign for this data.

For the case of the second and third step lasers, shifts were typically 10$\times$ and between 100-1000$\times$ less sensitive respectively. Also, the $n\mathrm{P}_{3/2}$ states generally suffered smaller shifts than the $n\mathrm{F}_{7/2}$ states. These shifts were dependent on which Rydberg level was being studied, and were therefore more complex to address. Frequencies extrapolated to zero power were extracted for each state and for each of the lasers. For each of the four states studied, the spread of the extrapolated measurements (around the original measurement) was taken as the estimated maximum power dependent shift from all three lasers. Alternatively, extrapolation with the summed laser power also yielded similar results. To estimate the maximum error for the $n\mathrm{P}_{3/2}$ series of states, an average of the

$36\mathrm{P}_{3/2}$ and $63\mathrm{P}_{3/2}$ shifts was taken. The same procedure was carried out for the $n\mathrm{F}_{7/2}$ series with the $33\mathrm{F}_{7/2}$ and $60\mathrm{F}_{7/2}$ states.

6.8.3 DC-Stark shifts

From the study in Section 6.6.2, assuming stray electric fields around the cell are no larger than $\sim$10 Vcm^{-1}, DC-Stark shifts will be negligible at $\ll$1 kHz for all the states measured in this work. However the possibility of a small field, originating from within the cell, cannot be ruled out. A powerful method to measure these fields is introduced in Chapter 7, and in Section 7.5.2 the effect of such a field on the measurements in this chapter is considered in detail.

6.8.4 First and second step transition frequencies

The uncertainty on the combined two-step transition $5\mathrm{S}_{1/2}, F = 3 \rightarrow 5\mathrm{D}_{5/2}, F = 5$ is $\pm$16 kHz (123). From Equation 6.4, this source of error will be 1.1 kHz at most on the Rydberg level measurement. The larger contribution comes from the first step uncertainty. This laser was comb-locked to the literature value from Reference (61) during all measurements, which has an uncertainty of $\pm$750 kHz. The uncertainty in the first step lock means that the third step laser may be interacting with a non-zero velocity class of atoms. From Section 6.7 one can estimate that, due to Doppler shifts, this would cause the Rydberg level position to be shifted by up to

$$\pm\frac{780}{1260} \times 750 \text{ kHz} = \pm 464 \text{ kHz}.$$

A nice feature of this experiment is that there is a handle on this source of error. By comparing measurements with opposite third step laser propagation directions, one expects opposite third step Doppler shifts. For the expected uncertainty, in the worst case, this would cause a 928 kHz difference between these two geometries, which is easily detectable in this experiment. To carry out this test, a flippable mirror was added in the path of the third step laser, allowing it to either co- or counter-propagate with the first step laser, without changing other experimental conditions. The setup is shown in Figure 6.33.

Measurements of the $63\mathrm{P}_{3/2}$ state were made with both geometries. The $63\mathrm{P}_{3/2}$ state was chosen because this state suffered some of the smallest power dependent shifts in

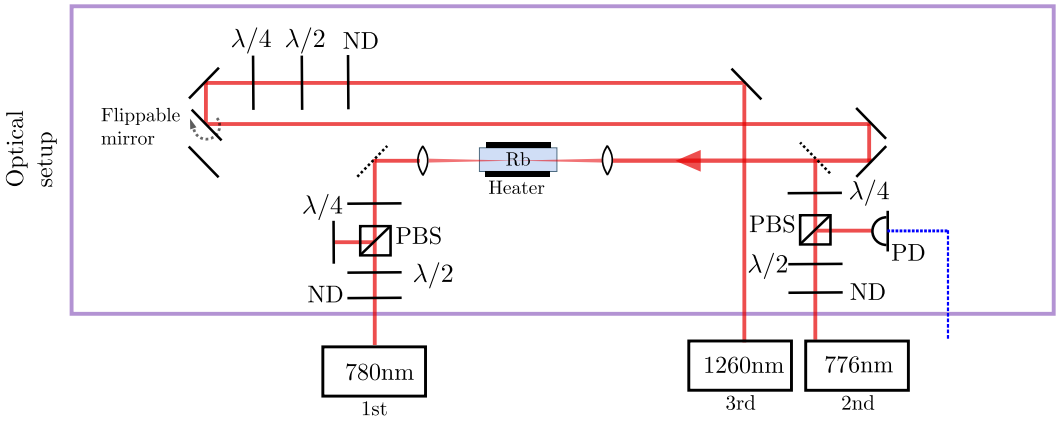

Figure 6.33: A modification to the optical setup to allow changeable third step propagation directions. ND: Neutral-density filter, PBS: Polarising beam splitter, PD: Photodiode.

Section 6.8.2, so minimal changes were expected from any differences in laser intensity. When comparing the measurements, a consistent difference of 1.39(16) MHz was found between the two geometries. Two typical scans are shown in Figure 6.34 overlaid on the same absolute frequency scale. This difference is significant within all other sources

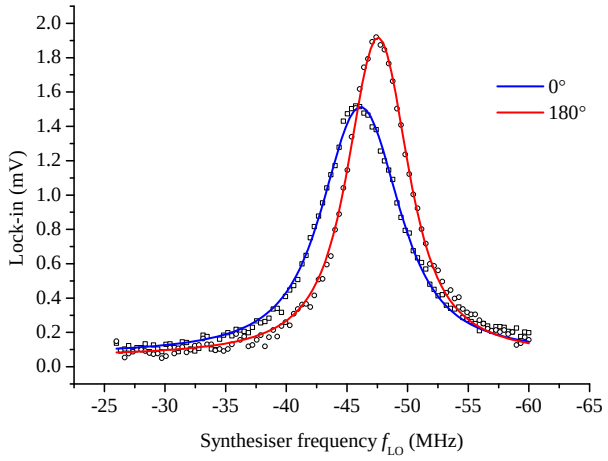

Figure 6.34: $63\mathrm{P}_{3/2}$ precision scans with the two different geometries, with angles of 0° and 180° between the first and third step laser beams. There is a clear difference of 1.4 MHz between the two. f_{beat3} had a negative sign in this work.

of error, and is larger than expected from the uncertainty on the first step transition

frequency (61). This suggests that the first step laser is locked 1.1 MHz too high in frequency, with the co- and counter-propagating signals being shifted up and down by 700 kHz respectively. A further check also showed a similar difference for the $33\mathrm{F}_{7/2}$ level, where one expects different behaviour from other possible sources of systematic shift that may be dissimilar between the two geometries.

Finally, the first and second step lasers were locked such that δ_{12}=-1.1 MHz and δ_{23}=1.1 MHz. In this configuration the Rydberg signals from the two geometries are overlapped, verifying that the observed splitting in Figure 6.34 was a true Doppler effect. This result is also interesting because Figure 4.21 in Chapter 4, although much less accurate, also predicted a lower first step frequency than that from Reference (61). Interestingly, it is stated in the paper itself (61) that the $5\mathrm{S}_{1/2}, F = 3 \rightarrow 5\mathrm{P}_{3/2}, F = 4$ transition (f') appeared to suffer large systematic shifts, and when comparing this measurement against the other D_2 line measurements in the paper, the result is not self-consistent; the measurement appears to be ∼1 MHz too high. To account for this error, a frequency of 700(80) kHz is subtracted from all Rydberg level measurements, leaving an uncertainty of 80 kHz.

6.8.5 Statistical errors and fit errors

To understand the random error of the system, a set of repeated readings of the $60\mathrm{F}_{7/2}$ level was taken over an hour time period. The histogram of these measurements can be seen in Figure 6.35; the standard deviation is 33 kHz. This can be compared with the stability data found in Section 5.5, which showed similar results. A similar set of readings was also taken for the $63\mathrm{P}_{3/2}$ level and a standard deviation of 53 kHz was found. In all cases the lower n states could be measured with a higher repeatability, therefore these estimates are expected to be upper bounds.

Fit errors depended on the SNR of the signal, but in general for a highly symmetric peak they were comparable to the random error. However, for a slightly asymmetric peak, large offsets of up to 200 kHz were often visible between the line centre and the fitted frequency. Importantly, these offsets were not accurately reflected in the fit parameter error. This was particularly troublesome for the $n\mathrm{F}_{7/2}$ states and emphasises the importance of having a reliable linear scanning method before attempting to lock to the signals to measure them.

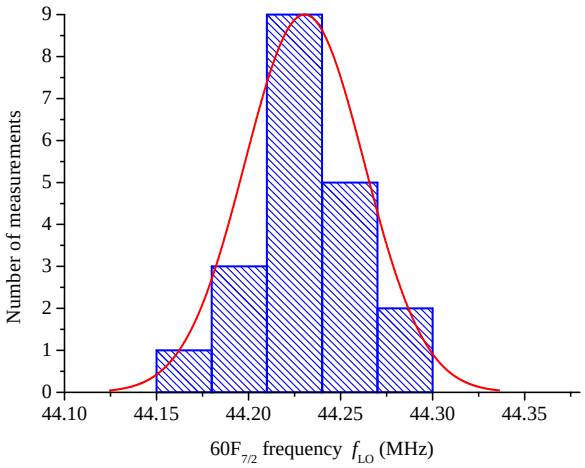

Figure 6.35: A histogram of 20 repeated measurements of the $60F_{7/2}$ state.

6.8.6 Laser frequency measurement and data acquisition

Throughout each scan, the laser frequencies were monitored using the frequency counters, with an absolute accuracy of 3 kHz. In Figure 6.5, the relative laser stabilities are all better than 1 kHz during the time scale of a single scan. The accuracy limit comes from the GPS disciplined Rb 10 MHz standard used to reference the comb, with an estimated relative accuracy of $\pm 5 \times 10^{-12}$ (115). This propagates to potential errors of 1 kHz and 2 kHz at 1260 nm and 780 nm respectively.

To eliminate potential errors from time delays in the data acquisition process, and from the time constant of the LIA, an equal number of measurements was always taken in both scan directions of the third step laser. The result was then averaged from these, eliminating any hysteresis error.

6.9 Conclusion

The new laser system outlined in this chapter dramatically simplifies the laser system for the micromaser experiment in our lab, and allows long term frequency stability, reproducible locking and precise control of laser detunings. The latter of these features can be used for accurate Doppler selection.

The setup has been tested by making an improved set of absolute frequency measurements of the $n\mathrm{P}_{3/2}$ and $n\mathrm{F}_{7/2}$ Rydberg series in ^{85}Rb. These measurements have absolute accuracies of 300 and 500 kHz respectively. From the $n\mathrm{P}_{3/2}$ measurements, a more accurate value for the ionisation threshold of ^{85}Rb can be derived of E_i=1010 024 723.9(3) MHz, limited by systematic uncertainty. Even with the existing frequency accuracy limitation of ∼1 kHz from the GPS reference, the accuracy of optical Rydberg spectroscopy using this new system could surpass that of current microwave spectroscopy techniques, which are at the ∼10 kHz level (80; 81). However, any future experiments will require detecting Rydberg levels with a narrower linewidth, to achieve higher accuracy fitting. Chapter 8 will discuss the future prospects of this research.

This chapter has also demonstrated that knowledge of the first step $5\mathrm{S}_{1/2}, F = 3 \rightarrow 5\mathrm{P}_{3/2}, F = 4$ transition frequency is critical for these types of measurement; this may become a limiting factor. Other than the ±750 kHz value used throughout this work (61), more accurate numbers for this transition are limited in the literature. A value of 384 229 241.999(30) MHz can be derived from Reference (94). However this is not from a *direct* measurement, and also (as was discussed in Section 1.5.3) there have been large discrepancies between these measurements in the past.

Chapter 7

Four-photon Rb spectroscopy in a vapour cell

After the success of the three-step laser excitation scheme in the vapour cell, and the construction of a reliable comb-locked laser system, the excitation of a fourth step using microwaves was considered. Dipole selection rules allow such a scheme to access the nG, nD and nS Rydberg series, which vastly expands the scope of the spectroscopy measurements. Of primary interest are the nG states, where only two previous (moderately recent) measurements of the quantum defect have been made (66; 81). Importantly, as described in Section 2.1.3, such high ℓ states are the only type which allow access to the core polarisability of the Rb^+ ion, for which there are no accurate experimental values. The addition of a microwave field also opens up a large amount of interesting physics which could be studied with this simple vapour cell sample. Some of these areas are microwave-dressed Rydberg atoms, Rabi flopping and possibly microwave-cavity interactions. Finally it is also found that the high ℓ states accessible with this scheme can be used as sensitive electric field probes for detecting small stray fields within the vapour cell. The experimental work in this chapter was carried out with my colleague Martin Jones.

7.1 Principle of four-photon spectroscopy

To begin, consider how a fourth step excitation could be detected using the existing scheme. Figure 7.1 displays the energy levels involved in this four-photon investigation. The fine structure of the Rydberg levels is not considered. Using the same arguments as in Section 2.10, a QA factor can be estimated. Exciting between the two Rydberg states n_1L_1 to

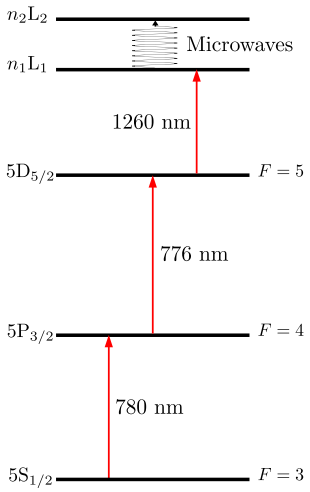

Figure 7.1: The energy levels involved in four-photon Rydberg spectroscopy. The first three steps are driven with lasers as in the previous chapters, and the fourth step between two Rydberg levels with $n_1 \approx n_2$ is driven with microwaves.

n_2L_2 will remove atoms from the 5D $\rightarrow n_1L_1$ cycle, for the lifetime of the n_2L_2 state. The amplification factor will be

$$A_q = \frac{\tau_{n_2L_2}}{\tau_{5P}} \frac{\tau_{5P}}{\tau_{5D}} \frac{\tau_{5D}}{\tau_{n_1L_1}} = \frac{\tau_{n_2L_2}}{\tau_{n_1L_1}}. \tag{7.1}$$

Two Rydberg states with $n_1 \approx n_2$ will have very similar lifetimes and this will lead to a negligible amplification factor of $A_q \sim 1$. However, the dipole matrix elements *between* Rydberg states can be very large and this means that QA is not necessarily required for detection of these transitions. For example, using the method outlined in Section 2.2.3, the 60F$\rightarrow$61G transition has a radial matrix element of $1.23\times10^3 ea_0$, compared to $44\times10^{-3} ea_0$ for the 5D$\rightarrow$60F transition; the coupling strength is larger by a factor of 10^9. Therefore these transitions can be driven very strongly with only small amounts of microwave power. One expects to see large changes in the first step absorption, even for $A_q \sim 1$.

7.2 Previous nG measurements

The nG series of Rydberg levels in Rb has been studied previously in only two papers, both of which consider ^{85}Rb. In Reference (81), a pilot measurement was made of $\delta(n) = 0.00400(9)$ using two-photon microwave spectroscopy. In contrast, Reference (66) has made a measurement of $\delta(n) = 0.00405(6)$ for the 30G state using electric field induced

resonant Rydberg-Rydberg interactions. Both of these experiments use a MOT apparatus, which is significantly more involved than the vapour cell arrangement in this work. nG spectroscopy with a vapour cell could lead to advances in this area.

7.3 Preliminary experiment

Using the nG quantum defect from Reference (81) and the $n\mathrm{F}_{7/2}$ quantum defects from Table 6.2, the expected positions of particular $n\mathrm{F}_{7/2} \rightarrow n$G microwave transitions were calculated. For example, the $56\mathrm{F}_{7/2} \rightarrow$57G transition is predicted to be 36.96 GHz.

7.3.1 Setup

A preliminary experiment was constructed using spare lab equipment in the microwave region of 17-40 GHz. A waveguide coupler was placed above the laser interaction region in the vapour cell, and a passive frequency doubler was used to obtain up to 40 GHz microwaves from a 20 GHz HP8341B tunable microwave synthesiser. Figure 7.2 shows the experimental setup. The optical arrangement used was identical to that in Figures 6.2 and 5.3, with all three lasers comb-locked to excite to the $56\mathrm{F}_{7/2}$ Rydberg state.

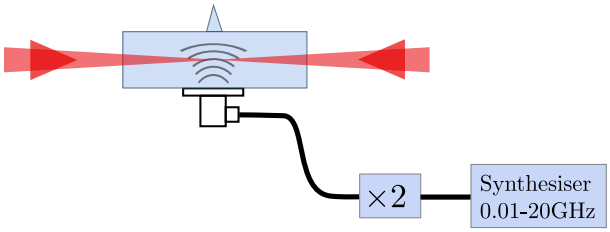

Figure 7.2: A schematic of the preliminary setup for exciting four-photon transitions. The synthesiser, frequency doubler and vapour cell are shown.

7.3.2 First swept scans

The microwave frequency was swept about 18.5 GHz and the LIA output was monitored on an oscilloscope to look for a change in the first step absorption through the cell. The LIA was referenced to a chopper in the third step laser path, and set to a time constant of 100 μs. In the vicinity of the expected transition frequency, a double-peaked feature was observed, see Figure 7.3. The widths of the peaks are both 300 MHz and the positions are 37.17(2) GHz and 38.19(3) GHz. The positions and separations of these peaks

approximately correspond to the expected positions of the $56F_{7/2}$ →57G/55G transitions at 36.96/38.04 GHz respectively. The optical excitation is Doppler-free along the axis of the cell and the Doppler broadening of the fourth step microwave excitation (which occurs perpendicular to this axis) is expected to be negligible; the broad linewidths are expected to originate from power broadening.

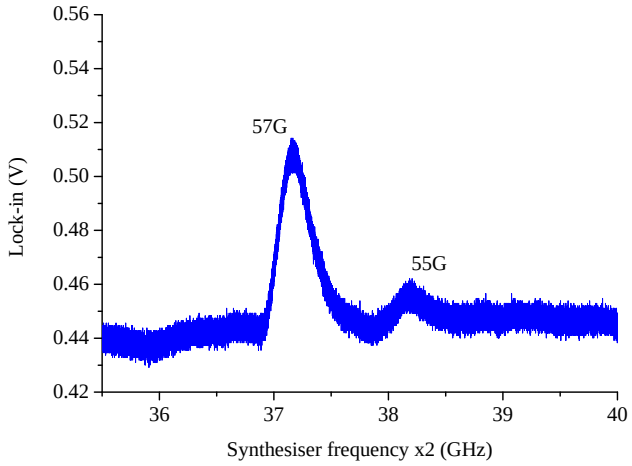

Figure 7.3: An oscilloscope scan over the $56F_{7/2}$ →57G and $56F_{7/2}$ →55G microwave transitions. A microwave synthesiser power of 6.5 dBm was used and a scan time of 5 s.

It is not surprising that the transition to the less energetic 55G state is also detectable in this scheme. The upwards and downwards transitions will behave almost identically, as the rates of stimulated emission and absorption from the $56F_{7/2}$ state will be similar. The two signals are different sizes because decay can occur from the more energetic 57G level back to the $56F_{7/2}$ level for a further cycle; this cannot occur for the less energetic 55G level.

7.3.3 Slow software stepped scans

The frequency axis of Figure 7.3 is only calibrated against a sweep voltage of the synthesiser, and is therefore not reliable for making high precision frequency measurements of the peak positions. To solve this, a stepped software-based scan scheme was constructed, allowing slow precision scans of the microwave synthesiser using a LabVIEW interface. LIA readings were collected through the same software via GPIB.

The slow scans expose much more of the fine spectroscopic detail, due to the use of longer scan times and longer LIA time constants. Figure 7.4 shows a broad scan over the $56F_{7/2} \rightarrow 55G/57G$ transitions, and is analogous to Figure 7.3. It is clear that there are other transitions visible at 36.53(1) GHz and 38.54(1) GHz, with much narrower linewidths of ∼2 MHz. These are in excellent agreement with the expected 56F→57F/55F transitions at 36.518 GHz/38.528 GHz respectively (calculated from the paramaters in Table 6.2). These may be two-photon transitions driven by microwaves at the fundamental synthesiser frequency, which leak through the passive frequency doubler.

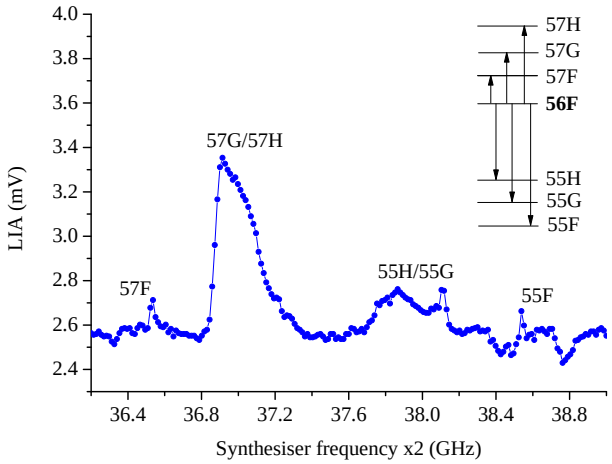

Figure 7.4: A slow stepped scan of the synthesiser across the region of the $56F_{7/2} \rightarrow 57G$ microwave transition. The microwave power was 7 dBm. The scan was completed in 200 s and the LIA time constant was set at 300 ms. There is a large amount of spectroscopic detail, which can be explained by several different one and two-photon transitions (see inset).

In the centre of the scan is a complex collection of spectral features, which lie close to the expected 55G/57G levels; this paints a more detailed picture of Figure 7.3. As well as two-photon transitions to the 57F/55F levels, one also expects two-photon transitions to the 55H and 57H levels. The nH levels are expected to be above the nG levels, with the nG-nH separations being smaller than the nG-nF separations (65). These central features therefore, may be an amalgamation of the transitions to the 55G, 57G, 55H and 57H levels, subject to additional broadening from external fields. This is depicted in the inset of Figure 7.4.

7.4 Precision measurements

7.4.1 A modified setup

To reduce the effects of external magnetic fields, the three layered μ-metal shield used in Section 6.5.2 was placed around the vapour cell. This required a different method for coupling the microwaves into the cell, and for this purpose a simple open loop antenna was chosen. The antenna was placed at the opening of the shield, clear of the laser beams, see Figure 7.5.

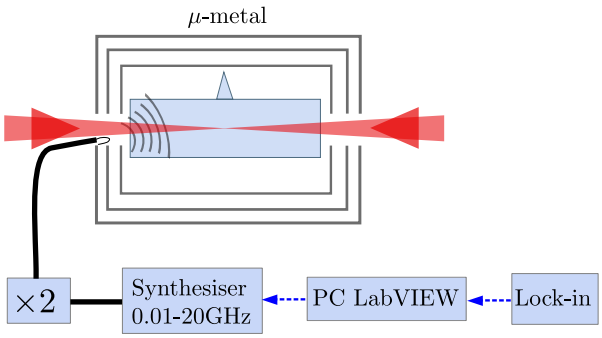

Figure 7.5: The new shielded cell setup uses a loop antenna to couple microwaves into the μ-metal shield and into the vapour cell. The synthesiser can now be stepped by precision intervals using a LabVIEW interface, as introduced in Section 7.3.3.

This simple method was very successful. The microwave coupling from the antenna into the laser excitation region is much more efficient compared to the waveguide coupler, and the nG signals therefore have a much higher SNR with this technique. Also, using the shielding results in narrow, symmetric peaks, when scanning over the $n\mathrm{F}_{7/2} \rightarrow n\mathrm{G}$ transitions. The broad line shapes seen in Figure 7.4 are eliminated. Figures 7.6 and 7.7 show stepped scans over the $56\mathrm{F}_{7/2} \rightarrow 57\mathrm{G}$ and $56\mathrm{F}_{7/2} \rightarrow 55\mathrm{G}$ transitions respectively, using this modified setup. The microwave power broadens the peaks by approximately 0.2 MHz/dBm; the microwave power was adjusted to achieve linewidths of around 4-7 MHz. As Doppler broadening will be negligible, the Gaussian component of the lineshapes is expected to originate from transit-time broadening.

7.4.2 Measurement of nG states

Using these scans, the frequencies of three $n\mathrm{F}_{7/2} \rightarrow n\mathrm{G}$ transitions were determined, see Table 7.1. The random error was estimated by taking eight repeated measurements of

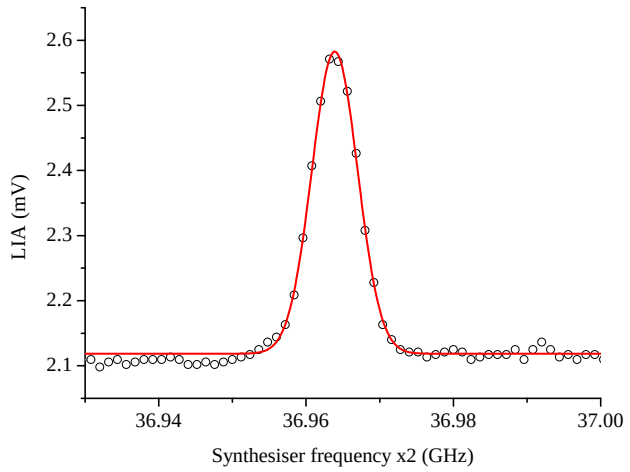

Figure 7.6: A precision scan over the $56F_{7/2} \rightarrow 57G$ microwave transition with 2 dBm of microwave power. The peak centre can be determined with high precision by fitting a Voigt profile. The peak has a FWHM of 7 MHz.

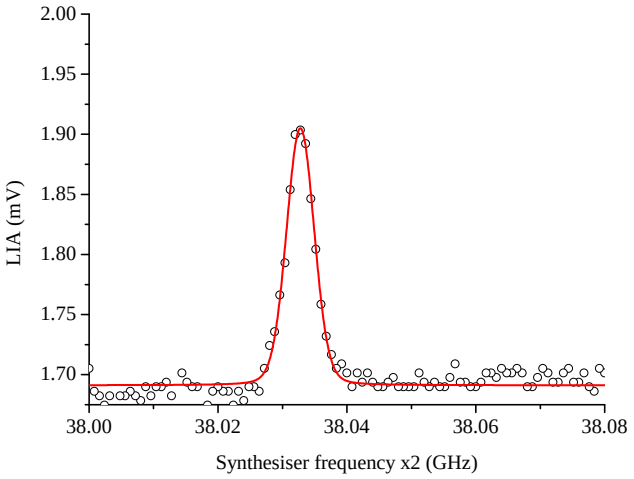

Figure 7.7: A precision scan over the $56F_{7/2} \rightarrow 55G$ microwave transition with 6 dBm of microwave power. The peak centre can be determined with high precision by fitting a Voigt profile. The peak has a FWHM of 5 MHz.

the $60F_{7/2} \rightarrow 61G$ transition; a standard deviation of 120 kHz was found. The absolute frequencies of these nG states relative to the ground state are deduced by adding the

Table 7.1: Fourth step frequencies, total absolute frequencies relative to the centre of mass of the ground states and quantum defects for a set of nG states in ^{85}Rb. Errors are estimated from the error analysis of the $n\mathrm{F}_{7/2}$ states in Section 6.8.

Transition	f_{45} (GHz)	E_n (MHz)	$\delta(n)$
$56\mathrm{F}_{7/2} \rightarrow 55\mathrm{G}$	38.0339(9)	1008937021.2(9)	$\delta_{55\mathrm{G}}$=0.00401(2)
$56\mathrm{F}_{7/2} \rightarrow 57\mathrm{G}$	36.9617(9)	1009012016.8(9)	$\delta_{57\mathrm{G}}$=0.00402(3)
$60\mathrm{F}_{7/2} \rightarrow 61\mathrm{G}$	30.1025(9)	1009140484.1(9)	$\delta_{61\mathrm{G}}$=0.00404(3)

frequencies of the initial $n\mathrm{F}_{7/2}$ states computed from Table 6.2. The quantum defects are derived using Equation 2.4 and the value of E_i from Table 6.2.

7.4.3 Observation and measurement of nH states

For broader scans over the $60\mathrm{F}_{7/2} \rightarrow 61\mathrm{G}$ transition, and with larger microwave powers, it was noticed that a peak was observable approximately 74 MHz higher in frequency. This feature is expected to be the 61H state, see Figure 7.8.

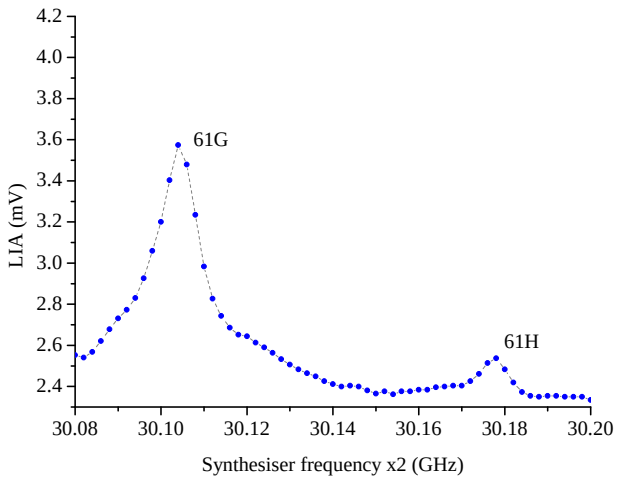

Figure 7.8: Observation of the 61H state, found 74 MHz above the $60\mathrm{F}_{7/2} \rightarrow 61\mathrm{G}$ microwave transition. A grey line is drawn to aid the eye.

Note that this transition is dipole-forbidden from the $60\mathrm{F}_{7/2}$ level, so one expects it to be a two-photon transition driven by the fundamental synthesiser frequency. Interestingly, the signal was only visible when using the frequency doubler, which rules out this

possibility and implies that the transition is one-photon and either electric-quadrupole in nature (E2, $\Delta\ell = \pm 2$) or the result of the 61H state obtaining some 61G character from a small stray electric field within the cell. Electric-quadrupole transitions in Rb have been studied recently using laser spectroscopy of atoms prepared in a MOT (134). However in this experiment, based on the microwave wavelength and the size of an $n = 60$ atom, it can be shown that such a $60F_{7/2} \rightarrow 61H$ transition would be $\sim 10^8\times$ weaker than the $60F_{7/2} \rightarrow 61G$ transition. Therefore, this concludes that there is a small stray electric field within the cell. The previous observation of nF$\rightarrow$ nF excitations in Figure 7.4 is expected to also be a result of this stray field. These fields will be considered in Section 7.5.

Eight repeated measurements of this $60F_{7/2} \rightarrow 61H$ transition were made with a standard deviation of 200 kHz. From this, a quantum defect can be extracted for the 61H state in the same manner as Section 7.4.2. This result is shown in Table 7.2. From the

Table 7.2: Fourth step frequencies, total absolute frequencies relative to the centre of mass of the ground states and quantum defects of a set of nH states in ^{85}Rb. Errors are estimated from the error analysis of the nF$_{7/2}$ states in Section 6.8.

Transition	f_{45} (GHz)	E_n (MHz)	$\delta(n)$
$56F_{7/2} \rightarrow 57H$	37.052(2)	1009012107(2)	δ_{57H}=0.00149(6)
$60F_{7/2} \rightarrow 61H$	30.1744(15)	1009140556.0(1.5)	δ_{61H}=0.00156(5)

quantum defect of the 61H state, the position of the $56F_{7/2} \rightarrow 57H$ transition is predicted to be 37.049 GHz using Equation 2.1. As a check, the three laser steps were locked to excite the $56F_{7/2}$ state and a microwave scan was carried out around this region. A peak was successfully found at 37.052 GHz, in excellent agreement with the prediction. This is strong evidence that these are nH states as they follow a simple Rydberg-Ritz relationship with a fixed quantum defect.

7.5 Stray fields

7.5.1 Calculating the size of stray fields

The observation of the 61H state gives a useful method for measuring the size of any stray electric fields within the vapour cell. If the perturbed 61H state is labelled as the 61H$'$ state, the excitation rates of the 61G and 61H$'$ transitions in Figure 7.8 are proportional to

the squares of the Rabi frequencies $\Omega_{60\mathrm{F}-61\mathrm{G}}$ and $\Omega_{60\mathrm{F}-61\mathrm{H}'}$. Using perturbation theory, one can then show that the ratio between these Rabi frequencies is given by

$$\frac{\Omega_{60\mathrm{F}-61\mathrm{H}'}}{\Omega_{60F-61G}} = \frac{\mathrm{E}}{\Delta E_{61\mathrm{G}-61\mathrm{H}}} \langle 61\mathrm{G}|r|61\mathrm{H}\rangle \,, \tag{7.2}$$

where E is the stray electric field, $\Delta E_{61\mathrm{G}-61\mathrm{H}}$ is the energy difference between the 61G and 61H states and $\langle 61\mathrm{G}|r|61\mathrm{H}\rangle$ is the dipole matrix element between these two states. Using Equation 7.2, along with the data in Figure 7.8, an approximate value of E=3(1) mVcm^{-1} can be deduced for the magnitude of the stray field. The uncertainty is introduced from the uncertainty in $\Delta E_{61\mathrm{G}-61\mathrm{H}}$.

7.5.2 DC-Stark shifts associated with stray fields

An electric field of 3 mVcm^{-1} would lead to negative Stark shifts of the observed nG states by a few megahertz, with the 61G state being the most sensitive in this study, having an expected frequency shift of -4 MHz. The nG shift is dominated by coupling with the nearby nH state of equal n. The observed 61H$'$ state will also be shifted from the unperturbed 61H state, and in this case the Stark shift will be dominated by coupling with the near-lying 61I state. However, without any knowledge of $\Delta E_{61\mathrm{H}-61\mathrm{I}}$, the shift can not be deduced. The nH frequency measurements can therefore only be taken as preliminary measurements until further studies are completed.

With knowledge of the size of potential stray electric fields within the cell, it is also interesting to return to the measurements made in Chapter 6 and consider what effect such fields would have on the values in Table 6.2. Hypothetical DC-Stark shifts, caused by a stray field of 3 mVcm^{-1}, were added to a set of $n\mathrm{F}_{7/2}$ and $n\mathrm{P}_{3/2}$ model frequencies, representing those from Table 6.1. The effect of these shifts on the fitted values of E_i, δ_0 and a were then considered. It was found that for the $n\mathrm{F}_{7/2}$ series of states, such a stray field could cause an error of 1.5 MHz on the value for E_i, and errors of 3×10^{-5} and 0.02 on δ_0 and a respectively. As expected, for the $n\mathrm{P}_{3/2}$ series of states the effects are much smaller, with a predicted error of 60 kHz on E_i, and errors of 1×10^{-6} and 1×10^{-5} on δ_0 and a respectively. Therefore the value of E_i extracted from the $n\mathrm{P}_{3/2}$ series, after accounting for stray fields, is expected to be well within the current estimated error budget of 297 kHz. Interestingly, Table 6.2 displays consistency of the E_i values from both the $n\mathrm{F}_{7/2}$ and $n\mathrm{P}_{3/2}$ series which suggests that internal stray fields were smaller than 3 mVcm^{-1} during the time of this data taking.

7.6 Discussion

7.6.1 Summary

Table 7.3 displays the values for the quantum defects extracted from this work and other previous measurements from the literature (66; 81). The defects are averaged over the states which were measured and the n dependence is not considered. Stark shifts from stray fields have been included when formulating the final error on the nG quantum defect, whilst the preliminary value for $\delta_{n\mathrm{H}}$ includes an estimated error based on the FWHM of the observed nH signals.

Table 7.3: Comparison of quantum defects for the nG and nH series in ^{85}Rb, n dependence is not considered.

Source	$\delta_{n\mathrm{G}}$	$\delta_{n\mathrm{H}}$
This work	0.00402(8)	0.0015(2)
(66) Afrousheh	0.00405(6)	-
(81) Han	0.00400(9)	-

The nG defect agrees with the best known measurements from the literature (66; 81) within error, and is comparable in accuracy to that from the work of Han *et al* (81). This is satisfying as each of these numbers has been measured using a completely different spectroscopic technique. The nH defect can only be treated as a pilot measurement, however to the best of my knowledge this is the first study involving nH states in ^{85}Rb. A more thorough study of systematic shifts from electric fields will be required before making a final measurement in the future.

7.6.2 The $^{85}Rb^{+}$ core polarisability

The inversion of the fine structure for the nF states in Rb indicates that these are the highest angular momentum states to exhibit core penetration (65). For such states, the quantum defect is purely a result of the interaction between the core electrons and the Rydberg electron (71). Therefore, by measuring the quantum defects for the nG and nH series, one can learn more about the Rb core polarisability and structure. For such high ℓ electron states, the quantum defect can be expressed using a core polarisation model [1]

$$\delta_{n\ell} n^{-3} = \frac{\alpha_d}{2} \left\langle r_{n\ell}^{-4} \right\rangle + \frac{\alpha_q}{2} \left\langle r_{n\ell}^{-6} \right\rangle , \tag{7.3}$$

[1] Equations 7.3 and 7.4 are in atomic units.

where α_d and α_q are the dipole and quadrupole polarisabilities of the core respectively (65). The other terms are expectation values of the Rydberg-electron wavefunction. With some rearrangement, a linear equation can be formulated

$$\frac{2\delta_{n\ell}n^{-3}}{\langle r_{n\ell}^{-4}\rangle} = \alpha_d + \alpha_q \frac{\langle r_{n\ell}^{-6}\rangle}{\langle r_{n\ell}^{-4}\rangle}. \tag{7.4}$$

The expectation values both scale with n^{-3} and are easily calculated from expressions for hydrogenic wavefunctions in Reference (65). Figure 7.9 is a plot of $\delta_{n\ell}n^{-3}/\langle r_{n\ell}^{-4}\rangle$ vs. $\langle r_{n\ell}^{-6}\rangle / \langle r_{n\ell}^{-4}\rangle$ using the 61F, 61G and 61H quantum defects from the work in this thesis.

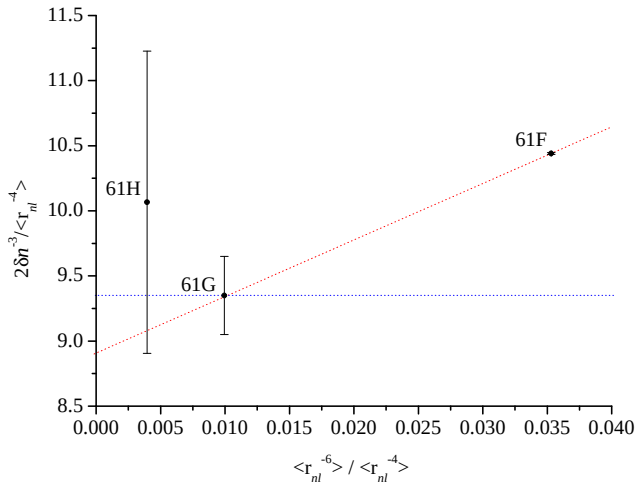

Figure 7.9: A plot of $\delta_{2n\ell}n^{-3}/\langle r_{n\ell}^{-4}\rangle$ vs. $\langle r_{n\ell}^{-6}\rangle / \langle r_{n\ell}^{-4}\rangle$ for n=61 states, based on the polarisation model of the quantum defect (71). The defect values are taken from the work in this thesis. The red dotted line is the case where the nF state is higher due to core polarisation effects only. The blue dotted line is a line of zero slope for the case where the 61F state is higher due to core penetration effects only.

Neglecting the preliminary 61H measurement for now, and following the same theme as Reference (81), Figure 7.9 can be used to put bounds on the core polarisabilities: The 61F state lies higher than the 61G state because of both core penetration and the contributions of α_q, which are both positive effects. Firstly, by considering the case where the 61F point is shifted up only by core penetration, one must have $\alpha_d = 9.4(3)a_0^3$ and $\alpha_q = 0$. Secondly, by considering the case where the 61F state experiences no core penetration and the point is shifted up only by α_q contributions, a line can be drawn through the 61F and 61G

points to get $\alpha_d = 8.9(4)a_0^3$ and $\alpha_q = 43(12)a_0^5$. Together, these two cases give bounds of $8.5a_0^3 < \alpha_d < 9.7a_0^3$ and $0 < \alpha_q < 55a_0^5$ for the $^{85}Rb^+$ core. These are in good agreement with recent theoretical computations of α_d (72) and older computations of α_q (135).

From Figure 7.9, notice that the nH point is also consistent with these bounds within the estimated error bar. Importantly, the nG and nH states are the two which are known to not exhibit any core penetration and should follow the polarisation model. A straight line described by Equation 7.4, with a positive ($\alpha_q \neq 0$) or zero ($\alpha_q = 0$) gradient, should pass through the 61G and 61H points. Therefore, with <1 MHz accuracy measurements of nH states in the future, actual values for α_d and α_q of $^{85}Rb^+$ could be extracted for the first time. It would then be possible to see by how much the nF states deviates from a polarisation model and therefore the degree of core penetration experienced by these states.

7.7 Conclusion

This chapter has demonstrated successful spectroscopy of nG Rb Rydberg states in a room temperature vapour cell, with a four-photon scheme. The precision measurements have given a new value of the quantum defect of the nG series, which agrees well with previous measurements (66; 81). The observation of transitions to Stark-induced nH states is also promising and has proven to be a useful method for determining the size of stray electric fields within the vapour cell. To the best of my knowledge, this is the first study of nH levels in Rb. If systematic errors on the nH level measurements can be understood and controlled at the 1 MHz level, precise values of the Rb^+ dipole and quadrupole polarisabilities could be obtained for the first time.

Chapter 8

Rydberg spectroscopy in a vapour cell: Future directions

The previous chapters have investigated the principles of high precision Rydberg spectroscopy with a vapour cell sample, and many successful measurements have been demonstrated. This is an elegant method for studying Rydberg atoms, with a simple setup. However, throughout this research a number of interesting observations have been made which will require further study to be properly explained. Some of these observations show potential new directions to take the research in the future. This chapter attempts to summarise these observations and also discuss some of the future areas of research inspired by them, for the cell-based Rydberg spectroscopy. The investigations discussed in this chapter were carried out using the same experimental setup as that used in Chapter 6. All data presented in this chapter was recorded and analysed by myself.

8.1 Electric fields

8.1.1 Transient response

Introduction

More can be learnt about the free-charges within the cell by studying the response of a Rydberg signal to a step-change in applied electric field (54). To carry out this study, the $60F_{7/2}$ Rydberg signal was observed with a real-time oscilloscope scan, similar to that in Figure 4.25. The behaviour was then monitored when switching on and off a large electric field, by switching a 200 V potential across the cell. After switching on the field, the signal is diminished as the field penetrates into the interaction region and DC-Stark shifts the

state far from the laser scan range. After a characteristic relaxation time, the signal then returns after the free-charges have rearranged to screen the interaction region. Careful observation also shows that the signal returns from *lower* frequency after the relaxation time, increasing in size, until finally reaching the original position in the centre of the scan. The direction of the shift is consistent with a DC-Stark shift. Identical behaviour was also found when the field is switched off.

In Reference (54), transient times of a few hundred microseconds were observed in a similar EIT-based Rydberg cell experiment. However, in this work the transient times are found to be several seconds; it is even possible to observe the returning signal in a real-time scan with the naked eye. To study this in greater detail, the Rydberg signal size was monitored during a transient. All three laser steps were comb-locked on resonance, with the third step locked at the top of the $60F_{7/2}$ Rydberg signal. The LIA output was monitored as the field was switched and the time constant was set to 100 ms. Figure 8.1 shows a typical switch-on/switch-off trace; the signal is absent for almost 10 s.

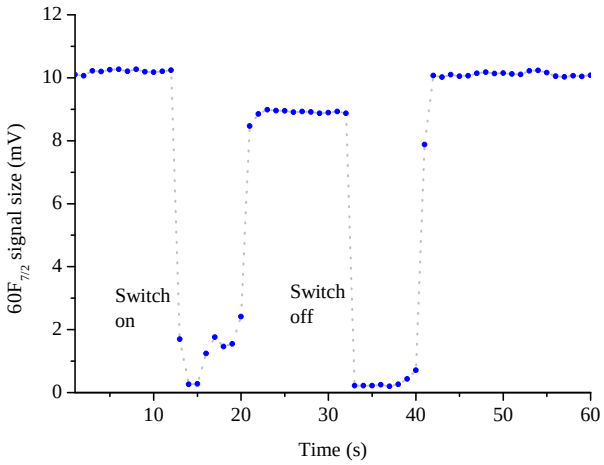

Figure 8.1: Typical transient behaviour of the $60F_{7/2}$ Rydberg signal. A potential of 40 V was applied over the cell and then subsequently switched off. The grey line is drawn only to aid the eye.

Effect of field strength and laser powers

In a similar manner to Reference (54), these transient times were studied to see how they were affected by laser power and field strength. Figure 8.2 shows a linear relation (red

line) between the transient time and the switch-on voltage. Figures 8.3 and 8.4 show approximate exponential relations (red lines) between the transient time and the laser power for all of the three laser steps. Notice that the transient time can be up to three minutes long when very weak laser power is applied.

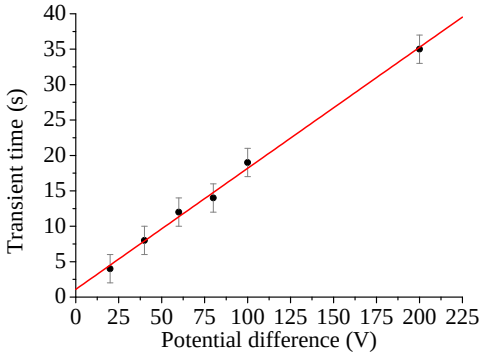

Figure 8.2: The relation between transient time and different switch-on voltages. The potential was switched from 0 V to the quoted value.

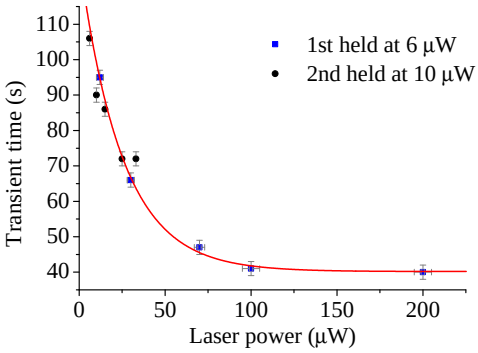

Figure 8.3: The relation between transient time and the first and second step laser powers. The third step laser power was held at 1.1 mW. The potential was switched from 0 V to 200 V in all cases.

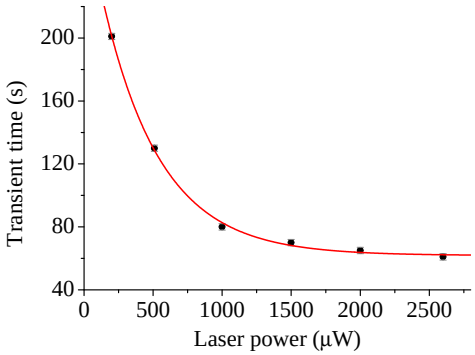

Figure 8.4: The relation between transient time and the third step laser power. The first and second step laser powers were held at 6 μW and 10 μW respectively. The potential was switched from 0 V to 200 V in all cases.

8.1.2 Response to white light

During this research, it was also discovered that the Rydberg signals detected in the cell are sensitive to white light, an effect which has not been noticed in previous papers. This sensitivity is largest for the high $n\mathrm{F}_{7/2}$ states, where the application of torch light from a distance of over 1 m can extinguish the Rydberg signal completely. The plots in Figure 8.5 show real-time traces of the $60\mathrm{F}_{7/2}$ Rydberg signal as light of increasing brightness is applied to the vapour cell.

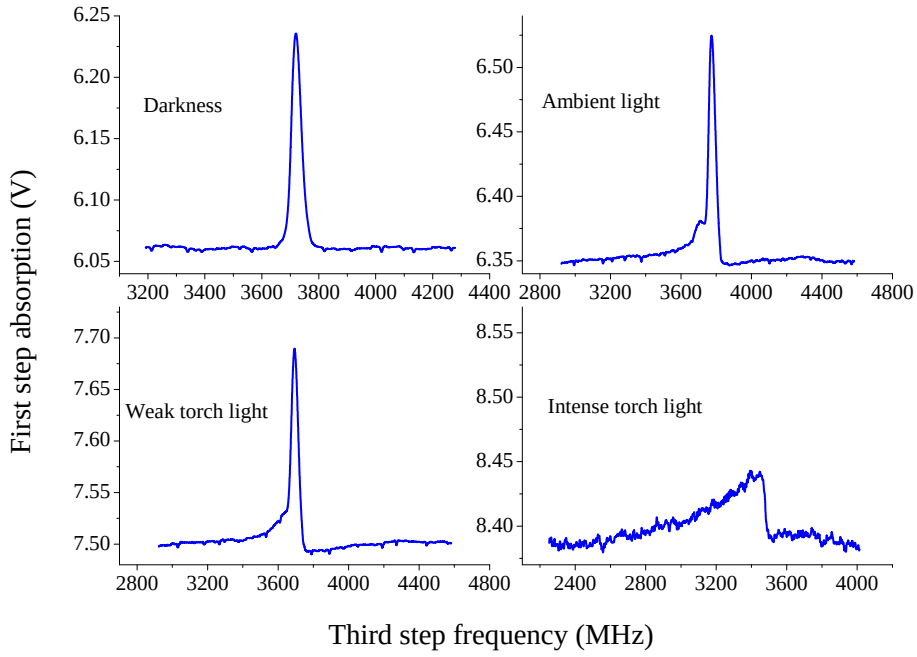

Figure 8.5: Real-time third step laser scans over the $60\mathrm{F}_{7/2}$ Rydberg level. The vapour cell was exposed to four different levels of white light. The frequency axis was calibrated with a Fabry Pérot etalon, the voltage scales are AC-coupled.

This effect is closely related to the DC-Stark shift findings. Firstly, the signal moves in the same direction and follows a similar line shape to the case of a transient electric field, consistent with a DC-Stark shift. Secondly, it is the $n\mathrm{F}_{7/2}$ states with largest n which are most affected. Another significant link between the two effects is that the application of white light can affect the transient response. Transient times were compared for a non-illuminated cell and a cell illuminated at one end with a torch, with all other experimental

parameters left identical. The transient times were reduced by more than a half for the illuminated cell and the signal could even be forced to return rapidly with the application of intense light.

8.1.3 Possible explanations

Screening

A simple calculation estimates that $\sim 10^8$ free electrons or Rb^+ ions would be required to shield a 200 V potential across the field plates. As already stated in Reference (54), there appears to be mobile charges within the cell which can re-distribute to cancel any externally applied electric field.

It has been found by Bouchiat *et al* (136) that glass can become electrically conductive when exposed to alkali vapour. It is possible for a substantial amount of the alkali to be absorbed inside the glass. The conductivity then arises from the gas of free electrons that are present in this film of absorbed alkali. Alternatively, in the situation where the alkali atoms are spread more sparsely over the glass, conductivity can still be achieved if the atoms become ionised, supplying electrons which can hop between different ions trapped on the surface (136). The long transient times seen in this work suggest the latter case, because in the former case transients would be similar to the transit-time of an electron across the cell, which is ~ 10 μs (54).

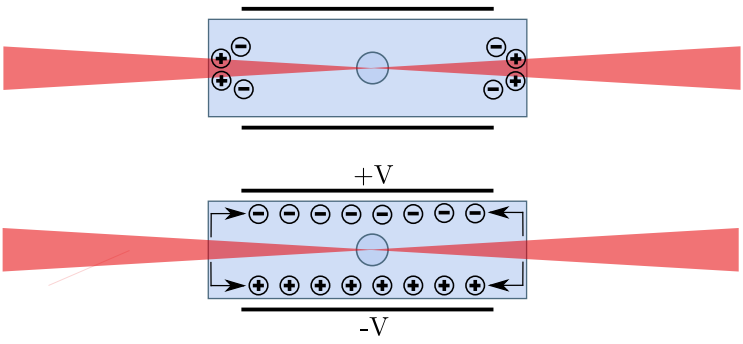

Figure 8.6: The shielding of the interaction region in the vapour cell. The top figure is the case where no field is applied and charge ejection reaches an equilibrium situation. The lower figure is the case where there is an applied field and the ejected charges move to cancel the field.

In this work, when light with an energy above the Rb work function is incident on the glass one expects Rb atoms trapped on the surface to be photo-ionised. This is

discussed in the more recent paper by Bason *et al* (137). One can therefore picture the screening mechanism as follows: With no applied electric field, Rb atoms trapped over the cell windows eject electrons due to photo-ionisation by the laser beams. These electrons recombine with positive ions at some steady rate. With an applied field, after ejection, these electrons begin to move about the cell surface to cancel the external field. Finally after some period of time, enough electrons have been ejected to cancel the field completely, giving rise to a characteristic transient time. Figure 8.6 depicts these two situations. More laser power results in a higher rate of charge ejection and therefore the field can be cancelled in a shorter time period.

The photoelectric work function of Rb is 2.1 eV, equivalent to ∼600 nm (138). Therefore in Reference (54), where the two-step EIT scheme is used and a 200 mW 480 nm laser is applied as the pump beam, it is understandable that the main source of charge ejection is from photo-ionisation. In contrast, in this experiment all the lasers are in the NIR and below the work function, therefore the origin of the free charges is not as obvious. This appears to have a very large effect on the observable transient times between the two systems, which differ by four orders of magnitude. However, the observed dependence of the transient time with laser power in this work (see Figures 8.3 and 8.4) still indicates that photo-ionisation is causing some of the charge ejection. This may be explainable because the ionisation energy for an absorbed alkali atom can be considerably lowered compared to free alkali atoms (136).

Source of charge: Rydberg atoms

Interestingly, Figures 8.3 and 8.4 share similarities with the saturation curves of the Rydberg signal amplitude, seen in Figures 6.17 and 6.19. This suggests that the transient time may be linked with the creation rate of Rydberg atoms, implying that perhaps collisional- or photo-ionisation (65) of the Rydberg atoms themselves is the dominant source of free-charge in this scheme. A simple test was carried out to disprove this idea: The third step laser was tuned off resonance to halt the creation of Rydberg atoms. The applied potential was then switched from 0 V to 200 V and after the expected 'on-resonance' transient time of 64 s, the third step laser was tuned back on resonance. There was zero time delay before the Rydberg signal returned, implying that the charge creation is a non-resonant effect, at least for the third laser. Interestingly carrying out the same test, but detuning the first or second step lasers, resulted in a 20 s additional delay, indicating that the screening is

related in some way to the creation rate of $5D_{5/2}$ atoms. This could be an indirect effect of the 420 nm fluorescence from these atoms, which is above the work function.

Source of charge: Other

To check for other possible sources of charge, not related to applied light, a second test was carried out: The cell was blocked from both laser and ambient light and the applied potential was switched from 0 V to 200 V. After the expected 'on-resonance' transient time of 95 s, the cell was unblocked. The delay before the signal returned was approximately 20 s, as opposed to 95 s. This result suggests that although applied light speeds up the screening process, there is a process which ejects charge and allows screening of an unilluminated cell. This other process could be thermionic emission of the Rb atoms trapped over the cell surface (136), due to room temperature.

White light

The application of white light could affect the Rydberg atoms in several ways. One expects them to suffer some amount of photo-ionisation, plus the levels will experience an AC-Stark shift (65). However, what appears most likely from the observations so far, is that white light changes the level of charge ejection from the cell walls. Applying white light to one end of the vapour cell would result in two things: More free-charge ejected from the cell surface, resulting in lower transient times. Also, more positive ions on one end of the cell than the other and therefore an asymmetric charge distribution on the inside windows, resulting in a DC-Stark shift of the Rydberg levels. Both of these effects are observed experimentally.

Residual stray fields

Although the free charges act to cancel externally applied electric fields, there is also the possibility of a residual electric field originating from inside the cell. Such a field was found in Chapter 7 and measured to be approximately 3 mVcm^{-1}. For example, a residual field would exist if there was an imbalance of positive charge between the cell windows, which is an effect that has been confirmed by Mohapatra *et al* (54). Interestingly, it has also been seen in Reference (137) that free charges inside the cell tend to equalise any residual electric field across the interaction region.

8.1.4 Future work

It is important to have a thorough understanding of the screening effect, especially when optical Rydberg spectroscopy in a vapour cell is to be used for precision measurements. The following future areas of study will be invaluable in achieving a deeper understanding:

- The effect of controlled light intensities, at controlled wavelengths and in controlled geometries
- The n and ℓ scaling of the transient times and white light sensitivity
- The response to AC-electric fields and study of the electron dynamics
- The effect of temperature on the transient times: At higher temperatures one expects less Rb on the cell walls and also more thermionic emission
- The minimisation of stray residual fields inside the cell by changing cell temperature and/or adjusting the cell position relative to the laser beam waists. The nH signal size (see Chapter 7) can be used as a meter for this minimisation
- The white light can be used as a modulation technique. For example, one could use a periodically flashing LED by the side of the cell, referenced to a LIA, to learn more about the frequency response

8.2 n>100 Rydberg states

The precision measurements made in Chapter 6 were for $n \leq 63$ Rydberg states and the results in Table 6.2 demonstrate that possible systematic shifts that scale with n are well understood. This is because of both the high symmetry of the n=60 Rydberg signals and also the excellent agreement of the quantum defect parameters with those from microwave spectroscopy (80; 81). Nevertheless, one expects that at some higher value of n, the atomic radius will approach the mean atomic spacing of the Rydberg atoms in the laser excitation volume. At this point there will be measurable shifts and broadenings of the levels due to Rydberg-Rydberg interactions (127). Unfortunately, higher n states also couple less strongly to the third step laser and are therefore harder to observe. Even so, in this work measurable signals were detectable up to the $130F_{7/2}$ and $150P_{3/2}$ states using the setup described in Section 6.2. The comb parameters required to excite these states can be found in Appendix B.

8.2.1 Observations

With higher n there were three observations made: The peaks become broader, asymmetric and the positions of the states can no longer be predicted with a high degree of accuracy using the defect parameters in Table 6.2 (which were derived from n=33-63 states). Figure 8.7 displays comb-stabilised laser scans over different $5D_{5/2}, F = 5 \rightarrow nF_{7/2}$ Rydberg tran-

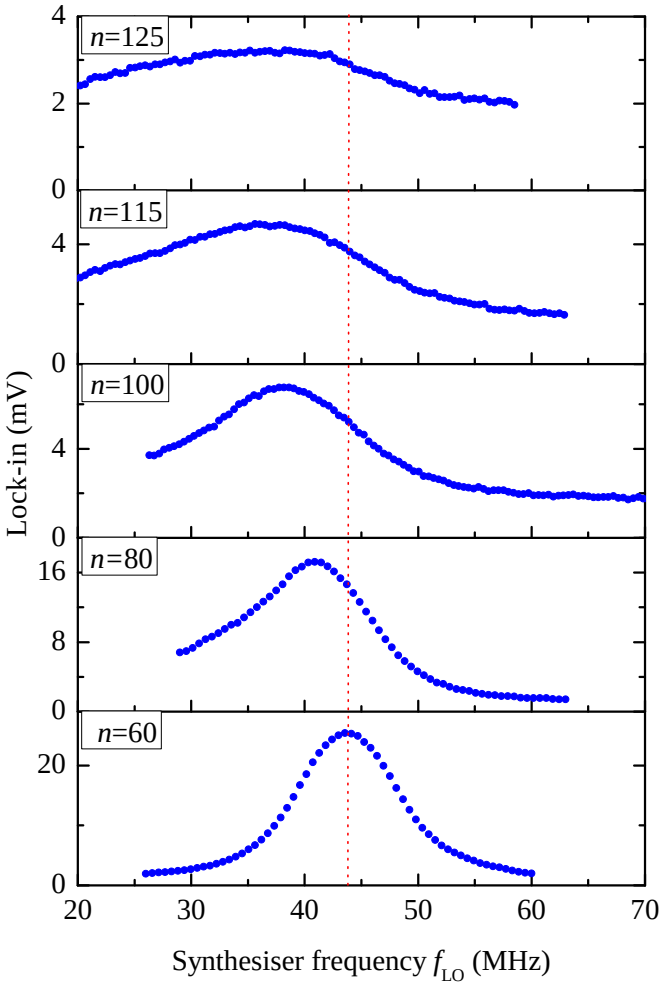

Figure 8.7: Third step comb-stabilised laser scans over $5D_{5/2}, F = 5 \rightarrow nF_{7/2}$ Rydberg transitions with high n. For clarity, the beat signs have all been normalised to the positive case. The red dotted line indicates the expected position of the state, as predicted by the defect parameters in Table 6.2. There is a gradual deviation with $\sim n^4$.

sitions, with increasing n. In all cases the centre is pulled to *lower* frequencies than that predicted. The frequency shift and FWHM of the signals appear to follow an approximate n^4 scaling.

The $n\mathrm{P}_{3/2}$ levels were also found to follow the same behaviour but were generally less sensitive. For example, the $90\mathrm{P}_{3/2}$ state was found to be shifted down by only ~1 MHz and had a comparable width and symmetry to the previous measurements at n ~60. If these shifts are from a residual electric field, one would expect a significantly higher n^7 scaling. This suggests that the effect may be from a different process, such as Rydberg-Rydberg interactions (127). Such shifts and broadenings have been considered before by Stoicheff *et al* for significantly higher ground state densities of 10^{13} cm^{-3} and lower principal quantum numbers of n ~70 (139).

8.2.2 Rydberg-Rydberg interactions

Principle

The dominant form of interaction between two Rydberg atoms in states nL (assuming no overlap of the two), is a standard electrostatic interaction between two electric dipoles, separated by distance R (127). If the two Rydberg atoms are in the two-atom state $|n\mathrm{L}, n\mathrm{L}\rangle$ with energy E, the interaction between the atoms will be affected by other two-atom states $|n_A\mathrm{L}_A, n_B\mathrm{L}_B\rangle$ nearby in energy (the energy defect is $\delta_E = E_A + E_B - 2E$). The Rydberg-Rydberg energy shift is described from Reference (127) by the equation

$$\Delta = \frac{\delta_E}{2} - \mathrm{sign}(\delta_E)\sqrt{\frac{\delta_E^2}{4} + \frac{C^2 D_\phi}{R^6}}, \tag{8.1}$$

where $C = e^2 \langle\psi|r|\psi_A\rangle \langle\psi|r|\psi_B\rangle$ and D_ϕ is usually between 0 and 1. This factor describes the relative strengths for different collision channels and Zeeman subslevels (140). Throughout this work, D_ϕ will be taken as 1 to predict a maximum shift.

Importantly, the shift changes nature at a characteristic crossover distance $R_c^3 = CD_\phi^{1/2}/\delta_E$. For $R \gg R_c$ it behaves as an non-resonant van der Waals interaction and for $R \ll R_c$ it behaves as a resonant dipole-dipole interaction. The two forms are

$$R \gg R_c \qquad \Delta \approx -\frac{C^2 D_\phi}{\delta_E R^6}, \tag{8.2}$$

$$R \ll R_c \qquad \Delta \approx -\mathrm{sign}(\delta_E)\frac{CD_\phi^{1/2}}{R^3}. \tag{8.3}$$

From this one can conclude that the van der Waals interaction scales as n^{11}/R^6 and the dipole-dipole interaction scales as n^4/R^3. For this reason, the interaction between two Rydberg atoms can be very strong due to the small values of δ_E and the large dipole moments with neighbouring levels. Higher ℓ states are also expected to suffer larger shifts; as the states become more hydrogenic, neighbouring states become closer in energy and wavefunction overlaps become larger. This is identical to the increased sensitivity to electric fields. These strong dipole-dipole interactions are one of the key ideas behind quantum information applications with Rydberg atoms, by using the concept of dipole blockade (141).

This work

Figure 8.8 shows a plot of the level shift for a pair of 50F, 100F and 150F atoms. By calculating the values of C for different nearby two-atom states, it was found that the interaction is dominated by coupling between the $|n\text{F},n\text{F}\rangle$ state and the nearest $|n\text{G},n\text{G}\rangle$ state, where δ_E=1.3 GHz, 165 MHz and 49 MHz for n=50, 100 and 150 respectively. All dipole moments were calculated using the method described in Section 2.2.3. The shifts

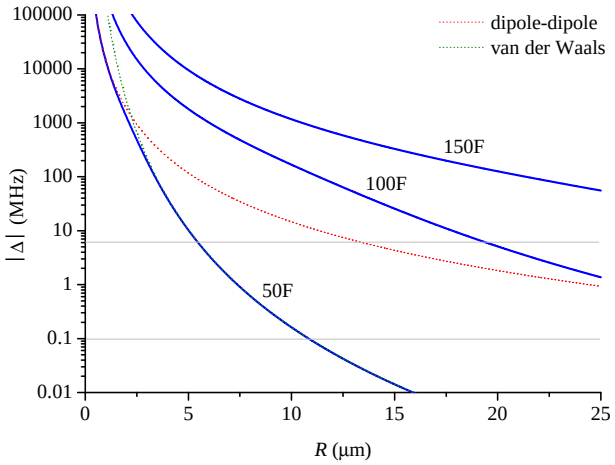

Figure 8.8: The Rydberg-Rydberg frequency shifts for a pair of 50F, 100F and 150F atoms. For the 50F case the red dotted line shows the resonant case, for $\delta_E = 0$ or $R \ll R_c$, and the green dotted line shows the off-resonance case for $\delta_E \neq 0$ or $R \gg R_c$. Horizontal lines indicate the ∼100 kHz accuracy of the apparatus in Chapter 6 and the 6 MHz shift of the 100F state which was observed in Figure 8.7.

are all to lower frequency, which is consistent with the data in Figure 8.7 and implies that enhancement is always from a more energetic two-atom state. Although an approximate n^4 scaling was observed for the broadening and shift, the experimental scaling is expected to be fairly complex. It will also be related to the Rydberg density (scaling with n^{-3}), the third step laser power (some function of wavelength) and the distance R_c (scaling with $n^{7/3}$).

In the room temperature vapour cell, the ground state number density is expected to be 7×10^9 cm^{-3}, calculated using Equation A.1. This results in a mean separation between ground state atoms of 3 μm. In comparison an n=150 Rydberg atom has a radius of 1 μm. Figures 8.7 and 8.8 indicate that the average Rydberg atom spacing in this experiment is $\sim$20 μm for the 100F$_{7/2}$ state, which implies that $\sim$0.1% of atoms in the interaction region are in Rydberg states, with a density of $\sim 10^7$ cm^{-3}. This agrees well with the observed signal size: The 100F$_{7/2}$ peak amplitude is 4 mV in size, which corresponds to 4×10^9 s^{-1} scattered 780 nm photons. Assuming a QA factor of $\sim$10 means that the Rydberg creation rate is 10^8 s^{-1}. If these Rydberg atoms leave the interaction region at a rate of 10^6 s^{-1} (given by the transit-time), in the steady state one expects around 100 Rydberg atoms in the interaction volume of 2×10^{-5} cm^3. This gives a density of $\sim 10^7$ cm^{-3}.

If all the Rydberg atoms in the excitation region were equally separated, and therefore equally affected, one would expect only a shift of the Rydberg signal. However, as the actual atom separations are spread around some statistical average, a broadening is expected as well as a shift.

8.2.3 Future work

There are a range of new experiments and investigations that could be carried out to understand these effects:

- Control the Rydberg atom density via the cell temperature and measure the density and n dependence of the shifts: Higher temperatures will increase the ground state density and allow larger Rydberg atom densities. This was originally studied in Section 4.4.3 with the wavemeter, although a more accurate study would be useful using the full accuracy of the comb
- Consider the D_ϕ coefficients in a more thorough modelling of shifts

- Study levels which have a $\delta_E = 0$ Förster resonance with neighbouring levels (127). From Figure 8.8 it can be seen that such levels should suffer much larger shifts due to resonant enhancement

8.3 Off-resonance excitation

In Chapter 6, the ∼8 MHz linewidth of the Rydberg signals was a limiting factor of the measurement accuracy. In particular, for the $n\mathrm{F}_{7/2}$ levels it was not possible to resolve the fine structure. A reduced linewidth could lead to much improved frequency measurements.

Unlike in optical EIT schemes, where linewidths of 1 MHz are readily achievable (54), in this experimental work all extremes of laser power were studied and the minimum achievable linewidth was 5 MHz. This is expected to be a result of the detection scheme relying on the population of the $5\mathrm{P}_{3/2}$ level. This state is easily power broadened and its 6 MHz FWHM means that all atoms in the $5\mathrm{P}_{3/2}$ level lie within atleast a ± 6 ms^{-1} velocity distribution. The model introduced in Section 2.3.3 shows that the second and third transitions can actually select much narrower velocity widths from this distribution because of their narrower natural widths. However, in a full picture of the system, one expects the coherence of the $5\mathrm{P}_{3/2} \rightarrow 5\mathrm{D}_{5/2}$ transition to in fact be damped by $5\mathrm{P}_{3/2}$ decay, limiting this transition's FWHM to 6 MHz. As a result all atoms in the $5\mathrm{D}_{5/2}$ level are expected to also lie in a ± 6 ms^{-1} velocity distribution. This equates to a residual Doppler limited width of 4 MHz for the Rydberg signals. When accounting for transit-time broadening and the laser linewidths, this is in good agreement with the limit of 5 MHz that was observed. Further contributions to this width could be from collisional broadening of the Rydberg levels (65) and/or a residual Doppler width due to focussing.

The typical natural linewidth for an n=60 Rydberg state is ∼3 kHz. Therefore, even if all other sources of broadening can be eliminated in this experiment, one expects to always be limited by the transit-time of ∼1 μs. One way of obtaining this transit-time limited linewidth is to use off-resonance excitations to the Rydberg levels. This would eliminate the problems from power broadening and the hyperfine structure of intermediate levels, making the excitation pathway unambiguous. Off-resonance multi-photon transitions can be very narrow because the signal linewidth is governed by the radiative lifetime of the final state (123). For example, the off-resonance three-photon transition $5\mathrm{S}_{1/2} \rightarrow 60\mathrm{F}_{7/2}$ would have a FWHM governed by the ∼10 μs lifetime of the $60\mathrm{F}_{7/2}$ state. Fortunately,

the new fully comb-stabilised laser system is ideally suited for off-resonance excitation schemes, where spectral features are not available for laser stabilisation.

8.3.1 $5S_{1/2} \rightarrow 5D_{5/2} \rightarrow 33F_{7/2}$ excitation

The simplest off-resonance solution is to eliminate the $5P_{3/2}$ level from the excitation path. This can be achieved by tuning the first step off-resonance and outside of the Doppler width of the $5S_{1/2} \rightarrow 5P_{3/2}$ transition, which was discussed in Section 2.3.5. This was attempted, and excellent resolution of the $5D_{5/2}$ hyperfine structure was observed using the two-step scheme, see Figure 8.9. The laser powers were 6 μW and 10 μW for the first and second

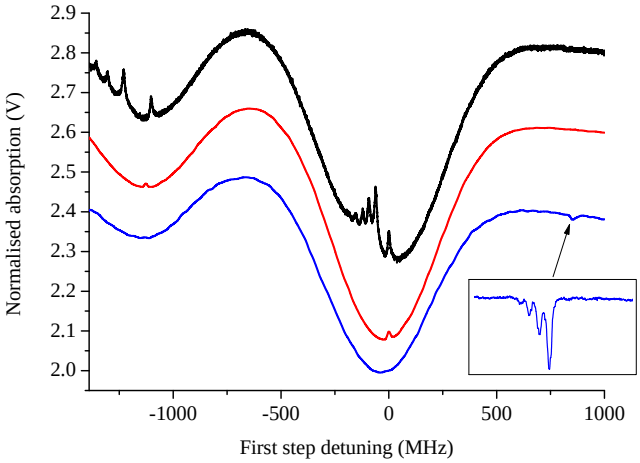

Figure 8.9: The first step laser absorption. The red line shows resonant step-wise $5S_{1/2} \rightarrow 5P_{3/2} \rightarrow 5D_{5/2}$ excitation, where the second step laser is tuned on resonance with the $5P_{3/2} \rightarrow 5D_{5/2}$ transition. The blue line shows off-resonance simultaneous two-photon excitation $5S_{1/2} \rightarrow 5D_{5/2}$, where the second step laser is red detuned by 850 MHz from the $5P_{3/2} \rightarrow 5D_{5/2}$ transition. A polarisation spectroscopy signal (black) is also shown for reference. The red and blue signals are from QA and two-photon absorption of first step photons respectively. The inset demonstrates the resolution that is achievable of the $5D_{5/2}$ manifold; notice the clear presence of four hyperfine features.

step lasers for the resonant QA case, and 6 μW and 7 mW for the off-resonance two-photon case. Large laser intensities are required to drive the off-resonance process. It was also possible to observe the crossover between the two signals as the second step was slowly tuned into the Doppler profile. This was predicted in Section 2.3.5 and is seen as a dispersion shape signal.

To study how this off-resonance regime could improve Rydberg spectroscopy measurements, the first and second step lasers were comb-locked to be blue and red detuned by 850 MHz respectively, therefore being in two-photon resonance (as in the blue trace of Figure 8.9). The third step laser was then precisely scanned over the expected $5D_{5/2} \rightarrow 33F_{7/2}$ transition frequency. Unfortunately no Rydberg signal was detectable in this arrangement. This is expected to be because of the much smaller excitation rate on the off-resonance $5S_{1/2} \rightarrow 5D_{5/2}$ transition, compared to the resonant $5S_{1/2} \rightarrow 5P_{3/2}$ transition, leading to a greatly reduced detection sensitivity using QA.

8.3.2 $5S_{1/2} \rightarrow 5P_{3/2} \rightarrow 33F_{7/2}$ excitation

It was also possible to observe the simultaneous $5P_{3/2} \rightarrow 33F_{7/2}$ two-photon transition by tuning the second step laser off resonance. This again requires a large second step laser power, meaning that sharp EIT features were also observed in the first step absorption. Figure 8.10 displays a second step laser scan with the third step red detuned by 50 MHz from the $5D_{5/2} \rightarrow 33F_{7/2}$ transition. The $33F_{7/2}$ signal is seen off-resonance with a similar linewidth as the on-resonance case. This implies that most of the broadening occurs on the first step transition, as expected.

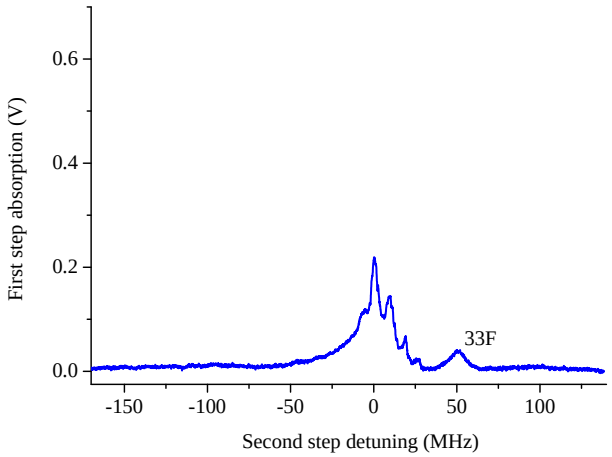

Figure 8.10: Off-resonance $5P_{3/2} \rightarrow 33F_{7/2}$ excitation seen as a QA signal in a scan of the second step laser. The third step laser was red detuned by 50 MHz from the $5D_{5/2} \rightarrow 33F_{7/2}$ transition. The first step laser was comb-locked on resonance for this scan. EIT peaks are seen on the $5P_{3/2} \rightarrow 5D_{5/2}$ transition (an offset has been removed from the vertical axis).

8.4 Fluorescence detection with a PMT

The last section's efforts were not successful in achieving narrower Rydberg signal linewidths. Detecting the weak absorption of an intense laser by off-resonance multi-photon excitations is not practical. When studying these types of transition, it is more advantageous to detect the scattered light with a PMT (24). This has several advantages over detecting the absorption with a photodiode: Firstly, the sensitivity is higher as one can count single photons. Secondly, the signals obtained are on a flat stable background. Thirdly, a very dense atomic sample can be used and there are no concerns regarding complete absorption of the probe laser, which contains the spectroscopic information [1]. In this brief study, a PMT was placed above the vapour cell, with a 25 mm focal length lens. An analogue output was obtained from the PMT by sending the count pulses through a low-pass filter.

8.4.1 420 nm fluorescence

As described in Section 4.3, transitions to the $5D_{5/2}$ level can be detected from 420 nm fluorescence, with these types of signal occurring on a zero background. In this work, a 420 nm optical band-pass filter was placed in front of the PMT. It was possible to detect resonant $5P_{3/2} \rightarrow 5D_{5/2}$ excitations with a better SNR compared to monitoring the first step absorption via QA. Also, the off-resonance $5S_{1/2} \rightarrow 5D_{5/2}$ transition had a fluorescence signal with much higher SNR when using the PMT, when compared with Figure 8.9. The higher SNR in both cases comes mainly from the stable and flat background.

For Rydberg spectroscopy, with the on-resonance $5S_{1/2} \rightarrow 5P_{3/2} \rightarrow 5D_{5/2} \rightarrow 33F_{7/2}$ scheme, Rydberg transitions could be detected by observing a dip in the 420 nm fluorescence. Such a trace is shown in Figure 8.11. In this case, the QA first step absorption signal gives a better SNR. This is thought to be because of the small solid angle captured by the PMT and the fact that neither of the signals occur on a flat background in this case. In conclusion, the clear advantage of PMT detection for Rydberg spectroscopy comes instead when monitoring the 297 nm fluorescence from the levels themselves (which will occur on a flat background).

[1] One may have to contend with complete absorption of the scattered light, although this generally occurs over a much shorter path length, depending on the cell geometry.

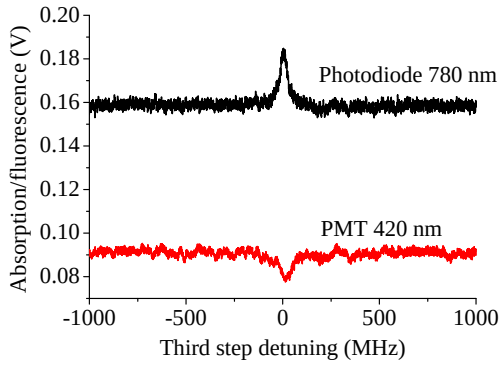

Figure 8.11: $5D_{5/2} \rightarrow 33F_{7/2}$ transitions detected from the decrease in 420 nm fluorescence with a PMT and the increase in 780 nm absorption with a photodiode. The traces were taken simultaneously and are both the average of five 0.1 s scans. The frequency scale was calibrated with a Fabry Pérot etalon.

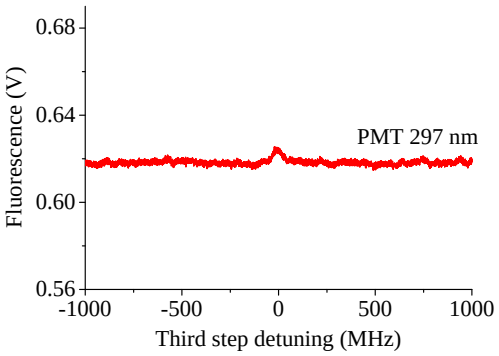

Figure 8.12: The $5P_{3/2} \rightarrow 33F_{7/2}$ transition detected from 297 nm fluorescence with a PMT. The trace is the average of 18 50 ms scans and the frequency scale was calibrated with a Fabry Pérot etalon.

8.4.2 297 nm fluorescence

A 297 nm optical band-pass filter was unavailable for this study so 420 nm background counts were eliminated by blue detuning the second step laser off resonance by 80 MHz (well outside the Doppler selected width of the first step). This results in the $5S_{1/2} \rightarrow 5P_{3/2} \rightarrow 33F_{7/2}$ excitation scheme. A peak was detected in the PMT output corresponding to the $33F_{7/2}$ Rydberg level, see Figure 8.12. The 780 nm fluorescence, which was not filtered, is expected to *decrease* when Rydberg atoms are excited; this is the basic principal of QA. Plus, any remaining 420nm fluorescence is also expected to decrease with Rydberg excitation. Therefore, the peak is expected to be from 297 nm fluorescence. It must be noted however that the UV transmission through the Pyrex cell is $<10\%$ (142), which will suppress the signal considerably. Complete off-resonance $5S_{1/2} \rightarrow 33F_{7/2}$ excitations were not detectable in this short study. However, in future work a cell with quartz walls and a 297 nm optical filter could be used to significantly improve the SNR and supply a true flat background.

8.5 Future work with a four-step scheme

8.5.1 Autler-Townes splitting with microwaves

In the work of Chapter 7, it was possible to observe an Autler-Townes splitting of the $56F_{7/2}$ Rydberg level when coupling the $56F_{7/2} \rightarrow 58D_{5/2}$ transition with microwaves (111). This was achieved by applying -2.0 dBm of microwave power at a frequency of 2×12.358 GHz across the cell. The splitting shows the general characteristics of becoming larger with increased microwave power, and moving its centre point with the microwave detuning. Figure 8.13 shows a laser scan of the third step over the $5D_{5/2} \rightarrow 56F_{7/2}$ transition with the applied microwave field. Alternatively, it was also possible to see the effect in a frequency

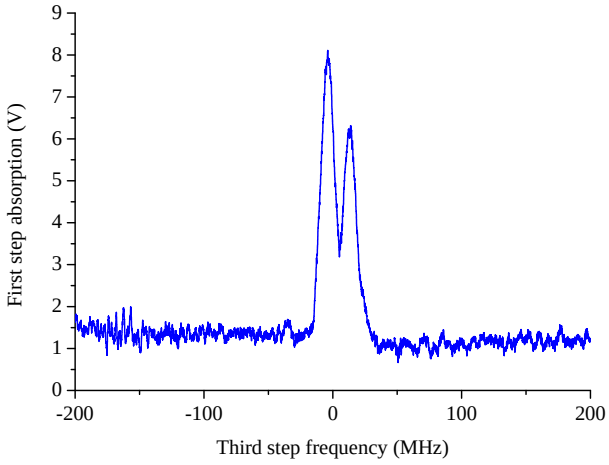

Figure 8.13: A scan of the third step laser over the $5D_{5/2} \rightarrow 56F_{7/2}$ transition. Autler-townes splitting of the $56F_{7/2}$ level occurs when applying resonant microwaves to the $56F_{7/2} \rightarrow 58D_{5/2}$ transition at 2×12.358 GHz.

scan of the microwave field, with the third step laser comb-locked at the top of the $56F_{7/2}$ peak. In this case, the effect is seen as a sharp dip with FWHM $\sim$1 MHz in the first step absorption, which occurs as the microwaves tune the centre of the splitting over the top of the $56F_{7/2}$ peak. This Autler-Townes splitting could have implications for improving the accuracy of the four-step Rydberg spectroscopy. In future work it would be interesting to see which other pairs of states show the same behaviour.

8.6 Future Rydberg catalogues

8.6.1 Future measurements with a three-step laser scheme

The work in this thesis has so far demonstrated that absolute frequencies of $n\mathrm{P}_{3/2}$ and $n\mathrm{F}_{7/2}$ Rydberg states can be measured accurately using three-step laser excitation and purely optical detection with a vapour cell. The four-step scheme has also shown very promising results for measuring nG and even nH states. This four-photon scheme will also allow nS and nD states to be measured very effectively in the future. The current experiment therefore offers the possibility to carry out precision frequency comb spectroscopy of the whole range of Rydberg series from $\ell = 0 - 5$, to a comparable accuracy to the measurements in Section 6.5 of <1 MHz. Other fine structure components can also be accessed by exciting through the $5\mathrm{D}_{3/2}$ intermediate level instead, which is achievable with the broadly tunable second step laser. This would allow access to the $n\mathrm{P}_{1/2}$ levels for example. A summary of the accessible states is shown in Figure 8.14. These types

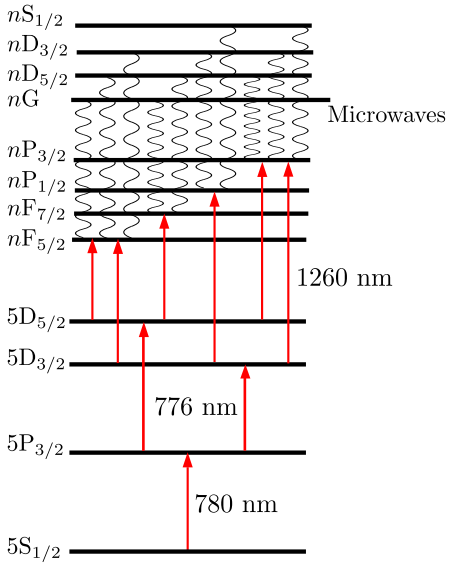

Figure 8.14: A summary of the Rydberg levels which are accessible, with dipole selection rules, using three laser steps and a microwave field.

of measurement would also provide accurate values of the fine structure splittings for the nP, nD and nF series. There is also the interesting idea of comparing absolute frequency measurements of analogous transitions in ^{87}Rb and ^{85}Rb. If a sufficient accuracy could be

achieved, it may be possible to extract nuclear information, which has been proposed by Wundt *et al* (143).

Although the measurements made throughout this thesis give greatly improved absolute transition frequencies, to improve upon the accuracy of quantum defect parameters (from microwave spectroscopy) will require narrower linewidth signals.

8.6.2 Narrower linewidths for improved accuracy

As mentioned in Sections 8.3 and 8.5.1, off-resonance excitation and Autler-Townes spectroscopy (using the same three-step laser system) are two potential options for reducing the Rydberg signal linewidth. Future work will involve investigating these in more detail. However, another option will be to move to a two-step laser scheme. Using two-step EIT (54) would immediately allow high precision absolute frequency measurements to be made of $n\mathrm{S}_{1/2}$ and $n\mathrm{D}_{3/2,5/2}$ Rydberg states, with the typical 1 MHz wide EIT signals giving an unprecedented level of precision. This could be completed with a 480 nm frequency doubled diode laser and an additional comb amplification stage at 960 nm. The frequency metrology and laser scanning setups would be the same. However, it is important to note that in the EIT scheme the measurements will always be limited by the accuracy to which the probe laser transition frequency is already known. There is no way to check for Doppler offsets with this scheme and therefore the chosen probe transition on the D_2 line would need to be well measured previously.

One interesting and novel technique may be to combine the microwave spectroscopy of Chapter 7 with a two-step EIT laser scheme. If similar behaviour could be observed as of that in Section 8.5.1, a splitting of the EIT feature may be possible by driving an $n\mathrm{S}\rightarrow n\mathrm{P}$ or $n\mathrm{D}\rightarrow n\mathrm{P}/n\mathrm{F}$ Rydberg to Rydberg transition with microwaves. Due to the narrow width of the EIT signal, this splitting could be used to accurately determine transition frequencies. The scheme has been theoretically considered by Sandhya *et al* (105) and should be experimentally viable. This would allow the Rydberg series with $\ell = 0 - 3$ to be measured with the advantage of the 1 MHz narrow EIT linewidth, giving a complete set of high accuracy measurements. The possibility of narrow coherent EIT features in N-level ladder systems (where N>4) has also been theoretically treated in Reference (106). This may open up the possibility of developing more exotic multiple-photon, laser and microwave excitation schemes in the future.

8.6.3 Other considerations

The vapour cell sample has shown excellent performance as a sample for Rydberg spectroscopy, especially with regard to sensitivity to external electric fields. However, Sections 7.5 and 8.2.2 have shown that the main future limitations will be from residual electric fields originating inside the cell and Rydberg-Rydberg frequency shifts. The nH signal size is a useful meter for minimising residual fields, although Rydberg-Rydberg interactions inside the cell will need to be better understood in order to make more accurate measurements. It will also be important in the future to have a full semi-classical model of the atomic system. Such a model could describe the coherences between the levels and describe all the competing effects discussed throughout this work.

Chapter 9

Frequency comb spectroscopy of the Rb D lines

In Chapter 6 it was found that to significantly improve the three-step Rydberg spectroscopy it would be advantageous to have more accurate measurements for the lower lying Rb D line transitions. There has been a large body of work on precision frequency measurements of the D lines in the alkali metals which have become progressively more accurate, as new techniques have been developed. This chapter will begin by presenting some of these measurements and discussing the discrepancies that exist in the literature. The development of a complete apparatus is described, which has been constructed for making a new set of frequency comb measurements of these D lines using both atomic beam and vapour cell samples. Finally, the chapter presents a new set of measurements for the D_1 line at 795 nm in ^{85}Rb and ^{87}Rb to an absolute accuracy of ~50 kHz. These results are compared with previous measurements and their integrity is tested with a number of self-consistency checks. Some surprising systematic error sources are found which would need to be carefully considered in future experiments of this type. All the work in this chapter was carried out by myself.

9.1 Precision spectroscopy of the Rb D lines

9.1.1 Discrepancies in the literature

Absolute measurements

Since Barwood *et al*'s work (61), absolute frequency measurements have been made by Ye *et al* (92), Banerjee *et al* (62; 94), Marian *et al* (45) and most recently Maric *et al* (64).

References (62; 92; 94) have focussed on SAS to make measurements, whilst References (45; 64) have used cold atomic samples held in a MOT. Out of these, it is only Marian *et al* (45) and Maric *et al* (64) that have used a frequency comb as an absolute reference, where Marian *et al* has demonstrated the novel approach of direct frequency comb spectroscopy.

The serious discrepancies occur in the D_1 line measurements at 795 nm. Reference (62) has measured absolute frequencies of the D_1 lines using a novel ring resonator method, and shows serious disagreement against Reference (61) for the a, b, c, d, a' and c' transitions. These new measurements disagree by up to 7σ in some cases, see Figure 9.1(a), (b) and (c). The more recent single measurement of c from Reference (45), is also in very bad agreement with Reference (62), see Figure 9.1(a). These differences were one of the motivations of the work by Maric *et al* (64), where a frequency comb was used to clear up any ambiguity in the numbers. Although the numbers from Reference (64) agree with those from Barwood *et al* (61) on all accounts, the work was only able to access the a, c, a' and c' transitions and not those from the other ground state, due to an essential re-pumper laser. Therefore, Banerjee *et al* (62) give the only recent measurements for the b, d, b' and d' transitions. Note that the b and d measurements from this work show poor self-consistency with the highly precise ground state splitting measurement from Arimondo *et al* (91) (Figure 9.1(f)); this indicates that these measurements may be in error.

The D_2 line measurements currently have very few discrepancies, however this could be due to a lack of recent absolute measurements. From Ye *et al* (92), the absolute frequencies of the entire D_2 line in ^{87}Rb can be computed. Successful consistency checks with the ground state splitting also shows the reliability of these numbers. From the other work by Banerjee *et al* (94), absolute frequencies of the entire D_2 line in ^{85}Rb can also be computed. In this work the same ring resonator method was used as was in Reference (62), which appeared to give erroneous results. However, this different paper shows good consistency with both Reference (61) and the b/f crossover from Reference (92), plus overall good consistency with the ground state splitting (see Figure 9.1(f)). Nevertheless, it is still important to have another recent set of *direct* measurements for comparison, especially after the inconsistencies that were observed for the D_1 line. This is especially true for the f and f' transitions which make up the first step of the Rydberg spectroscopy scheme, and where Barwood *et al* reported anomalous measurements (61).

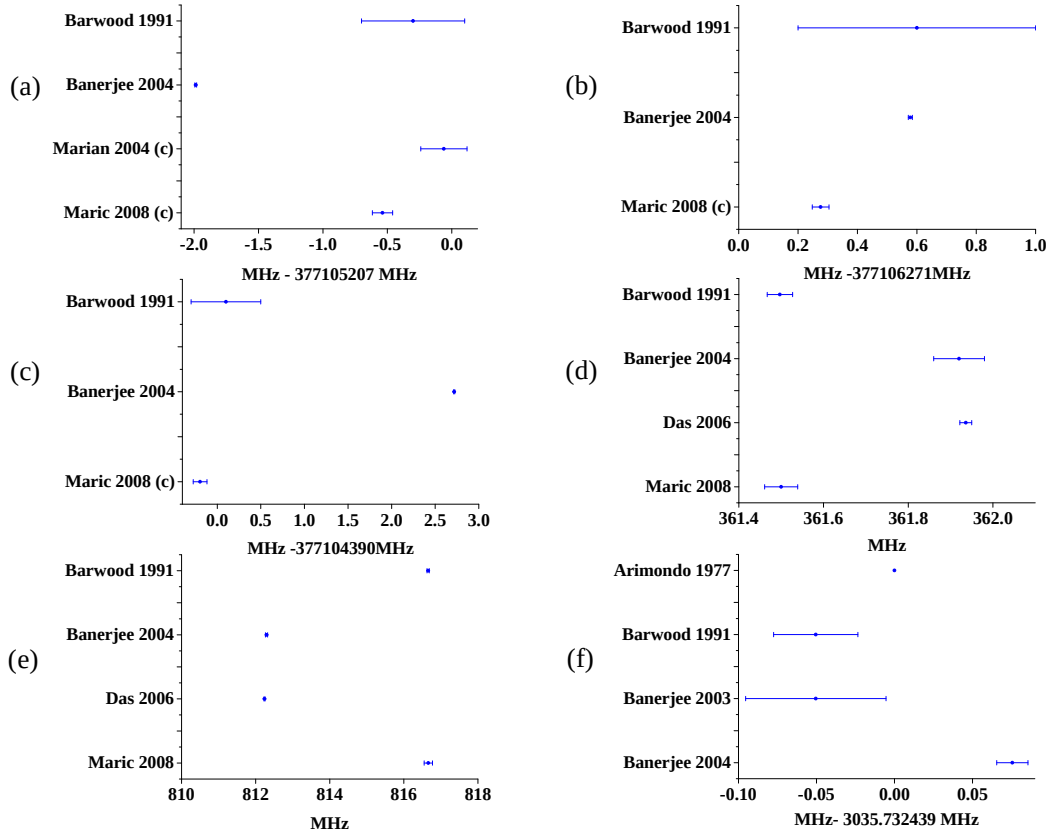

Figure 9.1: Some of the discrepancies that exist in the literature from References (45; 61; 62; 63; 64; 94). (a), (b) and (c) show absolute frequency measurements of the D_1 c, c' and a transitions. (d) and (e) are the hyperfine splitting measurements of the $5P_{1/2}$ state in ^{85}Rb and ^{87}Rb respectively. (f) shows derived $5S_{1/2}$ ground state splitting frequencies against the microwave measurement of Arimondo (91).

Relative measurements

Since Barwood *et al*'s work (61), recent works by Das *et al* (63) and Rapol *et al* (95) have measured the $5P_{1/2}$ and $5P_{3/2}$ hyperfine splittings directly with an AOM technique. Ye *et al* (92) also made true direct measurements of the $5P_{3/2}$ hyperfine splittings with two spectrometers. These studies have all used SAS to make measurements. The absolute frequency measurements of References (62; 64; 94) are also able to supply values for these splittings, by subtracting two numbers (the direct measurements are expected to be more precise).

Significant problems occur for the $5P_{1/2}$ hyperfine splitting measurements in both

isotopes. Deriving the splittings from the absolute measurements in Reference (62) gives very different results to Reference (61) by an impressive 100σ. These large differences were the motivation of the work of Das *et al* (63), to use an AOM technique (first used in Reference (95)) to clear up any ambiguity. The measurements from Reference (63) are in excellent agreement with the absolute measurements of Reference (62), but also in very bad agreement with Barwood *et al* (61) and the most recent absolute measurements from Maric *et al* (64) (see Figures 9.1(d) and (e)). In contrast, the $5P_{3/2}$ splittings show very few discrepancies. Generally the measurements from References (61; 92; 94; 95) show good agreement at the 2σ level. This excludes the case of the electric quadrupole constant $B(5P_{3/2})$ in ^{85}Rb, which still shows some large 7σ inconsistencies with Reference (61).

9.1.2 Discussion

The most recent measurements by Maric *et al* (64) have caused a large divide between parties; this is very prominent in Figures 9.1(c), (d) and (e). The transitions which are of most interest to remeasure are the D_1 line transitions in both isotopes and the D_2 line transitions in ^{85}Rb. A full set of direct absolute measurements will also give a new set of measurements of the hyperfine splittings in the $5P_{1/2}$ and $5P_{3/2}$ states. This is also a powerful way to assess systematic errors. For example, the $5P_{1/2}$, $5P_{3/2}$ and $5S_{1/2}$ hyperfine splittings can be computed in several different ways to check for both self-consistency and consistency against highly accurate microwave spectroscopy numbers (91).

9.2 Experimental setups

Two types of spectrometer have been constructed for carrying out D line measurements: An SAS setup based around a vapour cell sample and a beam fluorescence spectrometer based around a collimated atomic beam sample. Comparing measurements from two different spectrometers is another powerful way of eliminating sources of systematic error. It is also one way of understanding the large sources of discrepancy discussed in Section 9.1.1.

9.2.1 SAS spectrometer

Apparatus

The apparatus for the SAS spectrometer is shown in Figure 9.2. The setup uses pump and probe beam powers of 7 μW and 1 μW respectively, with both beams having a 2 mm diameter. A long arm length of 76 cm allows a small angle between the pump and probe beams of 7 mrad at the point of intersection inside the cell. This angle leads to a residual Doppler width of approximately 2 MHz at room temperature. Both laser beams are linearly polarised with PBS cubes. The vapour cell is made from Pyrex and contains natural Rb with no buffer gas, it is 75 mm in length and 25 mm in diameter. The cell is placed inside a three layered μ-metal shield to reduce magnetic fields within the cell. An electro-optic modulator (EOM) is used to chop the pump beam and lock-in detection is used to extract the SAS signals on a flat background. Alternatively, the EOM can be deactivated and the laser frequency can be modulated. Lock-in detection can then be used to extract third derivative signals of the SAS peaks.

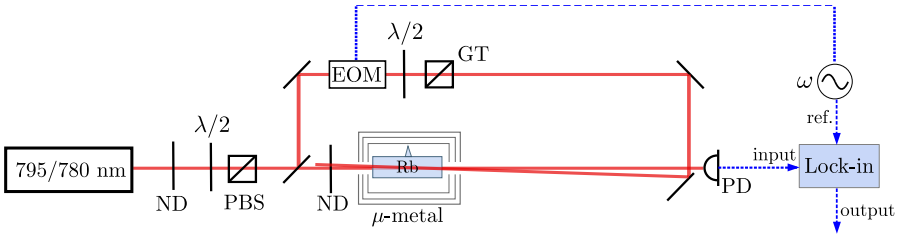

Figure 9.2: The SAS spectrometer optical setup. ND: Neutral-density filter, PBS: Polarising beam splitter, EOM: Electro-optic modulator, GT: Glan-Thompson polariser, PD: Photodiode.

Several different optical layouts were also considered: One alternative is to separate the pump and probe beams using beam splitters, which allows the beams to counter-propagate with zero residual angle. However with these setups, problems were found with optical interference between the pump and probe beams on the photodiode.

Broad scans over the D_1 line

Figure 9.3 shows a broad frequency scan over the D_1 line of ^{85}Rb and ^{87}Rb from the SAS spectrometer, using a 795 nm Toptica DL100 ECDL laser. The laser was scanned by

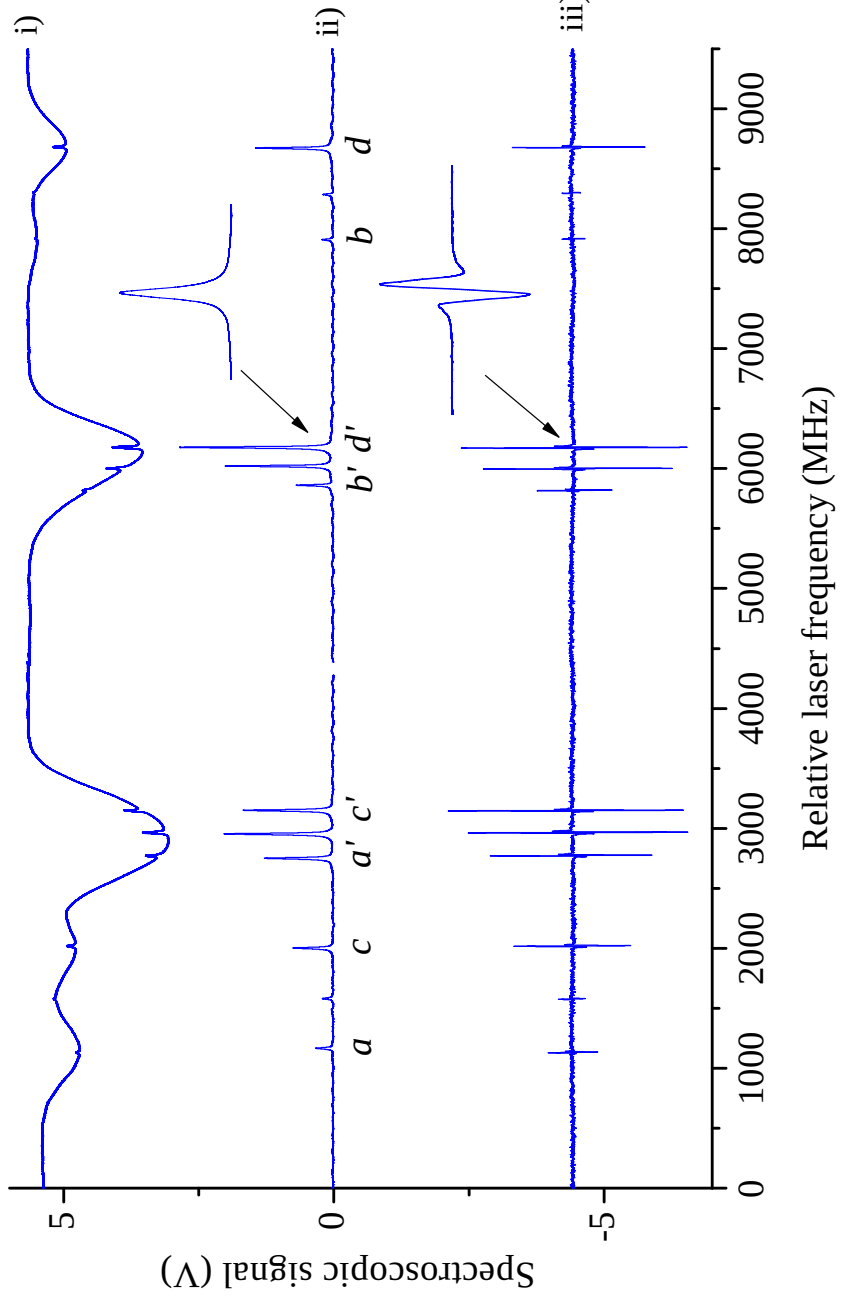

Figure 9.3: A broad scan over the ^{85}Rb and ^{87}Rb D_1 lines from the SAS spectrometer. i) is the raw signal from the photodiode with the Doppler background. ii) shows the SAS peaks with the Doppler background removed by chopping the pump beam and using lock-in detection. iii) is the third derivative signal, obtained by frequency modulating the laser frequency and using lock-in detection at the third harmonic. The inset figures show close-ups of the d' transition. The frequency axis is calibrated from the known hyperfine splittings.

tuning the grating piezo and the scan was completed in two 20 s sections. Trace i) shows the Doppler broadened spectrum with the SAS peaks. Trace ii) shows the SAS peaks from the LIA with the Doppler background removed; the pump beam was chopped with the EOM at 7 kHz. Trace iii) shows the SAS peaks extracted using $3f$ FM spectroscopy. For this, an AOM was used to modulate the laser frequency by 6 MHz at a rate of 3 kHz and the LIA was used to extract the signal at the third derivative. Because the Doppler background appears almost linear in the vicinity of an SAS peak, it is predominantly removed in the third derivative signal, without the need for chopping the pump beam (144). This technique is ideal for extracting signals for laser stabilisation purposes, where the Doppler background can pull the lock position off line centre. Notice that there are also crossover signals found exactly midway between each pair of transitions which share a common ground state.

The oscillations seen on the base line of Figure 9.3 ii) are optical interference fringes between the pump and probe beam at the photodiode; this was quite problematic where pump light was reflected off the cell window and reached the photodiode. To solve this problem Brewster angled cell windows are often used, however by significantly tilting the cell this problem can be minimised. In the latest incarnation of the optical setup these oscillations were eliminated.

9.2.2 Atomic beam spectrometer

The atomic beam apparatus was originally constructed for an improved test of Lorentz invariance using two counter-propagating Rb atomic beams. These beams were to be probed with lasers simultaneously, forming an Ives-Stillwell experiment (145; 146). However, the apparatus was easily converted to carry out precision spectroscopy measurements of Rb, by moving to a perpendicular excitation arrangement as outlined in Section 1.2.2.

First order Doppler shifts in beam spectroscopy

One disadvantage of the collimated beam method over the SAS method is that any misalignment from θ =90° (between the atomic beam vector $\mathbf{v}$ and laser wave-vector $\mathbf{k}$) leads to a finite first order Doppler shift of the transition frequency. This results in a shift equal to $\Delta f_{\mathrm{Dopp}} = k\mathrm{v}\cos\theta/2\pi$. Fortunately, one can precisely measure θ by probing the atomic beam from the opposite direction with a second laser beam (147). This laser beam can be derived from the same laser but must counter-propagate accurately with the original

beam. The atoms will experience equal and opposite Doppler shifts from each beam, giving a measurement of the misalignment error. As an example, a misalignment of 5 mrad, with a 780 nm laser and 160 ms^{-1} beam, will lead to frequency shifts of ± 1 MHz .

Apparatus

The atomic beam source in this work is a commercially available alkali metal dispenser (AMD) from Saes Getters (148). These Rb sources have been used for Doppler-free D line spectroscopy (149), Doppler-free Rydberg spectroscopy (87) and are routinely used for loading MOTs (150). The dispenser consists of $\sim$1 mg of natural Rb, a quantity of chromate and a reducing agent, all contained in a folded electrode. By applying a current of 5-8 A through the electrode filament, Rb atoms are ejected across a hemisphere at an approximate rate of 10^{17} s^{-1} (75). The velocity distribution of these sources has been studied with a time-of-flight technique, and the results show that the peak velocity occurs at 160 ms^{-1} with a FWHM of $\sim$300 ms^{-1} (75).

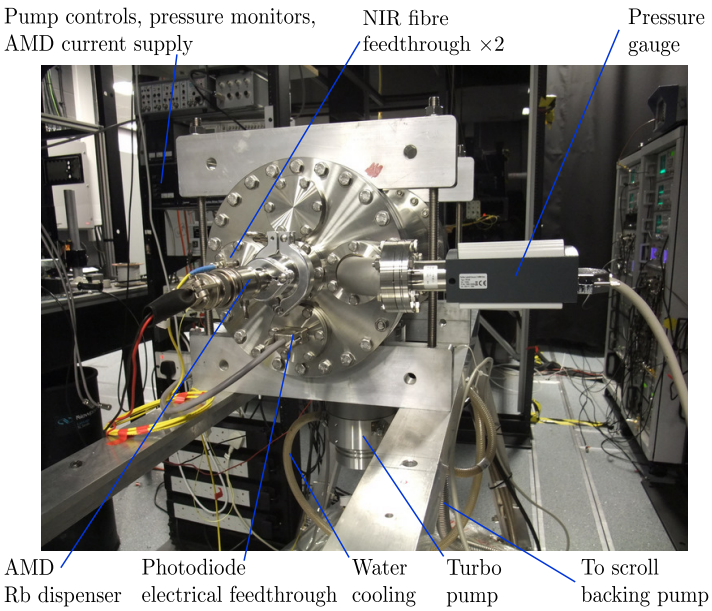

Figure 9.4: The vacuum chamber setup for the atomic beam apparatus. AMD: Alkali metal dispenser, NIR: Near infra-red.

The beam setup which has been constructed can be seen in Figure 9.4. The system consists of a 10 inch diameter vacuum chamber, which is evacuated with a water cooled

turbo pump (which has a scroll type backing pump). The vacuum chamber pressure is typically 4×10^{-7} mbar, which is monitored with an ion gauge. Fibre and electrical feedthroughs allow laser light and electrical signals to be coupled in and out of the chamber.

Within the vacuum chamber is a 38×229 mm optical bench, allowing optical components to be arranged in several geometries if required. The optical bench is held by a home-made stand so that components along the bench lie along the axis of the vacuum chamber. Rb atoms leave the dispenser and travel a distance of 400 mm before being collimated by a 1 mm diameter pinhole at the end of the bench. This gives an approximate divergence angle of 14 mrad. One can therefore expect a Doppler width of 4 MHz to a perpendicular observer. Based on the flux, and most probable velocity, the atomic density in the interaction region is estimated to be $\sim10^9$ cm^{-3} (approximately 10× lower than a room temperature vapour cell). After being collimated, the atoms enter the interaction region where they are excited by laser light from one of two opposite directions. Two

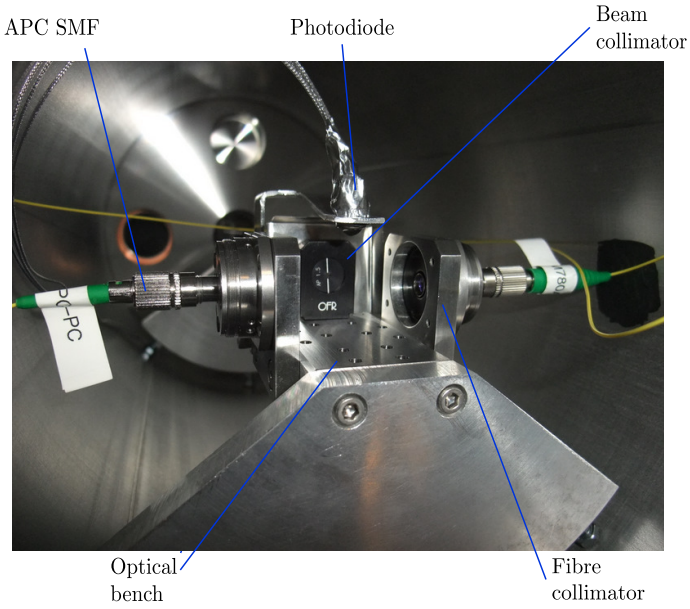

Figure 9.5: The atomic beam excitation region and detection scheme. APC-SMF: Single-mode fibre with angled-physical-contact connector.

identical angled-physical-contact (APC) single-mode anti-reflection-coated fibre couplers launch the laser light inside the chamber. The bench ensures that they are aligned with the pinhole and atomic beam. The two fibre couplers are mode matched and aligned relative

to one another to ensure equal and opposite Doppler shifts from any beam misalignment. The laser beam diameters are 2.9 mm, giving a transit-time of 20 μs. Polarisers provide the option of purifying the laser polarisation after the fibres to minimise Zeeman shifts, which is discussed in Section 9.5.5. A photodiode above the excitation region detects the scattered light from the beam, this fluorescence is the measurable signal.

Detecting the atomic beam fluorescence

In this preliminary search for a beam, a 780 nm New Focus Vortex ECDL was used. The typical laser power was 1 mW inside the chamber, giving an intensity of 15 mWcm^{-2} in the interaction region. A simple cell-based SAS spectrometer was also set up next to the vacuum apparatus using the same laser. This supplied a reference signal when exciting the beam. Two methods of lock-in detection were used to detect the atomic beam fluorescence; the probe beam was chopped with a chopper wheel or frequency modulated via the injection current.

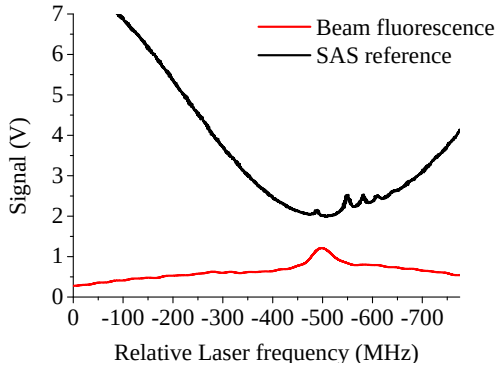

Figure 9.6: Atomic beam fluorescence of the $5S_{1/2}$, $F = 3 \rightarrow 5P_{3/2}$, $F = 4$ transition detected using a LIA, by chopping the probe beam. The frequency axis is calibrated from the known hyperfine splittings.

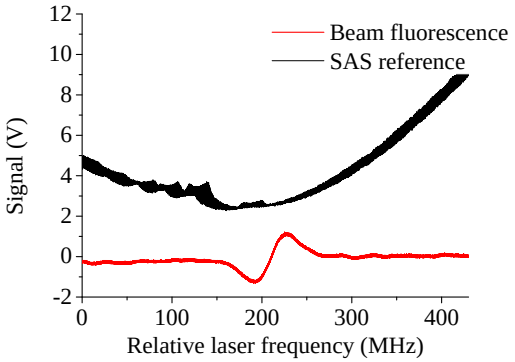

Figure 9.7: Atomic beam fluorescence of the $5S_{1/2}$, $F = 3 \rightarrow 5P_{3/2}$, $F = 4$ transition captured using a LIA, by modulating the probe beam frequency. The frequency axis is calibrated from the known hyperfine splittings.

Limitations

The atomic beam spectrometer requires significant improvements before it can achieve a comparable SNR and resolution to the SAS spectrometer. These must be made before it

can be used for high precision measurements. Large probe laser powers of 1 mW were required to detect the signals in Figures 9.6 and 9.7. This has two effects: Firstly, only the $5S_{1/2}$, $F = 3 \rightarrow 5P_{3/2}$, $F = 4$ cycling transition is visible, because for all other $5P_{3/2}$ hyperfine states the atomic population is rapidly pumped into the $5S_{1/2}$, F=2 ground state. Secondly, this will cause the transition linewidth to be power broadened to 13 MHz. The limiting factor is the detection sensitivity; if this could be increased, lower laser powers could be considered.

The larger observed linewidth of 60 MHz in Figures 9.6 and 9.7 is dominated by residual Doppler broadening, due to the velocity distribution of the atoms and a small misalignment between the laser and atomic beam. There is also a small broad Doppler background in Figure 9.6. This is from stray atoms which are excited by the laser but which are not within the beam.

9.3 AOM setup for precision laser scanning

Two identical AOM systems were constructed for the improved Lorentz invariance experiment (145; 146) to allow accurate and independent frequency tuning of two probes, derived from a single laser. These AOM systems are also ideal for carrying out precision laser scans over atomic transitions with the two spectrometers. They allow the frequency of a laser to be tuned by a well defined RF (151). The AOMs used in this work are Brimrose TEF-200-50 models, based on TeO_2 crystals with a 0.75 mm active aperture size. They are driven by voltage-controlled, high power RF drivers with a centre frequency of 200 MHz and tuning range of $\pm$25 MHz.

9.3.1 Optical layout

The AOM systems were designed to be fully fibre-coupled so that 780 nm or 795 nm lasers could be interchanged, and so that lasers could be sent to either of the spectrometers without any complex realignment (see Figure 9.8). The systems are based on a double-pass scheme, see for example Reference (151). This scheme removes the frequency dependence of the deflection angle and ensures optimum beam pointing stability after the AOM. The double-pass scheme also means that the AOM frequency shifts the laser up/down by twice the applied RF. This results in a centre frequency of 400 MHz and an increased scan range of $\pm$50 MHz. Polarisation-maintaining (PM) fibres ensure well controlled laser

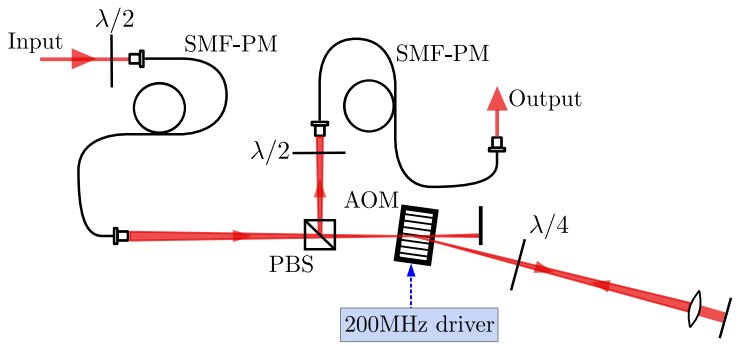

Figure 9.8: The AOM setup. SMF-PM: Single-mode polarisation-maintaining fibre, PBS: Polarising beam splitter, AOM: Acousto-optic modulator.

polarisation, and $\lambda/2$ zero-order wave plates match the laser polarisation with the slow axis of the fibres. The fibre collimators have adjustable collimation and therefore laser light is focussed directly into the centre of the AOM to achieve maximum diffraction efficiency. The focussing is achieved over a long distance to minimise the convergence angle of the beam; this ensures optimum matching with the diffraction angle.

9.3.2 Efficiency

Various efficiency plots of one of the AOM systems are shown in Figure 9.9. The RF input was supplied by a high power Brimrose voltage controlled oscillator (VCO), with inputs for frequency and power tuning. It was possible to achieve up to 80% diffraction efficiency on a single pass, and around 70% on a second pass, giving double-pass efficiencies of more than 50%. The double-passed output beam was coupled into a single-mode optical fibre. The pointing stability in front of the fibre is excellent and the fibre-coupled output shows an almost identically shaped efficiency curve to the double-passed beam.

9.3.3 Frequency shift

To carry out precision scans over the D lines requires knowing the exact frequency shift applied by the AOM. This can be achieved by driving the AOM with a stable synthesiser, which is amplified up to the required power. An amplifier was not available in this work, so instead a method for monitoring the frequency of the VCO was developed. To do this the beat note between the un-shifted and shifted light from the AOM was monitored at 400 MHz with an avalanche photodiode (APD), see Figure 9.10.

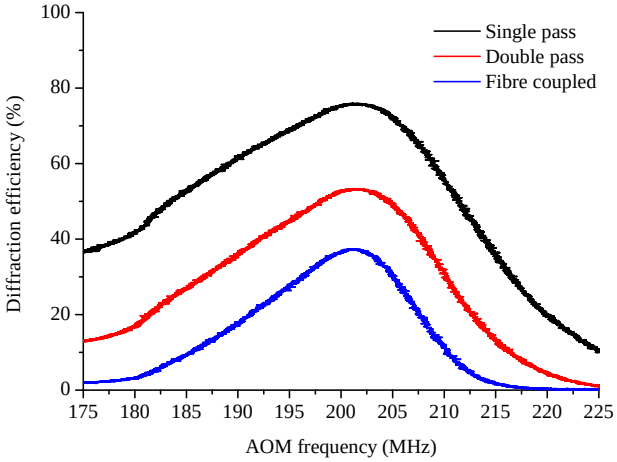

Figure 9.9: AOM efficiency plots for the single-pass, double-pass and fibre-coupled double-pass beams.

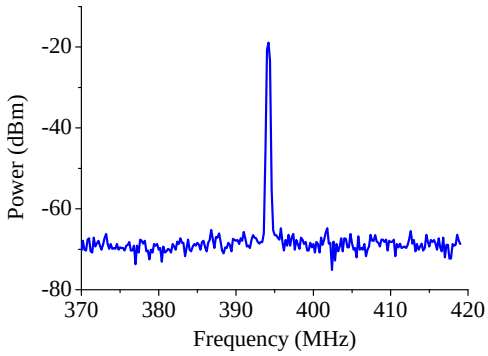

Figure 9.10: The beat note between the shifted and un-shifted laser, before and after the AOM, has a SNR of 50 dB. An RBW of 200 kHz was used for this trace.

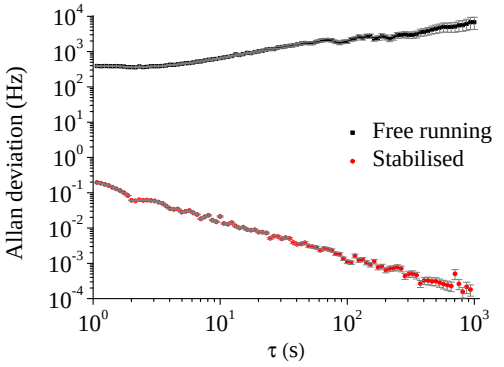

Figure 9.11: The Allan deviation (118) of the free running and stabilised AOM system.

9.3.4 Frequency stability

Figure 9.11 displays a plot of the Allan deviation (118) of the free running AOM over 1000 s. The AOM VCO driver frequency can drift by 7 kHz over 15 minute time periods and the linewidth of the beat note is around 52 kHz due to jitter on shorter time scales. For this reason, an absolute voltage to frequency relation will always have accuracy limitations. To

overcome this, the VCO driver frequency was actively phase-locked to a stable synthesiser using a PLL (92). A DBM was used to down-convert the 400 MHz AOM beat to 20 MHz via a synthesiser. This 20 MHz signal was then sent to one of the spare comb lockboxes for phase locking (see Section 3.1.3). The experimental arrangement is shown in Figure 9.12 and the stability of the AOM after stabilisation is also shown in Figure 9.11. When locked the frequency drifts are eliminated. This stability could be maintained over an AOM tuning range of 90 MHz, making this an ideal scheme for accurate stabilised laser scans.

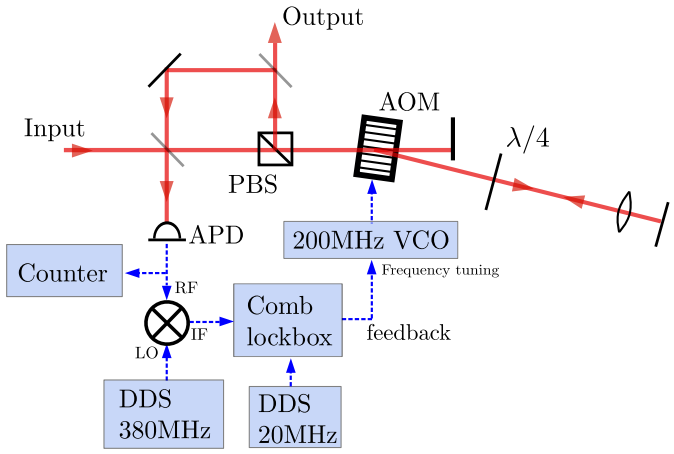

Figure 9.12: The setup used for stabilising the AOM VCO using a PLL. The optical fibres have been removed for clarity. APD: Avalanche photodiode, PBS: Polarising beam splitter, VCO: Voltage controlled oscillator, RF: Radio frequency input, LO: Local oscillator input, IF: Intermediate frequency output, DDS: Direct digital synthesiser.

9.3.5 Limitations

The AOM frequency performance exceeds the minimum requirements for the D line precision spectroscopy, however the diffraction efficiency is still a large problem. A change in probe power of just 1% leads to a change in voltage at the photodiode, that in most cases is many times larger than the SAS peak being studied. For example, when scanning by 5 MHz this change can be as large as 5%. Therefore intensity stabilisation is also required. The apparatus in Figure 9.13 was constructed to resolve this problem.

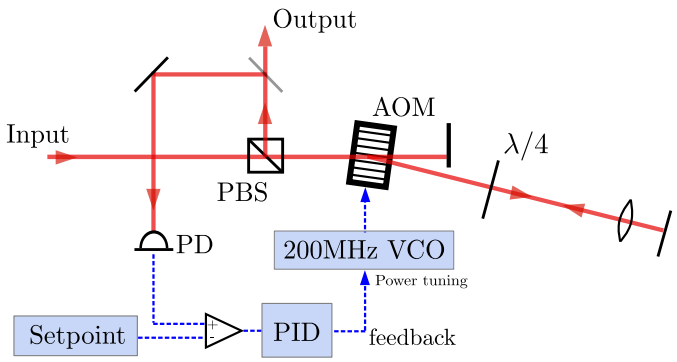

Figure 9.13: A setup for stabilising the AOM output intensity using active feedback. The optical fibres and beat detection scheme are removed for clarity. PD: Photodiode, PBS: Polarising beam splitter, VCO: Voltage controlled oscillator, PID: Proportional-integral-differential controller.

9.4 EOM for FM spectroscopy

Adding FM to a commercial diode laser via the injection current is a trivial task. However, attempting to lock the central laser frequency to a line of the comb at the same time will only act to compensate the modulation within the locking bandwidth. Therefore external frequency modulators are useful, leaving the un-modulated laser available for comb-locking or other experiments. Although the frequency shift of an AOM can be varied to modulate the laser frequency, the disadvantage, as discussed in Section 9.3.3, is that the frequency shift must always be measured and stabilised. This requires that the PLL used to stabilise the AOM driver frequency tracks the applied modulation, or that the AOM is driven by a stable amplified synthesiser with FM. There is also the added concern of RAM from the AOM, which needs to be carefully corrected, see for example Reference (92).

An EOM is a nicer solution as it modulates the phase of the laser, which has the effect of modulating the laser frequency around the carrier. There is therefore no frequency shift to be calibrated. Also, alignment is simpler, with fewer optical components. An EOM system was developed for the purpose of FM spectroscopy using a Thorlabs EO-PM-NR modulator based on a $LiNbO_3$ crystal, with a 170 V half-wave voltage at 780 nm. For high-frequency, low-depth FM spectroscopy, the optimum modulation frequency is the FWHM of the peak being studied (24), which in this case is 6 MHz.

9.4.1 *LC* tank circuit

To achieve a sufficient modulation depth, a large AC voltage of 10-100 V amplitude must be applied over the EOM at 6 MHz; this is not possible with a synthesiser alone as the EOM is essentially a 14 *p*F capacitor. One way to achieve high voltages over the EOM is to place the unit in a resonant *LC* circuit (152). A circuit was designed using a 47 μH inductor in series with the EOM, see Figure 9.14. The inductor was chosen so that the

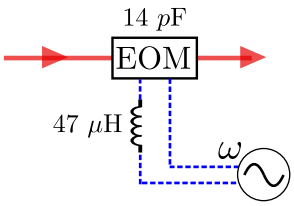

Figure 9.14: The *LC* circuit constructed for frequency modulation with an EOM.

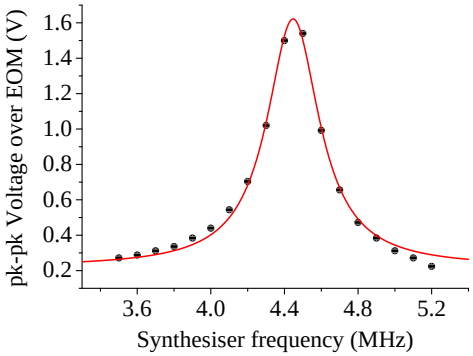

Figure 9.15: A plot of the *LC* circuit resonance.

series circuit resonates at 6.2 MHz. On resonance, the output of the driving synthesiser is amplified by the *Q* factor of the resonant circuit. Figure 9.15 shows the circuit resonance as the synthesiser frequency is tuned. The resonance has a linewidth of 350 kHz, which equates to a *Q* factor of approximately 17. The resonance occurs at 4.4 MHz as opposed to 6.2 MHz; this can be attributed to the extra capacitance of the cables and connectors that make the circuit.

9.4.2 Laser sidebands

To study the performance of the system, the EOM was placed in the path of a 780 nm Toptica DL100 ECDL. This was then coupled into a BDU of the frequency comb to observe the beat notes of the laser sidebands against a line of the comb. Figure 9.16 shows these beat notes for a range of synthesiser peak-to-peak amplitudes over the EOM. It is clear from the plots that a good depth is achievable with this simple setup, which is ideal for FM spectroscopy of Rb.

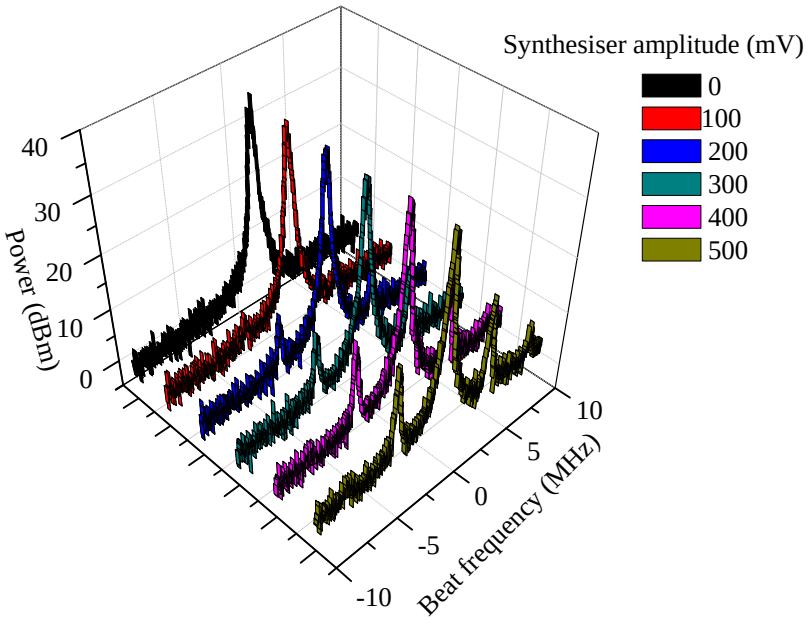

Figure 9.16: Beat notes between a frequency modulated laser and a line of the frequency comb. As more voltage is applied over the EOM, more laser power is distributed to the first order sidebands at ±4 MHz.

9.5 Absolute frequency measurement of the D_1 line from the SAS spectrometer

9.5.1 Laser metrology and control

The scannable comb offset-lock, which was developed and demonstrated in Chapter 6, is able to achieve the properties of the AOM scans discussed in Section 9.3, without the difficulties and limitations that were found. This method was therefore chosen to carry out a set of pilot absolute frequency measurements of the D_1 line of Rb using the SAS spectrometer.

A 795 nm Toptica DL100 ECDL was stabilised to a line of the frequency comb using feedback to the FET input of the diode injection current. The scanning scheme is identical to that used for the third step laser in Section 6.5 (see Figure 6.1 for details). The only difference is that beat detection is carried out with 795 nm comb light in a 795 nm BDU. Figure 9.17 shows the 795 nm laser beat note against the comb. The comb-locked laser

linewidth has a FWHM of 1.1 MHz; this is higher than the specified linewidth and comes mostly from lab noise, which was also found in Section 6.2.4. Figure 9.18 shows a plot of the stability of this laser whilst locked to the comb. The laser stability reaches a minimum of 56 Hz at 20 s. This stability could be maintained across a tuning range of f_{beat}=10-40 MHz.

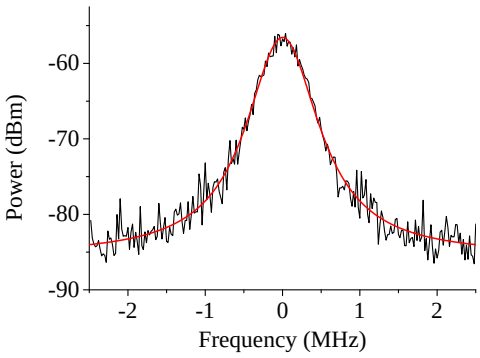

Figure 9.17: A close-up of the beat note between the 795 nm laser and a line of the frequency comb whilst comb-locked. The laser has a FWHM linewidth of 1.1 MHz. This was taken with an RBW of 5 kHz.

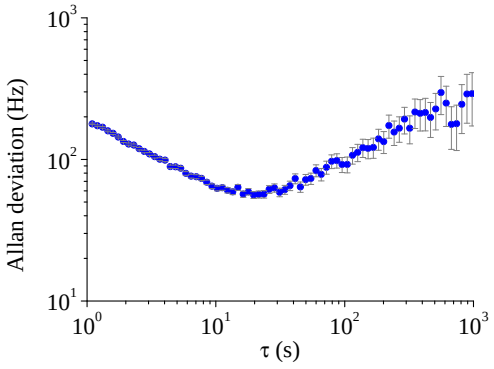

Figure 9.18: The stability (118) of the 795 nm probe laser when comb-locked. This was computed from a 6000 s data set.

For each hyperfine component of the D_1 lines of ^{85}Rb and ^{87}Rb, the comb was arranged so that f_{beat}=+25 MHz corresponded to the centre of the targeted transition from Reference (61). f_{beat}=+25 MHz corresponds to the centre of a 10-40 MHz scan of f_{beat}, which is equivalent to a 30-60 MHz scan of f_{LO}. For a single laser experiment, as opposed to the three-step scheme, it is simple to find a suitable repetition rate for each transition by using Equation 4.1 and the procedure outlined in Section 4.2.2. A table of the comb parameters which were used when targeting each transition can be found in Appendix C; all beat signs were chosen to be positive.

9.5.2 D_1 spectroscopy

To make the D_1 line measurements the EOM was instead used as a low frequency amplitude modulator, chopping the pump beam in the SAS spectrometer at a frequency of 4.5 kHz (see Figure 9.2) and removing the Doppler background. This form of detection was

chosen over the $3f$ FM technique because it is the most basic scheme with which to begin this investigation, requiring only linear scanning, with no FM involved. Data was captured from the LIA via GPIB, using the same LabVIEW program as that used in Section 6.5. The LIA time constant was set to 100 ms and scans were typically completed in 60 s with 60 points. Figure 9.19 shows an example of a laser scan over the d' transition. The signal is highly symmetric, which is reflected in the residuals. The transition FWHMs, at

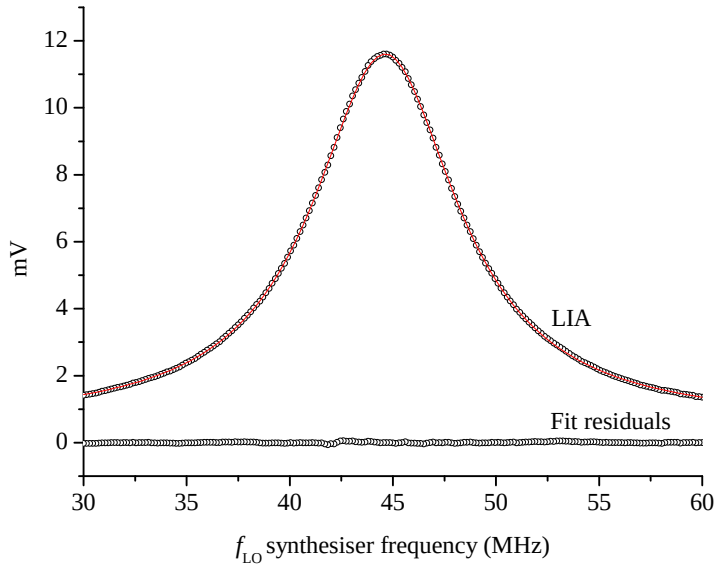

Figure 9.19: A comb-stabilised scan of the 795 nm laser over the d' hyperfine transition in the SAS spectrometer, with 200 points taken over 200 s. The red line is a Lorentzian fit to the data. The peak is highly symmetric which is demonstrated by the flat fit residuals.

the chosen pump/probe laser powers of 7/1 μW, were typically 8 MHz. By extrapolating to zero laser power, the FWHM approaches 6.7(2) MHz, in comparison with the natural linewidth of 5.75 MHz (103). The additional width is expected to be from the residual Doppler width and the laser linewidth.

9.5.3 Absolute frequency measurements

The set of absolute frequency measurements made for the D_1 lines from the SAS spectrometer are shown in Table 9.1.

Table 9.1: Absolute frequency measurements of the D_1 line transitions. Where available, frequencies from Reference (64) are also shown for comparison.

transition	This work (kHz)	Maric *et al* (64) (kHz)
a	377 104 389 819(51)	377 104 389 803(79)
a/c	377 104 798 142(51)	-
c	377 105 206 502(51)	377 105 206 462(79)
a'	377 105 909 799(45)	377 105 909 777(28)
a'/c'	377 106 090 615(45)	-
c'	377 106 271 364(45)	377 106 271 276(28)
b'	377 108 945 576(45)	-
b'/d'	377 109 126 375(45)	-
d'	377 109 307 123(45)	-
b	377 111 224 471(51)	-
b/d	377 111 632 825(51)	-
d	377 112 041 149(51)	-

9.5.4 Consistency checks

There are several consistency checks that can be made with the frequencies in Table 9.1. Firstly, the crossover resonances should lie exactly midway between their respective states (98). Secondly, the ground state splittings, derived by subtracting the relevant transition frequencies, should agree with microwave spectroscopy numbers, and be self-consistent. Finally, the hyperfine splittings of the $5P_{1/2}$ level should be self-consistent; these are also derived by subtracting the relevant transition frequencies. Table 9.2 summarises these checks. The results indicate that the measurements are consistent within the predicted absolute errors, see Table 9.3.

9.5.5 Error analysis

Table 9.3 is a summary of the estimated errors on the D_1 absolute frequency measurements. These are discussed throughout this section.

Random error and fit error

The repeatability of the frequencies were studied by taking repeated readings for several states. Transitions with large peak sizes, such as those in ^{85}Rb, showed a standard deviation of 7 kHz for a set of 15 readings. In contrast, transitions with smaller peak sizes, such as those in ^{87}Rb, showed a standard deviation of 22 kHz for a set of 15 readings. This

Table 9.2: Consistency checks for the D_1 line frequency measurements. Cross-over resonances are compared with self-predictions, $5S_{1/2}$ hyperfine splittings are compared with microwave spectroscopy numbers from Reference (91) and $5P_{1/2}$ hyperfine splittings are compared with self-mean values.

	Predicted (MHz)	Measured (MHz)	Difference (kHz)
a/c crossover	377 104 798.161(36)	377 104 798.142	19
a'/c' crossover	377 106 090.582(32)	377 106 090.615	-33
b'/d' crossover	377 109 126.350(32)	377 109 126.375	-25
b/d crossover	377 111 632.810(36)	377 111 632 825	-15
a'-b' separation	3035.732439	3035.777(64)	-45
c'-d' separation	3035.732439	3035.758(64)	-26
a'/c'-b'/d' separation	3035.732439	3035.760(64)	-28
a-b separation	6834.68261284	6834.652(72)	31
c-d separation	6834.68261284	6834.647(72)	36
a/c-b/d separation	6834.68261284	6834.683(72)	0
	Measured (MHz)	Mean (MHz)	Difference (kHz)
a-c spacing	816.683(72)	816.681(72)	2
b-d spacing	816.678(72)	-	-3
a'-c' spacing	361.565(64)	361.556(64)	9
b'-d' spacing	361.547(64)		-9

Table 9.3: Error budget. All errors are 1σ and in units of kilohertz. The total error is the sum in quadrature of the different sources.

Source	^{85}Rb	^{87}Rb
Residual angle	44	44
Pressure shifts	5	5
Random error	7	22
Power shifts	-	12
Laser frequency	4	4
Recoil energy	3.7	3.6
2nd order Doppler shift	0.2	0.2
Magnetic fields	0.1	0.1
Total	45 kHz	51 kHz

larger spread comes from fit errors and the fact that slight asymmetries in the peaks can become more prominent on smaller signals.

Fit errors are potentially large sources of systematic error in this regime. At this level of accuracy, one is attempting to locate the centre of the line to 1/1000th of the linewidth.

Asymmetries manifesting as systematic residuals of just 1% of the signal size, can easily pull the line centre measurement off by over 30 kHz. In this experiment, if the laser mode was not optimum, the peaks would often inherit a slight asymmetry, barely visible by eye but enough to cause a shift. For this reason, great care was taken so that each scan was highly symmetric by checking that the fit residuals were made of structureless noise. Fortunately, the comb-stabilised scanning technique gives a truly linear frequency scan so unlike other techniques these asymmetries can be studied in great detail and removed.

Optical pumping and Zeeman shifts

Optical pumping was avoided by using purely π polarised light in both beams. This was achieved using PBS cubes with a 1:1000 extinction ratio. Nevertheless, reflection from optical components and birefringence of the cell windows will still cause a slight ellipticity to the light. This will result in a small degree of optical pumping. In the presence of a small magnetic field, the effect of this is to cause an asymmetry in the lineshape and a small frequency shift due to preferential populating of certain non-degenerate m_F sublevels (63). This possibility is avoided by placing the vapour cell inside a three layered μ-metal shield which reduces the ambient magnetic fields around the cell. Using a fluxgate magnetometer, the magnetic fields inside the cell were measured to be 0.5 μT with a single layer of μ-metal and $<$0.01 μT with three layers (limited by the magnetometer resolution). The maximum Zeeman shift will therefore be $\sim$100 Hz.

Residual angle between pump and probe beams

Assuming an isotropic velocity distribution in the cell, a small angle between the pump and probe beams should lead only to a broadening of the SAS peak due to a residual Doppler width. However, in Reference (61), large systematic frequency shifts of the transitions were observed due to this angle. It was therefore important to check that the small 7 mrad angle in this setup was not a significant source of systematic shift.

The d' transition was measured with $\pm$7, $\pm$8, $\pm$12, $\pm$21 and $\sim$0 mrad angles between the pump and probe, see Figure 9.20. As expected, the peak became more Gaussian as the angle was increased, due to a larger residual Doppler width. No clear trend was visible between increased angle and frequency, although shifts of up to 190 kHz were seen throughout the study. These observed shifts are dominated not by the angle itself, but by the reproducibility of the pump-probe intersection point inside the cell. This will be

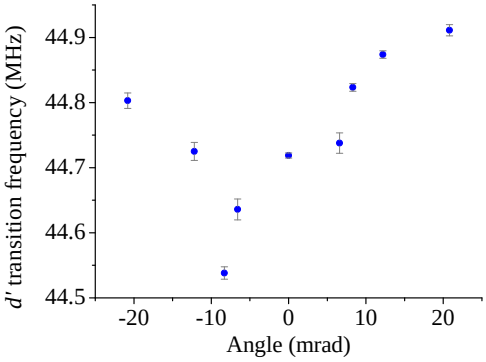

Figure 9.20: Measurements of the d' transition frequency with various pump-probe intersection angles. The error bars are based on the spread of a set of repeated measurements. The transition frequencies are written as f_{LO} values.

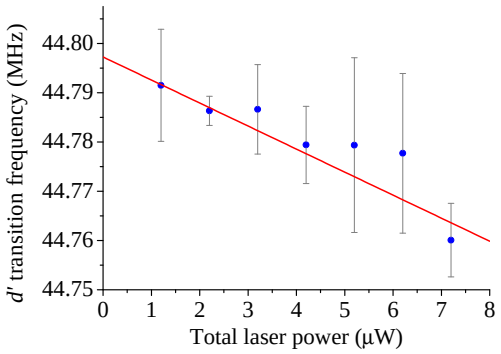

Figure 9.21: Measurements of the d' transition frequency with different total laser powers. The error bars are based on the spread of a set of repeated measurements. The transition frequencies are written as f_{LO} values.

discussed in Section 9.7.1. As a check, the d' transition was independently measured five separate times after realigning the pump and probe beam to the operating angle of 7 mrad. The measurements were spread by 44 kHz, which gives an estimated error contribution.

AC-Stark shifts

The AC-stark shift (light shift) of an atomic level, by off-resonance coupling of the laser with neighbouring hyperfine states, is given by the equation (98):

$$f_{\text{AC-Stark}} \approx \frac{\Omega^2}{4\delta}. \tag{9.1}$$

Ω is the transition Rabi frequency and δ is the detuning from a non-resonant state, which is equal to the hyperfine splitting of the $5P_{1/2}$ level in this case [1]. AC-Stark shifts of 100 Hz/(μW/cm^2) and 47 Hz/(μW/cm^2) are expected for ^{85}Rb and ^{87}Rb transitions respectively (64). In this setup the total laser intensity is approximately 260 μW/cm^2 and therefore light shifts of around 26 kHz are expected in ^{85}Rb.

For ^{85}Rb each transition was measured at seven different pump-probe laser powers and these measurements were extrapolated to zero laser power. These are the measurements shown in Table 9.1. As an example, for the c' transition, a light shift of 4 kHz/μW

[1] Equation 9.1 is valid for $\Omega \ll \delta$, as is the case in this experiment.

was detected, leading to a total shift of 33±15 kHz. This is in good agreement with the prediction. Figure 9.21 shows light shift data for the d' transition.

For ^{87}Rb transitions it was not possible to detect light shifts due to the larger random error. Therefore shifts for these transitions were added as a possible error source of 12 kHz, which is estimated from the laser powers used. The ^{87}Rb measurements in Table 9.1 are the average of four repeated measurements taken with the normal working laser powers.

Second order Doppler shifts

A moving atom also experiences a second order Doppler shift, which is independent of the direction of motion relative to the laser (98). In SAS, the atoms are still in motion in a plane perpendicular to the pump and probe lasers and therefore this term appears as a systematic frequency shift. It is given by

$$f_{\text{Dopp 2nd}} = \frac{v^2}{c^2} f, \tag{9.2}$$

where v is the atomic velocity, and f is the laser frequency. Based on the most probable velocity of atoms in the cell, this shift equates to 240 Hz.

Photon momentum

The photon momentum has two effects on the transition frequency (153). Firstly, it causes it to shift up by the recoil energy $hf^2/2mc^2$, where f and m are the transition frequency and mass of the the Rb atom respectively. These shifts are 3.6 kHz and 3.7 kHz for ^{87}Rb and ^{85}Rb respectively. Secondly, each recoil modifies the velocity of the atom, and therefore the laser has the effect of slightly redistributing the velocities in the interaction region. This manifests itself as an asymmetry of the SAS peak (154). The highly symmetric line shapes of the scans in this work (see Figure 9.19) indicate that any redistribution is negligible.

Collisional shifts

It is expected that collisions between Rb atoms will cause a systematic frequency shift, which will scale with the Rb vapour pressure (24). To check for such systematic shifts, the d' transition was measured in a heated cell. The cell temperature was varied from 25-60 °C and the transition was measured across two days, which is displayed in Figure 9.22. From

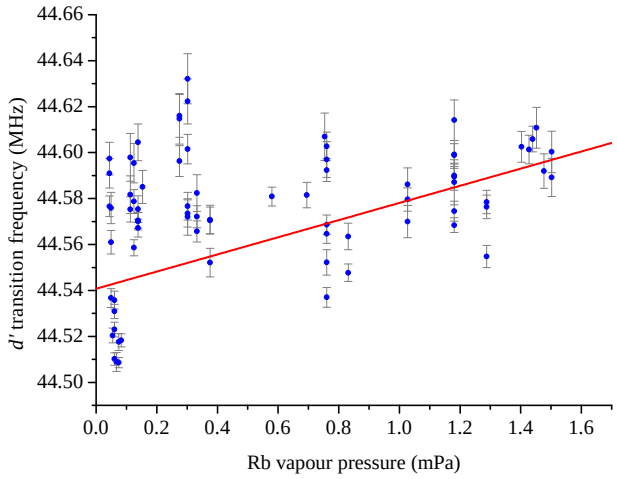

Figure 9.22: Measurements of the d' transition taken with various different Rb vapour pressures. The error bars are the uncertainties in the Lorentzian fits to the peaks. The transition frequencies are written as f_{LO} values.

the data, the maximum pressure shift could be 37 kHz/mPa. For a room temperature Rb vapour pressure of 0.05 mPa, this equates to a shift of the transition frequencies by no more than 2 kHz. There is also the possibility of frequency shifts from collisions with other foreign molecules inside the cell, although based on work from other groups, such shifts are expected to be no more than a few kilohertz (92; 123). Also, the fact that the extrapolated zero-power linewidth of 6.7 MHz is fully accounted for by the laser linewidth and residual Doppler width of the cell indicates that collisional effects are negligible.

Time delays in data acquisition

By choosing a sensible scan speed and LIA time constant, measurement differences between upwards and downwards laser scans were less than the random error of 7 kHz. This was checked with the d' transition. To be sure this had no effect on the measurements, for every transition studied, equal numbers of scans were made in each direction and averaged.

Laser frequency errors

From the GPS referenced Rb standard, the comb system's relative absolute accuracy is expected to be 5×10^{-12} (115), equating to 2 kHz at 795 nm. To check for laser lock

errors, the scannable offset-lock was monitored during each laser scan using a frequency counter. On average, lock errors were no more than 3 kHz. The stability of the laser during a single scan was typically a few hundred hertz from Figure 9.18.

9.5.6 Long term reproducibility

The d' transition frequency was found to be reproducible to 17 kHz on a daily basis, with the associated minor adjustments in alignment, laser power and laser mode. Figure 9.23 shows measurements of this transition taken across four weeks.

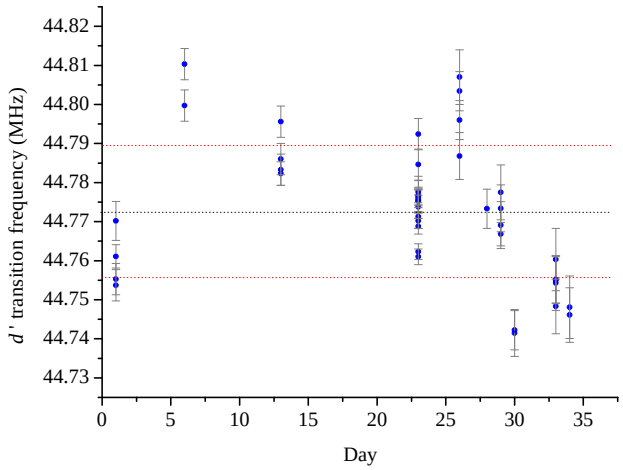

Figure 9.23: Measurements of the d' transition taken over four weeks, the red dotted lines are 1σ bounds and lay at ± 17 kHz of the mean. The error bars are the uncertainties in the Lorentzian fits to the peaks. The transition frequencies are written as f_{LO} values.

9.6 Comparison with previous measurements

9.6.1 Absolute measurements

Figure 9.24(a), (b), (c) and (d) compare the results from this work with previous measurements by other groups. Interestingly, all the measurements made in this work agree within error with the results of Maric *et al* (64). Plus, the results of Banerjee *et al* (62) could not be reproduced in this experiment.

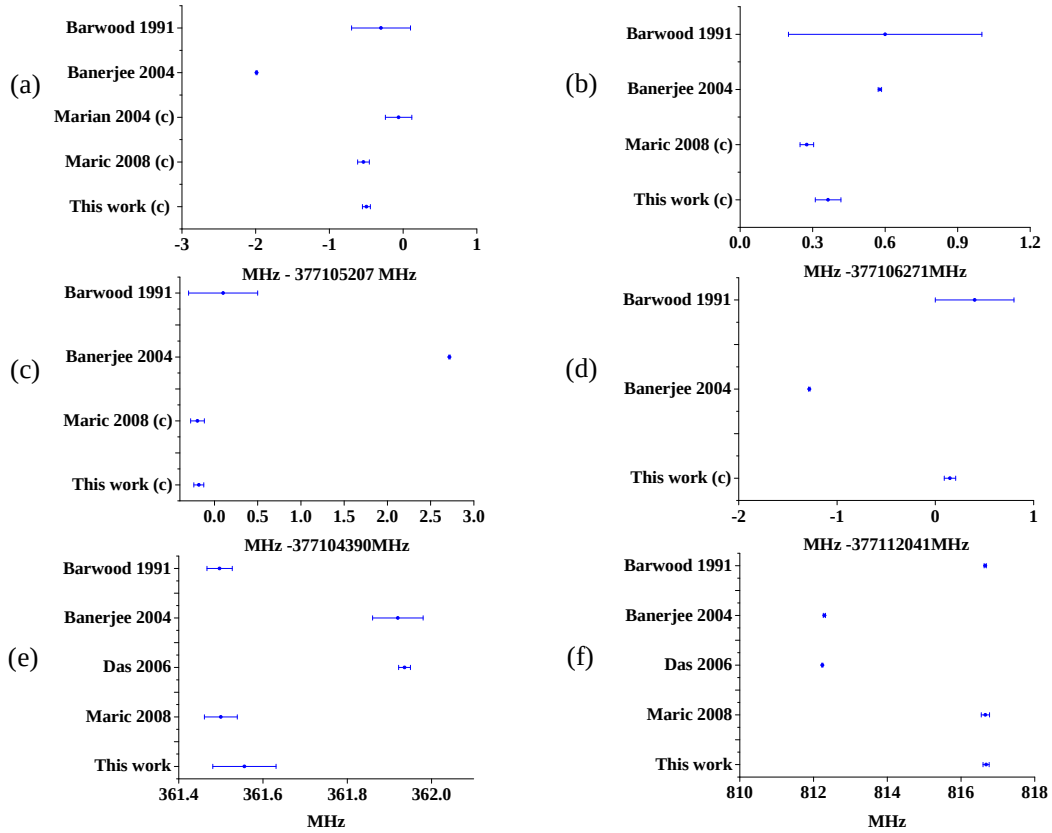

Figure 9.24: Some of the new measurements displayed against those from References (45; 61; 62; 63; 64). (a), (b), (c) and (d) show absolute frequency measurements of the c, c', a and d transitions, (e) and (f) are the hyperfine splitting measurements of the $5P_{1/2}$ state in ^{85}Rb and ^{87}Rb respectively.

It was suggested in Reference (64) that some of the discrepancies observed may be a result of using SAS, and that unaccounted shifts may not have been addressed. For this reason they chose to use a MOT to eliminate any systematic errors associated with the atomic motion, and that of cell-based spectroscopy. These new results show that measurements from SAS appear to agree well with the MOT measurements, indicating that SAS is a perfectly viable method at this level of accuracy. Moreover, SAS offers extra self-consistency checks over the MOT method.

The b, d, b' and d' transitions were not directly measured by Maric *et al* (64) and therefore cannot be compared. However, based on the self-consistency checks in Section 9.5.4, the new measurements for these transitions made in this chapter appear to be

reliable. These numbers are of particular importance for the b and d transitions where the most recent measurements made in Reference (62) significantly disagree with Barwood *et al* (61), see Figure 9.24(d).

9.6.2 Relative measurements

Figures 9.24(e) and (f) compare the $5P_{1/2}$ hyperfine splitting derived from this work with previous measurements. Table 9.4 summarises previous measurements of the magnetic dipole constant $A(5P_{1/2})$. These constants are equal to the $5P_{1/2}$ hyperfine splitting divided by three and two for ^{85}Rb and ^{87}Rb respectively (see Appendix A.5). The hyperfine

Table 9.4: The magnetic dipole constant $A(5P_{1/2})$ from this work and other previous works (61; 62; 63; 64; 93). All units are in megahertz.

Source	^{85}Rb (MHz)	^{87}Rb (MHz)
This work	120.519(21)	408.341(36)
Maric *et al* 2008 (64)	120.500(13)	408.330(56)
Das *et al* 2006 (63)	120.645(5)	406.119(7)
Banerjee *et al* 2004 (62)	120.640(20)	406.147(15)
Barwood *et al* 1991 (61)	120.499(10)	408.328(15)
Beacham *et al* 1971 (93)	120.72(50)	406.2(1.5)

constants measured in this work agree in all cases with Maric *et al* (64) and Barwood *et al* (61), but disagree with Banerjee *et al* (62) and Das *et al* (63) by up to 77σ. The 4 MHz difference in Figure 9.24(f) is particularly concerning.

9.6.3 Discussion

The disagreement in previous absolute frequency measurements is not fully understood. It could be related to the absolute reference that was used in Reference (62). For example, in this paper a D_2 transition from the work of Reference (92) is used as a reference when calibrating a ring resonator. The ring resonator is then used to measure the frequency gap to other D line transitions. This process adds a set of potential systematic errors associated with the three additional locking circuits required, each of which needs to be locked accurately within a few tens of kilohertz to a 6 MHz transition peak. Also, there are additional systematic errors associated with the resonator itself, as one is actually comparing wavelengths and not frequencies. For other Rb absolute measurements, frequencies

have been counted *directly*. In Reference (92), measurements are made directly against a 778 nm reference laser (locked to a narrow two-photon transition), whilst in References (45; 64) and the work in this chapter, measurements are made directly with a comb.

Putting the above discrepancies aside, the most dramatic result is that of the hyperfine splitting measurements, with still up to 4 MHz disagreement. It is reassuring that the difference measurements from this work in Table 9.2 agree with one another to well within error. There is no other obvious source which could cause such a large shift. The hyperfine splittings are expected to be the most reliable numbers because most of the sources of frequency shift will affect the two hyperfine levels equally and will therefore cancel out in a difference measurement. Even the unlikely situation of an inaccurately referenced frequency comb would not affect the measurement. It is therefore expected that there may be a more general factor involved between the previous works (61; 62; 63; 64): 4 MHz is 60% of the transition linewidth, such a difference is not likely to come from the spectrometer but most likely from the measurement procedure.

Some of the systematic shifts found in this investigation raise concerning questions about other papers where locking techniques have been used to measure transitions (62; 63). As already discussed in Section 9.5.5 (and also in Section 6.8.5), locating the centre of a 6 MHz peak at the 10 kHz level requires extremely high symmetry of the signal. It would therefore be essential that a linear scan is carried out across the locking signal beforehand to check for asymmetries. Otherwise, the central lock point cannot necessarily be trusted at 10 kHz accuracies. There is also the fact that other papers have not mentioned a frequency shift with pump-probe alignment in an SAS spectrometer, which in this work was the dominant source of systematic shift. In conclusion, this work has shown that achieving <10 kHz uncertainties on absolute *or* relative measurements of the Rb D lines is an experimental challenge.

9.7 Outlook

9.7.1 Improvements

Atomic beam spectrometer

The limiting factor of the atomic beam spectrometer was the broad 60 MHz linewidth of the peaks and the detection sensitivity. It is possible to optimise the alignment, and minimise the linewidth, by probing the atoms with both counter-propagating lasers simultaneously.

The atomic beam direction would then need to be precisely adjusted to minimise Doppler shifts and the associated broadening. The detection sensitivity could be improved by eliminating electrical noise from the turbo pump, which adds a large amount of noise to the photodiode. The collection sensitivity of the beam fluorescence could also be improved using lenses or mirrors. Another option would be to move to a more sensitive detector, such as a PMT. The future setup will also include tuning fork choppers which oscillate at 75 Hz. This will allow the atomic beam to be chopped, which will eliminate problems from stray atoms or scattered light inside the chamber.

SAS spectrometer

The three largest sources of error in the SAS absolute frequency measurements were from the pump-probe alignment, power shifts and random error. The cause of the alignment error is a result of Doppler averaging and is described in Reference (155). For finite crossing angles, the position of pump-probe intersection in the cell is very important. Any deviation from the exact centre will lead to a frequency shift due to unbalanced Doppler averaging; the larger the angle, the larger the sensitivity to position. There may also be a shift contribution from the curvature of the laser wavefronts in the interaction region (156). In Reference (92), the pump and probe lasers are carefully mode matched, collimated and propagate with zero angle and no alignment systematic shifts above 3 kHz were reported. This could be achieved in this experiment with a good spatial filter, collimator stage and a different zero-angle optical setup.

Increasing the SNR will decrease the random error, which could be achieved with a larger beam diameter and with more attention to technical noise. In this initial work, a 2 mm beam diameter was chosen only to match the EOM aperture in the pump beam path. FM spectroscopy will not require this if $3f$ detection is used to remove the Doppler background (144). With lower random error other systematic shifts can be studied to higher accuracy, such as power shifts.

Laser system

The measurements from this chapter show that the scannable comb offset-lock technique is far simpler and less complex than the AOM method of scanning. One of the current disadvantages of the offset scanning method is that laser scans are carried out via the laser injection current. This gives a small associated ramp in laser power and can also affect the

laser mode during the scan. It was noticed that both of these factors could cause small but troublesome asymmetries in the signals. An improvement will involve dividing the comb-locking feedback to the piezo for slow changes, and to the injection current for fast changes. This way the laser can be scanned with the large travel of the piezo, without the limitations mentioned above. This large travel would also allow gigahertz-range comb-stabilised laser scans by tuning instead the comb repetition rate. This would mean the entire $P_{1/2}$ or $P_{3/2}$ hyperfine manifold could be measured in a single scan.

Ultimately, when other error sources are controlled to less than 4 kHz, the stability and accuracy of the Rb standard used to reference the comb must be addressed. This can be achieved using Common-View GPS techniques (116) or by comparing the Rb standard against a more accurate standard at a National Standards lab. Higher accuracies could also be achieved with longer averaging times, by locking onto the transitions and counting the laser frequency. For example, in Reference (116) it was possible to achieve <1 kHz uncertainties from a GPS referenced comb with over an hour of averaging.

9.7.2 FM comb spectroscopy

With the scannable comb offset-lock it was also possible to carry out FM spectroscopy of the D lines. An FM of 4 kHz was applied to f_{LO} in Figure 6.1, via the synthesiser. Because the feedback to the laser has ∼100 kHz bandwidth, the comb-lock is able to track the modulation. Therefore FM is added to the laser around its comb-locked centre frequency. To demonstrate this as a proof of principle, a comb-stabilised scan was carried out across the d' transition using this technique. The LIA was referenced to the first harmonic of the modulation frequency. The scan is shown in Figure 9.25 with a Wahlquist first derivative fit (see Equation 4.5). The centre frequency from this scan agrees within the fit error with that from the chopping technique, that was used in Section 9.5.3. Unfortunately in this example $3f$ spectroscopy was not possible; the synthesiser that was used had a minimum modulation frequency greater than 1/3 of the photodiode bandwidth.

Faster modulation frequencies will allow more suppression of technical noise sources (24). The EOM system introduced in Section 9.4 could be used to apply 4 MHz sidebands and a fast photodiode could then be used to monitor the probe laser. Alternatively, sidebands could be added to the laser directly via the Bias-Tee connection to the laser diode. If the applied sidebands lie outside the range of the band-pass filter of the BFD100 unit of the comb (±3 MHz), they will not affect counting or locking of the laser carrier,

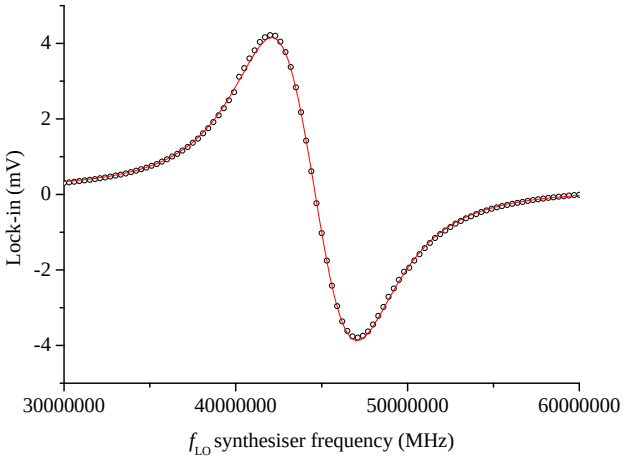

Figure 9.25: Proof of principle: A comb-stabilised laser scan over the d' transition, with FM added to the laser via f_{LO}. The signal is demodulated via a LIA, the red line is a Wahlquist first derivative fit (126).

which could still be comb-stabilised with feedback to the FET. This configuration would allow high frequency (6 MHz) FM spectroscopy with a comb-stabilised laser, with no need for external modulators. Both of these FM techniques also offer the option of locking the laser onto the transition and counting the laser frequency across long time scales.

9.8 Conclusion

This chapter has outlined the construction of two Doppler-free Rb spectrometers for probing the hyperfine structure of the Rb D_1 and D_2 lines. AOM and EOM modulator systems have been described which can be used to carry out precision scans and FM spectroscopy with the spectrometers. The SAS spectrometer has been used to make a new complete set of absolute frequency measurements of the D_1 line in both Rb isotopes. The results show excellent agreement with the most recent, and also comb-based, study (64). There still appears to be a clear divide between results in the literature, especially concerning the magnetic dipole constant $A(5P_{1/2})$ (61; 62; 63; 64). The results of this chapter have exposed several potentially large sources of systematic error in cell-based SAS, which could be responsible. The comb-based laser scanning system from Chapter 6 has proven to be very reliable and can be improved further with modifications to the laser feedback. In the

future it will be possible to obtain complete sets of highly accurate measurements for the D_1 and D_2 lines from both spectrometers, which will give more evidence as to the causes of the current discrepancies in the literature.

Chapter 10

Conclusion

10.1 Overview

The work in this thesis has demonstrated that vapour cells can be used to carry out high precision, absolute frequency measurements of Rybderg levels in Rb. After several improvements to the experimental setup, including full comb-locking of all three laser steps, the results from Chapter 6 have demonstrated the first sub-megahertz accuracy optical Rydberg spectroscopy. In 1977 Lee *et al* (82), when measuring nS Rydberg levels using two-photon spectroscopy, made an interesting quote when discussing their Rydberg-Ritz fit:

"It seems remarkable that eight-digit accuracy for ≈40 transitions is essentially totally preserved with only four constants."

In the work of Chapter 6 it is found that for the $n\mathrm{P}_{3/2}$ series, eleven-digit accuracy is preserved across 27 transitions and with only three constants. This nicely demonstrates both the improvements that have been made in accuracy and the excellent validity of the Rydberg-Ritz formula (Equation 4.7). These new measurements have been made significantly simpler by the excellent screening properties of external electric fields by the cell. Despite the strong n^7 scaling of the Rydberg polarisability, stray electric fields around the cell do not act as a large source of systematic shift. Even so, the observation of Stark-induced transitions in Chapter 7 indicates that small stray fields originating inside the cell can exist and these must also be considered for high accuracy measurements. Although the mechanisms behind these effect have been briefly studied in this thesis, there is clearly

a large body of work to be carried out in the future regarding the free charges within the cell.

Although quantum defects can still be more accurately measured with microwave spectroscopy (80; 81), it is the new value for the ionisation threshold E_i which has been most successful from this work, improving upon the accuracy of previous measurements by 20×. Figure 10.1 shows previous determinations of this value in chronological order.

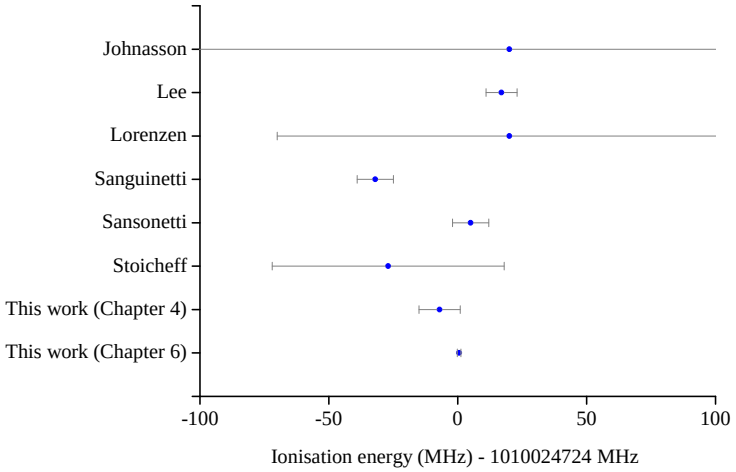

Figure 10.1: Previous measurements of the ionisation energy E_i from References (82; 83; 85; 86; 87; 90) and the measurements from this thesis, plotted in chronological order.

This work has also solved the long-standing problem of third step laser stabilisation for the micomaser experiment in our lab. Using the cell, the third step can now be stabilised onto the $5D_{5/2}, F = 5 \rightarrow 63P_{3/2}$ transition with a stability of a few hundred kilohertz over an hour. The comb-stabilised scannable offset-lock also gives the option to stabilise this laser via the comb. This will allow precise tuning of the laser frequency for characterising electric fields in the cryostat for example, or Doppler selection in the case of the first step laser.

The new comb-stabilised laser scheme has the potential to allow further orders of magnitude improvement in accuracy for Rydberg measurements. By moving to off-resonant excitation schemes or other two/three/four-step configurations, narrower linewidths will be achievable. This will allow significantly better determinations of transition frequencies and systematic shifts. In this case quantum defects may even be extracted with greater ac-

curacy than microwave spectroscopy methods, although a careful study of the systematic shifts observed at high n will also be required to achieve this goal. Improvements in the comb-locking scheme can also be made; with improved SNRs of the three laser-comb beat notes, and improvements in the locking servos, phase-locked operation could be achieved on all three steps. This will open up the feasibility of fully phase-coherent excitation of a four-level system.

The coupling of microwaves into the cell as a form of spectroscopy has shown great prospects for extracting the quantum defects of high ℓ Rydberg states of Rb. High SNRs are possible and the screening from electric fields becomes an even more pleasing feature in this case. The first observation of nG and nH states in the cell is an excellent starting-point for extracting a precision measurement of the Rb^+ core polarisability (for which there is currently a lack of experimental measurements (72)). The nH states have also proven to be useful for indicating and measuring residual electric fields inside the cell.

Finally, precision spectroscopy of the D_1 line has shown that SAS measurements appear to agree with recent measurements from a MOT (64) to within 50 kHz. As a result, the current discrepancies in the literature (61; 62; 63; 64) are becoming better understood; the work in this thesis shows agreement with one set of papers and disagreement with another. Similar measurements of the D_2 lines will be useful for future Rydberg measurements. Interestingly, some of the systematic errors discovered from the D_1 spectroscopy, such as the residual-angle shift (155), will also need to be considered in future cell-based Rydberg spectroscopy if the accuracy is to be increased further.

10.2 Recent developments

Since the completion of the work in this thesis, Mack *et al* (157) have completed a set of absolute frequency measurements of nS and nD Rydberg states in ^{87}Rb with a frequency comb. They have used a vapour cell and the two-step EIT detection scheme (see Reference (54)) [1] and have extracted a value for the ionisation energy with 300 kHz uncertainty. Adjusting their value to the centre of mass of the $5S_{1/2}$ hyperfine ground states gives

[1] Note that Mack *et al* have also observed irregular and broad lineshapes for states with $n \sim 180$

$$E_{i\,\mathrm{Rb}_{87}} = 1010\,024\,892.9(3)\ \mathrm{MHz},$$

compared to the value from the $n\mathrm{P}_{3/2}$ measurements of Section 6.5:

$$E_{i\,\mathrm{Rb}_{85}} = 1010\,024\,723.9(3)\ \mathrm{MHz}.$$

The difference between these two measurements gives a highly accurate value for the isotope shift of the $5\mathrm{S}_{1/2}$ state of Rb:

$$169.1(4)\ \mathrm{MHz}.$$

This will have contributions from the specific mass shift and the volume shift (98). It is the most accurate determination of this value to date, and improves the accuracy of previous measurements by 20×. Table 10.2 shows previous measurements of the isotope shift and this new value; the values are plotted together in Figure 10.2.

Table 10.1: Values for the $5\mathrm{S}_{1/2}$ isotope shift calculated from References (82; 85; 89; 157) and the work from this thesis. All units are in megahertz.

Source	$5\mathrm{S}_{1/2}$ Isotope shift (MHz)
Kato *et al* (89)	160(12)
Lee *et al* (82)	177(8)
Stoicheff *et al* (85)	167(10)
This work and Mack *et al* (157)	169.1(4)

With the results from this new paper, Table D.1 in Appendix D summarises the most recent precision Rydberg spectroscopy measurements in Rb, for which measurement uncertainties translate to <1 MHz on the optical frequencies E_n. This table encapsulates the current state of the field.

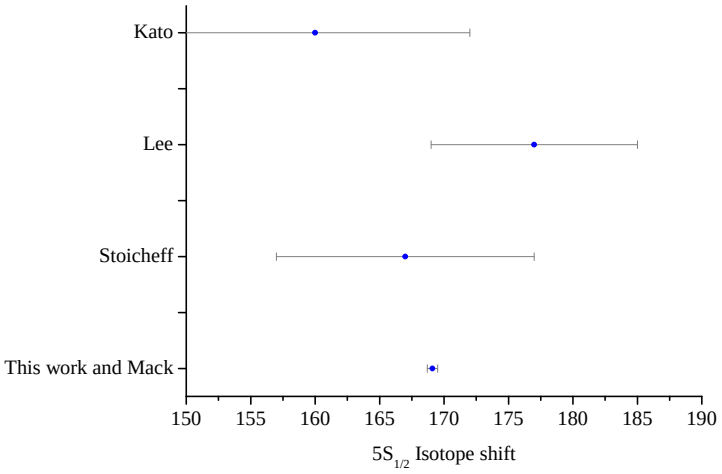

Figure 10.2: Previous measurements of the Rb $5S_{1/2}$ isotope shift from References (82; 85; 89) and the measurement derivable from this thesis and the measurement of Mack *et al* (157). The points are plotted in chronological order.

Appendix A

Rubidium

A.1 Physical properties

Rb is naturally abundant in two isotopes ^{85}Rb and ^{87}Rb. Table A.1 shows a table of physical properties (158; 159).

Table A.1: Some physical properties of the two natural isotopes of Rb.

	^{85}Rb	^{87}Rb
Atomic number	37	37
Total nucleons	85	87
Atomic mass	$1.409993199(70)\times10^{-25}$ kg	$1.443160648(72)\times10^{-25}$ kg
Natural abundance	72.17(2)%	27.83(2)%
Nuclear spin I	5/2	3/2

A.2 Electronic structure

Rb has a ground state electronic shell structure of (98)

$$1s^2.2s^2.2p^6.3s^2.3p^6.3d^{10}.4s^2.4p^6.5s.$$

A.3 Number density

Figure A.1 shows the number density of Rb with temperature using the Killian method (160), described by the equation

$$N = 10^{26.41-\frac{4132}{T}-\log_{10}(T)}, \tag{A.1}$$

where T is the vapour temperature in kelvin and N is in m^{-3}.

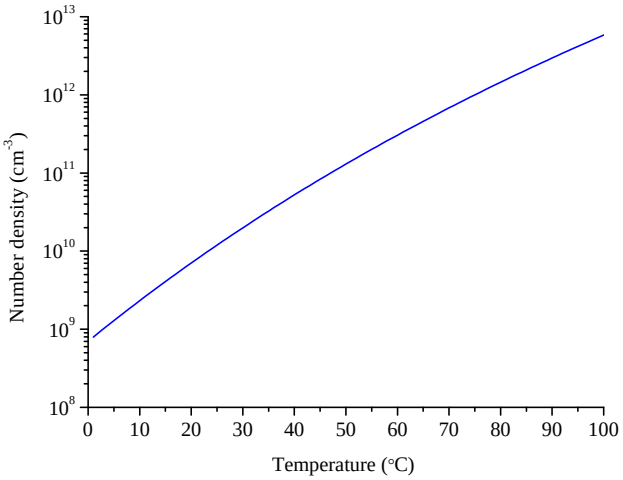

Figure A.1: The number density of Rb vapour.

A.4 Landé g factor

The Zeeman shift of a hyperfine state with quantum number F, with magnetic sublevel m_F, is given by $\Delta f_{\text{Zeem}} = \mu_B g_F m_F B_z$ (98), where B_z is the magnetic field strength and g_F is the Landé g factor given by

$$g_F \simeq g_J \frac{F(F+1) - I(I+1) + J(J+1)}{2F(F+1)}. \tag{A.2}$$

g_J is a further Landé g factor for the total electron angular momentum

$$g_J \simeq 1 + \frac{J(J+1) + S(S+1) - L(L+1)}{2J(J+1)}. \tag{A.3}$$

A.5 Hyperfine structure

The fine structure states $n\mathrm{L}_J$ are split via the hyperfine interaction (91), which is due to the coupling of the electronic angular momentum J and the nuclear spin I. The hyperfine states are defined by the quantum number F. The hyperfine structure of the two D lines in ^{85}Rb and ^{87}Rb are shown in Figure 1.9. The Hyperfine interaction energy is given by

$$E_{HF} = \frac{1}{2}hAK + hB\frac{\frac{3}{2}K(K+1) - 2I(I+1)J(J+1)}{2I(2I-1)2J(2J-1)}, \tag{A.4}$$

where $K = F(F+1) - I(I+1) - J(J+1)$, A is the magnetic dipole coupling constant and B is the electric quadrupole coupling constant. In Cs there has also been evidence of an octupole contribution to this interaction energy (147).

Appendix B

Comb parameters for Rydberg spectroscopy

Table B.1: Comb parameters used for exciting $n\mathrm{P}_{3/2}$ Rydberg levels. For $n \leq 63$ $f_{beat\,3}$ values are from measurements, for $n > 63$ $f_{beat\,3}$ values are from predictions. All frequencies are in megahertz.

n	f'_{rep}	f_o	$f_{beat\,1}$	$f_{beat\,2}$	$f_{beat\,3}$
36	20.137 132	+20.000 000	+19.908 202	+29.453 984	+27.942
39	20.710 296	+20.000 000	- 19.966 124	+30.231 742	+25.690
42	20.018 692	+20.000 000	+20.922 376	+30.549 545	- 29.719
45	21.212 916	+20.000 000	- 20.392 595	- 29.635 668	- 30.329
48	20.027 908	+20.000 000	- 19.969 898	- 29.804 617	- 28.466
51	20.137 132	+20.000 000	+19.908 202	+29.453 984	- 32.792
54	20.284 240	+20.000 000	+20.531 200	- 30.470 499	- 29.928
57	20.165 768	+20.000 000	+20.453 396	- 30.465 736	+27.157
60	20.592 372	+20.000 000	- 19.084 651	+29.814 243	+30.459
63	20.027 908	+20.000 000	- 19.969 898	- 29.804 617	- 25.415
90	20.473 180	+20.000 000	- 20.796 050	+29.804 617	+22
120	20.018 044	+20.000 000	+19.893 721	+29.804 617	- 22
150	20.521 268	+20.000 000	+20.771 228	- 29.804 617	- 24

Table B.2: Comb parameters used for exciting $n\mathrm{F}_{7/2}$ Rydberg levels. For $n \leq 60$ $f_{beat\,3}$ values are from measurements, for $n > 60$ $f_{beat\,3}$ values are from predictions. All frequencies are in megahertz.

n	f'_{rep}	f_o	$f_{beat\,1}$	$f_{beat\,2}$	$f_{beat\,3}$
33	20.492 612	+20.000 000	+20.087 520	+29.406 741	+22.654
36	20.829 548	+20.000 000	- 19.620 841	+29.192 879	- 20.788
39	20.027 908	+20.000 000	- 19.995 898	- 29.770 617	+21.110
42	20.018 692	+20.000 000	+20.896 376	+30.583 545	+20.794
45	20.473 828	+20.000 000	- 19.566 373	+29.461 176	- 25.077
48	20.255 596	+20.000 000	+20.426 924	+29.959 869	- 23.017
51	20.283 592	+20.000 000	+19.344 062	- 30.229 548	- 21.996
54	20.254 948	+20.000 000	+19.280 075	+30.181 110	+23.776
57	20.254 948	+20.000 000	+19.280 075	+30.181 110	- 20.266
60	20.047 324	+20.000 000	+20.372 636	- 30.403 821	+24.337
80	20.858 224	+20.000 000	- 19.179 044	- 30.897 684	+20
100	21.540 444	+20.000 000	- 20.440 383	+30.667 443	+23
110	20.046 676	+20.000 000	+19.355 695	- 30.078 348	+23
115	20.847 696	+20.000 000	+19.126 740	+29.622 180	- 25
120	20.473 180	+20.000 000	- 20.796 050	+29.573 265	- 25
125	20.047 324	+20.000 000	+20.398 636	- 30.403 821	- 21
130	20.046 676	+20.000 000	+19.355 695	- 30.078 348	+24
150	20.046 676	+20.000 000	+19.355 695	- 30.078 348	- 25
200	20.373 440	+20.000 000	+19.817 520	+30.619 680	+24

Appendix C

Comb parameters for D_1 line spectroscopy

Table C.1: Comb parameters used for the D_1 line spectroscopy of ^{85}Rb and ^{87}Rb. f_{beat} values are predictions based on Reference (61). All frequencies are in megahertz.

transition	f'_{rep}	f_o	f_{beat}
b	19.999 760 5826	+20.000 000	+25.000 000
b/d	19.999 517 5064	+20.000 000	+25.000 000
d	19.999 937 3634	+20.000 000	+25.000 000
a	19.999 536 0782	+20.000 000	+25.000 000
a/c	19.999 955 9247	+20.000 000	+25.000 000
c	19.999 712 8255	+20.000 000	+25.000 000
b'	19.999 683 9906	+20.000 000	+25.000 000
b'/d'	19.999 500 3517	+20.000 000	+25.000 000
d'	19.999 979 6505	+20.000 000	+25.000 000
a'	19.999 589 2508	+20.000 000	+25.000 000
a'/c'	20.000 068 5537	+20.000 000	+25.000 000
c'	19.999 884 9131	+20.000 000	+25.000 000

Appendix D

Summary of precision Rb Rydberg measurements

Table D.1: A summary of recent precision measurements of Rb Rydberg states from laser spectroscopy (red) and microwave spectroscopy (blue). The values are compiled from References (80; 81; 157) and the work of this thesis (**bold**). Only measurements giving uncertainties of <1 MHz on the optical frequency E_n are shown.

Isotope	E_i (MHz)	State	δ_0	a
^{85}Rb	**1010 024 723.9(3)**	$S_{1/2}$	3.1311804(10)	0.1784(6)
		$P_{1/2}$	2.6548849(10)	0.2900(6)
		$P_{3/2}$	**2.641 6711(13)**	**0.2968(13)**
			2.641 6737(10)	0.2950(7)
		$D_{3/2}$	1.34809171(40)	-0.60286(26)
		$D_{5/2}$	1.34646572(30)	-0.59600(18)
		$F_{5/2}$	0.0165192(9)	-0.085(9)
		$F_{7/2}$	**0.016 533(12)**	**-0.078(12)**
			0.016 5437(7)	-0.086(7)
		G	**0.00402(8)**	-
			0.00400(9)	-
^{87}Rb	1010 024 892.9(3)	$S_{1/2}$	3.1311807(8)	0.1787(2)
		$P_{1/2}$	-	-
		$P_{3/2}$	-	-
		$D_{3/2}$	1.3480948(11)	-0.6054(4)
		$D_{5/2}$	1.3464622(11)	-0.5940(4)
		$F_{5/2}$	-	-
		$F_{7/2}$	-	-
		G	-	-

Bibliography

[1] T. H. Maiman. Stimulated optical radiation in ruby. *Nature*, 187(4736):493–494, August 1960. 1, 2

[2] C. Borde. Saturated absorption spectroscopy of various molecules using lasers with carbonic gas and nitrogen protoxide. *Comptes Rendus Hebdomadaires des Seances de L'Academie des Sciences Serie B*, 271(6):371, 1970. 1, 4

[3] T. W. Hänsch, M. D. Levenson, and A. L. Schawlow. Complete hyperfine structure of a molecular iodine line. *Physical Review Letters*, 26(16):946–949, April 1971. 1, 4, 5

[4] M. D. Levenson and N. Bloembergen. Observation of two-photon absorption without Doppler broadening on the $3S - 5S$ transition in sodium vapor. *Physical Review Letters*, 32(12):645–648, March 1974. 1, 5

[5] T. W. Hänsch, K. Harvey, G. Meisel, and A. Schawlow. Two-photon spectroscopy of Na $3s-4d$ without Doppler broadening using a cw dye laser. *Optics Communications*, 11(1):50–53, May 1974. 1, 5

[6] Th. Udem, R. Holzwarth, and T. W. Hänsch. Optical frequency metrology. *Nature*, 416(6877):233–237, March 2002. 1, 6, 7, 8

[7] M. Niering, R. Holzwarth, J. Reichert, P. Pokasov, Th. Udem, M. Weitz, T. W. Hänsch, P. Lemonde, G. Santarelli, M. Abgrall, P. Laurent, C. Salomon, and A. Clairon. Measurement of the hydrogen $1S - 2S$ transition frequency by phase coherent comparison with a microwave cesium fountain clock. *Physical Review Letters*, 84(24):5496–5499, June 2000. 1

[8] M. Fischer, N. Kolachevsky, M. Zimmermann, R. Holzwarth, T. W. Hänsch, M. Abgrall, J. Grünert, I. Maksimovic, S. Bize, H. Marion, P. Dos Santos, P. Lemonde, G. Santarelli, P. Laurent, A. Clairon, C. Salomon, M. Haas, U. D. Jentschura, and C. H. Keitel. New limits on the drift of fundamental constants from laboratory measurements. *Physical Review Letters*, 92(23):230802, June 2004. 1, 6

[9] O. Arnoult. Optical frequency measurement of the 1S-3S two-photon transition in hydrogen. *European Physical Journal D*, 60:243–256, September 2010. 1

[10] C. Schwob, L. Jozefowski, B. de Beauvoir, L. Hilico, F. Nez, L. Julien, F. Biraben, O. Acef, J. J. Zondy, and A. Clairon. Optical frequency measurement of the $2S-12D$ transitions in hydrogen and deuterium: Rydberg constant and Lamb shift determinations. *Physical Review Letters*, 82(25):4960–4963, June 1999. 1

[11] R. Pohl, A. Antognini, F. Nez, F. D. Amaro, F. Biraben, J. M. R. Cardoso, D. S. Covita, A. Dax, S. Dhawan, L. M. P. Fernandes, A. Giesen, T. Graf, T. W. Hänsch, P. Indelicato, L. Julien, Cheng-Yang Kao, P. Knowles, E. Le Bigot, Yi-Wei Liu, J. A. M. Lopes, L. Ludhova, C. M. B. Monteiro, F. Mulhauser, T. Nebel, P. Rabinowitz, J. M. F. dos Santos, L. A. Schaller, K. Schuhmann, C. Schwob, D. Taqqu, J. F. C. A. Veloso, and F. Kottmann. The size of the proton. *Nature*, 466(7303):213–216, July 2010. 1, 13

[12] S. Bize, S. A. Diddams, U. Tanaka, C. E. Tanner, W. H. Oskay, R. E. Drullinger, T. E. Parker, T. P. Heavner, S. R. Jefferts, L. Hollberg, W. M. Itano, and J. C. Bergquist. Testing the stability of fundamental constants with the ^{199}Hg+ single-ion optical clock. *Physical Review Letters*, 90(15):150802, April 2003. 1

[13] J. Walz, A. Pahl, K. S. E. Eikema, and T. W. Hänsch. Towards laser spectroscopy of antihydrogen. *Hyperfine Interactions*, 127(1):167–174, August 2000. 1

[14] M. Doser. Precision experiments with antihydrogen: an outlook. *Journal of Physics: Conference Series*, 264(1):012006, January 2011. 1

[15] S. Reinhardt, G. Saathoff, H. Buhr, L. A. Carlson, A. Wolf, D. Schwalm, S. Karpuk, C. Novotny, G. Huber, M. Zimmermann, R. Holzwarth, Th. Udem, T. W. Hänsch, and G. Gwinner. Test of relativistic time dilation with fast optical atomic clocks at different velocities. *Nature Physics*, 3(12):861–864, November 2007. 1

[16] C. Novotny, G. Huber, S. Karpuk, S. Reinhardt, D. Bing, D. Schwalm, A. Wolf, B. Bernhardt, T. W. Hänsch, R. Holzwarth, G. Saathoff, Th. Udem, W. Nörtershäuser, G. Ewald, C. Geppert, T. Kühl, T. Stöhlker, and G. Gwinner. Sub-Doppler laser spectroscopy on relativistic beams and tests of Lorentz invariance. *Physical Review A*, 80(2):022107, August 2009. 1

[17] C. W. Chou, D. B. Hume, T. Rosenband, and D. J. Wineland. Optical clocks and relativity. *Science*, 329(5999):1630–1633, September 2010. 1

[18] H. Muller, A. Peters, and S. Chu. A precision measurement of the gravitational redshift by the interference of matter waves. *Nature*, 463(7283):926–929, February 2010. 1

[19] J. Fraunhofer. Bestimmung des Brechungs- und FarbenzerstreuungsVermoegens verschiedener Glasarten, in Bezug auf die Vervollkommnung achromatischer Fernroehre. *Gilbert's Annalen der Physik*, 56:264–313, 1817. 1

[20] R. W. E. Bunsen. Untersuchungen ueber das Sonnenspektrum und die Spektren der Chemischen Elemente. *Abhandlungen der Kniglich Bhmischen Gesellschaft der Wissenschaften*, 1861, 1863. 2

[21] A. J. Angström. *Recherches sur le spectre solaire*. Upsal: W. Schultz, 1868. 2

[22] J. J. Balmer. Note on the spectral lines of hydrogen. *Annalen der Physik und Chemie*, 25(80), 1885. 2

[23] N. Bohr. On the constitution of atoms and molecules. *Philosophical Magazine*, 26(6):1–25, 1913. 2

[24] W. Demtröder. *Laser spectroscopy*. Springer, November 2002. 2, 7, 35, 36, 167, 187, 196, 203

[25] C. H. Townes and A. L. Schawlow. *Microwave spectroscopy*. McGraw Hill Books, 1955. 2

[26] K. W. Meissner. Application of atomic beams in spectroscopy. *Reviews of Modern Physics*, 14(2-3):68–78, April 1942. 4

[27] W. E. Lamb. Theory of an optical maser. *Physical Review*, 134(6A):A1429–A1450, June 1964. 5

[28] T. W. Hänsch, I. S. Shahin, and A. L. Schawlow. High-resolution saturation spectroscopy of the sodium D lines with a pulsed tunable dye laser. *Physical Review Letters*, 27(11):707–710, September 1971. 5

[29] T. W. Hänsch. Optical resolution of the Lamb shift in atomic hydrogen by laser saturation spectroscopy. *Nature*, 235:63–65, January 1972. 5

[30] T. W. Hänsch, M. H. Nayfeh, S. A. Lee, S. M. Curry, and I. S. Shahin. Precision measurement of the Rydberg constant by laser saturation spectroscopy of the balmer α line in hydrogen and deuterium. *Physical Review Letters*, 32(24):1336–1340, June 1974. 5

[31] C. Wieman and T. W. Hänsch. Doppler-free laser polarization spectroscopy. *Physical Review Letters*, 36(20):1170–1173, May 1976. 5, 56

[32] L. S. Vasilenko. Line Shape of two photon absorption without Doppler broadening. *Letters to the Journal of Experimental and Theoretical Physics*, 12:113–116, 1970. 5

[33] T. W. Hänsch, S. A. Lee, R. Wallenstein, and C. Wieman. Doppler-free two-photon spectroscopy of hydrogen $1S-2S$. *Physical Review Letters*, 34(6):307–309, February 1975. 6

[34] T. W. Hänsch, J. Alnis, P. Fendel, M. Fischer, C. Gohle, M. Herrmann, R. Holzwarth, N. Kolachevsky, Th. Udem, and M. Zimmermann. Precision spectroscopy of hydrogen and femtosecond laser frequency combs. *Philosophical Transactions of the Royal Society A: Mathematical, Physical and Engineering Sciences*, 363(1834):2155–2163, September 2005. 6, 13

[35] A. Javan, W. R. Bennett, and D. R. Herriott. Population inversion and continuous optical maser oscillation in a gas discharge containing a He-Ne mixture. *Physical Review Letters*, 6(3):106–110, February 1961. 7

[36] K. Razdan and D. A. Van Baak. Demonstrating optical beat notes through heterodyne experiments. *American Journal of Physics*, 70(10):1061, October 2002. 7

[37] K. M. Evenson, J. S. Wells, F. R. Petersen, B. L. Danielson, and G. W. Day. Accurate frequencies of molecular transitions used in laser stabilization: the 3.39-μm transition in CH_4 and the 9.33- and 10.18-μm transitions in CO_2. *Applied Physics Letters*, 22(4):192–195, February 1973. 8

[38] H. Schnatz, B. Lipphardt, J. Helmcke, F. Riehle, and G. Zinner. First phase-coherent frequency measurement of visible radiation. *Physical Review Letters*, 76(1):18–21, January 1996. 8

[39] D. E. Spence, P. N. Kean, and W. Sibbett. 60-fsec pulse generation from a self-mode-locked Ti:sapphire laser. *Optics Letters*, 16(1):42–44, January 1991. 8

[40] Th. Udem, J. Reichert, R. Holzwarth, and T. W. Hänsch. Absolute optical frequency measurement of the cesium D_1 line with a mode-locked laser. *Physical Review Letters*, 82(18):3568–3571, May 1999. 10

[41] T. W. Hänsch. Unpublished: Confidential - Proposal for a universal optical frequency comb synthesizer, March 1997. 10, 11

[42] J. K. Ranka, R. S. Windeler, and A. J. Stentz. Visible continuum generation in air-silica microstructure optical fibers with anomalous dispersion at 800 nm. *Optics Letters*, 25(1):25–27, January 2000. 11

[43] D. J. Jones, S. A. Diddams, J. K. Ranka, A. Stentz, R. S. Windeler, J. L. Hall, and S. T. Cundiff. Carrier-envelope phase control of femtosecond mode-locked lasers and direct optical frequency synthesis. *Science*, 288(5466):635–639, April 2000. 11

[44] MenloSystems. *FC1500 Optical Frequency synthesizer operator manual*. Menlo systems GmbH, Munich, Germany, 2007. 12, 43, 46, 48, 49, 93, 104

[45] A. Marian, M. C. Stowe, J. R. Lawall, D. Felinto, and J. Ye. United time-frequency spectroscopy for dynamics and global structure. *Science*, 306(5704):2063–2068, December 2004. 12, 17, 18, 173, 174, 175, 199, 201

[46] J. E. Stalnaker, S. A. Diddams, T. M. Fortier, K. Kim, L. Hollberg, J. C. Bergquist, W. M. Itano, M. J. Delany, L. Lorini, W. H. Oskay, T. P. Heavner, S. R. Jefferts,

F. Levi, T. E. Parker, and J. Shirley. Optical-to-microwave frequency comparison with fractional uncertainty of 10^{-15}. *Applied Physics B: Lasers and Optics*, 89(2):167–176, November 2007. 12

[47] Th. Udem, J. Reichert, R. Holzwarth, and T. W. Hänsch. Accurate measurement of large optical frequency differences with a mode-locked laser. *Opt. Lett.*, 24(13):881–883, July 1999. 12

[48] R. Holzwarth, Th. Udem, T. W. Hänsch, J. C. Knight, W. J. Wadsworth, and P. St. J. Russell. Optical frequency synthesizer for precision spectroscopy. *Physical Review Letters*, 85(11):2264–2267, September 2000. 12

[49] Long-Sheng Ma, Zhiyi Bi, A. Bartels, L. Robertsson, M. Zucco, R. S. Windeler, G. Wilpers, C. Oates, L. Hollberg, and S. A. Diddams. Optical frequency synthesis and comparison with uncertainty at the 10^{-19} level. *Science*, 303(5665):1843–1845, March 2004. 12

[50] M. Zimmermann, C. Gohle, R. Holzwarth, Th. Udem and T. W. Hänsch. Optical clockwork with an offset-free difference-frequency comb: accuracy of sum- and difference-frequency generation. *Opt. Lett.*, 29(3):310–312, February 2004. 12

[51] J. E. M. Goldsmith, E. W. Weber, and T. W. Hänsch. New measurement of the Rydberg constant using polarization spectroscopy of Hα. *Physical Review Letters*, 41(22):1525–1528, November 1978. 13

[52] M. H. Anderson, J. R. Ensher, M. R. Matthews, C. E. Wieman, and E. A. Cornell. Observation of Bose-Einstein condensation in a dilute atomic vapor. *Science*, 269(5221):198–201, July 1995. 13

[53] J. R. Brandenberger, C. A. Regal, R. O. Jung, and M. C. Yakes. Fine-structure splittings in ^2F states of rubidium via three-step laser spectroscopy. *Physical Review A*, 65(4):042510, April 2002. 13, 16, 29

[54] A. K. Mohapatra, T. R. Jackson, and C. S. Adams. Coherent optical detection of highly excited Rydberg states using electromagnetically induced transparency. *Physical Review Letters*, 98(11):113003, March 2007. 13, 16, 26, 28, 82, 89, 128, 129, 152, 153, 156, 157, 158, 164, 171, 208

[55] P. Thoumany, Th. Germann, T. W. Hänsch, G. Stania, L. Urbonas, and Th. Becker. Spectroscopy of rubidium Rydberg states with three diode lasers. *Journal of Modern Optics*, 56(18):2055–2060, August 2009. 13, 16, 26, 28, 29, 33, 54, 65, 69, 70, 82, 89, 112, 128

[56] P. Thoumany, T. W. Hänsch, G. Stania, L. Urbonas, and Th. Becker. Optical spectroscopy of rubidium Rydberg atoms with a 297 nm frequency-doubled dye laser. *Optics Letters*, 34(11):1621–1623, June 2009. 13, 16, 26, 28, 29, 33, 89

[57] J. R. Brandenberger and G. S. Malyshev. Fine-structure splittings in high-lying ^2F states of rubidium via three-step laser spectroscopy. *Physical Review A*, 81(3):032515, March 2010. 13, 16, 26, 28, 70

[58] P. J. Blythe and B. T. H. Varcoe. A cavity-QED scheme for cluster-state quantum computing using crossed atomic beams. *New Journal of Physics*, 8(10):231, October 2006. 13, 27, 89, 96

[59] M. L. Jones, G. J. Wilkes, and B. T. H. Varcoe. Single microwave photon detection in the micromaser. *Journal of Physics B: Atomic, Molecular and Optical Physics*, 42(14):145501, July 2009. 13, 27, 89, 96

[60] D. Meschede, H. Walther, and G. Müller. One-atom maser. *Physical Review Letters*, 54(6):551, February 1985. 13, 26, 96

[61] G. P. Barwood, P. Gill, and W. R. C. Rowley. Frequency measurements on optically narrowed Rb-stabilised laser diodes at 780 nm and 795 nm. *Applied Physics B: Lasers and Optics*, 53(3):142–147, June 1991. 13, 17, 18, 58, 67, 88, 94, 101, 110, 131, 134, 136, 138, 173, 174, 175, 176, 190, 194, 199, 200, 201, 204, 208, 216

[62] A. Banerjee, D. Das, and V. Natarajan. Absolute frequency measurements of the D1 lines in ^{39}K, ^{85}Rb, and ^{87}Rb with 0.1 ppb uncertainty. *Europhysics Letters*, 65(2):172–178, January 2004. 13, 17, 18, 173, 174, 175, 176, 198, 199, 200, 201, 204, 208

[63] D. Das and V. Natarajan. Precise measurement of hyperfine structure in the $5^2P_{1/2}$ state of Rb. *European Physical Journal D*, 37:313–317, March 2006. 13, 18, 175, 176, 194, 199, 200, 201, 204, 208

[64] M. Maric, J. J. Mcferran, and A. N. Luiten. Frequency-comb spectroscopy of the D_1 line in laser-cooled rubidium. *Physical Review A*, 77(3):032502, March 2008. 13, 17, 18, 103, 173, 174, 175, 176, 192, 195, 198, 199, 200, 201, 204, 208

[65] T. F. Gallagher. *Rydberg atoms*. Cambridge University Press, October 1994. 13, 14, 22, 23, 24, 26, 27, 69, 75, 82, 143, 149, 150, 157, 158, 164

[66] K. Afrousheh, P. Bohlouli Zanjani, D. Vagale, A. Mugford, M. Fedorov, and J. D. D. Martin. Spectroscopic observation of resonant electric dipole-dipole interactions between cold Rydberg atoms. *Physical Review Letters*, 93(23):233001, November 2004. 14, 139, 140, 149, 151

[67] M. P. Robinson, B. Laburthe Tolra, M. W. Noel, T. F. Gallagher, and P. Pillet. Spontaneous evolution of Rydberg atoms into an ultracold plasma. *Physical Review Letters*, 85(21):4466–4469, November 2000. 14

[68] V. Bendkowsky, B. Butscher, J. Nipper, J. P. Shaffer, R. Low, and T. Pfau. Observation of ultralong-range Rydberg molecules. *Nature*, 458(7241):1005–1008, April 2009. 14

[69] G. W. F. Drake and R. A. Swainson. Quantum defects and the $1/n$ dependence of Rydberg energies: Second-order polarization effects. *Physical Review A*, 44(9):5448–5459, November 1991. 14, 24

[70] M. S. Safronova, W. R. Johnson, and A. Derevianko. Relativistic many-body calculations of energy levels, hyperfine constants, electric-dipole matrix elements, and static polarizabilities for alkali-metal atoms. *Physical Review A*, 60:4476–4487, December 1999. 14, 17

[71] R. R. Freeman and D. Kleppner. Core polarization and quantum defects in high-angular-momentum states of alkali atoms. *Physical Review A*, 14(5):1614–1619, November 1976. 14, 24, 149, 150

[72] I. S. Lim, J. K. Laerdahl, and P. Schwerdtfeger. The static electric dipole polarizability of Rb+. *Journal of Physics B: Atomic, Molecular and Optical Physics*, 33(3):L91, February 2000. 14, 151, 208

[73] I. Lindgren and A. M. Maartensson. Analysis of the atomic fine structure, using a nonrelativistic many-body and a relativistic central-field approach. *Physical Review A*, 26(6):3249–3267, December 1982. 14

[74] D. Jaksch, J. I. Cirac, P. Zoller, S. L. Rolston, R. Côté, and M. D. Lukin. Fast quantum gates for neutral atoms. *Physical Review Letters*, 85(10):2208–2211, September 2000. 14

[75] M. L. Jones. *Construction of a new micromaser system*. Dphil thesis, University of Sussex, 2008. 14, 27, 65, 89, 128, 180

[76] A. Osterwalder and F. Merkt. Using high Rydberg states as electric field sensors. *Physical Review Letters*, 82(9):1831–1834, March 1999. 14

[77] H. R. Kratz. The principal series of potassium, rubidium, and cesium in absorption. *Physical Review Online Archive (Prola)*, 75(12):1844–1850, June 1949. 14

[78] J. Farley and R. Gupta. Fine-structure measurements in the 6^2F and 7^2F states of rubidium by radio-frequency spectroscopy. *Physical Review A*, 15(5):1952–1957, May 1977. 14

[79] D. Meschede. Centimeter-wave spectroscopy of highly excited rubidium atoms. *Journal of the Optical Society of America B*, 4(3):413–419, March 1987. 14, 15, 75

[80] Wenhui Li, I. Mourachko, M. W. Noel, and T. F. Gallagher. Millimeter-wave spectroscopy of cold Rb Rydberg atoms in a magneto-optical trap: Quantum defects of the *ns*, *np*, and *nd* series. *Physical Review A*, 67(5):052502, May 2003. 15, 27, 75, 87, 98, 100, 123, 125, 127, 138, 159, 207, 217

[81] Jianing Han, Yasir Jamil, D. V. L. Norum, P. J. Tanner, and T. F. Gallagher. Rb nf quantum defects from millimeter-wave spectroscopy of cold ^{85}Rb Rydberg atoms. *Physical Review A*, 74(5):054502, November 2006. 15, 27, 75, 83, 84, 85, 87, 98, 100, 123, 125, 127, 138, 139, 140, 141, 149, 150, 151, 159, 207, 217

[82] S. A. Lee, J. Helmcke, J. L. Hall, and B. P. Stoicheff. Doppler-free two-photon transitions to Rydberg levels: convenient, useful, and precise reference wavelengths for dye lasers. *Optics Letters*, 3(4):141–143, October 1978. 15, 27, 100, 125, 127, 206, 207, 209, 210

[83] C. J. Sansonetti and K. H. Weber. High-precision measurements of Doppler-free two-photon transitions in Rb: new values for proposed dye-laser reference wavelengths. *Journal of the Optical Society of America B*, 2(9):1385–1391, September 1985. 15, 100, 125, 127, 207

[84] K. C. Harvey and B. P. Stoicheff. Fine structure of the n^2D series in rubidium near the ionization limit. *Physical Review Letters*, 38(10):537–540, March 1977. 15, 27

[85] B. P. Stoicheff and E. Weinberger. Doppler-free two-photon absorption spectrum of rubidium. *Canadian Journal of Physics*, 57(12):2143–2154, July 1979. 15, 27, 127, 207, 209, 210

[86] C. J. Lorenzen and K. Niemax. Quantum defects of the $n^2P_{1/2,3/2}$ levels in ^{39}K I and ^{85}Rb I. *Physica Scripta*, 27(4):300–305, February 1983. 15, 27, 125, 127, 207

[87] B. Sanguinetti, H. O. Majeed, M. L. Jones, and B. T. H. Varcoe. Precision measurements of quantum defects in the $nP_{3/2}$ Rydberg states of ^{85}Rb. *Journal of Physics B: Atomic, Molecular and Optical Physics*, 42(16):165004, August 2009. 15, 27, 52, 79, 84, 85, 121, 125, 127, 180, 207

[88] A. Ferguson and M. Dunn. Detection of the Rydberg states of rubidium using a frequency doubled CW dye laser. *Optics Communications*, 23(2):227–230, November 1977. 15, 28

[89] Yoshiaki Kato and B. P. Stoicheff. Two-photon absorption to highly excited D states of Rb atoms. *Journal of the Optical Society of America*, 66(5):490–492, May 1976. 15, 28, 209, 210

[90] I. Johansson. Spectra of the alkali metals in the lead-sulphide region. *Arkiv foer Fysik*, 20:135–146, 1961. 16, 54, 84, 86, 87, 207

[91] E. Arimondo, M. Inguscio, and P. Violino. Experimental determinations of the hyperfine structure in the alkali atoms. *Reviews of Modern Physics*, 49(1):31–75, January 1977. 17, 30, 80, 125, 174, 175, 176, 193, 212

[92] J. Ye, S. Swartz, P. Jungner, and J. L. Hall. Hyperfine structure and absolute frequency of the ^{87}Rb $5P_{3/2}$ state. *Optics Letters*, 21(16):1280, August 1996. 17, 18, 88, 173, 174, 175, 176, 186, 187, 197, 200, 201, 202

[93] J. R. Beacham and K. L. Andrew. Optical study of the hyperfine structure of the rubidium resonance lines. *Journal of the Optical Society of America*, 61(2):231–235, February 1971. 17, 200

[94] A. Banerjee, D. Das, and V. Natarajan. Precise frequency measurements of atomic transitions by use of a Rb-stabilized resonator. *Optics Letters*, 28(17):1579–1581, September 2003. 17, 18, 138, 173, 174, 175, 176

[95] U. D. Rapol, A. Krishna and V. Natarajan. Precise measurement of hyperfine structure in the state of Rb. *European Physical Journal D*, 23:185–188, April 2003. 18, 175, 176

[96] L. A. M. Johnson, H. O. Majeed, B. Sanguinetti, Th. Becker, and B. T. H. Varcoe. Absolute frequency measurements of ^{85}Rb $n\mathrm{F}_{7/2}$ Rydberg states using purely optical detection. *New Journal of Physics*, 12(6):063028, June 2010. 19, 54, 125, 127

[97] L. A. M. Johnson, H. O. Majeed, and B. T. H. Varcoe. A three-step laser stabilisation scheme for excitation to Rydberg levels in ^{85}Rb.
Applied Physics B: Lasers and Optics, 106(2):257–260, November 2011. 19, 88

[98] C. J. Foot. *Atomic Physics (Oxford Master Series in Atomic, Optical and Laser Physics)*. Oxford University Press, USA, February 2005. 25, 31, 35, 36, 41, 75, 82, 192, 195, 196, 209, 211, 212

[99] S. A. Bhatti, C. L. Cromer, and W. E. Cooke. Analysis of the Rydberg character of the $5d7d\,^1D_2$ state of barium. *Physical Review A*, 24(1):161–165, July 1981. 25

[100] M. L. Zimmerman, M. G. Littman, M. M. Kash, and D. Kleppner. Stark structure of the Rydberg states of alkali-metal atoms. *Physical Review A*, 20(6):2251–2275, December 1979. 25

[101] B. V. Numerov. Note on the numerical integration of $d^2x/dt^2 = f(xt)$. *Astronomische Nachrichten*, 230:359–364, 1927. 25, 31

[102] H. Dehmelt. Mono-ion oscillator as potential ultimate laser frequency standard. *IEEE transactions on instrumentation and measurement*, 31(2):83–87, 1982. 32

[103] U. Volz and H. Schmoranzer. Precision lifetime measurements on alkali atoms and on helium by beam-gas-laser spectroscopy. *Physica Scripta Volume T*, 65:48–56, January 1996. 33, 37, 191

[104] D. Sheng, A. Pérez Galván, and L. A. Orozco. Lifetime measurements of the $5d$ states of rubidium. *Physical Review A*, 78(6):062506, December 2008. 33, 37

[105] S. N. Sandhya and K. K. Sharma. Atomic coherence effects in four-level systems: Doppler-free absorption within an electromagnetically-induced-transparency window. *Physical Review A*, 55(3):2155–2158, March 1997. 34, 42, 171

[106] D. McGloin. Electromagnetically induced transparency in N-level cascade schemes. *Optics Communications*, 190(1-6):221–229, April 2001. 34, 171

[107] J. J. Olivero and R. L. Longbothum. Empirical fits to the Voigt line width: A brief review. *Journal of Quantitative Spectroscopy and Radiative Transfer*, 17(2):233–236, February 1977. 38, 117

[108] P. R. Berman. Effects of collisions on linear and non-linear spectroscopic line shapes. *Physics Reports*, 43(3):101–149, July 1978. 41

[109] J. G. Banacloche, Yong Q. Li, Shao Z. Jin, and Min Xiao. Electromagnetically induced transparency in ladder-type inhomogeneously broadened media: Theory and experiment. *Physical Review A*, 51(1):576–584, January 1995. 41, 115, 116

[110] M. Fleischhauer, A. Imamoglu, and J. P. Marangos. Electromagnetically induced transparency: Optics in coherent media. *Reviews of Modern Physics*, 77(2):633–673, July 2005. 41, 42, 62, 116

[111] S. H. Autler and C. H. Townes. Stark effect in rapidly varying fields. *Physical Review Online Archive (Prola)*, 100(2):703–722, October 1955. 42, 62, 116, 169

[112] A. M. Akulshin, R. J. McLean, A. I. Sidorov, and P. Hannaford. Coherent and collimated blue light generated by four-wave mixing in Rb vapour. *Optics Express*, 17(25):22861–22870, December 2009. 42, 59

[113] R. L. Barger and J. L. Hall. Pressure shift and broadening of methane line at 3.39 μm studied by laser-saturated molecular absorption. *Physical Review Letters*, 22(1):4–8, January 1969. 47

[114] G. Kramer and W. Klische. Extra high precision digital phase recorder. *Frequency and Time Forum, 2004. EFTF 2004. 18th European*, 595–602, April 2004. 48

[115] B. R. Walton, H. S. Margolis, V. Tsatourian, and P. Gill. Transportable optical frequency comb based on a mode-locked fibre laser. *IET Optoelectronics*, 2(5):182, October 2008. 48, 102, 137, 197

[116] R. W. Fox, S. A. Diddams, A. Bartels, and L. Hollberg. Optical frequency measurements with the global positioning system:tests with an iodine-stabilized He-Ne laser. *Applied Optics*, 44(1):113–120, January 2005. 48, 203

[117] Stanford Research Systems. *PRS10 Rubidium frequency standard data sheet*. Stanford Research Systems Inc, Sunnyvale, CA, 2011. 49

[118] D. W. Allan. Statistics of atomic frequency standards. *Proceedings of the IEEE*, 54(2):221–230, February 1966. 50, 51, 52, 57, 96, 97, 108, 185, 190

[119] M. Fischer, Menlosystems, private correspondence. 2010. 50

[120] HighFinesse. *WS7 wavemeter user manual*. HighFinesse GmbH, Tübingen, Germany, 2007. 51, 79

[121] B. Sanguinetti. *Building a modern micromaser: atoms and cavities*. PhD thesis, University of Leeds, 2009. 52, 56, 65, 66, 88, 94, 110, 116

[122] H. Majeed. *Rubidium Rydberg spectroscopy for the micromaser*. PhD thesis, University of Leeds, 2009. 56, 65, 66, 88

[123] F. Nez. Optical frequency determination of the hyperfine components of the $5S_{1/2}$-$5D_{3/2}$ two-photon transitions in rubidium. *Optics Communications*, 102(5-6):432–438, October 1993. 59, 75, 80, 94, 101, 110, 112, 125, 131, 134, 164, 197

[124] W. T. Hill and C. H. Lee. *Light-matter interaction: Atoms and molecules in external fields and nonlinear optics*. Wiley-VCH, 1st edition, January 2007. 76, 123

[125] H. E. White and A. Y. Eliason. Relative intensity tables for spectrum lines. *Physical Review Online Archive*, 44(9):753–756, November 1933. 76

[126] H. Wahlquist. Modulation broadening of unsaturated Lorentzian lines. *The Journal of Chemical Physics*, 35(5):1708–1710, April 1961. 78, 79, 204

[127] M. Saffman, T. G. Walker, and K. Mølmer. Quantum information with Rydberg atoms. *Reviews of Modern Physics*, 82(3):2313–2363, August 2010. 80, 126, 159, 161, 164

[128] W. C. Martin. Series formulas for the spectrum of atomic sodium (Na I). *Journal of the Optical Society of America*, 70(7):784–788, July 1980. 83, 84

[129] R. P. Abel, A. K. Mohapatra, M. G. Bason, J. D. Pritchard, K. J. Weatherill, U. Raitzsch, and C. S. Adams. Laser frequency stabilization to excited state transitions using electromagnetically induced transparency in a cascade system. *Applied Physics Letters*, 94(7):071107, February 2009. 89, 98

[130] P. B. Zanjani, K. Afrousheh, and J. D. D. Martin. Optical transfer cavity stabilization using current-modulated injection-locked diode lasers. *Review of Scientific Instruments*, 77(9):093105, September 2006. 89

[131] A. Weis and S. Derler. Doppler modulation and Zeeman modulation: laser frequency stabilization without direct frequency modulation. *Applied Optics*, 27(13):2662–2665, July 1988. 94

[132] Won-Kyu Lee, Dae-Su Yee, and Ho S. Suh. Direct frequency counting with enhanced beat signal-to-noise ratio for absolute frequency measurement of a He-Ne/I_2 laser at 633 nm. *Applied Optics*, 46(6):930–934, February 2007. 99, 102, 104

[133] F. Du Burck and O. Lopez. Correction of the distortion in frequency modulation spectroscopy. *Measurement Science and Technology*, 15(7):1327, July 2004. 102

[134] D. Tong, S. M. Farooqi, E. G. M. van Kempen, Z. Pavlovic, J. Stanojevic, R. Côté, E. E. Eyler, and P. L. Gould. Observation of electric quadrupole transitions to Rydberg *nd* states of ultracold rubidium atoms. *Physical Review A*, 79(5):052509, May 2009. 147

[135] R. M. Sternheimer. Quadrupole polarizabilities of various ions and the alkali atoms. *Physical Review A*, 1(2):321–327, February 1970. 151

[136] M. A. Bouchiat, J. Guéna,Ph. Jacquier, M. Lintz, and A. V. Papoyan Electrical conductivity of glass and sapphire cells exposed to dry cesium vapor. *Applied Physics B: Lasers and Optics*, 68(6):1109–1116, April 1999. 156, 157, 158

[137] M. G. Bason, M. Tanasittikosol, A. Sargsyan, A. K. Mohapatra, D. Sarkisyan, R. M. Potvliege, and C. S. Adams. Enhanced electric field sensitivity of RF-dressed Rydberg dark states. *New Journal of Physics*, 12(6):065015, June 2010. 157, 158

[138] H. Mayer. Photoelectric and optical properties of thin alkali metal films. *Thin Solid Films*, 5:389–406, June 1970. 157

[139] B. P. Stoicheff and E. Weinberger. Frequency shifts, line broadenings, and phase-interference effects in Rb**+Rb collisions, measured by Doppler-free two-photon spectroscopy. *Physical Review Letters*, 44(11):733–736, March 1980. 161

[140] Thad G. Walker and M. Saffman. Consequences of Zeeman degeneracy for the van der Waals blockade between Rydberg atoms. *Physical Review A*, 77(3):032723, March 2008. 161

[141] M. D. Lukin, M. Fleischhauer, R. Cote, L. M. Duan, D. Jaksch, J. I. Cirac, and P. Zoller. Dipole blockade and quantum information processing in mesoscopic atomic ensembles. *Physical Review Letters*, 87(3):037901, June 2001. 162

[142] Thorlabs *Gas reference cells, technical specifications.* *http://www.thorlabs.com*, 07/2011 168

[143] B. J. Wundt and U. D. Jentschura. Proposal for the determination of nuclear masses by high-precision spectroscopy of Rydberg states. *Journal of Physics B: Atomic, Molecular and Optical Physics*, 43(11):115002, June 2010. 171

[144] A. J. Wallard. Frequency stabilization of the helium-neon laser by saturated absorption in iodine vapour. *Journal of Physics E: Scientific Instruments*, 5(9):926, September 1972. 179, 202

[145] M. P. Hill. *A test of Special Relativity using coherent optical phenomena.* PhD thesis, University of Leeds, November 2009. 179, 183

[146] J. P. Cotter. *A precision test of Relativity using coherent optical phenomena.* PhD thesis, University of Leeds, June 2008. 179, 183

[147] D. Das and V. Natarajan. High-precision measurement of hyperfine structure in the D lines of alkali atoms. *Journal of Physics B: Atomic, Molecular and Optical Physics*, 41(3):035001, February 2008. 179, 213

[148] Saes Getters. *http://www.saesgetters.com*, 8/2011. 180

[149] T. M. Roach and D.Henclewood. Novel rubidium atomic beam with an alkali dispenser source. *Journal of Vacuum Science & Technology A: Vacuum, Surfaces, and Films*, 22(6):2384–2387, October 2004. 180

[150] U. D. Rapol, A. Wasan, and V. Natarajan. Loading of a Rb magneto-optic trap from a getter source. *Physical Review A*, 64(2):023402, June 2001. 180

[151] E. A. Donley, T. P. Heavner, F. Levi, M. O. Tataw, and S. R. Jefferts. Double-pass acousto-optic modulator system. *Review of Scientific Instruments*, 76(6), June 2005. 183

[152] I. S. Grant and W. R. Phillips. *Electromagnetism.* Wiley-Blackwell, 2nd edition, 1990. 188

[153] S. Falke, E. Tiemann, C. Lisdat, H. Schnatz, and G. Grosche. Transition frequencies of the D lines of ^{39}K , K^{40} and ^{41}K measured with a femtosecond laser frequency comb. *Physical Review A*, 74(3):032503, September 2006. 196

[154] R. Grimm and J. Mlynek. The effect of resonant light pressure in saturation spectroscopy. *Applied Physics B: Lasers and Optics*, 49(3):179–189, September 1989. 196

[155] S. Park. Dispersion-like signals in velocity-selective saturated-absorption spectroscopy. *Optics Communications*, 192(1-2):49–55, May 2001. 202, 208

[156] J. L. Hall and C. J. Bordé. Shift and broadening of saturated absorption resonances due to curvature of the laser wave fronts. *Applied Physics Letters*, 29(12):788–790, December 1976. 202

[157] M. Mack, F. Karlewski, H. Hattermann, S. Höckh, F. Jessen, D. Cano, and J. Fortágh. Measurement of absolute transition frequencies of ^{87}Rb to ns and nd Rydberg states by means of electromagnetically induced transparency. *Physical Review A*, 83(5):052515, May 2011. 208, 209, 210, 217

[158] D. A. Steck. Rubidium 85 D Line Data. *http://steck.us/alkalidata/rubidium85numbers.pdf*, September 2011. 211

[159] D. A. Steck. Rubidium 87 D Line Data. *http://steck.us/alkalidata/rubidium87numbers.pdf*, September 2011. 211

[160] T. J. Killian. Thermionic phenomena caused by vapors of rubidium and potassium. *Physical Review Online Archive (Prola)*, 27(5):578–587, May 1926. 211